UNIVERSITY *of*
TASMANIA
AUSTRALIA

School of Physical Sciences

Dynamics and Synchrotron Emission from Radio-loud AGN

Ross James Turner
B.Sc. (Hons.)

June 2017

Submitted in fulfilment of the requirements for the Degree of
Doctor of Philosophy

Declaration

This thesis contains no material which has been accepted for a degree or diploma by the University or any other institution, except by way of background information and duly acknowledged in this thesis, and to the best of my knowledge and belief no material previously published or written by another person except where due acknowledgement is made in the text of the thesis, nor does the thesis contain any material that infringes copyright.

Specifically, some of the material in the literature review has previously been presented in my honours thesis, but is included for completeness, and the work in the second chapter has been published in the Astrophysical Journal.

This thesis may be made available for loan and limited copying in accordance with the Copyright Act 1968.

Signed:

June 26, 2017

Acknowledgements

This thesis would not have been possible without the help of a number of people, who provided valuable support at both a professional and personal level. I am indebted to them all.

First and foremost I would like to thank my supervisors Dr Stanislav Shabala and Prof Simon Ellingsen for their unwavering support and encouragement over the past three years. The 'slav's enthusiasm, feedback and support in particular has been invaluable throughout this project. Simon's help and advice securing funding and navigating the endless bureaucracy has been greatly appreciated. I am also grateful to Dr habil Martin Krause for his help in learning how to implement and run hydrodynamical simulations. I would further like to acknowledge the support of my CASS co-supervisor Dr Josh Marvil in helping me gain observing experience and secure travel funding.

During my candidature I have supervised the summer research project of Payton Rodman who explored the cause of the radio asymmetries in Radio Galaxy Zoo objects, and a project with fellow PhD student Jonathan Rogers who examined the spatial distribution of synchrotron electrons in low-powered radio sources. I am grateful both for the experience I have gained and contributions these students have made towards my work.

The opportunity to be duty astronomer at the Compact Array and participate in the observing projects of Elaine Sadler and Minh Huynh has greatly enhanced my connections to the wider Australian astronomy community. I also appreciated participating in the locally run AuScope VLBI observing project which has provided further observational experience.

While undertaking this research I have been a recipient of the University of Tasmania Elite Research Scholarship and a CSIRO Astronomy and Space Science studentship. This recognition and financial support has been very much appreciated.

I wish to thank Prof John Dickey, Prof Simon Ellingsen, Prof Larry Forbes and Dr Michael Brideson for entrusting me with the responsibility of lecturing and tutoring over ten mathematics and physics units over the course of my candidature. This has been a rewarding experience enabling me to interact with many of the undergraduate students and develop confidence in presenting to large audiences.

I am grateful for all the wonderful friends I have made whilst at the University of Tasmania. They have made my PhD an unforgettable experience, both professionally and socially. In particular, Daniel Reardon who I have had countless adventures with

including live comedies, snowboarding and visiting Canberra for the first time, and Frank Torok with whom I spent three weeks travelling around South America and am welcomed by his family each time I visit him in Sydney. I would also like to acknowledge my fellow PhD students Jonathan Rogers, Tristan Stark, Lucas Hyland and Jesse Swan who have been endlessly entertaining both at and outside of work.

And finally, I would like to thank my family, especially Mum and Dad, for all their support and encouragement over the years. But there is of course one other person I could not possibly forget, my loyal cat Peri. She sat with me through the wee hours of the morning whilst I toiled away researching and writing my thesis.

Abstract

I present a new analytical model describing the dynamics and luminosity evolution of Fanaroff-Riley type I and II radio active galactic nuclei (AGN), and the transition between these classes. The galaxy environments of a volume-limited low redshift ($0.03 \leqslant z \leqslant 0.1$) sample of observed AGN are quantified using a semi-analytic galaxy formation model, and the model applied to these objects to determine their distribution of jet powers and active lifetimes at the present epoch. This technique is refined for radio sources in the 3C survey with multi-frequency spectral coverage by including a constraint on the magnetic field strength. Further, the ability of the model to correct for selection biases in future surveys is investigated by performing detailed modelling of the spatial distribution of synchrotron electrons within the radio lobes. Finally, I apply the model to simulated and observed extended radio galaxies to construct standardisable candles.

Results of this AGN evolution model show that radio sources in massive galaxies remain active for longer, spend less time in the quiescent phase, and inject more energy into their hosts than their less massive counterparts. The jet power is independent of the host stellar mass within model uncertainties, consistent with the maintenance-mode AGN feedback paradigm. The environments of these AGN are in or close to long-term heating-cooling balance. I also examine the properties of high- and low-excitation radio galaxy sub-populations. The HERGs are younger than LERGs by an order of magnitude, whilst their jet powers are greater by a factor of four on average. The Eddington-scaled accretion rates and jet production efficiencies of these populations are consistent with LERGs being powered by radiatively inefficient advection dominated accretion flows (ADAFs), with HERGs being fed by a radiatively efficient accretion mechanism.

Kinetic jet power estimates based exclusively on observed monochromatic radio luminosities are highly uncertain due to confounding variables and a lack of knowledge about some aspects of the physics of radio AGNs. I present a new methodology to calculate the jet powers of the largest, most powerful radio sources based on combinations of their size, lobe luminosity and shape of their radio spectrum. An improvement on existing models is in parametrising the magnetic field strength in the radio lobes. The derived magnetic field strengths are inconsistent with equal energy in the particles and the fields at the 5σ level. Further, I find that jet kinetic power and field strengths can be reasonably well estimated even for unresolved sources, whilst source ages require an accurate size measurement.

Numerical simulations capture complex dynamics while analytical models are good at describing synchrotron loss processes. I combine these two approaches by implementing numerical dynamics for the flow of synchrotron electron packets whilst modelling their emissivity analytically. I have developed a lossy synchrotron emissivity model which traces the evolutionary histories of individual fluid particles. The limitations of future radio surveys when measuring AGN energetics are quantified using this model. In particular, the observed size of FR-I sources is found to depend on the survey sensitivity. At least some sources in the emerging class of FR0 objects (comprising GPS and CSS sources) can potentially be explained by a population of low-powered FR-Is.

Bright radio-loud AGNs provide an opportunity to construct standard candles detectable to high ($z \gtrsim 2$) redshifts. I present a new technique for creating standardisable candles, based on radio-frequency observations of the most powerful AGNs; specifically their radio flux density, lobe angular size, and radio spectrum. This technique is used to measure the distances to radio sources in the 3C and HeRGE surveys. These radio AGN standardisable candles are shown to be inconsistent with a non-accelerating universe at greater than the 6σ level, but are consistent with a flat universe. Dark energy and matter densities of $\Omega_{\rm m} = 0.289 \pm 0.012$ and $\Omega_{\Lambda} = 0.711 \pm 0.012$ are obtained, consistent with those found from baryon acoustic oscillations, CMB measurements and JLA type 1a supernovae. I further show that this distance measure provides accurate photometric redshifts for radio AGNs based exclusively upon multi-frequency radio observations.

Table of Contents

Chapter 1

Introduction

The measurement of our cosmology through various astrophysical techniques is crucial to understanding the origin of our universe and the formation of large-scale structure. Very large simulations of the formation history of dark matter haloes provide a platform for modelling the evolution of galaxies and their central supermassive black holes. The interaction between the central black hole, or active galactic nucleus (AGN), and its host galaxy needs to be considered to reconcile observations with models. This interaction or feedback process is dominated at recent cosmic times by the heating from jet inflated radio lobes emanating outwards from the central active nucleus. Knowledge of the physical properties, including kinetic power and lifecycles, of these jets is vital for quantifying the energetics of AGN feedback and its effect on the host galaxy formation and evolution. In this introductory chapter, I provide an overview of some of the key concepts underpinning the development and application of a new radio source evolution model, including: the current concordance cosmology, semi-analytic galaxy evolution models, AGN and their feedback mechanisms, and radio source lobe morphology.

1.1 Concordance cosmology

The origin of the universe and the formation of large-scale structures comprising galaxies is understood through models of cosmology. The concordance cosmology has been settled on through extensive observations of a diverse range of astronomical bodies including supernovae, galaxy clusters, quasars, and radiation emitted at the time of recombination.

1.1.1 Finding our cosmology

Following the discovery of the expanding universe by Hubble (1929) in the early twentieth century, cosmologists concentrated on measuring the slowing of expansion caused by gravity. For the next seven decades, the accepted form of Einstein's General Relativity postulated a universe comprising only ordinary matter and radiation, and whose expansion rate slows due to gravity. However, in 1998 two teams studying distant type 1a supernovae, the *Supernova Cosmology Project* and the *High-z SN Search*, independently concluded that expansion has been speeding up for the past 5 Gyr (Riess et al. 1998; Perlmutter et al. 1999). The discovery of this cosmic acceleration presented a significant problem, necessitating a seismic shift in our understanding of the physics of the cosmos. The two possibilities were that either: (1) approximately 70% of the energy density of the universe is found in some form of large negative pressure, or (2) that General Relativity breaks down on cosmological scales.

The negative pressure, termed dark energy, is associated with Einstein's cosmological constant Lambda (Λ) in current cosmological models. Einstein originally included this term as a mathematical fix to his General Relativity theory in order to obtain a static (no expansion or contraction) and finite universe (Einstein 1917). The cosmological constant was therefore dismissed upon the discovery of the expanding universe; but Zel'dovich (1968) realised that Lambda, mathematically equivalent to the energy density of empty space or a vacuum, could not be ignored. This vacuum space is actually not completely empty but filled with virtual particles; their effects have been measured in particle masses and the shifts of atomic lines. A major outstanding problem is that the cosmological constant predicted from the vacuum energy using quantum field theory is at least 100 orders of magnitude too large (Carroll 2001).

The strong observational evidence for cosmic acceleration, and thus indirectly Einstein's constant, has led cosmologists to adopt the so called ΛCDM model (Lambda cold dark matter; e.g. Spergel et al. 2007; Planck Collaboration 2016). The universe is accelerating, close to spatially flat, and composed of baryons, dark matter, and dark energy. At a much earlier epoch it underwent a rapid expansion phase known as inflation, which produced density and cosmic microwave background (CMB) radiation anisotropies from quantum fluctuations; gravitational instability of these density perturbations subsequently led to the formation of large-scale structure. The ΛCDM cosmological model is remarkably consistent with measurements of cosmic structure over a wide range of length and times scales. This model can simultaneously match the CMB fluctuations at $z \sim 1000$ and the structure seen in the $z = 3$ Lyα forest. The model results are also consistent with the present mass budget of the universe, the

observed baryonic fraction in rich clusters, and the theory of big bang nucleosynthesis.

1.1.2 Measurement techniques

Evidence for an accelerating universe, and constraints on the energy and matter content of the universe, have only strengthened since the original supernova measurements. Other observational techniques including anisotropies in the cosmic microwave background, baryon acoustic oscillations, optical quasars, and the gas fraction in clusters, together place very tight constraints on our cosmology.

Cosmic microwave background

The discovery of dark energy from measurements of the anisotropies in the cosmic microwave background (CMB) provided one of the first independent confirmations of the accelerating universe (Jaffe et al. 2001; Pryke et al. 2002). The CMB anisotropies probe the universe before the formation of large-scale structure at a time when photons were decoupling from matter (recombination); this occurred approximately 380 000 years after the Big Bang (Hu & Dodelson 2002). The angular power spectrum of anisotropies in the CMB temperature (or magnetic field) is dominated by peaks from gravity-driven sound waves in the photon-baryon fluid present at the time of recombination (see Figure 1.1). Theoretical ΛCDM spectra fitted to the acoustic peaks of the power spectrum enable this technique to retrieve cosmological parameters. The WMAP and *Planck* space probes have both found a spatially flat universe within measurement uncertainties (Spergel et al. 2007; Planck Collaboration 2016).

BAO and large-scale structure

The acoustic oscillation of the baryonic matter seen in the CMB anisotropies persists throughout cosmic time in the large-scale structure, in particular in the clustering of galaxies. A sharp feature in the two-point correlation function at a scale $\sim 100\,\mathrm{Mpc}$ (the BAO scale; an uncalibrated standard ruler) was first measured in SDSS luminous red galaxies, constraining the distance to redshift $z = 0.35$ to within 5% (Eisenstein et al. 2005). High-precision BAO measurements from galaxy clustering and the Lyman-α forest in the SDSS-III *Baryon Oscillation Spectroscopic Survey* (BOSS) provide a high confidence detection of dark energy (Aubourg et al. 2015).

The properties of the large-scale structure are also probed through the weak gravitational lensing of galaxies by this intervening dark matter structure (e.g. Kwan et al.

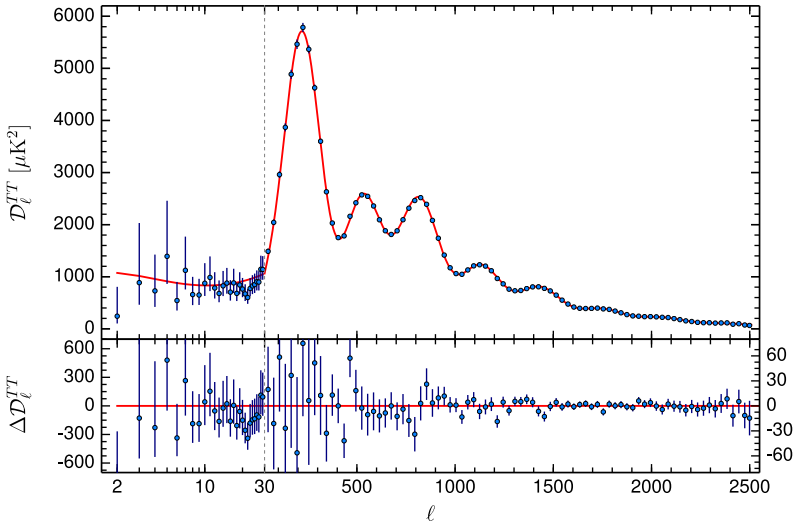

Figure 1.1: *Planck 2015* angular power spectrum measurements of the CMB temperature fluctuations as a function of the multipole ℓ. The best fit ΛCDM theoretical spectrum fitted to the power spectrum is plotted in red in the upper panel. Residuals with respect to this model are shown in the lower panel with 1σ errorbars. From Planck Collaboration (2016).

2017). Lensing is a powerful technique for mapping the density of dark matter and its clustering, in addition to constraining the amplitude of the primordial quantum fluctuations. Both lensing and baryon acoustic oscillations are frequently combined with CMB measurements to provide approximately orthogonal constraints (Planck Collaboration 2016).

Type 1a supernovae

Type 1a supernovae are a class of supernova that occur in binary systems, and produce a characteristic light curve that can be used to construct standardisable candles (Phillips 1993, see Figure 1.2). However, several concerns exist about the robustness of supernovae evidence for acceleration; it was suggested the distant supernovae may be fainter due to dust extinction, not acceleration (Drell et al. 2000), though this is now disfavoured (Riess et al. 2007). More concerning is that ultraviolet and optical photometry of low-redshift type 1a supernovae has uncovered two distinct colour groups, composed of NUV-red and NUV-blue events. The relative proportion of these two classes in the supernovae population changes with redshift, producing a distance bias that increases with redshift and could significantly bias measurements of cosmological parameters (Milne et al. 2015). Supernovae observed on current 8m class optical telescopes (Gemini, VLT, Keck) to consider the effect of these biases find weaker evidence for an accelerating universe (Nielsen et al. 2016), though are consistent with the higher precision measurements of the other techniques.

X-ray clusters

Measurements of the gas fraction in galaxy clusters, $f_{\rm gas}$, can also be used to measure the dark energy density. The value calculated for the gas fraction depends on observations of the X-ray flux and temperature but also varies with the distance to the cluster. Galaxy clusters are assumed to have a constant gas fraction throughout cosmic time, which is nearly equal to the baryon fraction of the universe; i.e. $f_{\rm gas} \approx \Omega_{\rm b}/\Omega_{\rm m}$, the ratio of the baryon density $\Omega_{\rm b}$ to total matter density $\Omega_{\rm m}$. The cosmology which produces distances that make the apparent $f_{\rm gas}$ constant in redshift is therefore taken as the best estimate. Allen et al. (2008) used observations from the *Chandra X-ray Observatory* to obtain a value for the dark energy density consistent with the supernovae measurements.

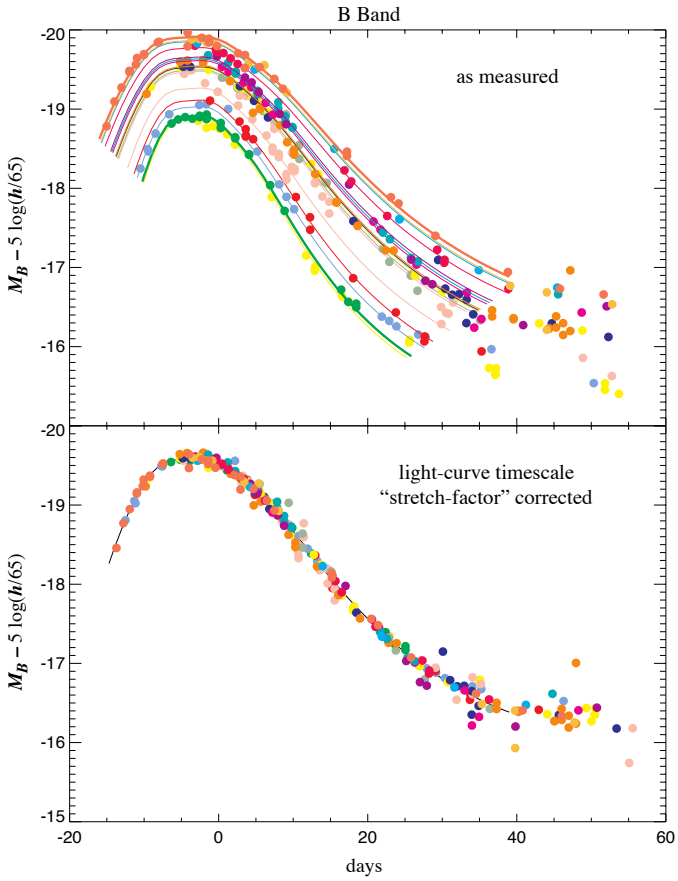

Figure 1.2: B-band light curves for low-redshift type 1a supernovae from the Calan-Tololo survey (Hamuy et al. 1996) before and after a one-parameter correction for the brightness-decline correlation (top and bottom panel respectively). From Kim (2004).

Optical quasars

Quasars, or the more general active galactic nuclei (AGNs) class, have proved a tantalising opportunity to construct standard candles for cosmology since their discovery over five decades ago. Crucially AGNs are very numerous with between 10 and 30 per cent of all large galaxies hosting an active nucleus at their centre (Best et al. 2007), whilst their high luminosities can be detected from the present epoch out to the early universe at $z > 7$. These characteristics make AGNs ideal tools for constraining cosmology if their flux density, size or emission lines can be used to create standardisable candles.

There are currently several methods being explored to construct optical AGN standard candles. Watson et al. (2011) showed that the cosmological parameters can be constrained using the known relation between AGN optical luminosity and the size of the broad emission line region based on $z < 0.3$ quasars (see also Haas et al. 2011; Czerny et al. 2013; King et al. 2014). The time lag between the optical continuum and the dust continuum is also found to correlate with luminosity and thus too can be used to construct a standard candle (e.g. Oknyanskij et al. 1999; Oknyanskij & Horne 2001; Hönig et al. 2014; Yoshii et al. 2014). The broad emission line lags can be measured out to redshift $z > 4$ (e.g. King et al. 2014, 2015), whereas the more accurate dust time lags can only reach redshifts up to $z \sim 1$ with current generation telescopes (e.g. Hönig et al. 2017).

1.1.3 Concordance ΛCDM cosmology

The "standard" ΛCDM cosmological model is constructed from the Friedmann-Lemaître-Robertson-Walker metric, the Friedmann equations and the cosmological equations of state to describe the expansion of the observable universe after the inflationary epoch (implementation discussed in Wright 2006). The concordance ΛCDM cosmology is determined by combining the measurements from the various observational techniques described in the previous section. In this cosmology, the universe is 13.8 billion years old and made up of 4.9% baryonic matter, 25.9% dark matter and 69.1% dark energy (Planck Collaboration 2016). The Hubble constant for this model is $H_0 = 67.7 \pm 0.5\,\mathrm{km\,s^{-1}\,Mpc^{-1}}$. This ΛCDM cosmology is assumed throughout the thesis, except in Chapter 5 when independently fitting the cosmology.

1.2 Galaxy formation and evolution

Large-scale structures form by the amplification of the overdensities originating in the CMB at the time of recombination (Section 1.1). These structures comprise large voids surrounded by long, intertwined strings of dark matter termed filaments (see Figure 1.3). Dark matter only simulations of the accepted ΛCDM cosmology (Spergel et al. 2007; Planck Collaboration 2016), such as the Millennium (Springel et al. 2005) and Bolshoi simulations (Klypin et al. 2011), provide a platform for modelling the formation and evolution of galaxies. The formation history of dark matter haloes can be modelled by implementing hierarchical merging tree algorithms on this simulated data (Croton et al. 2006). The density and temperature structure of these dark matter haloes has been studied extensively using numerical simulations. The dark matter density profile is well fitted by the form $\rho(r) \propto 1/[(r/r_{\rm s})(1 + r/r_{\rm s})^2]$, where r is the radius from the halo centre and $r_{\rm s}$ is a dimensionless radius dependent on the halo mass (Navarro et al. 1997).

The dark matter couples to the baryons only through gravity and its distribution on scales of galaxy haloes is thus only weakly affected by the details of galaxy formation (Croton et al. 2006). The effect of baryons on the dark matter is generally neglected (Somerville & Davé 2015, review and references therein) so that the evolution of the dark matter and the baryons can be modelled separately. Consequently, the dark matter evolution only needs to be simulated once; semi-analytic models are subsequently applied to the stored histories of all dark matter objects to analyse the baryonic component in different paradigms (Kauffmann et al. 1999). The computational challenges related to modelling the baryonic and dark matter components simultaneously have precluded the adoption of this approach until the advent of very powerful supercomputers. Cosmological hydrodynamical simulations including Horizon-AGN (Dubois et al. 2014), EAGLE (Schaye et al. 2015) and Illustris (Figure 1.3; Vogelsberger et al. 2014) consider the expansion of the universe, the gravitational attraction of matter, the hydrodynamics of cosmic gas, and the formation of stars and black holes.

1.2.1 Luminosity function of galaxies

The baryonic matter accreted at the centres of dark matter haloes (White & Rees 1978) is responsible for observable galaxy properties. If one assumes the ratio between the halo mass and the galaxy bolometric luminosity (i.e. mass-to-light ratio) is constant across a broad range of halo masses, the number of high- and low-luminosity galaxies is overestimated compared with observations. This mismatch at the high end of the

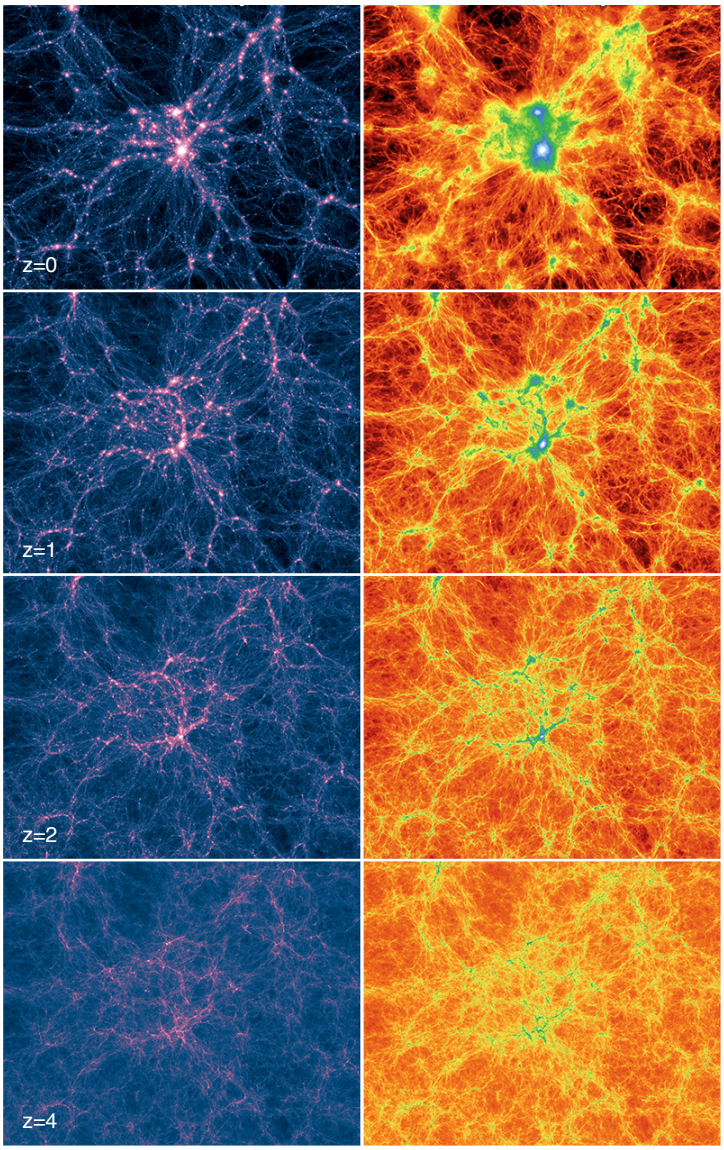

Figure 1.3: Illustris cosmological hydrodynamical simulation showing the redshift evolution of the dark matter density (left) and gas density (right) of a trimmed, whole box slice from $z = 4$ to $z = 0$. Large-scale structures form due to the gravitational pull of matter onto itself, amplifying overdensities seen in the early universe. From Illustris Collaboration (2017).

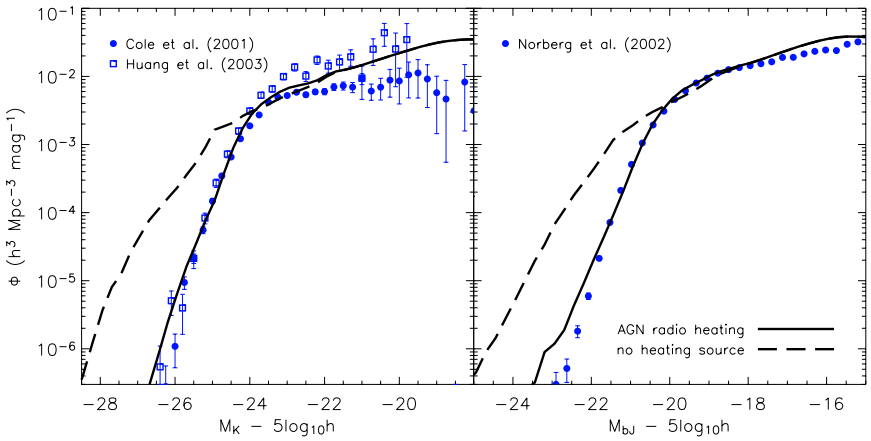

Figure 1.4: Galaxy luminosity functions in the K (left) and $b_{\rm J}$ (right) bands, plotted with and without radio mode feedback (solid and dashed lines respectively). The inclusion of AGN heating in the galaxy formation model provides a good fit to the observations (indicated by the symbols, with authors cited in figure). Without this heating the model overpredicts the luminosities of massive galaxies by about two optical magnitudes (i.e. a factor of ~ 6). From Croton et al. (2006).

galaxy luminosity function is shown in Figure 1.4 (dashed line; also see Baugh 2006). Observations show most stars are located in galaxies with similar luminosity to the Milky Way, the so-called $L^\star$ galaxies. The galaxy abundance decreases faster than predicted (assuming a constant mass-to-light ratio) for brighter luminosities, implying that the fraction of mass in stars is lower in the most massive galaxies. Similarly the galaxy abundance for fainter luminosities increases more slowly than expected, so that few stars are in dwarfs (Croton et al. 2006).

These inconsistencies were initially tackled by proposing cooling inefficiencies to suppress gas condensation in massive systems, and supernova feedback to reduce star formation efficiency in dwarfs (White & Rees 1978; White & Frenk 1991). However, additional feedback processes beyond the cooling effects are required in massive systems for the theory to match observations (Thoul & Weinberg 1995). In particular, Bower et al. (2006) and Croton et al. (2006) showed that the inclusion of heating from the active nucleus can reproduce the cut-off at the bright end of the galaxy luminosity function (solid line in Figure 1.4).

1.2.2 Gas distribution in galaxy clusters

The X-ray emitting gas in galaxy groups and clusters provides a crucial tool to understand evolutionary processes including AGN activity, galaxy mergers and tidal stripping (Croston et al. 2008b). The relation between the X-ray luminosity and temperature, the $L_{\rm X}$–T relation, is a sensitive tool to measure the variations in gas fraction of galaxy clusters; the luminosity is dependent on the mass of gas in the intracluster medium (ICM) whilst the temperature is determined by the total gravitational mass of the cluster. Non-gravitational heating processes have been thought to determine the X-ray properties of galaxy clusters since the first evidence appeared that the gas fraction is not constant with cluster mass (e.g. Arnaud & Evrard 1999). This departure of the observed $L_{\rm X}$–T relation from the simple theoretical prediction implies an increased entropy in the cluster gas (e.g. Ponman et al. 2003; Pratt et al. 2006). Radiative cooling and feedback processes, including galaxy winds and AGN feedback, have been invoked to explain these results (e.g. Voit 2005).

The structure of the ICM has been probed through radial surface brightness profiles since the first X-ray imaging of clusters. Observations of X-ray surface brightness distribution in galaxy clusters using the ROSAT telescope were found to be well modelled by a simple power law outside the core region, but with a large dispersion in the central regions (e.g. Neumann & Arnaud 1999). Clusters cores have since been better resolved using the Chandra and XMM-Newton telescopes; more complex models are required to fit the surface brightness profiles in these regions (e.g. Pratt & Arnaud 2002; Vikhlinin et al. 2006). The slope of the gas density profile is also found to steepen at large radii in some clusters (e.g. Vikhlinin et al. 1999, 2006). The pressure profiles of the hot gas haloes in which radio galaxies reside are a crucial input parameter to any model of the AGN–host galaxy interaction.

1.2.3 Suppression of cooling flows

Hot baryonic gas in the intracluster medium cools through the deceleration of electrons by Bremsstrahlung radiation, collisional cooling, and at early epochs ($z \gtrsim 10$) through inverse-Compton scattering (e.g. Sutherland & Dopita 1993). This cooled gas sinks to the centres of galaxy clusters; hot gas lying above replenishes the cooled gas leading to a steady, pressure-driven inward flow of gas at a rate of up to $1000\,{\rm M}_{\odot}\,{\rm yr}^{-1}$ (Fabian 1994). However, the first X-ray maps of clusters revealed that the gas at their centres is not condensing and forming stars, despite observations implying a cooling time much less than the age of the system (Boehringer et al. 1993). X-ray spectroscopy from the

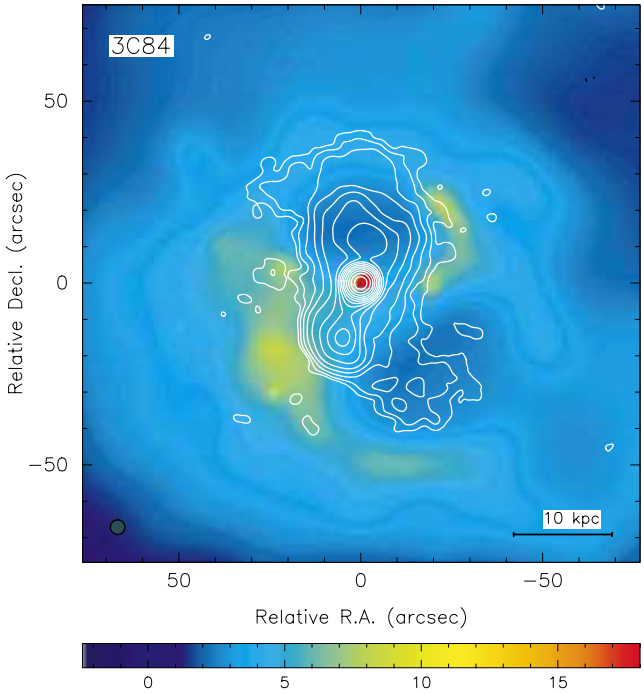

Figure 1.5: Radio contours corresponding to the radio lobes are overlaid on X-ray images mapping the gas density (red is higher density) in the Perseus cluster. The radio contours coincide with a deficit in gas; i.e. the radio lobes push out the gas. From Fabian et al. (2000).

XMM-Newton observatory has since shown there is much less gas cooling below one-third the temperature of the outer cluster gas than expected for a steady cooling flow (Peterson et al. 2001; Tamura et al. 2001). Direct evidence of an interaction between radio lobes and the intracluster gas is found in overlaid radio and X-ray images (e.g. Boehringer et al. 1993; Fabian et al. 2000, 2003, see Figure 1.5), suggesting that radio galaxies may regulate cooling flows. The mechanism driving this interaction is explained in Section 1.4.4. Mittal et al. (2009) found that 75% of clusters contain a radio source at their centre which is spatially coincident (to within $\sim 50\,\mathrm{kpc}$) with a peak in X-ray emission due to its cooling core. Moreover, they found that all clusters with cooling times less than 1 Gyr contain a radio AGN.

1.2.4 Galaxy colours

The hierarchical growth structure in a ΛCDM cosmology predicts low mass dark haloes form first with the most massive haloes assembling at a more recent epoch (Lacey & Cole 1993). However, observations show the most massive galaxies, which are

associated with the massive dark matter haloes, are systematically redder (using their optical colours) than lower mass galaxies. Massive galaxies thus comprise the oldest stars and finished star formation earlier than their lower mass counterparts (Bender & Saglia 1999). This is consistent with ultraviolet flux density measurements that show the peak star formation rate in radio galaxies occurred between redshifts $z = 1$ and 2 (Giavalisco et al. 2004). That is, higher mass galaxies form first in contradiction with predictions from hierarchical structure formation models. This scenario, termed "cosmic downsizing" (Cowie et al. 1996), can be explained by the suppression of cooling flows in massive radio galaxies at recent cosmic times; star formation is prevented in such galaxies (see Section 1.3). This results in a sharp high mass cut-off in the galaxy luminosity function as is observed.

1.2.5 Black hole - host galaxy correlations

Observations reveal a number of direct relationships between the active nucleus and the properties of its host galaxy. A strong correlation is observed between the black hole mass and the bulge stellar velocity dispersion of the form $M_{\rm BH} \propto \sigma^{(3.96\pm0.42)}$ (Gültekin et al. 2009; also see Tremaine et al. 2002), known as the $M_{\rm BH} - \sigma$ relation. Most galaxies have a stellar velocity dispersion of $\sigma < 400\,{\rm km\,s^{-1}}$ (Fabian 2012). A typical velocity dispersion of $\sigma = 220\,{\rm km\,s^{-1}}$ corresponds to a black hole mass of $\sim 2\times10^8\,{\rm M_\odot}$, using the mean values of this observed relation. A similar correlation is observed between the black hole mass and the bulge stellar mass as $M_{\rm BH} = (1.4 \pm 0.4) \times 10^{-3} M_{\rm bulge}$ (Häring & Rix 2004). The linear proportionality is consistent to within the uncertainties of many authors (e.g. Marconi & Hunt 2003; McConnell & Ma 2013), though there are some exceptions (e.g. Laor 2001). Further, the star formation rate (SFR) in galaxies is seemingly linked to AGN activity; the cosmological evolution of the AGN luminosity density function is strikingly similar to the SFR density (Boyle & Terlevich 1998), including a similar "cosmic noon" for both. Such correlations support the hypothesis that the evolution of the central black hole and its host galaxy are closely linked. Silk & Rees (1998) argue that AGN feedback can produce these observed black hole–host galaxy correlations; however cause and effect is not at all obvious: for example, galaxy mergers could cause both to grow more or less in step.

1.3 AGN feedback

The formation and evolution of galaxies is closely related to that of the supermassive (typically $10^6 - 10^9\,{\rm M_\odot}$) black holes at their centres (Magorrian et al. 1998; Häring

& Rix 2004; Gültekin et al. 2009). The interaction between the black hole and its surroundings, termed active galactic nucleus (AGN) feedback, can suppress (negative feedback) or trigger (positive feedback) star formation in the host galaxy. The clearest observational evidence for AGN feedback is found in very massive galaxies (e.g. Fabian 2012, review and references therein). Conversely, there is little evidence for AGN feedback in low mass galaxies where stellar feedback processes are dominant. I discuss the physical characteristics of AGN including their modes of feedback, accretion flow mechanisms and relationships with the host galaxy.

1.3.1 The active nucleus

Active galactic nuclei (AGN) have high bolometric luminosities of up to 10^{41} W, four orders of magnitude greater than that of a typical field galaxy (Krolik 1999). By contrast, X-ray luminosities of the surrounding gas typically lie in the range 10^{36} to 10^{38} W, corresponding to temperatures of 10^{7} to 10^{8} K (McNamara & Nulsen 2007). These AGN thus have the heating capacity required to suppress cooling flows in massive galaxies. The radiation is emitted over a large range of frequencies including the X-ray and radio spectral bands. However, less than $\sim 1\%$ of the AGN bolometric luminosity is emitted at radio frequencies, even for radio-loud AGN.

The activity of this central engine is linked to the evolution of the galaxy through infalling matter accreted onto the supermassive black hole. Gravitational energy is extracted from this infalling gas, with a fraction released into the surrounding galaxy in both radiative and kinetic forms (Penrose & Floyd 1971). The dominant modes through which AGN interact with their host galaxies in the early universe ($z \sim 2-3$) are winds and radiation pressure (radiative or quasar-mode feedback; Fabian 2012). However, in the present epoch jet-mode feedback becomes more prevalent, a mechanism in which jets of plasma directly interact with the host environment. This kinetic feedback has been invoked to explain the lack of star formation in the most massive galaxies (Croton et al. 2006), and the suppression of cooling flows in the cores of massive clusters (see Section 1.3.3). The jet mode of feedback must therefore be considered to understand the mismatch at the bright end of the galaxy luminosity function.

Bipolar anti-parallel jets are emitted perpendicular to the accretion disk of the central black hole with lengths of tens of kiloparsecs to a few megaparsecs. Structure inflated by these jets are seen in large-scale radio images, whilst the accelerating part of the jet can be seen on sub-parsec scales in VLBI observations (e.g. M87; Asada & Nakamura 2012). These jets are thought to be generated by extracting rotational energy from the dragging of the magnetic field lines (Penrose & Floyd 1971) that thread either the

central black hole and accretion disk (Blandford & Znajek 1977), or just the Keplerian part of the disk (Blandford & Payne 1982). The relativistic jets thus may be powered in part by the spin of the accreting black hole (Narayan & Quataert 2005), with rapid black hole rotation associated with stronger jets (Meier 2001). The rate of accretion of the surrounding gas strongly influences the geometry and dynamics of the accretion flow (Narayan & Quataert 2005). The power imparted to the relativistic jets in turn depends on the mass accretion rate and the mass of the black hole.

1.3.2 Accretion mechanisms

Properties of AGN central engines can be studied using their narrow or broad emission lines (see e.g. Hardcastle et al. 2009; Best & Heckman 2012). In this approach, AGN are partitioned into two populations, high- and low-excitation radio galaxies (or HERGs and LERGs), based on either line ratios or line equivalent widths. Low-excitation objects show no strong narrow or broad emission lines, and their optical and X-ray nuclear emission is consistent with originating purely in a jet (Hardcastle et al. 2006). By contrast, high-excitation radio galaxies have emission-line spectra similar to those of type II Seyfert galaxies. These two populations are thought to host black holes powered by different accretion flow mechanisms (e.g. Hardcastle et al. 2007; Best & Heckman 2012), with LERGs fuelled by an advection dominated accretion flow (ADAF, Narayan & Yi 1995) and the radiatively efficient HERGs by a thin (Shakura & Sunyaev 1973) or possibly slim (Abramowicz et al. 1988) disk flow. The physics of these accretion flow mechanisms is understood by studying black hole X-ray binaries (BHXRBs), which are thought to behave the same as for AGNs (Jester 2005, and references therein). These BHXRBs exhibit two dominant types of spectra: high/soft (soft spectrum and high luminosity) and low/hard (hard spectrum, low luminosity).

Thin disk accretion

In BHXRBs, the high/soft state corresponds to the standard Shakura & Sunyaev (1973) geometrically thin accretion disk (i.e. $H \ll R$, where H is the disk height and R is the radial distance to the central black hole) and has an optically thick accretion flow. The gravitational potential energy of infalling matter is assumed to be immediately radiated away by viscous dissipation (Park & Ostriker 2001), producing a quasi black body spectrum. That is, the viscous heating is balanced by the radiative cooling preventing the occurrence of advective cooling. This standard thin disk is therefore radiatively efficient and as such is associated with high luminosities and weak jets relative to the total accretion energy. The thin disk phase is dominant for

accretion rates between approximately $\dot{m} = 0.01$ and 0.1, where $\dot{m} \equiv \dot{M}_{\rm BH}/\dot{M}_{\rm Edd}$ is the black hole accretion rate in Eddington units (i.e. $\dot{M}_{\rm BH}$ is the black hole accretion rate and $\dot{M}_{\rm Edd}$ is the Eddington rate; Best & Heckman 2012).

Advection dominated accretion

The low/hard state (Narayan & Yi 1995) is by contrast identified with an optically thin accretion flow whilst the disk radiation contributes only a small fraction of the total emitted energy; much of the energy is instead output into the jets. The cooling times in this phase are longer than the accretion timescale, and thus trapped radiation is advected inward resulting in a "puffed", geometrically thick disk (i.e. $H \sim R$; Park & Ostriker 2001). The resulting quasi-spherical advection dominated accretion flow (ADAF) is thus radiatively inefficient and results in the low radiative luminosity. This low/hard ADAF phase is dominant for accretion rates between approximately $\dot{m} = 10^{-4}$ and 10^{-2} (Best & Heckman 2012).

Slim disk accretion

At high sub-Eddington accretion rates ($\dot{m} \sim 0.2 - 0.3$), the standard thin accretion disk becomes unstable when the radiation pressure dominates the gas pressure (Jester 2005). Beyond $\dot{m} \sim 0.3$, the viscosity generated heat does not have sufficient time to transform into photons and radiate from the disk before being driven inwards by the pressure of the infalling gas. The heating/cooling imbalance triggers the advection cooling mechanism (as for the ADAF phase), generating a geometrically "slim" accretion disk (i.e. $H \lesssim R$; Abramowicz et al. 1988). These slim accretion disks are assumed to be slim enough to satisfy the height integrated equations of thin disk solutions. The slim disk reproduces the characteristics of the thin disk at lower accretion rates (i.e. $\dot{m} < 0.2$), but extends the standard model to higher accretion rates and luminosities. The flow can reach super-Eddington luminosities, with the radiative efficiency decreasing from ~ 0.1 as $\dot{m}$ increases (Park & Ostriker 2001, their Figures 1 and 2). The spectrum of a slim disk is predicted to be identical to the soft thin disk spectrum at sub-Eddington accretion rates, but becomes redder in the extreme UV than that of an equivalent thin disk (Szuszkiewicz et al. 1996). The slim disk phase is thus sometimes referred to as the very high/soft state.

Disk Type	ADAF	Thin Disk	Slim Disk
Accretion Rate	$\dot{m} \ll 0.01$	$0.01 \lesssim \dot{m} \lesssim 0.3$	$0.3 \lesssim \dot{m}$
Jet Power	moderate (10^{36} W)	low (10^{34} W)	high (10^{39} W)
Spectrum	hard	soft	soft
Cooling Process	advection	radiation	advection
Optical Depth	thin	thick	thick
Disk Geometry	thick ($H \sim R$)	thin ($H \ll R$)	thick ($H \lesssim R$)

Table 1.1: The key properties of the three black hole accretion flow phases considered are summarised. The quoted jet powers are the typical order of magnitude for each disk type for a $10^9\,\mathrm{M}_\odot$ black hole, as discussed in the main text.

Jet power theory

Meier (2001) gives equations for the jet power generated by Kerr and Schwarzschild black holes for both the standard Shakura & Sunyaev (1973) thin disk or the advection dominated accretion flow. The jet power is approximately proportional to the Eddington scaled mass accretion rate $\dot{m}$, the black hole mass M_{BH}, and has weaker dependence on the black hole spin j and the disk viscosity responsible for the outward transport of angular momentum (Narayan et al. 1998). The ADAF can produce jets up to three orders of magnitude more powerful than in the thin disk phase for a given accretion rate and black hole spin. However, the accretion rates associated with the thin disk are typically much higher than for an ADAF, greater reducing this difference. The jet power of a black hole with mass $M_{\mathrm{BH}} = 10^9\,\mathrm{M}_\odot$ and a typical ADAF accretion rate of $\dot{m} \sim 10^{-3}$ (as per Best & Heckman 2012) is expected to lie in the range $Q_{\mathrm{ADAF}} \sim 3 \times 10^{35}$ to 2×10^{36} W, depending on the black hole spin (Meier 2001). By contrast, the jet power for a thin disk with typical accretion rate of $\dot{m} \sim 0.05$ is $Q_{\mathrm{TD}} \sim 4 \times 10^{34}$ W for a rapidly rotating black hole (i.e. $j \sim 1$), but only a factor of two lower with no spin. Typical jet powers for the ADAF phase are therefore greater than for a thin disk accretion flow by a factor of approximately 20 to 50.

The jet power produced in the slim disk phase increases drastically as the disk "puffs up" (i.e. $H \sim R$) from its lower accretion rate, thin disk predecessor. The jet power is proportional to the square of the equilibrium poloidal magnetic field B_{p} (see e.g. Meier 2002), which in turn is related to the ratio of the thickness of the disk H and its radius R by $B_{\mathrm{p}} \approx (H/R)B_\varphi$ (Livio et al. 1999), with B_φ the dominant azimuthal magnetic field component given by the disk structure equations. This results in jet powers up to 5 orders of magnitude higher than for the standard thin disk (Meier

2002). The slim accretion disk can therefore produce jets orders of magnitude more powerful than either the low accretion rate ADAF phase, or the standard thin disk. Table 1.1 provides a summary of the key properties of the three accretion flow phases that have been discussed.

1.3.3 Kinetic-mode feedback

The relativistic plasma jets emanating from the central supermassive black hole inflate underdense cocoons or lobes as they expand into the surrounding intracluster medium (ICM; see Section 1.4). Synchrotron emission from these lobes can be observed in the radio part of the spectrum. The energy from the AGN can profoundly affect the host galaxy through the heating or ejection of the intracluster gas; this is seen through observations of the interaction between these lobes and X-ray gas (e.g. Fabian et al. 2000, 2003), as shown in Figure 1.5. Heating increases the sound speed of the gas ($c_s \propto \sqrt{T}$, for temperature T) and correspondingly increases the Jeans' length by the same factor. Further, if AGN feedback clears much gas from the inner regions of the galaxy, the free-fall time of the remaining gas increases ($t_{\rm ff} \propto 1/\sqrt{\rho}$, for density ρ), further increasing the Jeans' length. Smaller or less massive gas clouds are now less susceptible to gravitational collapse. In this manner the active nucleus can suppress star formation in its host galaxy by an order of magnitude (Fabian 2012). Jet-mode feedback can explain the missing star formation in the most massive galaxies and clusters (Croton et al. 2006), with bow shocks driven by very powerful radio sources capable of suppressing star formation in not just their host but also other cluster galaxies (Rawlings & Jarvis 2004; Shabala et al. 2011).

The active galactic nucleus will inevitably be terminated as heating of the ICM decreases the rate of accretion onto the central black hole. Accretion can resume once the gas cools, or is replenished through an interaction or merger with another galaxy (Bahcall et al. 1997). The increase in accretion rate may eventually lead to the retriggering of the radio jets, completing the AGN feedback cycle. Evidence of the sporadic and intermittent nature of this feedback process is found in observations of rising radio bubbles (Churazov et al. 2001) and sources with multiple radio lobe pairs (e.g. Giovannini et al. 1998; Venturi et al. 2004). Observations of the radio-loud fraction of AGN in galaxies show the duty cycle (fraction of time the black hole is active) increases from 0.01% for low mass galaxies ($3 \times 10^{10}\,{\rm M}_\odot$) up to over 30% for massive galaxies ($> 5 \times 10^{11}\,{\rm M}_\odot$; Best et al. 2005). By fitting data to a sample of radio-loud AGN from the *Sloan Digital Sky Survey* (SDSS), Best et al. (2005) showed the best fit for the radio-loud fraction of the form $f_{\rm RL} \propto {M_{\rm BH}}^{\alpha}$ is $\alpha = 1.6 \pm 0.1$, where $M_{\rm BH}$ is

the central black hole mass. Additionally, Pope et al. (2012) developed a model which predicts the AGN duty cycle scales as $\delta \propto L_{\rm X}/\sigma^3$, where $L_{\rm X} \propto \sigma^m$ in which $m \sim 9$ is the X-ray luminosity of the hot gas in a cluster and σ is the host galaxy stellar velocity dispersion. Using $M_{\rm BH} \propto \sigma^4$, this gives the radio AGN duty cycle as approximately $\delta \propto \sigma^6 \propto {M_{\rm BH}}^{1.5}$.

The gas cooling rate has almost the same dependence on the black hole mass as the duty cycle (i.e. $\dot{M}_{\rm cool} \propto {M_{\rm BH}}^{1.5}$; Best et al. 2005), suggesting that the triggering of AGN activity for their low-powered radio sources may be related to the cooling of gas out of the hot host galaxy atmospheres. Furthermore, Mittal et al. (2009) found that all clusters with cooling times less than 1 Gyr contain a radio AGN; massive galaxies should therefore both harbour an AGN and have high cooling rates. Such AGNs may be powerful enough to suppress cooling in the host galaxy through heating by their jets. The heating these radio sources can provide to their host galaxy is investigated in Section 1.4.4. Quantifying the typical jet powers of these radio sources and the duration of their active state is crucial to understanding the energetics of AGN feedback, and whether it can explain the lack of recent star formation in massive galaxies and clusters.

1.4 Radio AGN energetics and morphology

The morphology of the AGN radio lobes (Fanaroff & Riley 1974) provides insight into the evolutionary history of the lobe, the host galaxy environment (e.g. Laing et al. 1994; Bicknell 1995; Kaiser & Alexander 1997), and potentially even the accretion flow mechanism powering the black hole (e.g. Meier 2001; Garofalo et al. 2010). Models of the physics in radio sources used to infer their energetics therefore need to carefully consider these morphological classes: Fanaroff & Riley (or FR) type I and II sources, and the emerging FR0 class of compact radio galaxies (Ghisellini 2011).

1.4.1 Radio source morphological dichotomy

Radio-loud AGN consist of twin jets emanating from the active nucleus in opposite directions. These jets interact with the surrounding medium, leading to the formation of a diffuse emission region. The radio luminosity of this region (the radio lobe) arises due to the synchrotron emission of shocked electrons (or positrons) injected from the jet. Fanaroff & Riley (1974) proposed that radio AGNs could be divided into two classes based on the distribution of radio surface brightness in their lobes. Fanaroff & Riley type II sources have well-defined jet termination shocks located

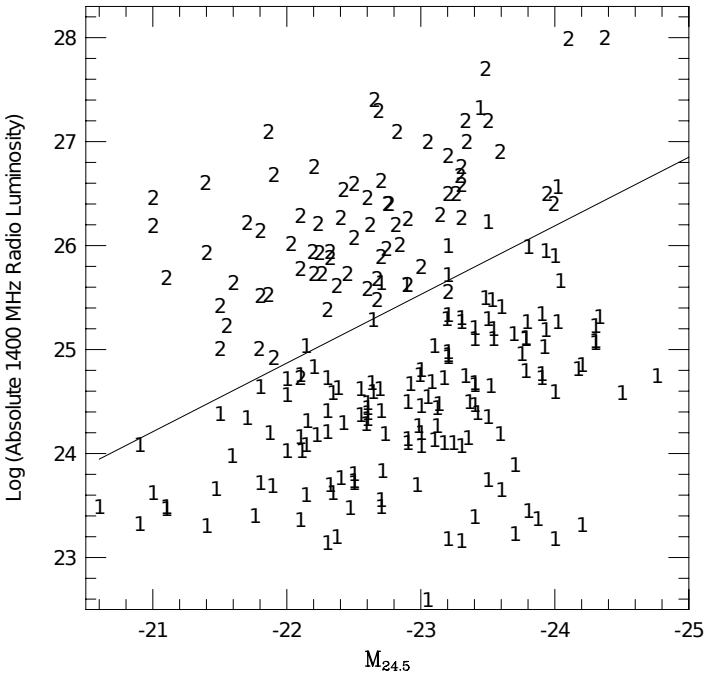

Figure 1.6: FR-I/II diagram for a sample of objects, as described by Owen & Ledlow (1994). The axes are the logarithm of the absolute radio power at 1.4 GHz and the absolute isophotal magnitude of the galaxy measured to 24.5 magnitudes arcsec^{-2} in the rest-frame of the galaxy. From Ledlow & Owen (1996), reprinted from (Owen & Ledlow 1994).

towards the ends of edge-brightened lobes, whilst type I sources have their regions of highest surface brightness close to the core. This morphological classification is strongly correlated with the radio luminosity of the source. Radio sources of type I typically have luminosities less than $6 \times 10^{24}\,\mathrm{W\,Hz^{-1}}$ at 1.4 GHz (Ledlow & Owen 1996), whilst FR-II radio sources generally have luminosities in excess of this value. The dividing radio luminosity between the two morphologies has since been shown to depend on the optical luminosity of the host galaxy (see Figure 1.6; Owen & Ledlow 1994). Because galaxy luminosity scales with black hole mass (and stellar mass), a weak dependence on the black hole mass is thus predicted in this FR-I/II dividing luminosity (Wold et al. 2007). However, Best (2009) pointed out that the FR-Is in this sample are located predominantly at redshifts less than 0.1, with the bulk of the FR-IIs found at $z > 0.25$. He found the separation between the two morphologies is still present when analysing objects from a volume-limited sample, but is less clearcut.

The more powerful FR-II class is typified by a well-defined jet (and sometimes counterjet) surrounded by prominent radio lobes. Each jet terminates at a hotspot at

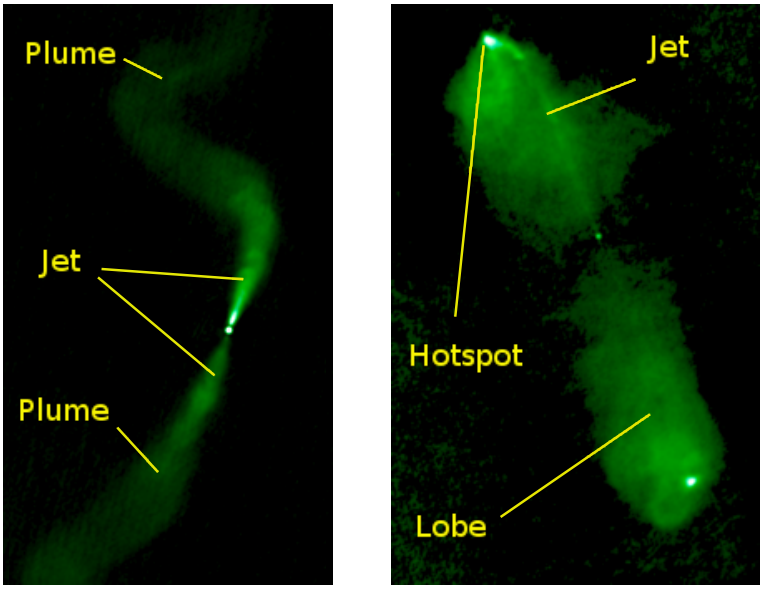

Figure 1.7: Typical FR-I (3C 31, left panel) and FR-II (3C 98, right panel) radio sources. The shock confined FR-IIs are edge-brightened, while radio emission is more core-dominated in the subsonic FR-Is. From Leahy et al. (2013).

the maximal extent of the radio lobe; leptons in the jet are shock accelerated and commence emitting synchrotron radiation. These sources are sometimes referred to as "classical doubles". The jets of many type I objects (e.g. 3C31; Leahy et al. 2013) appear to have been disrupted close to the core at a flare point, the FR-I equivalent of a hotspot. Analytical models and numerical simulations show that the jet plasma generates a recollimation shock when the sidewards ram pressure of the conical jet matches the pressure of the ambient medium (Krause et al. 2012). This recollimation shock stabilises the jet if it reaches the jet axis before the jet runs out of thrust, leading to an FR-II morphology. However, if the jet cannot be stabilised a flare point is expected to form. The outward flow of plasma may lead to backflow and the inflation of radio lobes, or eventually the prototypical smoke-like plumes. These two types of FR-Is are referred to in this work as "lobed" and "flaring jet" sources respectively. Typical "flaring jet" FR-I and "lobed" FR-II radio sources are shown in Figure 1.7.

The FR-I/II morphological dichotomy has been argued to arise due to either the influence of external environmental factors on the jet structure (e.g. Laing et al. 1994; Bicknell 1995; Kaiser & Alexander 1997; Krause et al. 2012, discussed above), or by parameters associated with the jet production mechanism (e.g. Meier 2001; Garofalo et al. 2010). Several radio sources have been observed to exhibit a mixed morphology (Kaiser & Best 2007), suggesting the FR-I/II dichotomy is at least partly due

to the environment. Both FR-I and FR-II radio sources are thought to initially expand supersonically (Marecki et al. 2003), and it has thus been suggested that FR-II radio sources may evolve into FR-Is when their jets are disrupted (Krishna & Wiita 1988; Kaiser & Best 2007); i.e. FR-IIs can be viewed as precursors of FR-Is. Radio sources with low power jets inhabiting dense environments and initially exhibiting an FR-II morphology are more susceptible to becoming FR-Is at later times. By contrast, sources with high power jets and lower density environments remain FR-IIs throughout their active lifetime. Hybrid morphology radio sources (HyMoRS, i.e. FR-I morphology on one side and FR-II on the other; Krishna & Wiita 2000) provide solid observational evidence that environment, rather than a property of the central nucleus, is very important factor in determining the lobe morphology.

The smallest radio sources may not belong to either of these two morphological classes, instead belonging to the emerging FR0 class of radio sources (Ghisellini 2011). This category comprises Gigahertz Peaked and Compact Steep Spectrum sources (GPS and CSS), which are of comparable size to the host galaxy and have their luminosity at lower radio frequencies (e.g. $< 1\,\mathrm{GHz}$) greatly reduced through synchrotron self-absorption or free-free absorption. This absorption leads to a peak in the radio spectrum at approximately 1 GHz. Next generation surveys such as ASKAP EMU (Norris et al. 2011) and MeerKAT MIGHTEE (Jarvis 2012) are expected to find many weaker and more compact radio sources. It is not clear whether compact sources are a homogeneous population; these low-powered objects will likely comprise: (1) the genuinely compact FR0 population (Baldi et al. 2016) and (2) extended, low-surface brightness FR-Is that appear compact due sensitivity limits. Many of these sources may either be unresolved or viewed at close to the survey flux detection limit. There is therefore an imperative to quantify the effect observational limitations of future radio surveys have on this population when considering AGN feedback, in addition to probing the more energetic but rarer FR-I and -IIs.

High- and low- excitation radio galaxies

The morphological classification of the radio lobes is closely correlated with their emission line properties, and thus the accretion flow powering the black hole (Section 1.3.2). Almost all FR-I type sources are in low-excitation radio galaxies, whilst many FR-IIs exhibit high-excitation emission lines (Hardcastle et al. 2007; Lin et al. 2010). There is, however, a significant population of FR-IIs with low-excitation lines (Laing et al. 1994), so that the HERG/LERG and FR-I/II segregations of the radio source population differ slightly. Lin et al. (2010) compared the host galaxy properties of the

most edge-brightened FR-IIs with strong emission lines with those of the other radio sources and found that this split was more closely aligned with the HERG/LERG segregation. The different accretion flow mechanisms associated with these two populations gives rise to a bimodal distribution in the accretion rates of AGN (Best & Heckman 2012). Regardless of the method of accretion powering a radio source we expect the evolution of its jets and radio lobes to be identical for the same jet power and environment.

The low-excitation galaxy population is dominant at low radio luminosities with the number of HERGs comparable beyond $L_{1.4\mathrm{GHz}} \sim 10^{26}\,\mathrm{W\,Hz^{-1}}$ (Best & Heckman 2012). Observations show that HERGs are bluer, smaller, less concentrated, and have lower 4000 Å (or Ca II) breaks than LERGs of the same stellar mass, black hole mass and radio luminosity (e.g. Kauffmann et al. 2008; Best & Heckman 2012). The black hole and stellar masses of HERGs are also systematically lower than that of LERGs with the same radio luminosity. The bluer colours and lower 4000 Å breaks imply the HERGs are associated with new and ongoing star formation. The triggering mechanism of the source may be responsible for the smaller average sizes and lower concentration of HERGs. Lin et al. (2010) found the FR-II subset associated with HERGs are hosted by lower mass galaxies, live in sparser environments, and have higher accretion rates than other radio sources. Conversely, LERGs that are regularly fuelled by accretion from their hot gas haloes are typically located at the centres of groups or clusters where the host galaxies are larger (Best & Heckman 2012). Further, high-redshift HERGs are found to inhabit richer environments than their low-redshift counterparts whilst LERG host galaxies show no redshift evolution (Ineson et al. 2015).

1.4.2 Measuring radio source energetics

The kinetic powers of AGN jets have previously been estimated using radio source dynamical models (Machalski et al. 2004; Krause 2005; Shabala et al. 2008; Punsly 2011), hot X-ray gas cavity observations (Rafferty et al. 2006; Bîrzan et al. 2008; Cavagnolo et al. 2010), lobe expansion speeds (Daly et al. 2012), strong shocks around the lobes (Croston et al. 2009), and measurements of the properties of the jet termination shocks (hotspots; Godfrey & Shabala 2013). However, there is a lack of reliable and generally applicable methods to estimate jet power. Many authors have attempted to simply convert radio luminosity directly to the jet kinetic power (e.g. Willott et al. 1999; Cavagnolo et al. 2010), though such an exercise is expected to result in up to two orders of magnitude uncertainty in the jet power (Willott et al. 1999). Jet power–luminosity relations are also plagued by confounding variables such as the age-

dependent electron loss processes (i.e. inverse-Compton, adiabatic and synchrotron; Kaiser et al. 1997), source size (Shabala & Godfrey 2013) and host environment (Kaiser et al. 1997; Barthel & Arnaud 1996). Further, observed jet power–luminosity relations are often merely the result of strong selection effects (Godfrey & Shabala 2016).

The determination of the energetics of radio AGN also requires the active lifetime of the source to be measured. The ages of AGN lobes have been estimated using radio source dynamical models (e.g. Shabala et al. 2008) and spectral ageing, a technique based on the steepening of the radio SED at high-frequencies due to synchrotron losses (e.g. Jaffe & Perola 1973; Myers & Spangler 1985; Alexander & Leahy 1987; Murgia et al. 1999; Jamrozy et al. 2008; Harwood et al. 2013). The current spectral ageing techniques require high-resolution images capable of resolving the source across a broad range of radio frequencies, in addition to a measurement of the magnetic field strength. This is reliably achieved through comparing measurements of synchrotron electrons inverse-Compton upscattered to X-ray energies to that expected based on the level of synchrotron emission at radio frequencies (e.g. Hardcastle et al. 2002; Croston et al. 2004, 2005).

1.4.3 Radio source dynamical models

The expansion and dynamical evolution of radio sources is critically important to quantifying the heating of galaxies and clusters by their central active nucleus. There are numerous models in the literature describing the temporal evolution of the powerful FR-II class (e.g. Kaiser & Alexander 1997; Blundell et al. 1999; Kaiser & Cotter 2002), and some models for the FR-I morphological class (e.g. Luo & Sadler 2010). These models typically make a number of simplifications to remain analytically tractable. External density profiles are usually approximated by a single power law with a constant exponent, inconsistent with X-ray observations of the gas density in clusters (e.g. Vikhlinin et al. 2006). Alexander (2000) and Shabala et al. (2008) developed models allowing for different power laws used for each of the core, galaxy and cluster regions of the surrounding environment, though their equations accumulate appreciable errors if extended to large numbers of power laws due to small discontinuities across the region boundaries. The separate FR-II and FR-I models also only consider the two limiting cases, where either the ram (for FR-IIs) or external pressure (FR-Is) component of the total pressure dominates; this greatly reduces the applicability of these present models. The luminosity of sources of either morphology is then calculated using a synchrotron emission model.

The dynamics of radio sources falling outside these limiting cases may be better mod-

elled through hydrodynamical simulations (Krause et al. 2012; Hardcastle & Krause 2013, 2014), or more sophisticated analytic models. In the numerical approach, the relativistic jet can be injected into an arbitrary environment; systems of partial differential equations describing the fluid flow are solved across a two/three-dimensional grid to determine the temporal evolution of the jet and the formation of any radio lobes (Mignone et al. 2007). However, hydrodynamical simulations are both very computationally intensive to run (order of a day per source on a supercomputer), and typically do not include synchrotron loss mechanisms in their luminosity calculation (but see Jones et al. 1999). However, they provide a physically robust test bed against which to compare the efficacy of current and future analytic models.

1.4.4 Kinetic feedback ICM heating

The general consensus is that, since $z = 1$, active galactic nuclei are feeding energy back into their host galaxy environments at a rate approximately balancing the loss of energy through cooling (e.g. Best et al. 2007; McNamara & Nulsen 2007). The supersonic expansion of powerful FR-II radio sources heats the intracluster medium (ICM) predominantly through the energy of their bow shocks (e.g. Worrall & Birkinshaw 2014). By contrast, for the weaker FR-I class sources, the coupling of the mechanical energy of the bubble to the surrounding gas results in gravitational heating and heating through viscous dissipation of sound waves.

Shock heating

The bow shock generated by a powerful FR-II sweeps-up the intracluster medium (ICM) in its path as it propagates outwards. The thermal evolution of this swept-up gas was considered by Alexander (2002). For a strong shock with Mach number $M_0 = 10$, the temperature of the swept-up gas lying between the lobe and bow-shock is approximately 31 times greater than that of the external medium, i.e. $T_{\rm shock} \sim 0.31{M_0}^2 T_{\rm x}$. The final state of this shocked gas lying between the lobe surface and the bow shock depends critically on whether it expands adiabatically or isothermally.

The mean temperature of the shocked gas in the isothermal case differs from the post-shock temperature by less than a factor of two for any host galaxy environment. For low Mach numbers the cooling time of the swept-up gas, $t_{\rm shock}$, can become short compared with that in the cluster, $t_{\rm x}$, with $t_{\rm shock}/t_{\rm x} > 0.05 M_0$. However, the cooling time of the external gas would have to be at least an order of magnitude less than the source age, $t_{\rm age}$, for the shocked gas to suffer significant radiative losses. Such

conditions are only possible at the centres of the strongest cooling flow clusters. Shock heating is therefore efficient for the case of the post-shock gas expanding isothermally. Radio sources will also be able to affect the gas on timescales much greater than the active lifetime of the AGN, since $t_{\rm x} \gg t_{\rm age}$.

If instead the shocked gas evolves adiabatically and the source expands into a steeply falling atmosphere, a dense narrow layer will form as the radio source lifts gas out of the cluster potential. This layer has a cooling time very much less than that of the gas just ahead of the radio source. Shock heating is thus inefficient in steep atmospheres with the gas expanding adiabatically. The dependence of the observed X-ray emissivity on the density and temperature in different energy bands can be used to distinguish between the adiabatic, isothermal and isobaric processes. The observed fluctuations of the ICM in M87/Virgo show adiabatic evolution of the weak shocks and the isobaric nature of gas entrained by the buoyantly rising bubbles (Zhuravleva et al. 2015; Arévalo et al. 2016).

The swept-up ICM also affects the evolution of the radio source, in particular as it approaches subsonic expansion. The swept-up gas preferentially accumulates on the sides of the lobe causing the lobe to be "pinched" and increasing its aspect ratio. For very steep atmospheres falling almost as fast as $1/r^2$ the source will not be affected by this gas (ballistic expansion for $\beta \geqslant 2$; Falle 1991) and will continue its expansion in a self-similar manner.

Buoyantly rising bubbles

The bubbles or cavities commonly observed in deep *Chandra X-ray Observatory*, *XMM-Newton* and *Suzaku* images of cool core clusters are inflated by jets emanating from the central black holes of active galaxies (e.g. Fabian 2012). These cavities usually coincide with the radio lobes of an FR-I type source (see Figure 1.5). Such bubbles are observed in the cool cores of most of the X-ray brightest clusters with cooling times less than 3 Gyr. A series of bubbles can be produced due to the intermittency of the AGN activity. The innermost bubbles are fairly spherical and are surrounded by a thick high-pressure region fronted by a weak shock.

The thermal energy within these early stage expanding bubbles is observed to be a factor of 3.7 times greater than a region of the surrounding medium of the same volume (Graham et al. 2008). Hence, bubbles can transfer approximately $3.7pV$ of energy to the external atmosphere, where p is the pressure of the cluster gas and V is the volume of the bubble. The energy required to slowly inflate the bubble is expected to be the sum of its internal energy, $pV/(\Gamma - 1)$ for adiabatic index Γ, and the pdV

work done by the expanding bubble on the cluster gas (Churazov et al. 2002). This energy is equal to $4pV$ assuming a relativistic plasma inside the bubble, and $2.5pV$ for a non-relativistic plasma, in approximate agreement with observations. The work done by the expanding bubble on the surrounding gas is dissipated by viscous damping of sound waves and mixing resulting in heating (e.g. Shabala & Alexander 2009a).

The jets of radio sources in dense environments or with low jet powers will be subject to disruption from the surrounding lobe material (e.g. Falle 1991; Kaiser & Alexander 1997). The overpressured lobe will expand at a progressively slower rate (i.e. $v \propto t^{(\beta-2)/(5-\beta)}$ for $\beta \sim 1$; Kaiser & Alexander 1997) until it comes into equilibrium with the surrounding gas. The hot lobe material will now be underdense compared to the external medium, and is "pinched" by the high pressure gas near the core. The underdense bubble will then rise buoyantly through the atmosphere. As bubbles rise they may become undetectable in radio observations and are termed ghost bubbles (Fabian 2012). Gas falls back into the cluster potential behind the bubble as it rises, converting gravitational potential into kinetic energy and thus heating the gas.

1.5 Thesis structure

This introductory chapter has provided a background to the production and classification of radio AGN, the importance of AGN feedback to the evolutionary histories of galaxies, and a brief overview of techniques used to model these processes. The subsequent chapters are structured as follows. Chapter 2 details the development of a new analytic radio source model, which describes the evolution of both FR-II and FR-I type "lobed" radio sources, and the transition between these morphologies. This model is applied to a local AGN sample to characterise their energetics, with their gaseous host atmospheres described using a semi-analytic galaxy formation model. In Chapter 3, I develop a new technique for calculating the jet powers and magnetic field strengths of radio AGNs based on the spectral curvature in their continuum emission. Crucially, this technique does not require measurements of the lobe length, enabling the jet powers of unresolved sources, such as those at high-redshift, to be estimated. Chapter 4 includes a discussion of the resolved synchrotron emissivity model, which provides an analytic description of the radiative loss mechanisms in spatially resolved sources, and can be applied atop existing dynamical models. I also develop a radio source model for low-powered "flaring jet" FR-Is. The resolved emissivity model is used to investigate the effect of observing radio sources close to the flux detection limit in future surveys. In Chapter 5, I investigate the use of radio-loud AGNs as high-redshift standardisable candles, constructed solely from radio frequency observa-

tions. These radio frequency standard candles are used to determine the distance to radio AGN and their associated galaxies, both to test the viability of this technique for providing photometric redshifts, and to constrain the cosmological constants. Finally, Chapter 6 provides a summary of the significant outcomes of this thesis, together with suggested future extensions of this work.

The spectral index, α, defined by $S = \nu^{-\alpha}$ (for flux density S and frequency ν) is assumed throughout the thesis.

Chapter 2

Radio-loud AGN in Semi-analytic Environments

Knowledge of how radio-loud AGN evolve and the feedback they provide to their host galaxies is essential to improve our understanding of galaxy formation and evolution processes. In this chapter, I present a comprehensive analytic model describing the evolution of Fanaroff-Riley type I and II radio AGN, and the transition between these classes. This radio source dynamical model is applied to a volume-limited low redshift ($0.03 \leqslant z \leqslant 0.1$) sample of observed AGN to determine the distribution of jet powers and active lifetimes at the present epoch. In Sections 2.1 and 2.2, I develop an analytic model describing the evolution of sources from FR-II through to FR-I type morphology. The energetics of a sample of local radio sources is quantified in Section 2.3 assuming environments derived using semi-analytic galaxy evolution models. Then in Section 2.4, I examine the relationship between the radio lobe–ambient gas interaction and radio source morphology. Finally, in Sections 2.5 and 2.6 the energetics estimated using the dynamical model are compared to the theoretical expectations for AGN feedback and used to examine the accretion properties of high- and low-excitation radio galaxies.

2.1 Radio source model

In this section, I develop the dynamical model. This model is largely based on the FR-II model of Kaiser & Alexander (1997), and the pressure-limited expansion model of Luo & Sadler (2010). I combine these two limiting cases in a single framework, and include a more complete treatment of the environments into which radio sources

expand. The key parameters defined in this section are summarised in Table 2.1.

2.1.1 Radio source dynamics

The FR-II dynamical model comprises a relativistic plasma jet emanating ballistically from the active nucleus with constant opening angle (Figure 2.1). A reconfinement shock will form further down the jet enabling it to transition from the ballistic regime into one of pressure equilibrium with its lobe (or cocoon). The radius of the jet will remain constant after this reconfinement shock since the lobe pressure remains uniform (due to the high sound speed; Kaiser & Alexander 1997). The jet terminates at an outwardly moving hotspot in a jet shock with the ram pressure of the jet material distributed over the working surface, generating a bow shock. The pressure exerted on the working surface is balanced by the pressure of the shocked ambient gas which surrounds the hotspot. The hotspot region is overpressured with respect to the rest of the lobe, and backflow of overpressured plasma inflates the lobe. The lobe and bow shock are expected to expand in a self-similar manner (Falle 1991; Kaiser & Alexander 1997). The luminosity of the lobe comes from the radio emission due to synchrotron electrons precessing about the magnetic field lines of the lobe.

In the FR-I model (Figure 2.1), a relativistic jet emerges from the central black hole, inflating a lobe, similar to the FR-II model. Particles will still be accelerated by jet shocks, however, these shocks occur closer to the nucleus for the low-power jets of FR-Is. The region where shocks occur is referred to as the flare region, the FR-I counterpart of the FR-IIs hotspots (e.g. Luo & Sadler 2010). The diffuse emission region, which extends well beyond the shock, is regarded as the plume or lobe in analogy with FR-IIs.

2.1.2 Environment assumptions

I model the expansion of the pressure-inflated radio lobe in a spherically symmetric external atmosphere with an arbitrary density and temperature profile. The external atmosphere is partitioned into small radial regions in which the external density and temperature are each approximated by a simple power law profile. The density profile in each small region is thus approximated by a power law of the form

$$\rho_{\rm x} = \rho_0 \left(\frac{r}{a_0}\right)^{-\beta} = k r^{-\beta}, \tag{2.1}$$

where r is the radial distance from the active nucleus at the centre of the source

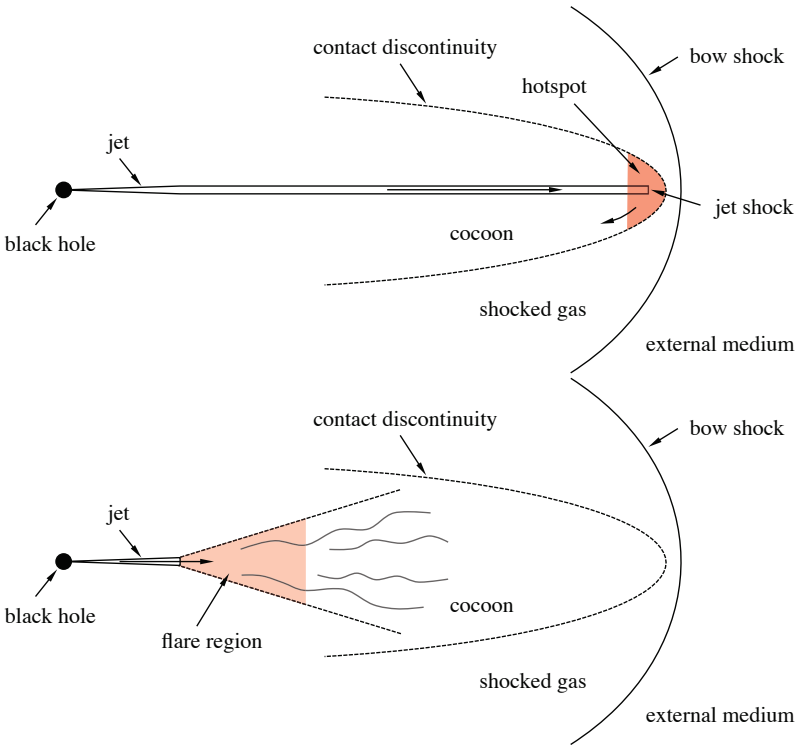

Figure 2.1: FR-II (top) and FR-I (bottom) model schematics. Jets and lobes (or cocoons) on only one side of the AGN are shown.

and the exponent β is constant in the region. The density parameter k is defined as $k = \rho_0 {a_0}^{\beta}$ for some radius a_0, with corresponding density ρ_0, located in the region approximated by the relevant power law.

The temperature of the external environment in each small region is similarly modelled as

$$\tau_{\rm x} = \left(\frac{\bar{m}}{k_{\rm B}}\right) l r^{-\xi}, \tag{2.2}$$

where the exponent ξ is constant in the region, $k_{\rm B}$ is the Boltzmann constant, $\bar{m} \sim 0.6 m_{\rm p}$ is the average particle number density for proton mass $m_{\rm p}$, and l is a constant of proportionality termed the temperature parameter[1].

2.1.3 Lobed FR-I/II dynamical model

Dynamical models of powerful type II radio sources show that the overpressured lobes expand self-similarly, i.e. the shape of the lobe remains fixed (Falle 1991; Kaiser & Alexander 1997). As the lobe expansion slows, however, the surface velocity of the inner parts of the lobe will fall below the local sound speed of the ambient gas. The expansion rate in this subsonic phase ($r \propto t^{1/(3-\beta)}$; Luo & Sadler 2010) is lower than for supersonic expansion ($r \propto t^{3/(5-\beta)}$, for realistic density profiles with $\beta < 2$; Kaiser & Alexander 1997), and thus the assumption of self-similar growth cannot be extended to this transonic regime. I therefore model the lobe as an ensemble of small volume elements in pressure equilibrium, where the growth of each element is otherwise independent. In the subsonic phase I further consider Rayleigh-Taylor instabilities expanding about the surface of this volume (see Section 2.2).

In order to quantify the energetics of the adiabatic expansion of the radio source I need expressions for the volume of the lobe and its pressure. The evolution of the lobe on one side of the central active nucleus is modelled explicitly, with the properties of the entire radio source calculated by assuming two identical, anti-parallel lobes. Below I derive expressions for the size and luminosity evolution of the radio lobes.

Lobe geometry

The radio lobe of the dynamical model is an ensemble of small angular volume elements in pressure equilibrium. Each element of fixed angular width is assumed to receive a

[1]The $\bar{m}/k_{\rm B}$ constant is introduced in this definition to simplify subsequent equations.

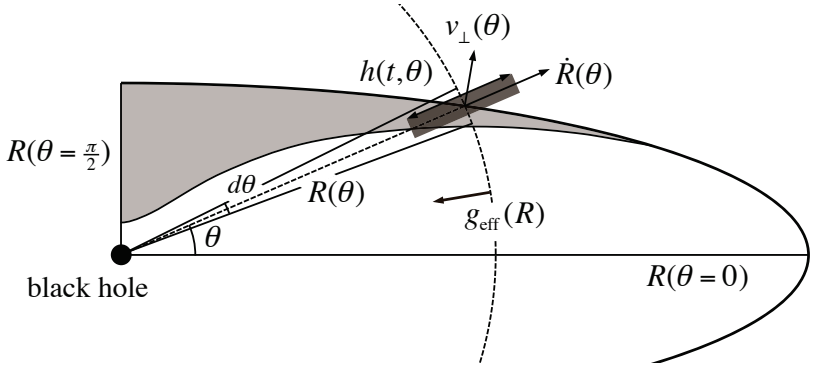

Figure 2.2: A cross section of the entire lobe (solid line), with the non-synchrotron emitting, Rayleigh-Taylor mixed region shaded in light grey. Geometric parameters are shown in this schematic for the ensemble element at angle θ. The shaded rectangle of length $h(t,\theta)$ represents the height of the mixing layer. The height of the mixing layer increases towards the lobe's semi-minor axis where the normal velocity and thus Mach number are lower.

constant fraction of the jet power as the lobe expands. This assumption yields self-similar expansion when the whole lobe is in the supersonic phase. The volume of each small angular lobe element $[\theta - d\theta/2, \theta + d\theta/2)$ is thus related to its radial length $R(\theta)$ by

$$dV(\theta) = \frac{2\pi R^3(\theta)}{3} \sin\theta d\theta, \tag{2.3}$$

where θ is the angle between the jet axis and the radial line passing through the volume element (Figure 2.2). The total volume of the lobe on one side of the central nucleus is the volume integral of Equation 2.3 over the domain $\theta \in (0, \frac{\pi}{2})$. To provide initial conditions for this model, I assume the lobe is initially ellipsoidal in shape with a circular cross-section along the jet axis. The ratio of the length of the lobe on one side of the central active nucleus, $R(\theta = 0)$, to the radius of the lobe transverse to the jet axis is defined by A, the lobe axis ratio[2].

Working surface pressure

The pressure at the working surface of highly supersonic FR-II radio sources is normally calculated using ram pressure arguments or the Rankine-Hugoniot jump condi-

[2]Hence for a sphere I have $A = 1$. This axis ratio is related to the aspect ratio $R_{\rm T}$ defined by Kaiser & Alexander (1997) as $A = 2R_{\rm T}$.

tions for a plane parallel shock (e.g. Kaiser & Alexander 1997; Luo & Sadler 2010). For a subsonic FR-I source, pressure due to such expansion is assumed insignificant with the working surface pressure taken to be equal to the external pressure (e.g. Luo & Sadler 2010). The working surface of the lobe is defined here as the location where the expanding lobe and external environment meet.

For a compressible fluid and ignoring external forces, the working surface pressure is related to the external pressure $p_{\rm x}(\theta)$ using the Rankine-Hugoniot jump conditions for a plane parallel shock. The working surface pressure approaches the external pressure as the lobe expansion speed nears the sound speed, i.e. $M_{\rm b} \to 1$ where $M_{\rm b}(\theta)$ is the Mach number of the bow shock. In the subsonic regime the working surface pressure is not expected to fall below the external pressure. The pressure at the working surface should thus equal the external pressure for subsonic expansion; this is the "pressure-limited expansion" of Luo & Sadler (2010). The general expression for the working surface pressure $p(\theta)$ of each ensemble element in the lobe is therefore

$$p = \begin{cases} \frac{2\Gamma_{\rm x} {M_{\rm b}}^2 - (\Gamma_{\rm x}-1)}{\Gamma_{\rm x}+1} p_{\rm x} & \text{for } M_{\rm b} \geqslant 1 \\ p_{\rm x} & \text{for } M_{\rm b} < 1, \end{cases} \tag{2.4}$$

where $\Gamma_{\rm x} = \frac{5}{3}$ is the adiabatic index of the external medium. This equation can be rewritten in terms of the radial length of the ensemble element $R(\theta)$, and the density and temperature parameters, k and l respectively. The pressure of the external medium is given by $p_{\rm x} = \rho_{\rm x}\tau_{\rm x}(k_{\rm B}/\bar{m}) = (kl)R^{-(\beta+\xi)}$, where the right hand equality is obtained using Equations 2.1 and 2.2. The Mach number of the bow shock is related to the expansion rate of the ensemble element as $M_{\rm b} = v_\perp/c_{\rm x}$, where $v_\perp(\theta) = \zeta\dot{R}/\eta$ is the velocity normal to the surface (see Appendix for derivation and definitions of the dimensionless radius and velocity, η and ζ) and $c_{\rm x}(\theta) = \sqrt{\Gamma_{\rm x} k_{\rm B}\tau_{\rm x}(\theta)/\bar{m}}$ is the sound speed. The Mach number can then be written as $M_{\rm b} = [R^{\xi}(\zeta\dot{R}/\eta)^2/(\Gamma_{\rm x} l)]^{1/2}$, and hence Equation 2.4 becomes

$$p = \begin{cases} \frac{2}{\Gamma_{\rm x}+1} k R^{-\beta}(\zeta\dot{R}/\eta)^2 - \frac{\Gamma_{\rm x}-1}{\Gamma_{\rm x}+1}(kl)R^{-(\beta+\xi)} & \text{for } M_{\rm b} \geqslant 1 \\ (kl)R^{-(\beta+\xi)} & \text{for } M_{\rm b} < 1. \end{cases} \tag{2.5}$$

The average pressure inside the lobe is calculated by weighting the surface pressure of each ensemble element by its volume, since the high sound speed is expected to yield uniform internal pressure.

Table 2.1: Environment and lobe geometry parameters.

Pressure profile parameters		
density parameter	k	$\rho_{\rm x} = kr^{-\beta}$
density exponent	β	
temperature parameter	l	$\tau_{\rm x} = lr^{-\xi}$
temperature exponent	ξ	
Ensemble element parameters		
angle of element from jet axis		θ
fraction of jet power in element		$d\lambda$
volume of ensemble element		dV
radius of ensemble element		R
radial velocity at element surface		v
Dimensionless constants		
dimensionless radius	$\eta = R(\theta)/R(\theta = 0)$	
dimensionless velocity	$\zeta = v_{\perp}(\theta)/\dot{R}(\theta = 0)$	

2.1.4 Adiabatic expansion

The adiabatic expansion of each angular volume element in the lobe ensemble is related to the pressure imparted on that element at the surface, $p(\theta)$, its volume $dV(\theta)$ and the jet power Q by

$$\dot{p}\, dV + \Gamma_{\rm c} p\, d\dot{V} = (\Gamma_{\rm c} - 1) Q\, d\lambda, \tag{2.6}$$

where $\Gamma_{\rm c} = \frac{5}{3}$ (Kaiser et al. 1997) is the adiabatic index of the lobe and the derivatives are with respect to the time t. The differential quantity $d\lambda(\theta)$ is the fraction of the jet power injected into the ensemble element $[\theta - d\theta/2, \theta + d\theta/2)$, derived in the Appendix. Note that Q is the kinetic power of one jet, i.e. the total AGN kinetic power is $Q_{\rm tot} = 2Q$. The source linear size (an observable quantity) is then related to the length of the ensemble element along the jet axis by $D = 2R(\theta = 0)$. The subsonic expansion phase, however, must be considered separately from the supersonic phase due to the discontinuity in lobe pressure in Equation 2.5. Note that the hotspot diameters of typical FR-II sources are approximately 100 times smaller than the linear size of their lobes (Hardcastle et al. 1998). The energy stored in these high pressure hotspots can therefore be neglected from Equation 2.6 since it is small compared to that stored in the rest of the lobe.

Supersonic expansion

I first consider the supersonic phase expansion of ensemble elements in the lobe. Substituting the relevant expressions for the pressure and volume of each element into Equation 2.6 yields a second order differential equation, which can not be solved analytically in general. I therefore adopt a numerical scheme using a fourth order Runge-Kutta method by rewriting the differential equation as a system of two first order ODEs. Thus for each ensemble element in the lobe the following system of equations must be solved:

$$\begin{aligned} \dot{R} &= v \\ \dot{v} &= \frac{3(\Gamma_{\rm x}+1)(\Gamma_{\rm c}-1)QR^{\beta-3}d\lambda}{8\pi v(\zeta/\eta)^2 k\sin\theta d\theta} + \frac{(\beta-3\Gamma_{\rm c})v^2}{2R} + \frac{(\Gamma_{\rm x}-1)(3\Gamma_{\rm c}-\beta-\xi)l}{4R^{\xi+1}(\zeta/\eta)^2}, \end{aligned} \tag{2.7}$$

where $v(\theta)$ is the radial velocity at which the lobe expands along each angle θ. The first of these equations thus gives the velocity of the expanding lobe and the second its acceleration.

Subsonic expansion

I now examine the expansion of ensemble elements in the subsonic phase. Substituting the expressions for the subsonic pressure (Equation 2.5) and volume (Equation 2.3) into Equation 2.6 yields a first order differential equation, which can be solved analytically. The solution to this differential equation is of the form $R \propto t^{1/(3-\beta-\xi)}$. However, this expression can only be used to model the evolution of a radio source that is subsonic for its entire lifetime. In particular, the ensemble element radius predicted by the subsonic solution at the sonic boundary differs from that of the supersonic phase (Equation 2.7), because the subsonic solution ignores the previous (supersonic) expansion history of the radio lobe. The expansion in the subsonic phase must therefore be solved numerically, using the supersonic phase solution as an initial condition. I thus rewrite the analytic solution as a system of differential equations,

$$\begin{aligned} \dot{R} &= v \\ \dot{v} &= \frac{(\beta+\xi-2)v^2}{R}, \end{aligned} \tag{2.8}$$

where again the first equation gives the velocity and the second the acceleration for each ensemble element.

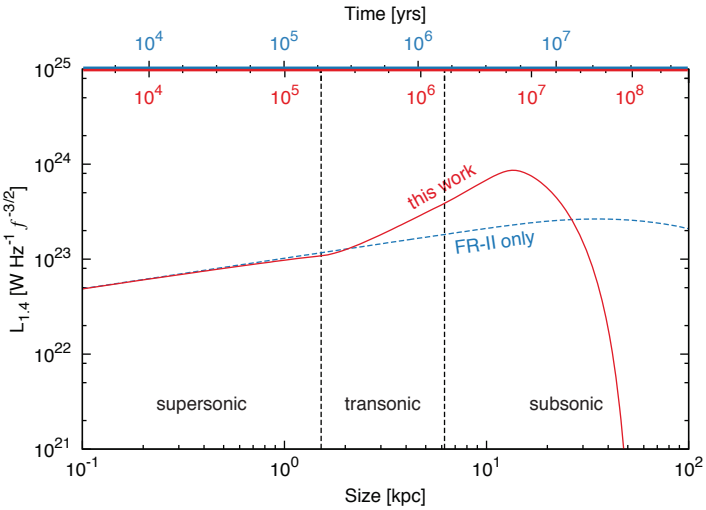

Figure 2.3: Luminosity–size profile (or $L-D$ track; red curve) for a $10^{11}\,\mathrm{M}_\odot$ stellar mass AGN host galaxy with a jet power of $Q_{\rm tot} = 10^{35.5}\,\mathrm{W}$ in a typical environment. The transonic phase occurs when some parts of the lobe are expanding subsonically, while others are still supersonic. The fall in luminosity beyond 10 Myr is due to the Rayleigh-Taylor mixing of the lobe with its environment. The dotted blue line shows the evolution predicted for my dynamical model using the supersonic solution throughout the source lifetime. Note the different time axes for the two models (lower axis for the full model, and upper axis for the FR-II only model). These models yield very different sizes and luminosities at ages exceeding 1 Myr.

Conditions of continuity

The differential equations derived in the previous sections are only applicable in an environment with constant density and temperature exponents (i.e. constant β and ξ). For general environments, in practice I approximate the density and temperature profiles as a series of power law segments (typically 100 segments per source), and ensure the continuity of ensemble element sizes and pressures across the region boundaries. These requirements are met by using the radius R and velocity $\dot{R}$ in each region as initial conditions for the next one.

2.1.5 Radio source luminosity

In order to observationally constrain the properties of radio AGN, I need to model the radio luminosity due to the synchrotron emission from the relativistic electrons in AGN lobes. Synchrotron-emitting electrons will lose energy through adiabatic, synchrotron

and inverse-Compton losses. I follow the formalism of Kaiser et al. (1997), modifying their Equation 16 to include a multi-power law pressure profile (see Chapter 4). The total lobe luminosity (i.e. both lobes) at frequency ν is then given by

$$L_\nu = \int_0^t \frac{4\sigma_\mathrm{T} c q_{\mathrm{B_p}}}{3\nu(q_{\mathrm{B_p}}+1)} (Qf^{-3/2}) n_0 \gamma {\gamma_\mathrm{i}}^{2-s} A^{2(1-\Gamma_\mathrm{c})/\Gamma_\mathrm{c}} \left(\frac{V_\mathrm{e}(t)}{V_\mathrm{e}(t_\mathrm{i})}\right)^{-(\Gamma_\mathrm{B}+1/3)} dt_\mathrm{i}, \qquad (2.9)$$

where σ_T is the Thompson cross-section, c is the speed of light, $\Gamma_\mathrm{B} = 5/3$ is the adiabatic index of the magnetic field, $s = 2.14$ is the electron energy injection index and $q_\mathrm{Bp} = (s+1)/4$ (Kaiser et al. 1997). Here, V_e is the volume of an electron ensemble where γ is the Lorentz factor of an electron emitting radiation predominantly at frequency ν, whilst γ_i are the Lorentz factors at the times t_i when the electrons are initially injected into the radio lobe. This Lorentz factor γ_i is calculated iteratively (over each power law) using Equation 10 of Kaiser et al. (1997), and finally used to determine the number density coefficient n_0 defined in their Equation 8.

There are significant uncertainties in the estimation of the radio source luminosity at a given jet power since the physics of these objects is not fully understood. Willott et al. (1999) described these uncertainties using a single factor f, which is observationally constrained to lie between ~ 1 and 20. However, the uncertainty factor is likely different for the two morphologies, since in particular FR-Is are known to require substantially larger departures from the equipartition magnetic field strength than FR-IIs to achieve pressure balance (e.g. Croston & Hardcastle 2014). In Section 2.4, I show that the lobed FR-I/II dynamical model is consistent with jet powers estimated from X-ray cavity measurements (Heckman & Best 2014) for $f \sim 5$. This factor flows through directly from these jet powers into measures of the AGN energetics, but also subtly affects estimates of the source age. For an uncertainty factor of $f = 5$, the estimated source age at a given size and luminosity is approximately 0.3 dex lower than that calculated using $f = 1$. That is, the source age decreases as roughly $f^{-1/2}$ in agreement with Equations 4 and 5 of Kaiser & Alexander (1997) for supersonic expansion. In this work, I calculate results using $f = 1$ but retain this uncertainty factor in equations so these results can be readily scaled for any realistic choice of this variable, e.g. $f \lesssim 5$. This cause of this uncertainty factor and techniques to constrain it observationally are discussed in Chapter 3.

A typical luminosity–size track produced by the lobed FR-I/II dynamical model is shown in Figure 2.3. This new model predicts a very different temporal evolution of AGN size and luminosity compared to the standard FR-II models. This has a large effect on the derived jet powers and ages of observed AGN. The luminosity increases

initially in the core regions where the density of the host environment is roughly constant (with radius) before decreasing as the density profile steepens towards $\beta = 2$. This behaviour is similar to that found in 3D MHD simulations of radio jets in a range of environments (Hardcastle 2013). By contrast, dynamical models which assume a single $\beta \sim 2$ power law profile (e.g. Kaiser et al. 1997; Blundell et al. 1999, not shown in figure) predict the luminosity decreases monotonically with increasing size. My model also predicts the source luminosity will rise suddenly upon entering the transonic expansion phase. This increase occurs since the lobe pressure equilibrates with that of the host environment rather than continuing to drop off at the rate predicted by the FR-II model. Luo & Sadler (2010) find a similar increase in luminosity using their pressure-limited expansion model for FR-Is. The fall in luminosity beyond 10 Myr is due to the Rayleigh-Taylor mixing of the lobe with the host environment as detailed in Section 2.2.

2.2 Rayleigh-Taylor mixing

The radio lobes of sources expanding above the ambient sound speed (i.e. classical double FR-IIs, or FR-Is with supersonic lobes inflated by uncollimated jets) become susceptible to the Rayleigh-Taylor instability as the expansion slows. Different parts of the lobe become subsonic with respect to the ambient medium at different times. As the lobe plasma becomes entrained by this surrounding medium, the high energy synchrotron electrons in the lobe will be collisionally reduced to the ambient energy level of the much denser surrounding atmosphere. The radio emission from these mixing regions is thus significantly reduced; here I assume it to be zero. The fluid mechanics of this situation are considered here in order to estimate the volume of the lobe that remains unmixed, and thus visible, as the lobe ages. Radio luminosities estimated using the equations of the previous sections will be modified by this visible fraction to account for the Rayleigh-Taylor mixing. Note that the magnetic field may suppress the Rayleigh-Taylor instabilities in some cases; e.g. B2 0755+37 is a lobed FR-I with no thermal material seen to penetrate to the lobe surface even close to the core, however the rotation measure structure is consistent with a magnetic field draping around the expanding cocoon (Guidetti et al. 2012).

The expanding surface of the underdense lobe will become Rayleigh-Taylor unstable (Rayleigh 1883; Taylor 1950) as it enters the subsonic phase. The thickness of the Rayleigh-Taylor mixing layer can be calculated based on the late time self-similar growth phase (Fermi & von Neumann 1953)[3]. The rate of expansion of this layer can

[3]The initial exponential growth phase is insignificant in comparison to the self-similar growth.

be shown (Cook et al. 2004; Ristorcelli & Clark 2004) to be described by

$$\frac{dh}{dt} = 2\left[\frac{\kappa(\rho_{\rm x} - \rho_{\rm coc})g_{\rm eff}h}{(\rho_{\rm x} + \rho_{\rm coc})}\right]^{1/2}. \tag{2.10}$$

Here h is the thickness of the mixing layer (see Figure 2.2), $\rho_{\rm x}$ and $\rho_{\rm coc}$ are the densities of the external medium and lobe respectively, and κ is a dimensionless growth parameter. Most lab-based experiments have returned values for κ in the range $0.03 < \kappa < 0.07$ (e.g. Dimonte et al. 2004). The effective gravitational acceleration, $g_{\rm eff}$, is the sum of the gravitational potential of the galaxy, $g_{\rm grav}$, and the acceleration of the lobe, $g_{\rm coc} = -\dot{v}$ (with $\dot{v}$ as defined in Equation 2.8 for the subsonic phase). The gravitational acceleration on the lobe is given by $g_{\rm grav} = {c_{\rm x}}^2(\beta/\Gamma_{\rm x}R)$, where $c_{\rm x}$ is the sound speed of the ambient medium with adiabatic index $\Gamma_{\rm x}$, and β is the exponent of the power law density profile just outside the lobe (e.g. Shabala & Alexander 2009a).

A general expression for the thickness of the mixing layer, for constant κ but with a time-dependent $g_{\rm eff}$, is then given by

$$h(t) = \left(\kappa^{1/2}\int_{t_0}^{t} {g_{\rm eff}}^{1/2}(t)dt + {h_0}^{1/2}\right)^2. \tag{2.11}$$

The initial conditions t_0 and $h_0 \sim 0$ in this equation are the time at which the flow first enters the self-similar growth phase and the corresponding thickness of the mixing layer. The integral in this equation can be solved numerically by considering small regions over which $g_{\rm eff}(t)$ is approximately constant. For large mixing times it can be assumed that $h_0 = 0$.

The lobe surface can only become Rayleigh-Taylor unstable some time after the corresponding ensemble element has entered the subsonic expansion phase. This ensemble element will thereafter entrain material from the external medium in the mixing region. The thickness of the mixing region will grow along the radial axis[4], as described by Equation 2.11. The mixing layer is assumed to move with the working surface, expanding equally inward and outward from this equilibrium radius. The visible radius of the lobe $R_{\rm v}$ at a given angle θ at each time step is thus $R_{\rm v}(\theta) = R(\theta) - \frac{1}{2}h(t,\theta)$. The visible, unmixed volume of the lobe element is thus $dV_{\rm v}(\theta) = \frac{2}{3}\pi {R_{\rm v}}^3(\theta)\sin\theta d\theta$

Using the linear stability theory of Rayleigh (1883) I found that a delay of 10 e-folding times yielded a less than 10% variation in the unmixed volume and hence luminosity.

[4]The same result is obtained if I instead assume that the mixing layer grows normal to the lobe surface with the effective gravity reduced by the angle θ between the radial axis and the normal (i.e. $g_{\rm eff\perp} = g_{\rm eff}\cos\theta$). For large times $t \gg t_0$, the mixing layer thickness is proportional to $g_{\rm eff}$, and thus the thickness along the radial axis is $h_\perp(t)/\cos\theta = \kappa g_{\rm eff\perp}/\cos\theta = \kappa g_{\rm eff} = h(t)$.

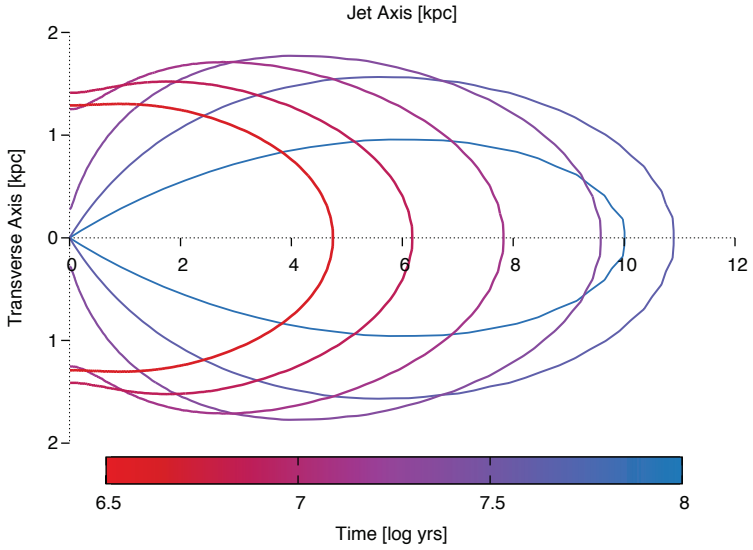

Figure 2.4: Visible cross-section for a radio source with $Q_{\rm tot} = 10^{35.5}$ W total jet power and initial axis ratio of $A = 2$, expanding into a host galaxy with typical external pressure profiles described in Section 2.3.2. The contours on this figure correspond to source ages of 3, 6, 12, 25, 50 and 100 Myrs. The lobe becomes subsonic and begins to entrain thermal material due to the Rayleigh-Taylor instability, first along the transverse axis (at ~ 0.2 Myrs), and later along the jet axis (at ~ 15 Myrs). This Rayleigh-Taylor mixing changes the shape of the visible lobe, eventually causing its length to *decrease* with time, after ~ 40 Myrs.

(c.f. Equation 2.3). The fraction of this total lobe volume that is unmixed and thus visible through radio emission is

$$\mathcal{F} = \frac{\int dV_{\rm v}(\theta)}{\int dV(\theta)} = \frac{\int {R_{\rm v}}^3(\theta) \sin\theta d\theta}{\int R^3(\theta) \sin\theta d\theta}. \tag{2.12}$$

The radio source luminosity calculated in Section 2.1 is reduced by this factor to yield the luminosity from the non-mixed, synchrotron emitting part of the lobe, $L_{\nu{\rm v}} = \mathcal{F} L_\nu$. Note that this equation assumes uniform luminosity through the unmixed regions of the lobe. This assumption may not strictly be valid in weak FR-I type sources where the luminosity is often dominated by the core.

Simulated cross-sections of the visible, unmixed lobe of a radio source are shown in Figure 2.4. Rayleigh-Taylor instabilities affect the slow-expanding narrow part of the radio lobe first, giving the lobe a characteristic hourglass shape observed in FR-II sources such as Cygnus A. The Rayleigh-Taylor mixing may also explain the observed

pinching and eventual separation of radio bubbles from their active nucleus (e.g. M87; Forman et al. 2007). In Section 2.4, I explore further the relationship between lobe entrainment and observed morphology.

2.3 Environment and parameter estimation

In this section, I describe the methodology by which I use the FR-I/II dynamical model developed in the previous section to constrain the physical properties of observed AGN. The intrinsic AGN parameters, in particular their jet powers and source ages, are determined for each radio source based on their observed size and luminosity. I quantify radio source environments using semi-analytic galaxy formation and evolution models.

2.3.1 Local radio-loud AGN sample

Shabala et al. (2008) constructed a complete, volume-limited sample of radio AGN at $0.03 \leqslant z \leqslant 0.1$ by cross-matching two VLA radio surveys at 1.4 GHz, the *NRAO VLA Sky Survey* (NVSS; Condon et al. 1998) and *Faint Images of the Radio Sky at Twenty-Centimeters* (FIRST; Becker et al. 1995), and the optical SDSS Data Release 2. The source classification in this sample should be quite robust since FIRST resolves compact objects whilst NVSS is sensitive to extended structure. I further pair this sample with the Yang et al. (2007) galaxy clustering catalogue to obtain an estimate of the galaxy stellar mass and the mass of the halo associated with the cluster. The masses of the central black holes are estimated using the Gültekin et al. (2009) determination of the $M_{\rm BH} - \sigma_\star$ relation for elliptical galaxies, where $\sigma_\star$ is the stellar velocity dispersion. This yields a sample of 615 radio-loud AGN with stellar and halo masses.

Best & Heckman (2012) analysed a similar (but larger) sample of AGN, and separated these into high- and low-excitation radio AGN. Cross-matching the revised Shabala et al. (2008) catalogue with theirs, I obtain nine HERG and 336 LERG classifications, with the remaining 270 galaxies unclassified. Both populations are mostly of elliptical galaxy morphology (HERGs 88% and LERGs 93%), and I hence adopt environments of simulated elliptical galaxies here (see Section 2.3.2). The emission line fluxes of the radio source host galaxies are taken from the value-added MPA-JHU catalogues (Tremonti et al. 2004). In particular, I use the [O III] 5007 line to calculate the accretion rate of the AGN in my sample.

2.3.2 Radio AGN environments

Hot gas density

Environments into which radio sources expand play an important role in determining the observed AGN properties. X-ray observations are not available for the majority of AGN in the sample, and in any case would be biased to rich environments. I therefore turn to the semi-analytic galaxy evolution (SAGE) model of Croton et al. (2006) to estimate realistic values for the total hot gas mass based on the mass of the cluster halo or galaxy sub-halo. The semi-analytic prescription for the growth of galaxies and their central supermassive black holes is implemented on top of the output of the Millennium N-body simulation (Springel et al. 2005), and is available from the *Theoretical Astronomical Observatory*[5]. In this work I use a subset of the mock galaxy catalogue spanning a simulation volume $30h^{-1}$ Mpc on the side. The mock galaxy catalogue consists of both elliptical and spiral galaxy populations. Radio-loud AGN in the sample are preferentially hosted by massive elliptical galaxies (Section 2.3.1, see also Best et al. 2005), and so I only consider these galaxies when quantifying radio source environments.

I compare the hot gas masses obtained from SAGE to observations of the gas mass in clusters (McGaugh et al. 2010; Gonzalez et al. 2013). The observed gas masses in these $> 10^{13.5}\,\mathrm{M}_{\odot}$ halo mass clusters are typically a factor of two lower than predicted by SAGE. I therefore lower the SAGE gas masses by this factor when using my dynamical model to estimate the physical parameters of AGN. In Section 2.3.3, I investigate the sensitivity of inferred AGN parameters to this choice of hot gas masses.

An interesting question is whether for AGN that are not hosted by brightest cluster galaxies (BCGs), the relevant hot gas mass is that of the host galaxy sub-halo, or of the whole cluster. I fit a typical density profile (see Section 2.3.2) to the simulated gas mass and virial radius of such haloes. The gas density contribution at a typical radio source size of 10 kpc from the active nucleus is modelled for both the cluster halo and sub-halo using simulated galaxies in SAGE with comparable stellar masses to the bulk of my sample (i.e. $> 10^{10.5}\,\mathrm{M}_{\odot}$). These two contributions to the gas density are plotted in Figure 2.5, and grouped by the radial location of the host galaxy within the cluster halo, r/r_{200}. Approximately 80% of these are BCGs (black points in the figure), but of the remainder, less than 2% have environments at 10 kpc with a greater gas density contribution from the cluster halo profile than the host sub-halo. Subsequently I therefore model the external environment using the simulated hot gas density of the

[5] `https://tao.asvo.org.au/tao/`

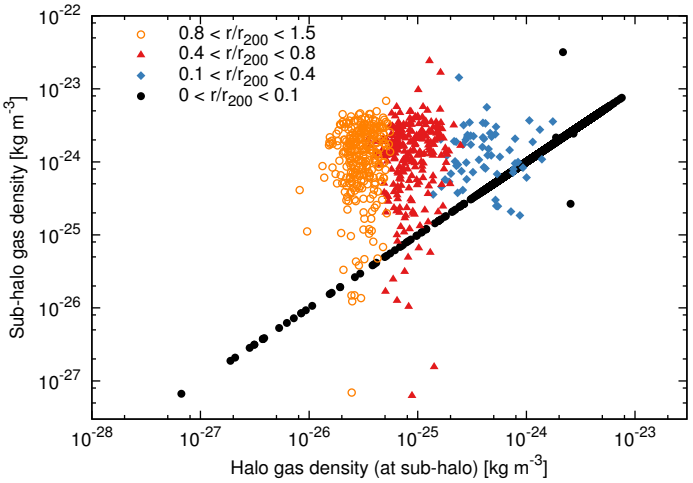

Figure 2.5: A comparison of main and sub-halo hot gas densities for the galaxies in my sample. The distance of these galaxies from the centre of their group or cluster (scaled by the virial radius) is indicated by the point colour. The straight line of points corresponds to brightest cluster galaxies whose sub-haloes are associated with the majority of the gas in their cluster.

host galaxy sub-halo.

Gas temperature

The temperature of the hot gas in clusters is known to scale with the halo mass as $T \propto {M_{200}}^{0.67 \pm 0.06}$ (e.g. Vikhlinin et al. 2006), in line with the virial temperature of the halo. However, the gas temperatures in this relationship exclude the central cooling cores and do not include any recent heating from AGN. O'Sullivan et al. (2001) compiled a catalogue of 401 early-type galaxies, including 13 AGN hosts, with X-ray luminosity observations as a function of the B-band optical luminosity. I convert these variables to temperature and halo mass (Bell et al. 2003) to obtain the dependence $T \propto {M_{200}}^{0.27 \pm 0.24}$. If only the ten AGN with haloes in the mass range of my sample are included I find no significant relationship ($T \propto {M_{200}}^{0.15 \pm 0.38}$). The temperature of the AGN environment may therefore have only a weak dependence on the mass of its cluster halo. At the median halo mass of my sample, the best fit temperature based on the X-ray luminosity of the AGN environment is $10^{\,7.0 \pm 0.3}$ K. In this chapter I present results that assume this constant mean gas temperature. Note that my findings are relatively insensitive to the choice of temperature profile, since very few AGN in my sample hosted by low-mass galaxies are expected to be in the subsonic expansion phase

where the effects of ambient pressure may be important.

External pressure profile

The radial dependence of the host gas density and temperature, which together form the overall pressure profile, is modelled using the cluster observations of Vikhlinin et al. (2006). Their sample comprises low redshift ($z < 0.3$) clusters with halo masses around $10^{14}\,\mathrm{M}_{\odot}$. The density profiles of these clusters are observed to have very similar shapes, when scaled to the core density and virial radius of the cluster. The temperatures of the clusters are similarly constrained, but show far less variability over the radius of the cluster than the density (i.e. $|\xi| \ll |\beta|$, using parameters in Table 2.1). The mean gas temperature (Section 2.3.2) is therefore adopted for all radii, with ξ taken as zero.

The gas density profile assumed in this work is a simplified form of the double-β profile derived by Vikhlinin et al. (2006, their Equation 3) for a sample of 13 local clusters. Only six of their thirteen clusters need a second, core region β profile in their fit, and as such I have chosen to neglect this term here to reduce the degrees of freedom. The simplified form of the hot gas density profile is thus

$$\rho(r) = \rho_0 \left(\frac{(r/a_0)^{-\alpha}}{(1 + r^2/{a_0}^2)^{3\beta' - \alpha/2}} \frac{1}{(1 + r^{\gamma'}/{r_\mathrm{s}}^{\gamma'})^{\varepsilon/\gamma'}} \right)^{1/2}, \tag{2.13}$$

where ρ_0 is the mass density in the core, a_0 is the core radius and $r_\mathrm{s} \gtrsim 0.3 r_{200}$ is the radius at which the profile steepens. The exponents α, β', γ' and ε set the slope of the profile, whilst a_0 and r_s are the core radius and the radius at which the double-β profile steepens. The means and standard deviations assumed for these variables in this work are summarised in Table 2.2. In my radio source modelling, this continuous density profile is approximated by a series of ~ 100 power laws (see Equation 2.1), conserving the total gas mass M_gas of the sub-halo within r_{200} as simulated using SAGE for a given host stellar mass. In Section 2.3.3, I show that the derived physical parameters for observed radio sources are relatively insensitive to realistic changes in these external pressure profiles.

2.3.3 Jet powers and ages

The external pressure profile $p_\mathrm{x}(r)$ of each observed galaxy is modelled by a set of 128 profiles based on the Vikhlinin et al. (2006) density and temperature profiles with parameters given in Table 2.2. For each profile, I sample the gas mass and virial radius

Table 2.2: Ambient pressure profile variables.

Fixed parameter		Value	
initial axis ratio	A	2	
slope (steepening)	ε	3	
	γ'	3	
steepening radius	r_s/r_{200}	0.7	
Sampled parameter		**Mean**	σ
slope (core)	α	1.7	0.3
core radius	a_0/r_{200}	0.08	0.03
slope	β'	0.6	0.1
temperature	$\log_{10}\tau_\mathrm{x}$	7.0	0.3
gas mass	M_gas	mock galaxy data	
virial radius	r_{200}		

distributions from the simulated SAGE galaxies, at the stellar mass of interest, and normal distributions (shown in Table 2.2) on parameters describing the shape of the density and temperature profiles. The radio source evolution is simulated for a range of jet powers Q_tot and ages t_age in each pressure profile. The goodness of fit of the simulated luminosity–size profile (or $L-D$ track) for each such environment to the observed galaxy size D_obs and luminosity L_obs (in log-space) is assessed using the χ^2 statistic,

$$\chi^2 = \left(\frac{D_\mathrm{pred} - D_\mathrm{obs}}{\sigma_\mathrm{D}}\right)^2 + \left(\frac{L_\mathrm{pred} - L_\mathrm{obs}}{\sigma_\mathrm{L}}\right)^2, \tag{2.14}$$

where D_pred and L_pred are the corresponding parameters predicted by the dynamical model. Here the uncertainty due to the model dominates and is taken as $\sigma_\mathrm{D} = \sigma_\mathrm{L} = 0.3\,\mathrm{dex}$. The likelihood of each simulation matching the observations is calculated as $P_\mathrm{pred} = e^{-\chi^2/2}$, yielding a joint probability distribution $P(Q_\mathrm{tot}, t_\mathrm{age}, p_\mathrm{x})$. The marginalised probability for the n-th value of the simulated jet power $Q_{\mathrm{tot\,n}}$ matching the observations is then

$$P(Q_{\mathrm{tot\,n}}) = \sum_{i=1}\sum_{j=1} P(Q_{\mathrm{tot\,n}}, t_{\mathrm{age\,i}}, p_{\mathrm{x\,j}}), \tag{2.15}$$

with an equivalent expression for the source age,

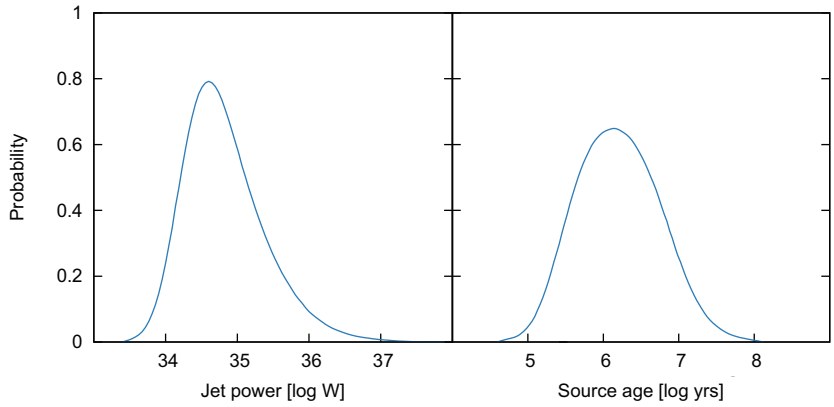

Figure 2.6: Marginalised, normalised one-dimensional probability distributions for the jet power (left) and source age (right) for typical AGN in my sample.

$$P(t_{\mathrm{age\,n}}) = \sum_{i=1} \sum_{j=1} P(Q_{\mathrm{tot\,i}}, t_{\mathrm{age\,n}}, p_{\mathrm{x\,j}}). \tag{2.16}$$

These probability distributions are approximately log-normal (Figure 2.6). The best estimates for the jet power and source age are thus taken as the peaks of the relevant marginal distributions, with the uncertainties taken as the FWHM. This procedure is repeated for each of the 615 AGN in my sample.

Robustness to jet power and age priors

The joint probability distribution is initially calculated assuming a flat prior (in log-space) for the jet power and source age, and a log-normal distribution for the host gas density. The estimated distributions of these parameters are coupled (e.g. both old, high jet power, and young, low jet power sources will appear faint and are thus more likely to be undetectable in radio surveys). I therefore relaxed the assumption of log-uniform priors, instead adopting the estimated distributions (from the first pass) of jet powers and ages in the marginalisation process. The results are robust to these changes in the priors on jet power and source age.

Robustness to environment

I further examine the reliability of the jet power and source age estimates by assessing their sensitivity to the host gas density prior. The jet powers and source ages are recalculated for gas density priors with a factor of two shift (i.e. 0.3 dex) in the

mean density of the distribution at each stellar mass. The shifts in the estimated jet power and source age distributions are shown in Figures 2.10 through 2.13. The higher pressure prior yields lower jet powers, in particular for lower mass hosts, and older sources in all galaxies. This is expected since higher external pressures yield higher luminosities (Kaiser et al. 1997, Equation 16) requiring a lower jet power to match observations. The source age is necessarily greater due to the increased resistance to expansion. Conversely, the lower pressure prior corresponds to higher jet powers and younger sources. These factor of two shifts in the mean of the external pressure distribution result in a less than 0.15 dex variation in the median jet power and source age. These variations are both much less than the intrinsic width in the derived jet power and source age distributions (0.6 and 0.9 dex respectively). Note that if the log-space uncertainty in the environment is larger by a given factor, the variation in the jet power and source age will increase by that same factor. I conclude that the jet power and source age parameter estimates are therefore robust to the moderate uncertainties in the distribution of the pressure profiles. These parameters are estimated to be accurate to better than a factor of 1.5 (in a statistical sense). Note that my assumption of a cluster-like pressure profile may not be applicable for low-mass AGN hosts. However, the assumed gas masses (from SAGE) are consistent with observed galaxy properties in a statistical sense, validating this approach.

2.3.4 Axis ratio

The initial supersonic phase value of the axis ratio, A (this is the ratio of lobe length and radius), is a free parameter in my model. I adopt a value of $A = 2$ here for all sources, noting that A increases once the lobe enters the transonic phase. The lobed FR-I/II dynamical model predicts the axis ratio increases to a present-time value of between 2 and 8, broadly consistent with the observed radio AGN population (Mullin et al. 2008). I defer a detailed investigation of lobe shape to Chapter 4.

2.4 Radio source morphology

The Fanaroff & Riley morphological dichotomy can be at least partly explained by the influence of external environmental factors on the jet structure (e.g. Laing et al. 1994; Bicknell 1995; Kaiser & Alexander 1997). In particular, shredding of the subsonic lobe by Rayleigh-Taylor mixing of the external medium makes the jet more liable to Kelvin-Helmholtz instabilities, leading to an FR-I like morphology. Here, I test whether the lobe expansion speed predicted by my dynamical model is related to radio source

morphology. In particular, I hypothesise that sources expanding supersonically will appear as FR-IIs, and those expanding subsonically as FR-Is. The morphology of radio sources in between these limiting cases is not clear-cut from this definition. For example, Centaurus A is observed to have an FR-I flaring inner jet whilst shocking its environment at larger radii (Kraft et al. 2007; Croston et al. 2009); by contrast the central regions of many FR-IIs are pinched due to subsonic mixing processes.

In my model, morphology is determined by calculating the fraction of their lives that radio sources of a given jet power and stellar mass spend in the subsonic and supersonic expansion phases. The source active lifetimes are constrained by fitting a multivariate regression to the jet power and stellar mass estimates I obtained for my sample. Because the lobe is non-spherical, parts of the surface become subsonic at different times. Hence the choice of the reference point for measuring the lobe expansion speed is important. Here I consider two locations, along the semi-minor (or transverse) and semi-major (or jet) axes of the lobe. These are parts of the lobe that become subsonic first (semi-minor) and last (semi-major axis).

I compare this simulated FR-I/II dichotomy with two sets of observations in Figure 2.7. Owen & Ledlow (1994) reported the observed correlation between R-band optical magnitude, 1.4 GHz radio luminosity and FR morphology for a sample of radio sources primarily found in Abell clusters. Best (2009) pointed out that, in this sample, the FR-Is are located predominantly at redshifts less than 0.1, with the bulk of the FR-II population being found at $z > 0.25$. By constructing a volume-limited sample, Best (2009) showed that the separation between FR-Is and FR-IIs in optical magnitude–radio luminosity phase space, albeit real, is much less clearcut than originally suggested by Owen & Ledlow (1994).

In Figure 2.7, the dashed and solid black lines represent fits from the dynamical model to the locations in jet power–stellar mass space where an equal fraction of the radio source active lifetime is spent in the subsonic (i.e. FR-I) and supersonic (i.e. FR-II) states. These fits are for a model using a constant 10^7 K temperature for environments hosting AGN from my sample, whilst the grey shading indicates the 1σ uncertainties corresponding to a factor of two variation in the temperature of the external medium. I convert stellar mass to R-band optical magnitude using the equations of Bell et al. (2003), and jet power to radio luminosity using my data. Based on my hypothesis, sources lying above the semi-minor axis sonic transition line are expected to be predominantly FR-IIs, with FR-Is lying below the jet axis line. The empirical separation between the observed FR-I and -II populations is consistent with the lines derived for the two subsonic points, and corresponds to a

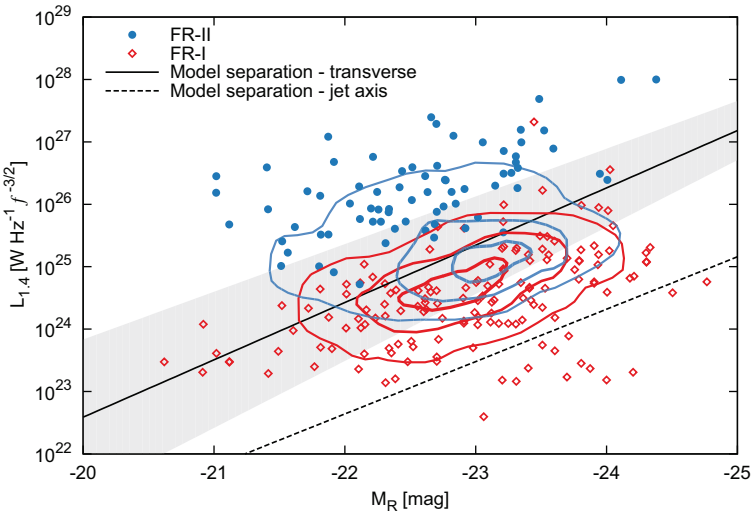

Figure 2.7: FR radio dichotomy as a function of R-band optical magnitude and 1.4 GHz luminosity. Observations are from Owen & Ledlow (1994, points) and Best (2009, contours). The contours correspond to locations with 16, 50 and 84% fewer sources than the peak phase space density. These observations are scaled assuming the modelled results used $f = 1$. Higher values in this uncertainty factor will cause these points to move to higher luminosities relative to my predictions. The straight lines correspond to model predictions where half the sources are still expanding supersonically, and the other half subsonically. Calculations for expansion speed along the jet axis (dashed line) and transverse to the jet (solid) are shown, assuming a constant 10^7 K temperature. The 1σ uncertainties due to variations in the temperature of the external medium are shown by the grey shading.

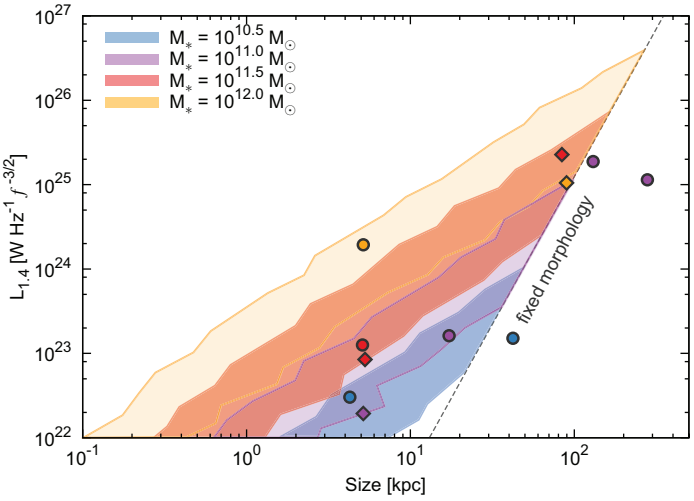

Figure 2.8: FR radio morphology as a function of source size, 1.4 GHz lobe luminosity and host galaxy stellar mass. The shading maps regions in this phase space where the dynamical model predicts transonic phase evolution. Sources above these dividing lines for the relevant mass bin are predicted to be FR-IIs, while those below should be FR-Is. Objects lying within the shaded transonic regions at a given stellar mass can have either morphology. The morphology of sources is not expected to change further upon entering the region beyond the grey dashed line. That is, a source retains its FR-II morphology if its $L-D$ track does not cross the morphological transition line before entering this region. Note the overlap between shaded regions for different host galaxy masses. Points show data from the CoNFIG sample of Gendre et al. (2010), with FR-IIs marked as circles and FR-Is as diamonds. Colours correspond to the stellar mass of the AGN host galaxy. These observed points have been scaled using $f = 1$.

surface location somewhere between these extreme cases. Interestingly, the region where these two populations overlap in the Best (2009) sample is coincident with the parameter space in which the predicted model morphologies are strongly environment-dependent. These conclusions are robust to realistic uncertainties in the jet power–luminosity relationship, e.g. $f \lesssim 5$. I conclude that a comparison of the expansion speed of the lobe to the local sound speed can thus successfully explain the observed FR-I/II dichotomy.

Based on these findings, I tentatively identify radio sources as FR-Is or FR-IIs based on the Mach number modelled at the time of observation. Sources which are entirely supersonic are labelled FR-IIs, and those which are entirely subsonic are FR-Is. Sources which fall between these two categories could have either morphology, with

the probability of being an FR-I increasing with the fraction of the lobe surface which is subsonic. The FR-II population is predicted to consist of both smaller and younger sources than the FR-I population, irrespective of which temperature model is used, consistent with observations by Best et al. (2007).

The locations in luminosity–size space in which FR-I and -IIs are thus expected to be found are plotted in Figure 2.8 for four host galaxy stellar masses. For each mass bin, the shading marks the regions in luminosity–size space at which the expansion of radio sources is in the transonic phase (i.e. supersonic at semi-major but subsonic at semi-minor axis). The shaded regions include the uncertainty due to simulated variation in the host environment within each mass bin. At a given mass and size, radio sources in the supersonic expansion phase (which I identify with FR-IIs) have higher luminosities than these dividing lines, whilst sources expanding subsonically (our FR-Is) are less luminous. Sources lying within the shaded regions defined by the semi-major and semi-minor axis sonic transitions can have either FR morphology in my model. Radio AGN inhabiting poor environments are more likely to be observed as FR-IIs than sources of the same size and luminosity in more massive hosts. However, the evolution of the larger sources is dictated mostly by the higher density environment at smaller radii. Sources which have reached sizes beyond the grey dotted line in Figure 2.8 without entering the transonic phase are thus expected to retain their FR-II morphology. The morphology of the largest radio AGN is therefore somewhat sensitive to the initial conditions, in particular their host environment. I compare these radio morphology predictions with observations of the local extended radio source populations (Gendre et al. 2010), and find the two to be in good agreement. That is, all their FR-IIs are in the supersonic or transonic expansion phase, whilst FR-Is are in the transonic or subsonic phase. This result holds true for realistic values of the scaling factor f in the jet power–luminosity relationship.

Finally, I note that the jet power estimates can be used to derive an empirical relationship for the jet power based on the source morphology, size and luminosity observables. A number of loss processes associated with the synchrotron emitting electron populations render luminosity (by itself) a useful but flawed predictor of jet power, especially for evolved radio galaxies (Shabala & Godfrey 2013). I defer a detailed investigation of the jet power–radio luminosity relation to Chapter 3, but now examine its dependence on the Fanaroff-Riley morphology. The jet power (calculated in Section 2.3.3) is plotted in Figure 2.9 as a function of size, luminosity and the tentative source morphology classification. Also plotted is the cavity relationship of Heckman & Best (2014), scaled assuming the modelled results had a jet power–luminosity uncertainty factor of $f = 5$. That is, my model is in good agreement with other reported measurements of the

jet power when assuming $f = 5$. This value agrees well with the findings of Daly et al. (2012) using a different method of estimating jet power, and is well within the plausible range $f \sim 1$ - 20 (e.g. Heckman & Best 2014).

The jet power in Figure 2.9 shows a strong positive correlation with the 1.4 GHz radio luminosity by itself, i.e. brighter sources tend to have higher jet powers. More of the variability in the jet power can be explained by considering the source size and morphology. The source size is plotted in Figure 2.9 for two size bins whilst the morphology is indicated by the point colour, with FR-Is in red and FR-IIs in blue. Larger sources tend to have higher jet powers than smaller sources of the same luminosity and morphology, consistent with the observations of Shabala & Godfrey (2013). Further, radio AGN of FR-II morphology have jet powers approximately a factor of two higher than FR-Is of the same size and luminosity (dashed lines in Figure 2.9). This is likely because at a given jet power, AGN expanding in poor environments are more likely to retain FR-II morphology; these sources will also be less luminous than their disrupted FR-I counterparts located in denser environments. Different empirical relationships will therefore apply for the two FR morphological classes, and thus radio AGN morphology must be considered in addition to size and luminosity in estimating jet power.

2.5 AGN energetics and feedback

2.5.1 Jet powers and lifetimes

Having estimated AGN kinetic powers and lifetimes (Section 2.3.3), I can now quantify the energetics of AGN feedback on galaxies. When drawing conclusions about the overall AGN population from my volume-limited sample selection effects must be taken into consideration. Low jet power sources ($Q_{\rm tot} \lesssim 10^{34}\,{\rm W}\,f^{3/2}$) are theoretically undetectable by the FIRST/NVSS surveys at any time in their evolution, whilst higher jet power sources will not be detectable at later times when loss mechanisms (in particular the inverse-Compton scattering of CMB photons) and Rayleigh-Taylor mixing cause the luminosity to fall rapidly. I quantify the fraction of undetected sources by modelling AGN with a range of jet powers, ages and environments. In this modelling, the AGN environments are assumed to be well described by the scaled SAGE hot gas masses (Section 2.3.2), and I adopt the observed mass dependence of the radio-loud AGN fraction to quantify AGN intermittency. The figures in the following sections indicate this drop-out region with blue lines corresponding to detectable fractions of 84, 50 and 16% of radio sources.

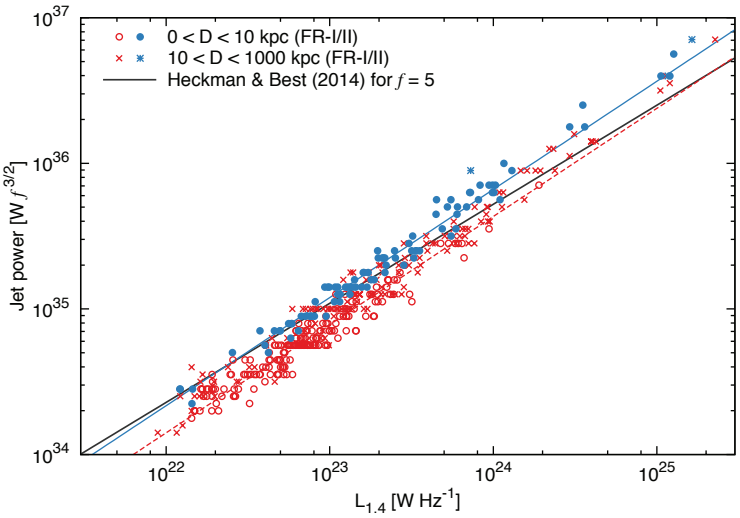

Figure 2.9: Jet power as a function of the source size, luminosity and predicted Fanaroff-Riley morphology. Radio AGN with sizes $D < 10\,\mathrm{kpc}$ are marked by circles, whilst the largest sources ($D > 10\,\mathrm{kpc}$) are shown with crosses. FR-Is are plotted with red, unfilled points and FR-IIs using blue, solid points. Here, FR-IIs are identified with sources that are still expanding supersonically, while FR-Is are those sources for which at least part of the lobe is expanding subsonically. Best fits to the smallest sources for both morphologies are plotted with dashed lines. The cavities relation derived by Heckman & Best (2014) is shown for comparison (grey), scaled using $f = 5$.

Jet powers

A combination of theoretical and empirical considerations suggest that the AGN jet power should to be largely independent of the host galaxy stellar mass. Jet generation models predict that the jet power increases approximately with the black hole accretion rate $\dot{M}_{\rm BH} \propto \dot{m} M_{\rm BH}$ (Meier 2001). The general consensus is that in massive ellipticals at low redshift, the active nucleus feeds energy back into its host galaxy at a rate balancing the loss of energy through radiative cooling (Best et al. 2007; McNamara & Nulsen 2007; Fabian 2012). Naively, one might expect this instantaneous accretion rate to balance the gas cooling rate, which scales with black hole mass (and thus stellar mass) as $\dot{M}_{\rm cool} \propto {M_{\rm BH}}^{1.5}$ (Best et al. 2005). The jet power would thus be expected to be proportional to the black hole and stellar masses as $Q_{\rm tot} \propto {M_{\rm BH}}^{1.5} \propto {M_\star}^{1.5}$. However, this jet power–stellar mass relationship needs to be modified for the AGN feedback cycle. Since there may be multiple AGN events within a single cooling time, I consider the time-averaged fuelling rate for the active nucleus, $f_{\rm RL}\dot{M}_{\rm BH}$, where $f_{\rm RL}$ is the radio-loud fraction. If the AGN are fuelled by the gravitational instability, $f_{\rm RL}$ is expected to scale with black hole mass as $f_{\rm RL} \propto {M_{\rm BH}}^{1.5}$ (Pope et al. 2012). In heating-cooling equilibrium (i.e. $f_{\rm RL}\dot{M}_{\rm BH} \propto \dot{M}_{\rm cool}$) the jet power should therefore be related to the black hole and stellar masses as $Q_{\rm tot} \sim \dot{M}_{\rm cool}/f_{\rm RL} \propto {M_{\rm BH}}^0 \propto {M_\star}^0$.

The jet powers calculated for my sample are plotted as a function of stellar mass in Figure 2.10. Unsurprisingly, a wide range of jet powers are observed at a given stellar mass. The relationship between these variables is analysed with a standard least squares linear regression (black line) yielding $Q_{\rm tot} \propto {M_\star}^{0.1\pm0.1}$. I also fit an L1 (least absolute errors) linear regression to provide a more robust estimate of the slope of $Q_{\rm tot} \propto {M_\star}^{0.0\pm0.1}$. By contrast, using their simpler FR-II only model Shabala et al. (2008) found a steeper relationship of $Q_{\rm tot} \propto {M_\star}^{0.6\pm0.2}$, but with a comparable mean jet power (purple line). Further, in this figure I show the region of jet power–mass space where sources are expected to have luminosities below the survey detection limits (blue lines and shading). Although detection limits may contribute to the lack of mass dependence for low jet powers ($Q_{\rm tot} < 10^{34.5}\,{\rm W}\,f^{3/2}$), the top end of the distribution corresponds to the real AGN population. This relation shows no dependence on the host galaxy mass, in agreement with the theoretical expectation assuming long-term heating-cooling balance. These results are therefore consistent with the maintenance nature of AGN feedback in the local universe.

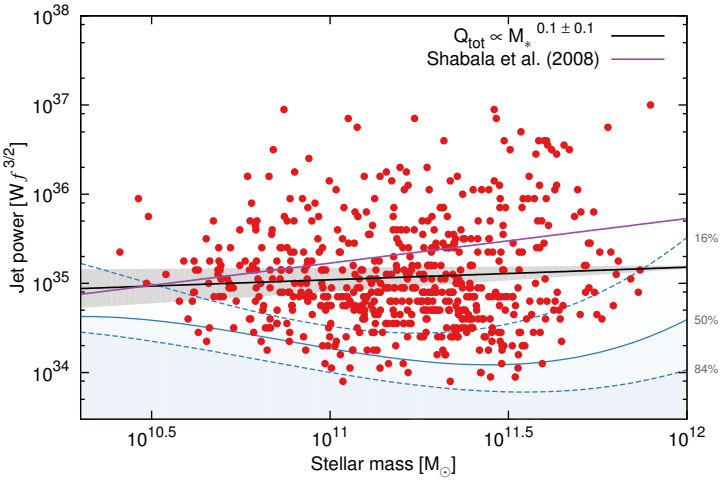

Figure 2.10: The correlation between jet power and observed stellar mass. Best fit is shown by a solid line, and uncertainties due to a factor of two variation in hot gas mass by the shaded region. The relationship obtained by Shabala et al. (2008) using their simplified model for these same radio galaxies is shown in purple. The blue lines show the region of jet power–mass space where 16, 50 and 84% of sources (from top to bottom) are expected to have luminosities below the survey detection limits.

Active and quiescent timescales

In Section 2.3 I derived the age of the radio source at the time of observation, not the total time over which the source is active. As sources age, they become less luminous due to a combination of synchrotron, inverse-Compton and adiabatic losses. Because source size also increases with age, the surface brightness of the oldest sources drops rapidly, taking many of these close to (or below) the survey sensitivity threshold. Through the marginalisation process some very long-lived sources should be selected early in their active lifetime whilst they are detectable. If these sources were active up to their maximum detectable age I would expect the source ages to follow a uniform, linear distribution. However, more than 90% of my sample sources are observed to be younger than half their maximum detectable age, with more than 70% at a tenth of that age. There is therefore a real overabundance of young sources. I conclude that these young sources, and all other sources, must be observed somewhat close to their active age. The source active lifetime is thus taken to be double the observed age, i.e. $t_{\rm on} = 2t_{\rm age}$, since the average source will be observed halfway through its evolution.

The relationship between the derived active lifetime and stellar mass for my radio AGN sample is shown in Figure 2.11. The mass dependence of the active lifetime is again cal-

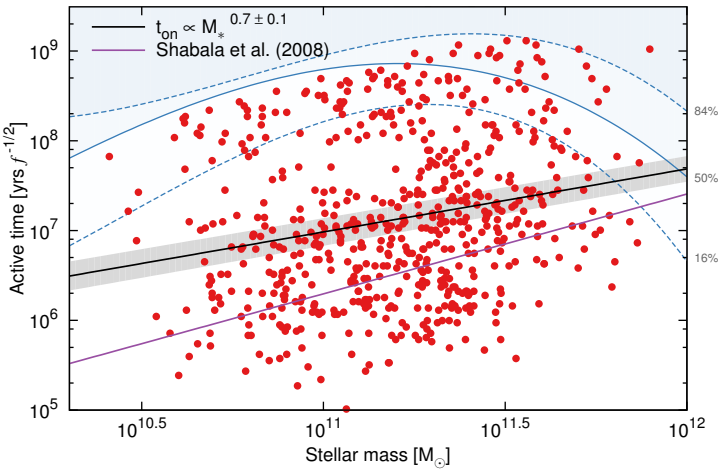

Figure 2.11: The active lifetime as a function of stellar mass. The blue lines are for the same fractions as in Figure 2.10 but with limits for both young and old sources.

culated using a linear regression yielding $t_{\rm on} = (4.8 \pm 0.5\,{\rm Myr}\, f^{-1/2})(M_\star/10^{11}\,{\rm M}_\odot)^{0.7\pm0.1}$. The derived normalisation for my sample is higher than the 1 Myr $f^{-1/2}$ lifetime estimated by Shabala et al. (2008) for a $10^{11}\,{\rm M}_\odot$ host galaxy, though the slope is comparable given their large uncertainties. Their younger ages result from the use of a simpler strong-shock limit supersonic expansion model for this mostly FR-I population. Finally, the AGN active lifetimes should scale as $t_{\rm on} = f_{\rm RL} t_{\rm host}/N$, where $t_{\rm host}$ is the total age of the host galaxy group or cluster and N is the number of AGN outbursts during this time (Pope et al. 2012). The triggering frequency is thus related to the stellar mass as $\omega_{\rm trig} = N/t_{\rm host} = f_{\rm RL}/t_{\rm on} \propto {M_\star}^{0.8\pm0.1}$. In general, the radio AGN in the most massive galaxies are therefore triggered more frequently, and are also active for longer in a given epoch.

The quiescent timescales (i.e. the time the AGN is inactive) are also relevant to understanding the AGN fuelling and triggering mechanisms. The active lifetime can be used to determine the quiescent timescale as $t_{\rm quiet} = t_{\rm on}(1 - f_{\rm RL})/f_{\rm RL}$. Here I use the scaled relationship for the duty cycle of Best et al. (2005). The quiescent timescales (plotted in Figure 2.12) exhibit a strong negative correlation with stellar mass, driven largely by the strong dependence of $f_{\rm RL}$ on $M_\star$. Many of the radio sources hosted by galaxies with stellar masses less than $M_\star \approx 10^{11}\,{\rm M}_\odot$ are expected to be inactive for longer than the Hubble time. A large fraction of these low mass galaxies may therefore have never been in the active state. Note that here I have used a source specific calculation of the active age, but a population average for the quiescent phase, which may not be applicable for individual sources. The quiescent

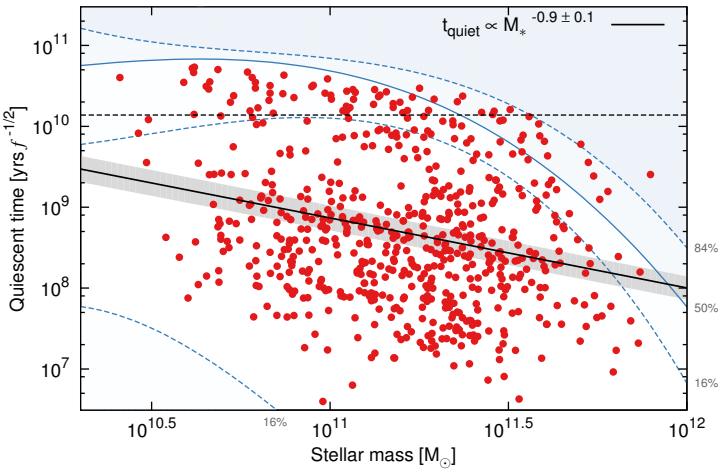

Figure 2.12: The distribution of quiescent timescales plotted as a function of stellar mass, as for Figure 2.11. The black dashed horizontal line is the Hubble time.

time is found to scale with mass as $t_{\rm quiet} \propto {M_\star}^{-0.9\pm0.1}$. In the absence of a heating source, I would expect $t_{\rm quiet} \propto {\dot{M}_{\rm cool}}^{-1} \propto {M_\star}^{-1.5}$ (Best et al. 2005). The fact that the observed relationship is not as steep may suggest that feedback from powerful radio sources in massive galaxies plays an important role, flattening out the relationship at high masses as first proposed by Shabala et al. (2008).

AGN energetics and feedback

Examining the energetics of AGN reveals which sources provide the most feedback in the low-redshift universe. The energy input by an AGN into its surroundings over an active phase is equal to the product of its jet power and the duration of the AGN event, $E_{\rm tot} = Q_{\rm tot} t_{\rm on}$. The input energies thus calculated for my sample are plotted in Figure 2.13 as a function of stellar mass. The relationship between these variables is again analysed using a linear regression yielding $E_{\rm tot} \propto {M_\star}^{0.8\pm0.2}$. The energy injected by an AGN into its host in an outburst thus increases approximately linearly with the galaxy mass. Since the AGN in massive hosts are also triggered more frequently, I find the average energy injected by the central nucleus over time to scale even more steeply with mass as $\bar{E}_{\rm tot} \propto \omega_{\rm trig} E_{\rm tot} \propto {M_\star}^{1.6\pm0.2}$. This scaling is similar to the theoretical expectation for a cluster in heating-cooling equilibrium of $\bar{E}_{\rm tot} \propto \dot{M}_{\rm cool} \propto {M_\star}^{1.5}$. The implications of these findings are discussed in more detail in Section 2.5.2. Massive hosts thus provide more feedback to their surroundings than their lower mass counterparts, as required by galaxy formation models (Croton et al.

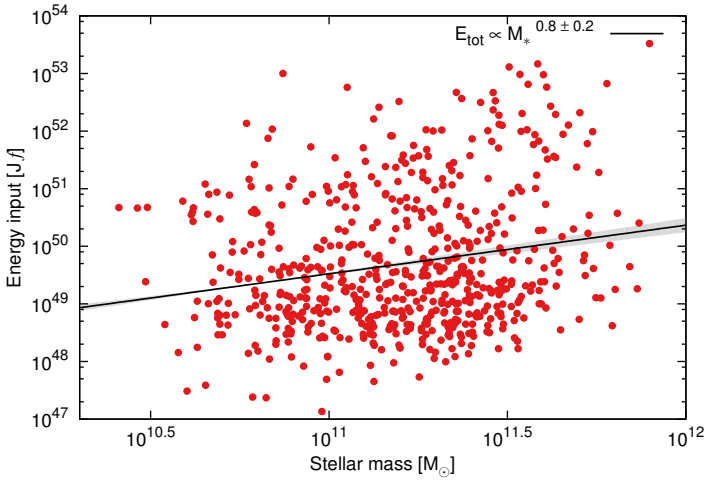

Figure 2.13: The energy input of the AGN into their surroundings as a function of stellar mass. Detection limits are not shown since the effect of selection bias is similar for all masses, with approximately 30% of sources undetected everywhere. While at a given stellar mass I observe a broad distribution in the total AGN energy output, there is a robust mass dependence for the average AGN.

2006; Bower et al. 2006).

I investigate which AGN provide the most feedback in the low-redshift universe by considering the number density of sources at a given stellar and radio luminosity, and their time averaged energy input, $\bar{E}_{\rm tot}$. The sources are binned in stellar mass and radio luminosity to yield luminosity functions (including $V/V_{\rm max}$ corrections) at a fixed stellar mass. The number densities in each bin are then weighted by the energy input of each radio AGN on a source-by-source basis. This energy flux (i.e. energy input per unit volume) is plotted as a function of radio luminosity in Figure 2.14 for two stellar mass bins and the entire sample. I plot the energy flux including corrections for the survey drop-out at low jet powers (solid lines) in addition to the uncorrected data (points and dashed lines). Poisson uncertainties (1σ level) are plotted for the raw data.

The energy flux of radio AGN in high mass galaxies ($M_\star > 10^{11.4}\,{\rm M}_\odot$) increases strongly with luminosity until $L_{1.4} = 10^{25}\,{\rm W\,Hz^{-1}}$ where it peaks. These high luminosity sources contribute a factor of ten times more energy to the total galaxy population than those at $10^{23}\,{\rm W\,Hz^{-1}}$. By contrast, the energy flux of radio sources in lower mass hosts has only a very weak dependence on luminosity. These sources contribute a factor of four less energy to the low-redshift galaxy population than those

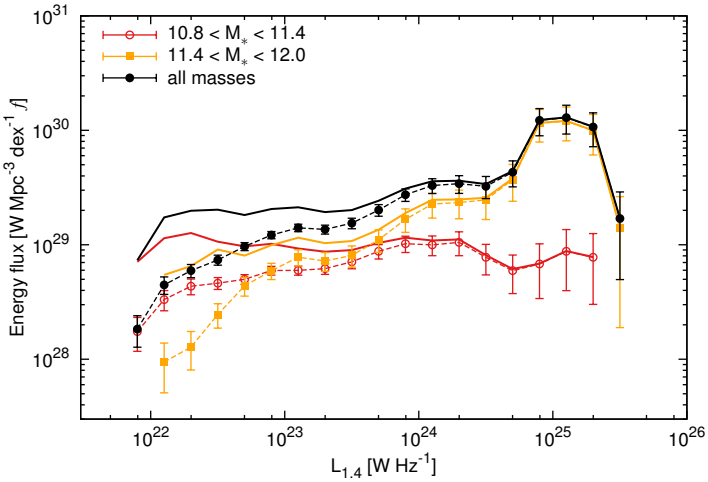

Figure 2.14: The radio AGN energy flux (energy input by AGN into their hosts per unit volume) as a function of the observed 1.4 GHz luminosity for two mass bins and the entire sample. I plot both the raw data (points and dashed lines) and also include curves that correct my data for survey selection effects (solid lines).

in the most massive hosts, despite their greater number density. These results hold when corrections for the survey selection effects are applied. The lower energy flux associated with low luminosity radio sources and those in less massive hosts implies the amount of feedback energy such sources provide on the total galaxy population is much less than for the most massive galaxies near the $\sim 10^{25}\,\mathrm{W\,Hz^{-1}}$ luminosity peak. Observing radio sources at even lower luminosities may therefore be unnecessary in further understanding the effect of AGN feedback on their host galaxies. Of course this does not take into account the very likely possibility of different coupling efficiencies with the gas for supersonic and subsonic lobes. As discussed in Section 2.4, lower mass galaxies preferentially host supersonic phase FR-IIs whilst their more massive counterparts harbour subsonic FR-Is. Even for a given radio source morphology, numerical simulations of radio jets suggest the efficiency of feedback is strongly dependent on how the energy is supplied to the gas, rather than just the total amount (Binney et al. 2007).

2.5.2 AGN heating and cluster cooling

In this section, I compare the time-averaged rate of heating from the AGN with the cooling in its host's hot environment. Our jet powers calculated on a source-by-source basis provide a much broader distribution at a fixed stellar mass than previous work

using empirical jet power–luminosity relationships (e.g. Best et al. 2007). I estimate the cooling rate, following the method of Best et al. (2007), by considering the fraction of X-ray luminosity arising from within the cooling radius, $r_{\rm cool}$. This rate is found as a function of the cluster velocity dispersion, $\sigma_{\rm v}$, by combining the results of Peres et al. (1998) and Ortiz-Gil et al. (2004), $L_{\rm X}(r < r_{\rm cool}) \approx 1.34 \times 10^{37} (\sigma_{\rm v}/1000\,{\rm km\,s^{-1}})^{4.1}\,{\rm W}$. Here, the cluster velocity dispersion is derived from the halo mass of each cluster using the relationship of Munari et al. (2012). The average rate of heating from the AGN is calculated using my results (from the previous section) as the product of the jet power and the observed radio-loud fraction, i.e. $\bar{H} = Q_{\rm tot} f_{\rm RL}(M_\star)$. Again I assume the black hole-duty cycle relationship of Best et al. (2005), but take $f_{\rm RL} = 1$ for the most massive black holes (Fabian 2012, and references therein). Based on my findings in Figure 2.9, I assume the uncertainty scaling factor in the jet power–luminosity relationship is $f \sim 5$ when comparing the heating and cooling rates.

The ratio of the time-averaged heating to the cluster cooling rate is plotted in Figure 2.15. Low mass galaxy haloes are consistent with a ratio of approximately unity (i.e. heating-cooling balance) for $f \lesssim 5$, however, high mass haloes ($> 10^{14.5}\,{\rm M_\odot}$) require an additional heating mechanism. Such clusters have time-averaged heating rates a factor of $200 f^{-3/2}$ lower than the cluster cooling rates, though due to the large scatter in jet powers this difference is only significant at the 1σ level for $f \sim 5$. This discrepancy was previously reported by Best et al. (2007).

Thermal conduction of energy from the reservoir of hot gas outside of the cooling radius into the cooler cluster centre may provide an additional source of heating in the most massive systems (see Best et al. 2007, and references therein). The heating rate due to this thermal conduction was originally calculated for a pure hydrogen gas by Spitzer (1962). Although this rate will be reduced in the presence of magnetic fields, Narayan & Medvedev (2001) argue that the suppression of thermal conduction may only be a factor of a few in the presence of turbulent magnetic fields. In Figure 2.15 I plot the effects of Spitzer conductivity for 25 and 100 per cent of the Spitzer value. The inclusion of this heating mechanism for realistic values of Spitzer conductivity can yield heating-cooling balance (within 1σ uncertainties) for all halo masses. That is, AGN feedback, in conjunction with thermal conduction, can maintain long term heating-cooling balance in even the most massive galaxy clusters, consistent with the findings of Best et al. (2007) using a different jet power estimation method.

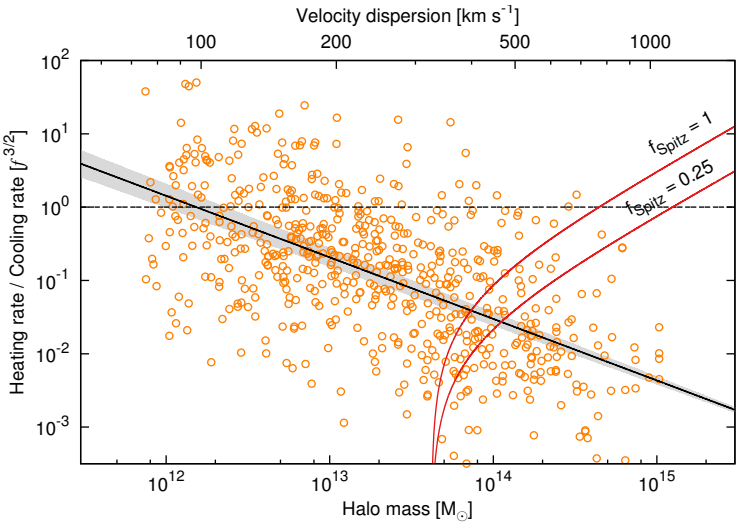

Figure 2.15: The ratio of the AGN heating and gas cooling rates in the host cluster as a function of halo mass. The orange circles are the ratio of the time-averaged energy input from the jet and the cluster cooling rate. The solid black line is a best fit to this distribution with the grey shading showing uncertainties arising from my assumptions about the hot gas density. Heating due to thermal conduction is plotted in red for two scaling factors.

2.6 Fuelling the monsters

In this section, I use the AGN intrinsic parameter fits to study black hole accretion flow mechanisms. This requires careful consideration of observational selection effects.

2.6.1 High- and low-excitation radio galaxies

First, I investigate whether the different black hole fuelling mechanisms of high- and low-excitation radio galaxies (HERGs and LERGs) correspond to differences in the active lifetime and jet power distributions, as might be expected if these objects probe different black hole accretion states (e.g. Hardcastle et al. 2007; Best & Heckman 2012). There are not enough HERGs in my sample to draw reliable conclusions, however, the relative locations of the HERG and LERG sub-populations in active age–jet power space are shown in Figure 2.16. The drop-out region of age–jet power space is marked with blue lines corresponding to detectable fractions of 84, 50 and 16% as discussed in Section 2.5.1. The observed "correlation" is thus largely a result of these survey selection effects, however the relative locations of HERGs and LERGs within this distribution are likely due to intrinsic differences.

The HERG population has a mean stellar mass 0.24 dex lower than for the LERGs, with this difference significant at the 3σ level. This is consistent with HERGs being fuelled by minor mergers, and LERGs through gas cooling which preferentially takes place in the most massive galaxies (Hardcastle et al. 2007; Best & Heckman 2012; Shabala et al. 2012). The HERG and LERG radio sources, however, show no preference for inhabiting different environments for a given halo mass (Figure 2.17). Hence, we are not just seeing young HERG AGN because they are in poor environments (at a given $M_\star$).

The mean jet power of the HERG population is higher than that of the LERGs by 0.58 dex (3σ significance), as shown in Figure 2.16. This result holds even when the nine HERGs are compared with a sub-population of LERGs with the same distribution of stellar masses. These higher HERG jet powers are expected due to the higher black hole accretion rates in minor mergers. Moreover, the mean active lifetime of the HERGs is 1.1 dex lower than for the low-excitation population, with this difference significant at the 5σ level. These younger HERG active ages likely result from these galaxies being associated with short lived epochs of high accretion arising from the merger of the host with a gas rich system (Hardcastle et al. 2007; Shabala et al. 2012). The timescales for the supply of cold gas in this scenario differ from the usual heating and cooling cycle of the IGM, which can fuel the lower accretion rate LERGs.

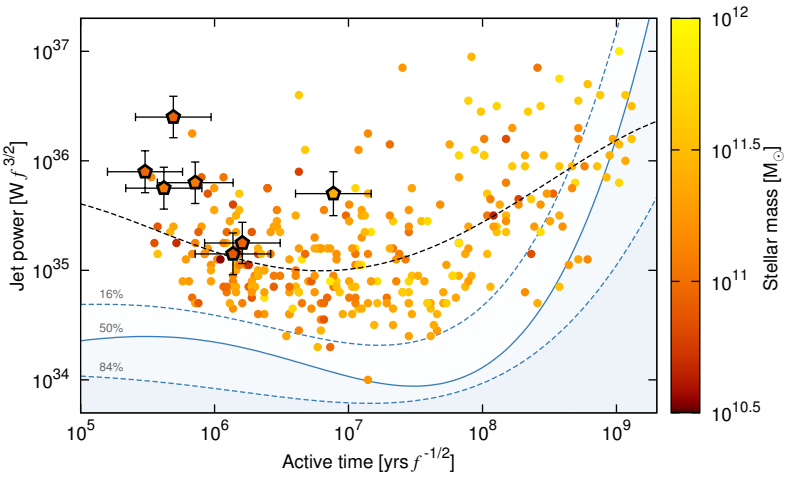

Figure 2.16: The distribution of high- and low-excitation radio galaxies, pentagons and circles respectively, in active age-jet power space. The black dashed curve is a best fit to the distribution of LERGs, used to remove the effect of the active lifetime and selection effects from comparisons with the HERGs. The colouring of the points denotes the host galaxy stellar mass, whilst the blue lines indicate the times at which lower jet power sources are theoretically too faint to be detected (solid–50% detectable, dashed–16 and 84% detectable).

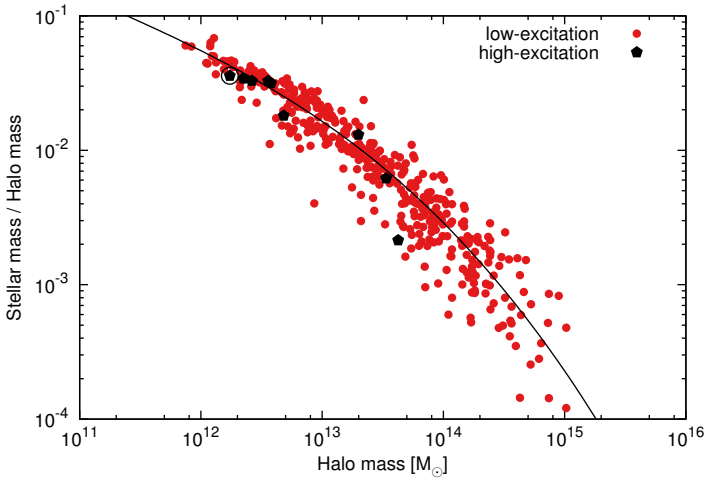

Figure 2.17: Stellar-to-halo mass ratio of HERG (black pentagons) and LERG (red circles) populations as a function of halo mass. There is no statistically significant difference between the stellar-halo mass ratio for the HERGs and the best-fit line (black) for the LERG population. The single HERG identified as a spiral (i.e. SDSS r-band $fracDeV$ parameter < 0.8, Padilla & Strauss 2008) is circled, and again is consistent with the LERG distribution.

2.6.2 Accretion rates and jet generation efficiencies

The different fuelling modes of HERGs and LERGs are expected to yield different accretion rates. I investigate the distribution of accretion rates for these populations by considering the kinetic power of the active nucleus relative to its Eddington luminosity, $L_{\rm Edd}$. The central black hole radiates energy directly from its accretion disk with the bolometric luminosity of the disk $L_{\rm rad}$ in addition to mechanical output of energy through the jets $L_{\rm mech} \equiv Q_{\rm tot}$. The power emitted by the AGN is thus related to the black hole mass accretion rate $\dot{M}_{\rm BH}$ as $(L_{\rm rad} + L_{\rm mech}) = \epsilon \dot{M}_{\rm BH} c^2$, where ϵ is the efficiency at which the accreted rest-mass energy is converted. The Eddington-scaled accretion rate is therefore

$$\dot{m} = \frac{\dot{M}_{\rm BH}}{\dot{M}_{\rm Edd}} = \frac{L_{\rm rad} + L_{\rm mech}}{L_{\rm Edd}}. \tag{2.17}$$

Note that this accretion rate is unaffected by realistic values of the jet power–luminosity scaling factor $f \lesssim 5$ since the mechanical jet power is much less than the disk bolometric luminosity. The bolometric radiative luminosity of each radio source is estimated using the observed luminosity of the [OIII] 5007 emission, and $L_{\rm rad} \approx 3500 L_{\rm OIII}$ (Heck-

man et al. 2004). The uncertainty on individual estimates of the bolometric radiative luminosity is ~ 0.4 dex. Although 43% of all radio sources in my sample have emission below the formal line flux uncertainties at the 3σ level, this fraction falls to less than 10% for objects classified as either HERGs or LERGs by Best & Heckman (2012). Following on from their work I adopt the 3σ upper limit to [O III] luminosity for such sources.

In order to compare my accretion rate estimates with the theoretical expectations I need to correct for the survey selection effects. There are two factors that must be considered: first, the drop-out of lower luminosity sources due to Rayleigh-Taylor mixing and late time loss mechanisms; and second, the greater likelihood of detecting long-lived sources from the total population compared to their younger counterparts. Specifically, the number density of sources in the population is probabilistically expected to be inversely proportional to its active age, $n_{\rm AGN}(t_{\rm on}) \propto 1/t_{\rm on}$. The number of radio AGN missing due to the drop-out of low-luminosity sources is insignificant in comparison, as I discuss here. The luminosity of simulated sources, with properties comparable to those fitted for my sample, typically peaks at approximately 10 Myrs (see Figure 2.3). That is, it should be possible to observe all sources with jet powers above $10^{34.5}\,{\rm W}f^{3/2}$ in this age range, as seen in Figure 2.16. By contrast, all high jet power sources ($> 10^{35.5}\,{\rm W}f^{3/2}$) younger than ~ 1 Gyr can be detected in the survey. The distribution of counts of these high jet power sources in active lifetime space can thus be scaled to the source count at lower jet powers to predict the number of missing objects. In this manner, I find that at least half of the $10^{34.5} \leqslant Q_{\rm tot} < 10^{35.0}\,{\rm W}f^{3/2}$ jet power sources expected from the counts of $10^{35.5} \leqslant Q_{\rm tot} < 10^{36.0}\,{\rm W}f^{3/2}$ sources are observed. By contrast, correcting for the likelihood of observing objects based on their lifetimes yields a factor of ten increase in number density of radio sources for each order of magnitude decrease in the active age. Moreover, the derived active ages cover a much larger range (4 orders of magnitude) than the jet power (2.5 dex). Hence, correcting observations for age bias is more important than the effects of different jet powers.

The distribution of accretion rates thus corrected is now plotted in the top panel of Figure 2.18 for the small population of HERGs (blue) and the much larger population of LERGs (red). The sub-population of LERGs has a mean accretion rate of $\dot{m} = 0.0006$ with a FWHM of 0.8 dex with typical (i.e. $\gtrsim 95\%$ of AGN) values in the range $10^{-4} < \dot{m} < 10^{-2.5}$. The high-excitation population clearly has higher accretion rates with a mean of $\dot{m} = 0.02$, with a difference significant at the 9σ level. In fact, all but one of these nine objects have accretion rates greater than $\dot{m} = 10^{-2.5}$ compared to less than 2% of LERGs. Note that sources with luminosities below the flux detection

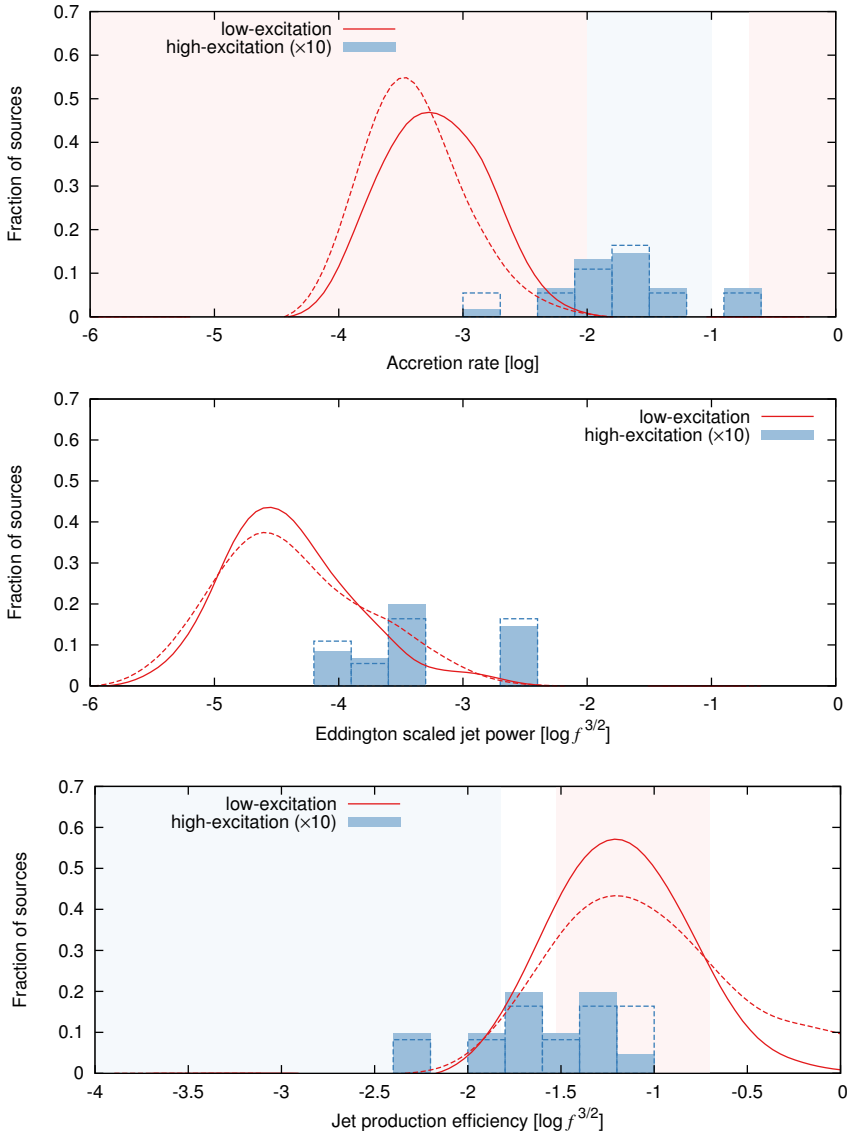

Figure 2.18: Top panel: distribution of Eddington-scaled accretion rates for LERGs (red) and HERGs (blue). The background shading shows the theoretically expected values for an ADAF (or slim disk; red) and a thin disk accretion flow (blue). The dashed lines show the uncorrected observed data, and solid lines are corrected for selection effects. Middle panel: mechanical jet power as a fraction of the Eddington luminosity. Bottom panel: efficiency of jet production. Fractions of the total AGN population are plotted, with HERGs scaled by a factor of ten to aid visibility.

limits of the FIRST and NVSS surveys for their entire lifetimes remain absent in these comparisons. These accretion rate distributions are consistent with the analysis of Best & Heckman (2012) for redshifts $z < 0.1$ (shown in their Figure 6), and largely with the theoretical division between the ADAF and thin disk accretion flow mechanisms at approximately $\dot{m} = 0.01$ (red and blue background shading in Figure 2.18; Meier 2001).

The middle panel of Figure 2.18 shows the mechanical jet power scaled by the Eddington rate, $L_{\rm mech}/L_{\rm Edd}$. The HERGs have Eddington luminosity scaled jet powers greater than those of the LERGs by approximately a factor of twelve (6σ significance). The relatively large fractional difference in accretion rates between the HERG and LERG populations compared to their Eddington-scaled jet powers indicates that the HERGs are much less efficient at producing jets. The jet production efficiency is plotted in the bottom panel of Figure 2.18. The LERG population has jet production efficiencies typically in the range $0.01 < \epsilon_{\rm jet,LERG}/f^{3/2} < 0.3$ with a mean efficiency of $\epsilon_{\rm jet,LERG}/f^{3/2} = 0.06$. By contrast, 82% of HERGs have efficiencies less than this value with a mean of $\epsilon_{\rm jet,HERG}/f^{3/2} = 0.02$. The high-excitation radio galaxies are therefore approximately a factor of three less efficient at producing jets than the LERGs, and this difference is significant at the 4σ level.

ADAFs

The accretion rates and jet production efficiencies of the HERGs and LERGs can be compared to the predictions of Meier (2001) for black holes powered by an advection dominated or thin disk accretion flow. The jet production efficiency of an ADAF powered rotating black hole is related to its jet power $Q_{\rm tot}$ (see Equation 7 of Meier 2001) and the Eddington-scaled accretion rate $\dot{m}$ by

$$\epsilon_{\rm ADAF}/f^{3/2} = \frac{Q_{\rm ADAF}/L_{\rm Edd}}{\dot{m}} = 0.05(0.55 + 1.5j + j^2). \tag{2.18}$$

The black hole spin $j \in [0, 1]$ is a difficult quantity to measure. Martínez-Sansigre & Rawlings (2011) have estimated that in the low-redshift universe the mean black hole spin is $\langle j \rangle \sim 0.35$, with approximately 24% of black holes having spins greater than $j = 0.5$. Variation in this parameter can generate jet production efficiencies in the range $0.03 < \epsilon_{\rm ADAF}/f^{3/2} < 0.2$, consistent with the peak in the drop-out corrected LERG distribution (solid red line; Figure 2.18, bottom) which I identify with ADAFs. The smaller "bump" in the observed distribution (dashed red line) at an efficiency of approximately $\epsilon_{\rm jet,LERG}/f^{3/2} \geqslant 0.5$ is not consistent with this theoretical model.

These sources have median radio luminosities a factor of 45 greater than the rest of the LERG population, whilst sizes, jet powers and active lifetimes are 25 times larger. The typical sizes of these sources' radio lobes are of the order of 100 kpc with a median active lifetime of 100 Myr $f^{-1/2}$. The transit time of plasma along their jets leads to a lag of order 10^6 to 10^7 years between changes in the central engine being reflected in the radio lobe emission. The observed radio luminosity from the lobe may therefore reflect an earlier time with higher accretion rates than the present. I speculate that these objects may be "dying" quasars.

Thin disks

The jet production efficiency of a thin disk accretion flow AGN (observationally identified with a HERG) is similarly derived using Equation 5 of Meier (2001). That is,

$$\epsilon_{\rm TD}/f^{3/2} = 0.005(1 + 1.1j + 0.29j^2)\left(\frac{M_{\rm BH}}{10^9\,{\rm M}_\odot}\right)^{-0.1}\dot{m}^{0.2}. \quad (2.19)$$

The highest efficiency that can be produced by this mechanism for the accretion rates of my sample is $\epsilon_{\rm TD}/f^{3/2} = 0.015$. Two of the nine HERGs in my sample have lower jet production efficiencies, however, seven have efficiencies exceeding this value rising up to $\epsilon_{\rm jet,HERG}/f^{3/2} = 0.09$. These observations may be explained by a "combined disk" accretion flow for $\dot{m} \lesssim 0.01$ (e.g. Narayan et al. 1996; Pu et al. 2012, noting that the high efficiency sources have such accretion rates). These accretion flows have a geometrically thin outer disk but a puffed up inner region like an ADAF. Black holes fuelled by such accretion flows could produce jets moderately efficiently due to the ADAF core but still exhibit the strong emission lines of HERGs.

2.7 Conclusions

I presented a new dynamical model for jet-driven radio source evolution. This model differs in three respects from previous models: (1) it includes both the supersonic and subsonic lobe expansion phases, (2) uses external pressure profiles based on semi-analytic galaxy formation models and X-ray observations, and (3) includes the Rayleigh-Taylor mixing of the lobe with the surrounding material. I applied this new model to a low-redshift volume-limited sample of radio AGN, and estimated the jet powers and active lifetimes of these objects. Radio sources in massive galaxies were found to remain active for longer, spend less time in the quiescent phase, and inject

more energy into their hosts than their less massive counterparts. The majority of AGN energy output in the low-redshift universe is provided by sources in massive hosts with $\sim 10^{25}\,\mathrm{W\,Hz^{-1}}$ luminosities. The relationship between the AGN jet powers and the stellar masses of their host galaxies, $Q_{\mathrm{tot}} \propto {M_\star}^{0.1\pm0.1}$, is in agreement with the theoretically expected (lack of) dependence for maintenance-mode AGN feedback. The host haloes of these AGN are likely to be in or close to long-term heating-cooling balance, when considering both thermal conduction and the suppression of gas cooling by the AGN. This dynamical model can also explain the observed FR-I/II radio morphology dichotomy.

High-excitation radio galaxies were found to have active lifetimes on average a factor of twelve lower and jet powers a factor of four higher than the low-excitation radio galaxies. This is consistent with the sporadic nature of their merger-driven cold gas accretion. The bimodality in LERG/HERG accretion rates is consistent with the divide between the ADAF and thin disk accretion flow mechanisms at approximately $\dot{m} = 0.01$. The high-excitation radio galaxies in a volume-limited sample were found to be a factor of three times less efficient at producing jets than the LERGs. The derived jet production efficiencies are broadly consistent with the ranges allowed by radiatively efficient and inefficient flow jet production models. The jet production efficiency of the lowest accretion rate HERGs exceeds the maximum predicted for a thin disk accretion flow, which I suggest provides support for the "combined disk" accretion flow model.

The improved characterisation of the interaction between AGN and their host galaxies resulting from this work should provide valuable input into galaxy formation and evolution models. This model will also be a useful tool in the interpretation of high redshift survey data, especially for *Square Kilometre Array* (SKA) pathfinder surveys. An important development will be extending the model to estimate intrinsics parameters from observed spectral indices (see Chapter 3), since the resolution of the radio lobes may not be possible except for the largest sources (e.g. 80 kpc at $z \sim 1$ for ASKAP EMU). At lower redshifts, future sensitive X-ray surveys of the gas density and temperature profiles of the AGN environments (e.g. ATHENA[6]) will be complementary to my work.

[6] `http://www.the-athena-x-ray-observatory.eu/`

Chapter 3

Spectral Constraints on AGN Energetics and Composition

Kinetic jet power estimates based exclusively on observed monochromatic radio luminosities are highly uncertain due to confounding variables and a lack of knowledge about some aspects of the physics of active galactic nuclei (AGNs). The jet powers and active lifetimes estimated in Chapter 2 encountered a lack of knowledge about the lobe magnetic field strength in particular, as encapsulated in the uncertainty factor f. In this chapter, I propose a new methodology to calculate the jet powers of the largest, most powerful radio sources based on combinations of their size, lobe luminosity and shape of their radio spectrum; this approach avoids the uncertainties encountered by previous relationships. Parametrisation of radio SED curvature and the development of the new jet power estimation method is described in Section 3.1. This method is applied to a sample of FR-II sources (described in Section 3.2) with the typical environments assumed for these sources detailed in Section 3.3. The lobed FR-I/II dynamical (Chapter 2) and synchrotron luminosity (Chapter 4) models are then calibrated based on observations in Section 3.4. Finally in Section 3.5, I describe the various fitting algorithms used to determine the jet power, source age and lobe magnetic field strength based on differing observational constraints.

3.1 Spectral evolution models

The jet power and age of radio AGNs in Chapter 2 were calculated using a maximum likelihood method based on the observed source size and 1.4 GHz luminosity. In that work I implicitly assumed the scaling between the jet power and luminosity

through the choice of the low-energy cut-off to the synchrotron-emitting electrons in the lobes, and by equating the energy density in the particles and the magnetic field (i.e. equipartition). However, in this chapter I attempt to derive jet powers using solely the physics incorporated in the dynamical and synchrotron luminosity models, in conjunction with known properties of observed radio AGNs. This means that the jet power is no longer able to be constrained using solely the source size and monochromatic luminosity, and an additional observable capable of constraining the intrinsic AGN properties must therefore be found. In this chapter, I use the shape of the observed radio spectrum as the additional constraint. The full treatment of the synchrotron emission derived in Chapter 4 is compared with simpler spectral ageing models, which enable the radio source spectrum to be readily parametrised in terms of a single variable.

The spectral ageing technique is not universally accepted as a reliable means of estimating the source dynamical age. The spectral age estimates for many powerful radio sources have been observed to be an order of magnitude lower than their dynamical ages (e.g. Rudnick et al. 1994; Blundell & Rawlings 2000; Harwood et al. 2015). This discrepancy has been explained by a departure from the assumed equipartition field strength or the presence of non-radiating particles arising from the entrainment of thermal material. Further, in Chapter 4 I show that the spectral ageing models applied to resolved radio sources measure the age of the youngest electrons in a given region of the lobe; in the well-mixed lobes of FR-IIs the age of these youngest electrons is always at least a factor of a few less than the source dynamical age. In Section 3.5 I discuss the theoretical advantage of using the synchrotron spectrum to yield reliable jet power estimates.

3.1.1 Spectral ageing models

The spectral age of radio AGNs can be derived from the steepening in the observed synchrotron emission spectrum due to the synchrotron and inverse-Compton loss processes (e.g. Jaffe & Perola 1973; Myers & Spangler 1985; Alexander & Leahy 1987; Murgia et al. 1999; Jamrozy et al. 2008). The observed spectra are typically fitted using either the Jaffe-Perola (JP; Jaffe & Perola 1973) or Kardashev-Pacholczyk (KP; Kardashev 1962; Pacholczyk 1970) models to find the injection spectral index $\alpha_{\rm inj}$ and the break frequency $\nu_{\rm b}$, with the latter used to derive the spectral age. These models assume a single particle injection event produces the initial power law distribution of electron energies $N(E) = N_0 E^{-s}$, where N_0 is a constant and $s = 2\alpha_{\rm inj} + 1$. The JP model assumes the pitch angle of electrons is isotropic only on short time-scales

relative to the radiative lifetime, and that the electron density and magnetic field are homogeneous along the source depth. The KP model instead assumes all electrons maintain the same pitch angle during their radiative lifetimes; however this model is unrealistic as any irregularities in the magnetic field will scatter electrons efficiently.

The other 'standard' model assumes the continuous injection of fresh particles over the lifetime of the source (CI model; Kardashev 1962; Pacholczyk 1970), yielding a different distribution of electron energies. The high-frequency steepening of the CI and JP models can be thought of as limiting cases (Carilli et al. 1991). The exponential cut-off of the JP model is the fastest the spectrum can steepen due to synchrotron losses whilst the CI model assumes minimum losses for a flatter spectrum.

These standard spectral ageing models assume a uniform magnetic field strength B_0. Tribble (1991) proposed an analytical method to describe the synchrotron emission in a locally non-homogeneous magnetic field. This model assumes the field is a Gaussian random field as would be found if the magnetic field were the result of homogeneous, isotropic turbulence. The magnetic field strength distribution in this paradigm is that of a Maxwell-Boltzmann distribution (Hardcastle 2013). The standard models can be modified to assume this more realistic magnetic field distribution, and are referred to as the 'Tribble' forms of the spectral ageing models (i.e. TJP, TKP and TCI; e.g. Harwood et al. 2013).

The radio source spectrum can be well fitted by spectral ageing models, either for a lobe section with constant age electrons (e.g. JP and KP models) or for the entire radio lobe (e.g. CI model). These models include losses due to synchrotron radiation and the inverse-Compton scattering of cosmic microwave background photons, but compared to full synchrotron emission models (such as discussed in Chapter 4) they ignore losses due to the adiabatic expansion of the lobe. The adiabatic losses can be neglected when fitting the spectral shape since they only translate the spectrum in the $\log \nu$–$\log S$ plane.

3.1.2 Synchrotron emissivity

Following the method of Hardcastle (2013) and Harwood et al. (2013) I derive expressions for the standard and Tribble form of the Jaffe-Perola, Kardashev-Pacholczyk and continuous injection models. The single-electron emissivity as a function of frequency is given by (Longair 2010)

$$j(\nu) = \frac{\sqrt{3}Be^3 \sin\xi}{8\pi^2 \epsilon_0 c m_\mathrm{e}} F(x) \tag{3.1}$$

where B is the local magnetic field strength, ξ is the electron pitch angle, e is the electron charge, m_e is the electron mass, c is the speed of light, and ϵ_0 is the permittivity of free space. The single-electron synchrotron radiation spectrum $F(x)$ is defined as (Rybicki & Lightman 1979)

$$F(x) = x \int_x^\infty K_{5/3}(y)\, dy, \tag{3.2}$$

which is vanishingly small for $x \gtrsim 20$ and asymptotes to $F(x) = 2.15x^{1/3}$ for small x (Pacholczyk 1970). Here $K_{5/3}$ is the modified Bessel function of order 5/3, and x is a dimensionless function of the frequency, field strength and energy:

$$x = \frac{\nu}{\nu_\mathrm{b}} = \frac{4\pi {m_\mathrm{e}}^3 c^4 \nu}{3eE^2 B \sin\xi} \tag{3.3}$$

where E is the electron energy, and ν_b is the spectral break frequency beyond which (higher frequencies) the spectrum steepens due to the loss mechanisms.

The emissivity of the entire radio source electron population can then be found by integrating the single-electron emissivity (Equation 3.1) over the magnetic field, electron energies and pitch angles (cf. Equation 4 of Hardcastle 2013),

$$J(\nu) = \int_0^\infty \int_0^\pi \int_0^\infty \frac{\sqrt{3} B e^3 \sin\xi}{8\pi^2 \epsilon_0 c m_\mathrm{e}} F(x) N(E) p_\xi p_\mathrm{B}\, dE\, d\xi\, dB \tag{3.4}$$

where p_ξ and p_B are the probability distributions of the pitch angle ξ and the magnetic field strength B respectively, and $N(E)$ is the electron energy distribution. The standard assumption for the pitch angle distribution of the electron population is that of isotropy, i.e. $p_\xi = \frac{1}{2}\sin\xi$. The magnetic field is generally assumed to be constant or a Maxwell-Boltzmann distribution as proposed by Tribble (1991). That is,

$$p_\mathrm{B} = \sqrt{\frac{2}{\pi}} \frac{B^2 \exp\left(-B^2/2{B_0}^2\right)}{{B_0}^3} \tag{3.5}$$

where B_0 is the mean magnetic field strength of the radio lobe.

Synchrotron age of electron population

The synchrotron age of the radio source electron population is determined from the lobe magnetic field strength B and the spectral break frequency ν_b through the relation

$$\tau = \frac{\upsilon B^{1/2}}{B^2 + {B_{\rm ic}}^2} \left[\nu_{\rm b}(1+z)\right]^{-1/2}. \tag{3.6}$$

where z is the source redshift and $B_{\rm ic} = 0.318(1+z)^2\,\mathrm{nT}$ is the magnitude of the magnetic field equivalent to the microwave background. Here, the constant of proportionality υ for the JP model is given by

$$\upsilon = \left(\frac{243\pi {m_{\rm e}}^5 c^2}{4{\mu_0}^2 e^7}\right)^{1/2} \tag{3.7}$$

in which μ_0 is the magnetic permeability of free space. This constant is reduced by a factor of 2.25 for the KP model (e.g. Nagai et al. 2006).

Jaffe-Perola and Kardashev-Pacholczyk models

The Jaffe-Perola and Kardashev-Pacholczyk models generally assume electrons are impulsively injected at the hotspot. The injected packet of constant age electrons then propagates away from the hotspot; this leads to an age gradient across the lobe through multiple such injection events. An initial power law distribution of electron energies $N(E) = N_0 E^{-s}\delta(\tau)$, in the presence of synchrotron and inverse-Compton losses, changes to (Pacholczyk 1970; Longair 2010)

$$N(E) = \begin{cases} N_0 E^{-s}(1-\kappa E\tau)^{s-2} & E < 1/\kappa\tau \\ 0 & E \geqslant 1/\kappa\tau \end{cases} \tag{3.8}$$

where κ is a constant such that $dE/d\tau = -\kappa E^2$ which takes account of both radiative and inverse-Compton losses. In this constant, I assume either the occurrence of synchrotron electron pitch angle scattering (JP model) or its absence (KP model). That is,

$$\kappa = \frac{2\sigma_{\rm T}}{3m_{\rm e}^2\mu_0 c^3} \begin{cases} B^2 + {B_{\rm ic}}^2, & \text{for JP model} \\ B^2\sin^2\xi + {B_{\rm ic}}^2, & \text{for KP model} \end{cases} \tag{3.9}$$

in which $\sigma_{\rm T}$ is the Thomson electron scattering cross-section. The radio spectra produced by these two spectral ageing models are shown in Figure 3.1 assuming either a constant or Maxwell-Boltzmann magnetic field distribution.

Continuous injection models

Determination of the spectral age from the integrated lobe luminosity, such as in unresolved sources, necessitates the consideration of a continuous injection of electrons rather than just a single impulsive burst. By fitting the integrated spectra, it can be seen that continuous injection models are unable to describe inhomogeneities in the underlying physics; however, these models should provide a useful tool for understanding the integrated emission from the approximately homogeneous lobes of powerful FR-IIs. Thus assuming a continuous injection of electrons, the initial power-law distribution of energies $N(E) = N_0 E^{-s}$ leads to the following electron energy distribution (Longair 2010):

$$N(E,\tau) = \frac{N_0 E^{-(s+1)}}{\kappa(s-1)} \begin{cases} 1-(1-\kappa E\tau)^{s-1} & E < 1/\kappa\tau \\ 1 & E \geqslant 1/\kappa\tau \end{cases} \tag{3.10}$$

Models describing a continuous injection of electrons can either assume that pitch angle scattering of the synchrotron electrons occurs (as for the JP model) or that it does not (as for the KP model). This assumption has negligible effect on the shape of the CI model spectrum for typical radio lobe properties; I therefore present a single continuous injection model allowing pitch angle scattering. This model is applied to the spectra of a 3C sub-sample comprising 71 FR-II radio sources using 0.01-10 GHz observations from Laing & Peacock (1980, described in Section 3.2); the CI model is found to fit the spectra of 86% of these objects at the 2σ confidence level increasing to 93% if a single outlying low-frequency point is excluded from the spectra of selected sources. The fit statistics for each object are included in Tables A2.1 and A2.2 in the appendix. The lower frequencies in the remaining sources are generally noisy or have reduced flux densities due to free-free or synchrotron self-absorption. These are well fitted upon supplementing the Laing & Peacock (1980) observations with additional literature data and excluding the low-frequency spectral curvature from the fit.

Harwood (2017) similarly investigated the ability of the CI model to fit the spectra of a range of radio sources and compared the resulting spectral ages to those derived using the JP model in their BRATS software package. The CI model fits the high-frequency end of the spectra well for the four (active) FR-IIs in their sample, but cannot fit the lower frequency observations of two of these objects, consistent with the results of our fitting for the same data. Harwood (2017) also found the spectral ages measured using the CI model differ by up to a factor of six compared to those calculated for resolved sources using the JP model. This inconsistency is not an indication of problems with the CI model age estimates; rather later in Chapter 4 I find that the JP model yields

spectral ages a factor of a few different from the dynamical age in well-mixed lobes of FR-IIs. This discrepancy occurs due to a violation of the JP model assumption that the spectrum results from a single injection of electrons, despite the oldest regions of the lobe comprising electron populations differing by a factor of up to a few in age.

3.1.3 Independence of magnetic field

The structure and magnitude of the magnetic field can potentially introduce a large source of error into the spectral ageing technique. In this section, I quantify the effect the structure of the lobe magnetic field has on the shape of the JP, KP and CI model spectra. These models are plotted in Figure 3.1 for two magnetic field distributions: (1) the constant field assumption of the standard form of the models, and (2) a Maxwell-Boltzmann distribution (Tribble form). Local inhomogeneities in the magnetic field lead to a spectrum arising from populations of electrons with spectra described by the standard form of the ageing models, but whose break frequencies are shifted due to the change in field strength. The spectra for the Tribble ageing models thus have more high-energy electrons and as a result have their spectral breaks shifted to higher frequencies. However, the continuous injection model spectra are largely unaffected by inhomogeneities in the magnetic field because a significant population of high-energy electrons already contribute to the spectra. That is, local inhomogeneities in the magnetic field have negligible effect on the shape of the integrated radio spectrum, in stark contrast to the large difference seen in the JP spectra investigated by Hardcastle (2013).

The difference in the standard and Tribble-CI spectra is quantified by fitting the standard form of the model to a Tribble-CI spectrum over a typical frequency range of 0.1 to 100 GHz; the break frequency fitted in this scenario is found to be a factor of 1.15 greater than for the original Tribble spectrum. This systematic error leads to an underestimation of magnetic field strengths and thus equipartition factors by a factor of 1.05. Local inhomogeneities in the magnetic field are therefore not expected to appreciably alter the CI spectra or any results derived from the fitted spectral index and break frequency.

The standard form of the continuous injection model, and the JP and KP models, assume a constant lobe magnetic field strength. The integral in Equation 3.4 can therefore be reduced from a triple to a double integral, with the field strength as a scaling factor. However, the single-electron synchrotron radiation spectrum $F(x)$ is dependent on the strength of the magnetic field. I seek to remove this dependence by parametrising the integral in terms of x, leaving only frequency independent terms

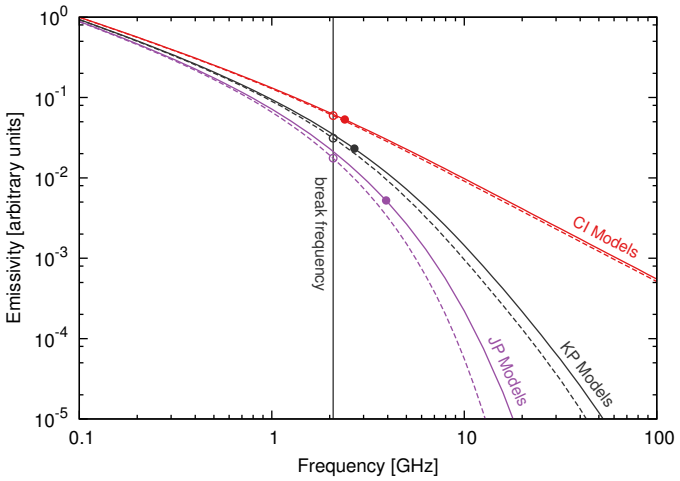

Figure 3.1: Spectral shape expected for the Jaffe-Perola (JP–purple), Kardashev-Pacholczyk (KP–grey) and Continuous Injection (CI–red) models, assuming either a constant (dashed) or Maxwell-Boltzmann distribution (Tribble model–solid) for the magnetic field. These models assume a field strength of $B = 10\,\mathrm{nT}$, an injection index of $s = 2.5$, and correspond to a spectral age of $\tau = 30\,\mathrm{Myrs}$. The vertical line marks the $\sim 2\,\mathrm{GHz}$ break frequency of the six spectral models (KP break scaled to match JP and CI breaks on plot); the circles show the break frequency derived by fitting the standard constant magnetic field forms of the models to the spectra over the 0.1 to 100 GHz frequency range.

involving the field strength. The integrated emissivity of the continuous injection model can thus be written in terms of integrals over only x and the pitch angle. That is,

$$J(\nu) = J_0 \nu^{-s/2} \int_0^{\pi/2} \sin^{(s+4)/2} \xi \int_0^{\infty} F(x)\mathcal{N}(x) dx d\xi \tag{3.11}$$

where J_0 is a frequency-independent constant, and $\mathcal{N}(x)$ is the frequency-dependent component of the electron energy distribution. For the continuous injection model this component of the electron energy distribution is then given by

$$\mathcal{N}(x) = x^{(s-2)/2} \begin{cases} 1 - x^{(1-s)/2}(x^{1/2} - \iota^{1/2})^{s-1} & x > \iota \\ 1 & x \leqslant \iota \end{cases} \tag{3.12}$$

where $\iota(\nu, \xi) = \nu/(\nu_\mathrm{b} \sin \xi)$ is the value of x corresponding to an energy of $E = 1/\kappa\tau$ (cf. Equation 3.10). Similar expressions can be obtained for the standard JP and KP models (Nagai et al. 2006).

The magnetic field strength of radio sources therefore does not need to be quantified in order to observationally constrain the injection index s of the electron ensemble or the spectral break frequency ν_b. However, the synchrotron age of the electron population does depend on the field strength through Equation 3.6.

Different techniques for estimating the lobe magnetic field strength exist in the literature. The most basic approach is to determine the field strength from the level of synchrotron emission under the assumption of equal energy density in the particles and the field (Burbidge 1956). However, in low-powered FR-Is which are expected to be in pressure equilibrium with their surroundings, this approach predicts underpressured lobes (Croston et al. 2008a) suggesting either the field may not be in equipartition or that additional pressure is provided by entrained and heated thermal plasma. A more direct approach uses the emission from relativistic electrons inverse-Compton scattered to X-ray energies to calculate the energy density in the synchrotron electrons. The magnetic field strength is derived by comparing the observed X-ray emissivity to model predictions derived from the level of synchrotron emission. Hardcastle et al. (2002), Croston et al. (2004, 2005) and Ineson et al. (2017) all find sub-equipartition magnetic field strengths in the lobes of FR-IIs. Spectral ages calculated assuming fields in equipartition will thus generally be greatly underestimated. In this work I instead use the lobed FR-I/II dynamical model (Chapter 2) to fit the magnetic field strength based on the source size and break frequency, additionally yielding estimates for the age and jet power.

3.1.4 Dynamical versus synchrotron ages

The ability of the CI model to provide a good empirical fit to observed spectra (and hence quantify their curvature) is tested using simulated spectra for radio sources with known field strengths and particle content. This enables the spectral age to be fitted and compared to modelled sources with a known dynamical age. The spectra of these simulated radio sources are generated using the lobed FR-I/II dynamical model described in Chapter 2 and synchrotron emissivity model developed in Chapter 4, which includes all radiative loss mechanisms and the temporal evolution of the lobe magnetic field strength. This synchrotron emissivity model provides a more complete description of the radio spectrum than standard spectral ageing models, however the CI spectrum is preferable for parameter fitting, when a good approximation, for two reasons: (1) the computation time increases with the number of observed frequencies, and (2) it does not provide a single measure of the curvature (e.g. $\nu_{\rm b}$) increasing the complexity of any parameter estimation method.

Boot-strapped integrated luminosity model

The formalism for the integrated radio lobe luminosity model (Chapter 4), which is applied to the lobed FR-I/II dynamical model, is based on the work of Kaiser et al. (1997). This model calculates the synchrotron emissivity based on the magnetic field strength at the time of electron injection rather than assuming a population average as for the approximating continuous injection model discussed in Section 3.1.3. Spatial variations in synchrotron emissivity due to an inhomogeneous magnetic field are also considered in the lobe luminosity model of Chapter 4, though are not simulated at this point due to a lack of knowledge about the field distribution. The general form for the lobe luminosity in the Kaiser & Alexander (1997, see also Chapter 4) synchrotron emission model is given by

$$L(\nu,s,t) = K(s)\nu^{(1-s)/2}\frac{q^{(s+1)/4}}{(q+1)^{(s+5)/4}(w+1)}p(t)^{(s+5)/4}V(t)\mathcal{Y}(\nu,s,t) \qquad (3.13)$$

where $q = u_{\rm B}/u_{\rm e}$ is the ratio of the energy density in the magnetic field to that in the synchrotron-emitting leptons, $w = u_{\rm t}/u_{\rm e}$ is the ratio of the energy density in the thermal particles and the electrons, $p(t)$ is the lobe pressure, $V(t)$ its volume, $\mathcal{Y}(\nu,s,t)$ the loss function, and $K(s)$ a radio source constant. This source-specific constant is a function solely of physical constants, the injection spectral index, the adiabatic index of the lobe $\Gamma_{\rm c}$, and the minimum Lorentz factor $\gamma_{\rm min}$ of the injected synchrotron

electron population. In this work, I assume lobes comprising a relativistic pair-plasma potentially supplemented by a non-relativistic thermal fluid (i.e. $4/3 \leqslant \Gamma_{\rm c} \leqslant 5/3$), though I find no more than a 0.1 dex variation in the fitted parameters between the extremes of entirely relativistic or non-relativistic fluids. Finally, the low-energy cut-off to the electron population is observationally constrained (see Section 3.4).

The loss function is the fractional reduction in luminosity relative to the lossless case due to the lobe adiabatic expansion, synchrotron radiation, and the inverse-Compton scattering of cosmic microwave background photons. In Chapter 4, I model the loss function both as a function of position in the lobe (c.f. JP and KP models) and for spatially unresolved lobes (c.f. CI models). Multi-frequency radio observations for unresolved lobes can therefore be simulated for radio sources evolved to any age using the lobed FR-I/II dynamical model.

Constant field strength in spectral ageing models

The continuous injection model implicitly assumes a constant magnetic field strength throughout the radio source lifetime. This is clearly false, noting that the field strength evolves with source age as $B \propto t^{(-4-\beta)/(10-2\beta)}$ in the strong-shock supersonic expansion limit, where the gas density of the host environment locally falls-off as $\rho \propto r^{-\beta}$ (Kaiser & Alexander 1997). The continuous injection model may yield reliable spectral age estimates though if the lobe emissivity results primarily from synchrotron electrons injected at times $t_{\rm i}$ with comparable field strengths to that of the observed source age t (i.e. $t_{\rm i}/t \sim 1$).

The age of the synchrotron electrons contributing most to the lobe emissivity is calculated using the lossy luminosity model described in Chapter 4. This model considers the evolution of the lobe magnetic field strength throughout the radio source lifetime, correctly estimating the synchrotron losses unlike the approximate form of the simpler continuous injection model. The emissivity at three frequencies across the radio spectra, but near the typically ~ 1 GHz spectral turnover, is plotted as a function of the synchrotron electron injection age ($t_{\rm i}/t$) in Figure 3.2 for a typical source viewed at ages of 1, 100 and 1000 Myrs. The emissivity contribution from the injected electrons is shown for a radio source with jet power $Q = 10^{40}$ W, inhabiting a $10^{11.7}$ $\rm M_{\odot}$ stellar mass galaxy at redshift $z = 0$, and with lobe magnetic field to particle energy density ratio of $q = 0.01$. The assumed value of $q = 0.01$ is chosen in this explanation to be consistent with the findings in Section 3.5. Lobes with stronger magnetic fields have greater loss rates due to synchrotron emission; the radio emissivity in such sources would come from more freshly injected electrons than for the $q = 0.01$ example. The

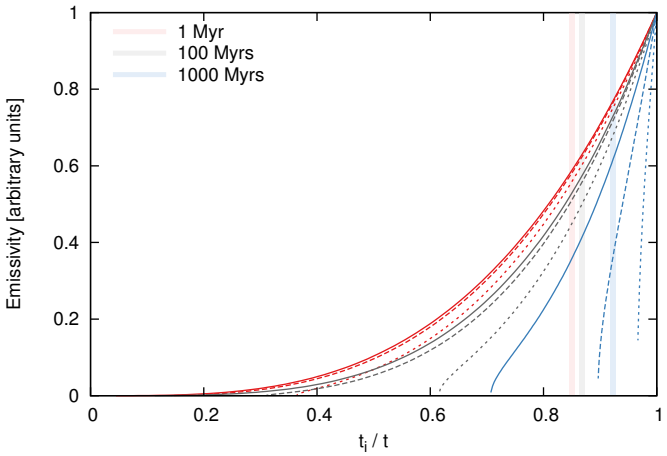

Figure 3.2: Radio lobe emissivity contribution from synchrotron electrons of injection age $t_{\rm i}$ at the observed source age t, plotted as a function of the ratio $t_{\rm i}/t$. The emissivity contribution from the injected electrons of a typical source is shown for ages of 1, 100 and 1000 Myrs in red, grey and blue respectively, whilst the solid, dashed and dotted lines plot the radio emissivity at 151 MHz, 1.5 GHz and 15 GHz. The loss rates are modelled here for a radio source with $Q = 10^{40}$ W jets, inhabiting a $10^{11.7}$ $\mathrm{M}_{\odot}$ stellar mass galaxy at redshift $z = 0$, and with a lobe magnetic field to particle energy density ratio of $q = 0.01$. The synchrotron emission at the time of observation results primarily from freshly injected electrons. The vertical lines show the median electron injection age contributing to the observed 151 MHz emission for each source age.

jet power and host environment have negligible effect on the loss mechanisms, however the inverse-Compton upscattering of CMB photons by the injected electrons is much more effective at high-redshift. These chosen parameters therefore provide a worst case estimate; the synchrotron emissivity for most sources is due to more freshly injected electrons than predicted here.

I find that the emissivity from 1 Myr old radio sources on average results from 0.15 Myr old electrons, i.e. injected at $t_{\rm i}/t \sim 0.85$. The host environment of this representative radio source falls-off as $\rho \propto r^{-0.83}$ (i.e. $\beta = 0.83$) at this source age, yielding a variation in the magnetic field strength of 10%. Similarly, the emissivity from the 100 and 1000 Myr old radio sources is due to electrons injected at a median of 0.87 and 0.92 times the source age respectively. The magnetic field strengths at the time of these median injection ages are higher than at the time of observation by 10% and 8% respectively. These variations in the magnetic field strengths should have minimal effect on the constant field strength assumption of the continuous injection model. Further, the resulting uncertainty in the spectral age calculated using Equation 3.6 is at most 12 to 15% depending on the source age. The parametrised form of the continuous injection model might therefore be expected to fit the curvature of radio source spectra using the single break frequency parameter. The validity of this method is further investigated in the following section by fitting the continuous injection model to simulated spectra with known dynamical age and field strength evolutionary history, and comparing the resulting spectral age estimate to the true age.

Simulated radio spectra

The radio spectra of a wide range of radio sources are simulated using the combined lobed FR-I/II dynamical model and synchrotron luminosity model. Jet powers of between 10^{34} and 10^{40} W are simulated for radio sources inhabiting 3×10^{10} to 10^{12} $M_{\odot}$ stellar mass hosts, whose lobes have initial axis ratios between $A = 2$ and 8, and with magnetic field strengths ranging from equipartition to a factor of 100 lower. The evolutionary tracks of these sources are analysed from 1 to 1000 Myrs, with simulated spectra produced at regular time-steps. The simulated spectra of a typical source are shown in Figure 3.3 for five time-steps, with the best continuous injection model fits for each age overplotted. The standard spectral ageing models (i.e. non-Tribble forms of JP, KP and CI models) have two free parameters, the injection spectral index $\alpha_{\rm inj}$ and the break frequency $\nu_{\rm b}$, in addition to a constant term. The relevant spectral model is fitted to these multi-frequency radio lobe spectrum simulations using a weighted log-space least squares regression to determine the best estimates and uncertainties

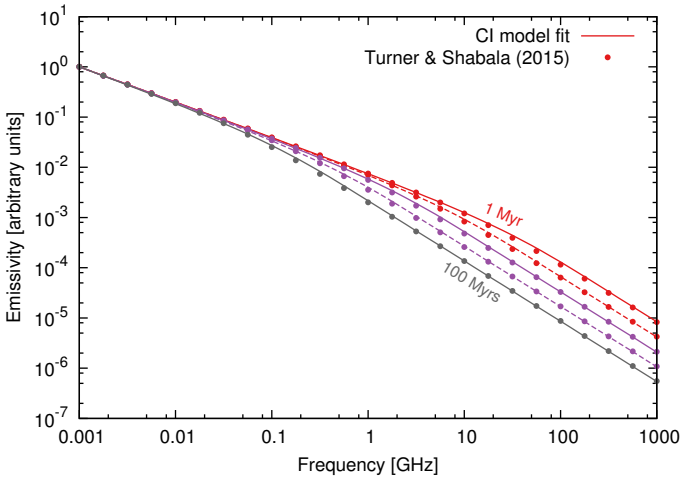

Figure 3.3: Fits of the standard continuous injection (CI) model to the simulated radio source spectra from the lobed FR-I/II dynamical model. These spectra are for a radio source with jet power of 10^{34} W inhabiting a $3 \times 10^{10}\,M_{\odot}$ host galaxy, equipartition lobe field strength, and electron energy injection index of $s = 2.4$. The points are scaled luminosities calculated using the dynamical model at 0.25 dex steps in frequency, coloured by the dynamical age of the source. The dynamical age increases top-to-bottom from 1 Myr (red – top) through to 100 Myrs (grey – bottom) in log-space steps of 0.5 dex. The solid and dashed lines both show the best fits obtained using the CI model for each dynamical age.

for these parameters. The parametrised form of the continuous injection model fits the simulated spectra extremely well for all time-steps, suggesting any comparison between the fitted spectral and simulated dynamical ages will be well-founded.

The best-fitting models to the simulated spectra yield estimates of the spectral break frequency and injection spectral index. The former is combined with the magnetic field strength to determine the age of the synchrotron electron population via Equation 3.6. For these simulated radio sources the magnetic field strength is found directly from the lobe pressure and equipartition factor computed as part of the dynamical model. The evolutionary tracks of all the simulated radio sources are plotted in Figure 3.4 in synchrotron–dynamical age space. The fitted synchrotron electron age is consistent with the dynamical age of the simulated radio source for all ages within the 1σ uncertainties. I am therefore justified in using the continuous injection model to fit the curvature of observed spectra based on the single parameter break frequency statistic, and further to equate the spectral age obtained using Equation 3.6 with the dynamical age.

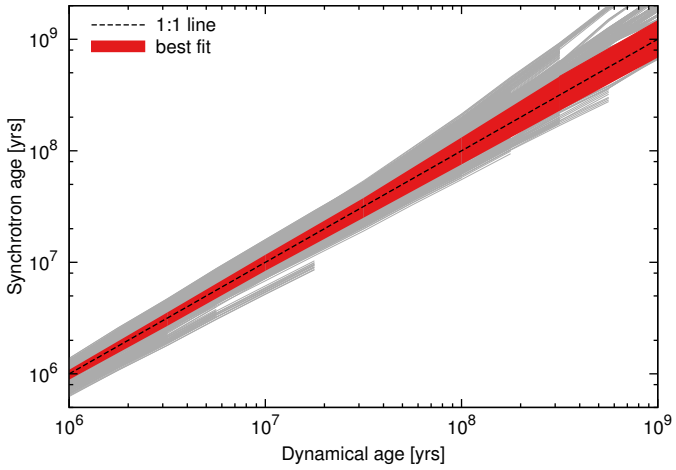

Figure 3.4: Synchrotron age as a function of the dynamical age for a broad range of simulated radio galaxies. The radio source jet power, magnetic field strength, synchrotron energy injection index, and host galaxy properties are varied in these simulations (grey lines). The thick red line plots the 1σ uncertainties in the synchrotron-dynamical age relationship.

The strong relationship found between the synchrotron and dynamical ages is contingent on accurate measurements of the lobe magnetic field strength. Note that mismeasurement of the magnetic field strength in existing spectral ageing methods leads to inaccuracies in the age as $\tau \propto B^{-3/2}$. Current measurement techniques require the lobe-related X-ray emission be measured; the surrounding X-ray emitting hot gas must be excluded (e.g. Hardcastle et al. 2002; Croston et al. 2004, 2005). However, compact sources and much of the high-redshift population are unresolved making this approach impractical at present. In this work, the magnetic field strength will be fitted using a Bayesian approach, constrained using other observables including the source size and radio spectral energy distribution of the source.

3.2 Powerful radio AGN sample

In this section, I apply the combined dynamical and synchrotron luminosity model to a well-studied sample of powerful radio galaxies. Mullin et al. (2008) presented a catalogue[1] of 98 $z < 1$ *Third Cambridge Catalogue of Radio Sources* (3C). Each object includes the measured 178 MHz radio lobe luminosity, R-band optical magnitude (for approximately three quarters of the sample), and the largest linear source

[1] http://zl1.extragalactic.info/

size, width and axis ratio of each lobe. The Mullin et al. (2008) dataset is compiled from the complete flux-limited sample of Laing et al. (1983) which includes all 3C sources with total 178 MHz flux densities $S_{178} > 10.9$ Jy. These 3C galaxies are further cross-matched with K-band near-infrared magnitudes and multi-frequency radio observations to enable estimation of the host stellar mass and fitting of the spectral curvature respectively. These spectral fits will provide an alternative method of constraining the source age, in contrast to the sole use of the size parameter in Chapter 2.

3.2.1 Spectral break frequencies

The integrated radio spectra of 88 3C sources in the full Mullin et al. (2008) sample are fitted using the parametrised form of the continuous injection model, with multi-frequency data taken from Laing & Peacock (1980). The limited frequency range of their observations makes it inevitable that only sources with a break of between 0.1-10 GHz will be fitted; it is vital that spectra with no clear curvature in this range are excluded. I use additional archival observations to confirm the fitted curvature is real and not due to random noise in a few points. The break frequency is confidently fitted for 37 sources and a lower limit of ~ 10 GHz is claimed for a further 34 objects; the injection index is fitted for all 71 of these objects. The spectral fit obtained for a typical radio source with a break frequency between 0.1 and 10 GHz is plotted in Figure 3.5. This limited break frequency range will bias any sample to the oldest radio sources at low-redshift, and younger objects at higher redshifts; however, a complete sample can be constructed by applying informed prior probability distributions (from the biased sample) to remaining objects with break frequency lower limits.

The spectra of some of the sources with multi-frequency observations are not fitted for one of the following reasons: (1) a sharp low-frequency turnover is present, due to either synchrotron self-absorption (Kellermann 1966) or free-free absorption (Bicknell et al. 1997; 3C268.3, 3C295), (2) the radio source has irregular lobe morphology (3C215, 3C351, 3C433), (3) the lobe has no or incomplete axis ratio measurements (3C254, 3C299, 3C321), or (4) the high-frequency emission is dominated by the core or Doppler-boosted components associated with the jets (3C109, 3C207, 3C216, 3C220.1, 3C263, 3C275.1, 3C334, 3C382, 3C390.3). These latter nine sources are removed based on the high-resolution 1.5-8.5 GHz observations compiled by Mullin et al. (2008); the cores of these sources comprise more than 10% of their total emission compared to a median core-to-lobe emissivity ratio of less than 1% for the rest of the sample. Note that it may be possible to correct the integrated emission by removing the core

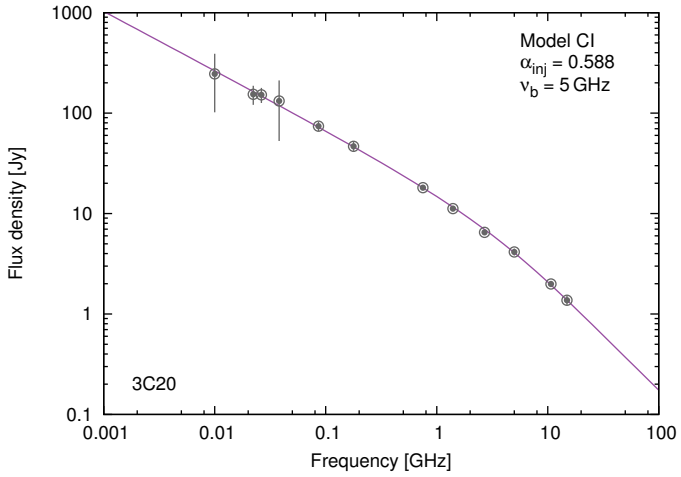

Figure 3.5: Spectral fit to the lobe synchrotron emission of the typical radio source 3C20. The observed flux densities taken from Laing & Peacock (1980) are plotted with grey circles and 2σ errorbars. The fit to these multi-frequency observations assumes the parametrised form of the continuous injection model (Section 3.1.3), with the fitted injection spectral index $\alpha_{\rm inj}$ and break frequency $\nu_{\rm b}$ parameters stated on the plot.

contribution based on literature observations at each observing frequency.

3.2.2 Stellar masses

The radio source evolution model developed in Chapter 2 requires some knowledge of the host environment. For massive AGN hosts ($M_\star > 3 \times 10^{10}\,{\rm M}_\odot$) the gas density was shown to be well approximated by a sequence of power law profiles whose scaling is based on the properties of the host galaxy halo. I discuss the applicability of this model for the environments of the 3C sub-sample in Section 3.3. Empirical relations determined from semi-analytic galaxy evolution models (SAGE; Croton et al. 2006, 2016) are used to determine the scaling of these profiles from the observed host stellar mass and redshift. Stellar masses must therefore be derived for the sub-sample of 3C galaxies.

The host galaxies of powerful radio AGNs have been observed to exhibit a tight relationship between redshift and their near-infrared K-band magnitudes, the 'K–z relation' or 'near-infrared Hubble diagram' (Lilly & Longair 1984). The dominant contribution to the K-band emission in such radio sources is stellar light (Best et al. 1998; Simpson et al. 1999). The stellar luminosities of these objects are therefore expected to remain largely constant over the last-half of Hubble time, consistent with

a passively evolving population formed at high redshift (e.g. Willott et al. 2003). The stellar masses of the 3C sub-sample are thus obtained using the observed K-band magnitudes from Willott et al. (2003). Their magnitudes include an aperture correction to a fixed metric aperture and an emission line contribution correction. McLure et al. (2006) have previously calculated the stellar masses of the 3C sources in the Mullin et al. (2008) sample with K band magnitudes by simply converting the magnitude to mass using the Bruzual & Charlot (2003) stellar population model. Best et al. (1998) use the same methodology to estimate the masses of a partially overlapping set of 3C objects, with results in good agreement with those of McLure et al. (2006). This method should be quite robust since the light from old stellar populations is dominant at rest-frame wavelengths longer than $\lambda \sim 1\mu$m.

Using this approach, approximately half of the sources in the Mullin et al. (2008) sample still lack stellar mass estimates. Optical R-band observations are available for 23 of these sources, whilst 36 of the sources observed in the K-band also include R-band measurements. The difference in the R and K-band magnitudes as a function of redshift should be approximately the same for all these AGN host galaxies, which have similar spectral energy distributions (SEDs). The 36 radio sources observed at both frequencies can effectively be used to derive an SED model for powerful 3C sources. The band magnitudes difference varies with redshift due to the different behaviours of the observing filters and mass-to-light ratio at these frequencies. Longhetti & Saracco (2009) derive empirical relationships for the k-correction and mass-to-light ratio at K-band as a function of redshift, but in this work I am only interested in the difference function. Based on an adapted form of their empirical relationship I derive an approximate conversion between the R and K-band magnitudes, enabling the calculation of the stellar mass. The validity of this method is verified through the strong correlation between stellar mass estimates for the 36 objects with both K and R-band observations ($r > 0.8$). Regardless, in Section 3.3 I find the radio source expansion and evolution is only weakly affected by the host environment, suggesting that a population average may be sufficient in this work.

In total I have stellar mass estimates for 73 of the 98 3C radio sources examined by Mullin et al. (57 of the 71 with fitted spectra; 2008); these mass estimates are plotted as a function of redshift in Figure 3.6. These 73 3C sources have a median stellar mass of $M_\star = 4.9 \times 10^{11}\,\mathrm{M}_\odot$, and show only a weak dependence on redshift. Further, the stellar masses of these 3C sources are very similar at all redshifts with a standard deviation of only 0.19 dex. Radio sources in such massive host galaxies are active for a greater fraction of the time and have greater lobe luminosities than their lower mass counterparts (Sadler et al. 2002; Best et al. 2007; Shabala et al. 2008), and

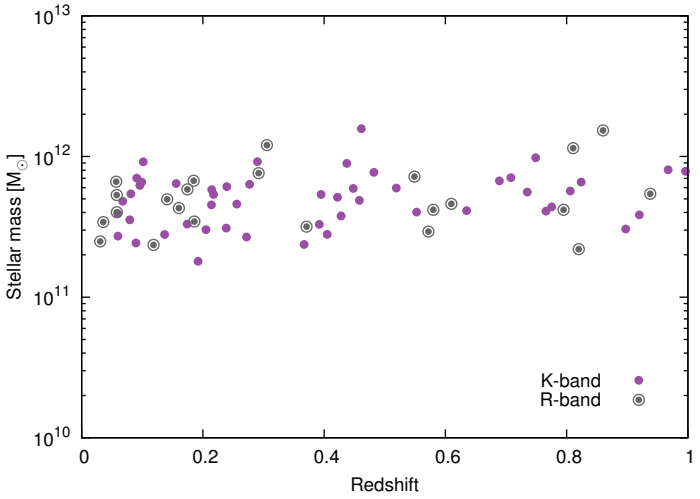

Figure 3.6: The stellar masses estimated for the 73 3C sources as a function of redshift. The 50 sources plotted with filled purple circles have their galaxy stellar masses calculated directly from observed K-band magnitudes and are consistent with the estimates of McLure et al. (2006, their Figure 1). A further 23 galaxies have K-band magnitudes, and thus stellar masses, estimated from the observed R-band magnitude (black circles).

are therefore likely to dominate the high-flux detection limit 3C survey. Moreover, in Section 3.3 I show that radio source expansion is only weakly affected by the host environment. A population average may therefore be sufficient in this work for the remaining 25 radio sources lacking X-ray or optical stellar mass estimates, enabling these objects to be included in the sample.

3.2.3 Viewing angle corrections

The observed linear sizes and axis ratios of radio sources will be affected by the viewing angle. At small angles the linear size and axis ratio should also be close to the intrinsic value ($\propto \cos d\psi$, where $d\psi$ is the angle between the line-of-sight and the normal to the jet axis). Moreover, since the typically rounded end of radio lobes comprise a spherical sector the same linear size is expected to be measured for any viewing angle within $d\psi < 1/\mathcal{A}$ radians of the normal to the jet axis, where $\mathcal{A}$ is the observed axis ratio. For a typical observed axis ratio of $\mathcal{A} = 6$ the linear size should be unchanged for viewing angles within 15 degrees of the normal to the jet axis. Combining these two effects, the length of a typical radio source viewed at 30 degrees from normal to the jet axis would be observed as 97% of its intrinsic length, reducing to 87% for a viewing

angle of 45 degrees. Objects viewed at more extreme angles may need to have their lobe lengths corrected for the viewing angle. The inclination angle is known to be anti-correlated with the fractional flux density in the core (Orr & Browne 1982); radio sources at extreme viewing angles should therefore have already been removed from the sample by the exclusion of objects with strong core emission.

3.3 Simulated AGN host environments

Knowledge of the environments into which radio sources expand is critically important when modelling their expansion and evolution. The radio source environment may be determined not only by the host galaxy but also the properties of the surrounding cluster. Observations of the hot X-ray gas surrounding 3C sources have been undertaken primarily at low-redshift (e.g. Allen 2001; Massaro et al. 2012). However, the radio sources examined in this work extend out to $z = 1$ (with a median of $z \sim 0.6$) necessitating the use of semi-analytic galaxy evolution models to describe the environments of many of these objects. In this section, the relative importance of the hot gas associated with the host galaxy sub-halo, and with the larger cluster halo is considered. I describe a model for the gas density and temperature of the environments surrounding the radio sources in the 3C sub-sample.

3.3.1 Sub-halo or large-scale cluster environment?

Within the framework of my model, the environments surrounding AGNs in central brightest cluster galaxies (BCGs) can be modelled solely using the host stellar mass to infer the hot gas mass of the central dark matter halo. However, for AGNs in smaller non-central galaxies the contribution from both the central halo and sub-halo associated with the host galaxy may need to be considered. The modelled evolution of any non-central sources inhabiting rich cluster environments will be affected if the cluster density contribution exceeds that of the sub-halo, causing the gas density profile to flatten greatly. The source evolution in the flat[2] cluster density profile will be very different to that of the rapidly declining sub-halo profile. The host galaxy's location within the cluster may therefore greatly affect the AGN environment, not only the mass of the associated sub-halo.

[2]The cluster contribution to the density profile is affected largely by the orientation of the jets relative to the cluster centre. Lobes pointing away from the centre will experience a declining profile whilst those towards it a rising density. Hence, assuming the jet angle is random the typical cluster environment at the AGN is an initially flat, then very slowly declining gas density profile.

The mass of the cluster dark matter halo can be determined using thermal X-rays, weak gravitational lensing, or by combining the masses of the sub-haloes associated with every galaxy in the cluster (e.g. Yang et al. 2007), though in practice these methods are only possible at low redshifts. The location of the sample AGN within their broader cluster environment is examined using the properties of approximately 100 000 simulated galaxies taken from the Semi-Analytic Galaxy Evolution (SAGE; Croton et al. 2016) model. The most massive non-central galaxies simulated using SAGE are all predicted to have stellar masses less than $M_\star = 2.1 \times 10^{11}\,\mathrm{M}_\odot$, compared to the observed mean of $4.9 \times 10^{11}\,\mathrm{M}_\odot$ for our 3C sample. The probability of a given 3C radio source in our sample (based on the mass distribution) inhabiting a non-central galaxy is only 3.5%, with a vanishingly small probability of there being numerous non-BCG radio AGNs. Moreover, these results are consistent with the analysis by Best (2000) of the environments surrounding high-redshift ($0.6 < z < 1.8$) 3C sources. The environments surrounding the radio sources in this work will therefore be modelled assuming the host is the central BCG.

3.3.2 Halo host environment

The environment into which these 3C radio sources expand can be modelled using an assumed gas density profile for the central halo (for the assumed BCGs) scaled by its total gas mass. The adopted cluster density and temperature profiles are described in the following.

Cluster gas density profile

The central halo gas density profile is modelled using the realisations of the Vikhlinin et al. (2006) profile as discussed in Chapter 2. These density profiles are observed to have very similar shapes when scaled by the gas mass associated with the halo and its virial radius. These cluster density profiles are only fitted out to approximately the virial radius (Figure 17 of Vikhlinin et al. 2006). The sizes of the sources in my sample relative to the virial radius of their host halo is examined in Figure 3.7. I find that only two of the sources in the 3C sub-sample expand beyond the virial radius, suggesting the fitted cluster profile is generally suitable throughout the radio source evolution.

I derive relationships for the gas mass and virial radius as a function of the halo mass to simplify the parametrisation of the host environment. Further, a conversion from the observed stellar mass to this halo mass can be obtained using the mock galaxies

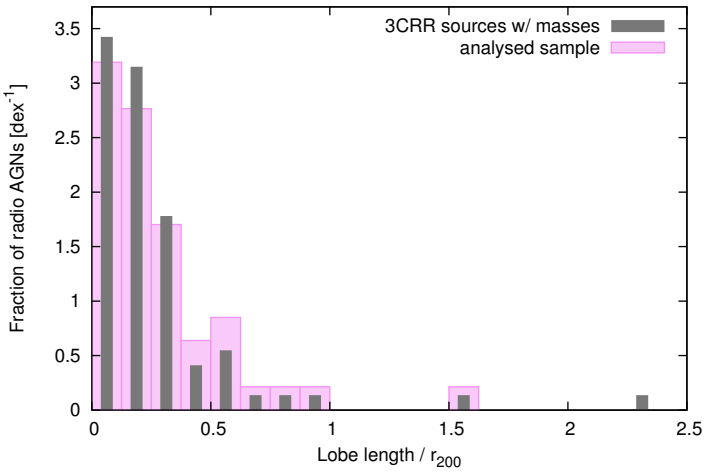

Figure 3.7: Distribution of the ratio of the observed lobe length (source length/2) and halo virial radius (r_{200}) for each 3C source in my sample. This distribution is shown both for all sources with mass estimates (grey) and only those included in the analysis in Section 3.5 (pink).

of SAGE simulated at the host galaxy redshift. These relationships enable the host environment of each radio source to be realistically modelled using solely the observed host galaxy stellar mass and its redshift. The mass of the AGN host galaxy's dark matter halo is related to its virial radius $r_{\rm vir}$ through

$$M_{\rm vir} = \frac{100}{G} H^2(z) {r_{\rm vir}}^3 \tag{3.14}$$

where G is Newton's gravitational constant, and $H(z)$ is the Hubble constant at redshift z. The baryonic fraction in the massive central haloes inhabited by 3C sources is observed to approach the universal value (McGaugh et al. 2010; Gonzalez et al. 2013). I therefore assume the gas mass of the halo environment is $M_{\rm gas} = f_{\rm b} M_{\rm vir}$ for cosmic baryon fraction $f_{\rm b} = 0.15$ (Planck Collaboration 2014).

The average gas densities of these AGN host haloes are independent of the host mass, and are a function solely of redshift through the Hubble constant, i.e. $\bar{\rho}_{\rm gas} = 100 f_{\rm b} H^2(z)/G$. However, the environments into which the radio sources expand are by no means identical since the density scales with increasing virial radius and thus mass. For a rough approximation of the gas density profile of the form $\rho(r) = \rho(r_0)[r/r_0]^{-\beta}$, the gas density at some scale radius $r = r_0$ is related to the virial radius by

$$\rho(r_0) = (3-\beta)\bar{\rho}_{\rm gas}\left(\frac{r_{\rm vir}}{r_0}\right)^{\beta} \tag{3.15}$$

where the exponent β is typically no greater than two (Kaiser & Alexander 1997). The gas density at this arbitrary radius reached by the expanding radio source increases with the halo mass as $\rho(r_0) \propto {M_{\rm vir}}^{\beta/3} \sim {M_\star}^{\beta/3}$. The gas density is therefore moderately insensitive to the observed stellar mass, varying by less than a factor of two within the 1σ level of uncertainty for the stellar mass estimates (Section 3.2.2). Further, the uncertainty in the baryon fraction in massive clusters is no greater than this factor (Gonzalez et al. 2013). Propagating this 1σ error in the host gas density yields a < 0.01 dex uncertainty in jet power estimates, 0.14 dex in source ages, and 0.08 dex in equipartition factors. This insensitivity to the observed host stellar mass (and environment in general) enables a typical 3C environment to be assumed for the remaining 25 objects in my sample lacking stellar mass estimates.

Host halo temperature

The temperature of the hot gas in clusters is known to scale with the halo mass as $T \propto {M_{\rm vir}}^{0.67}$ (e.g. Vikhlinin et al. 2006), in line with the virial temperature of the halo. In Chapter 2, I argued that the gas temperatures in smaller hosts may be higher due to heating from the AGN, however the 3C host galaxies examined here have stellar masses 0.5 dex higher than those in that chapter. Such massive AGN hosts are observed by O'Sullivan et al. (2001) to have comparable gas temperatures to other clusters. In this work, I will therefore consider hot gas temperatures which scale with halo mass as $T \propto {M_{\rm vir}}^{0.67}$ and neglect the constant temperature assumption for all but the lowest mass hosts.

3.4 Calibration of radio source model

The spectral ageing process discussed in Section 3.1 requires knowledge of the lobe plasma characteristics and radio source dynamics to derive the physical properties of real active galaxies. In the section, I assess the validity of the lobed FR-I/II dynamical model (Chapter 2) by comparing predicted radio source evolution to the detailed, albeit more computationally intensive, hydrodynamical simulations of Hardcastle & Krause (2013). The axis ratio evolution predicted by the lobed FR-I/II dynamical model is compared to that of their simulations in addition to measured 3C axis ratios. The synchrotron emission model of Chapter 4, which is based on the work of Kaiser

et al. (1997), is also calibrated in this section using various radio source observations.

3.4.1 Validation of radio source dynamics

The radio source evolution estimated by the lobed FR-I/II dynamical model is compared to two-dimensional, hydrodynamic numerical simulations of Hardcastle & Krause (2013), which is based on the PLUTO[3] code. The lobe length and volume evolution as a function of source age is compared in Figure 3.8 for radio sources with 10^{38} W jets expanding into 16 different environments. These host environments are modelled using a King profile (used by Hardcastle & Krause 2013) with core density $n = 1.5 \times 10^4\,\mathrm{m}^{-3}$ and temperature $k_\mathrm{B}T = 1.5\,\mathrm{keV}$, but with differing core radii and density fall-off rates. The ages estimated by Hardcastle & Krause (2013) are somewhat sensitive to the sound speed of the host environment leading to a horizontal shift in their results in my Figure 3.8. Their model also assumes a jet half opening angle of 15°, corresponding to an initial axis ratio of $A = 3$ for relativistic fluid flow (Komissarov & Falle 1998). I find that the lobe length evolution estimated by both models is consistent in all 16 environments, however their lobe volumes are a factor of a few lower at early times (approximately 10 Myrs for these sources). The spike in the Hardcastle & Krause (2013) simulations results from their explicit modelling of the jet before the formation of the radio lobes.

These simulations are further compared to the standard analytic radio source expansion models of Kaiser & Alexander (1997). This model assumes the lobe length expands with a constant power law dependence as $\mathcal{L} \propto t^{3/(5-\beta)}$ throughout the radio source evolution, rather than changing with the lobe expansion speed and steepening host environment. Similarly their lobe volume increases with age as $V \propto t^{9/(5-\beta)}$. The evolutionary tracks predicted using this model therefore diverge considerably from both the lobed FR-I/II dynamical model and the simulations of Hardcastle & Krause (2013). My dynamical model thus appears to be more representative of lobe dynamics.

Evolution of lobe axis ratio

Most existing dynamical models predict that the axis ratios of powerful FR-II radio sources expand in a self-similar manner, maintaining their initial axis ratio through to the present-time (Leahy & Williams 1984; Leahy et al. 1989). However, the largest radio sources ($D > 100\,\mathrm{kpc}$) are typically more elongated than smaller radio galaxies (Mullin et al. 2008), suggesting an increase in axis ratio with size. The radio AGNs in

[3] `http://plutocode.ph.unito.it/`

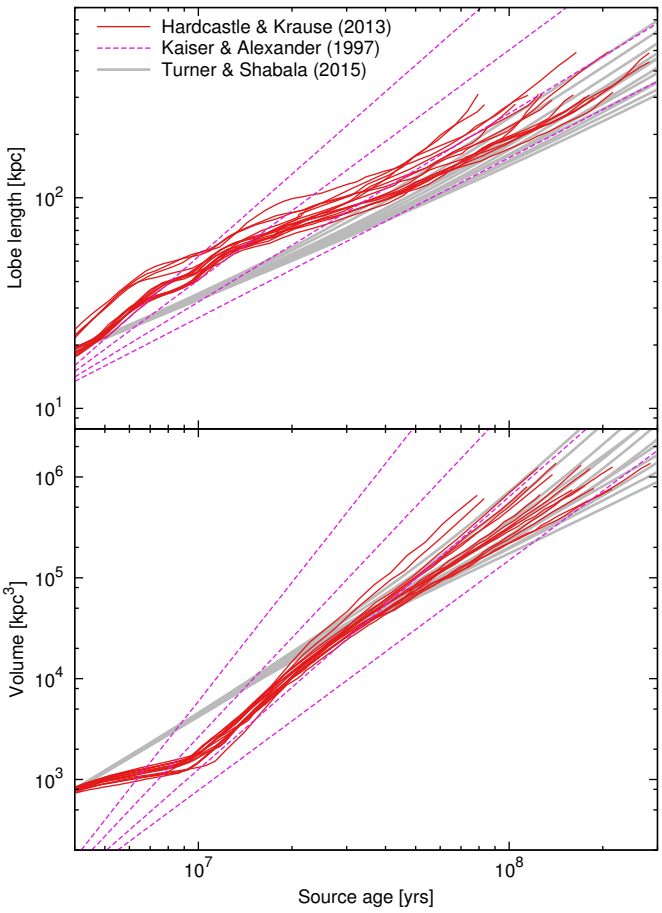

Figure 3.8: Radio source evolution estimated using the lobed FR-I/II dynamical model compared to that predicted by the hydrodynamical simulations of Hardcastle & Krause (2013). The top panel plots the average length of each lobe as a function of the source age for 10^{38} W jets expanding into 16 host environments modelled by using different King profiles. The Hardcastle & Krause (2013) evolutionary tracks are shown in red with that of the lobed FR-I/II dynamical model plotted in grey for the same parameters. The standard analytic radio source expansion model of Kaiser & Alexander (1997) is also shown in pink (dashed) for four comparable environments. The bottom panel plots the lobe volume as a function of source age, noting that the Hardcastle & Krause (2013) definition of which particles constitute the lobe may differ from mine.

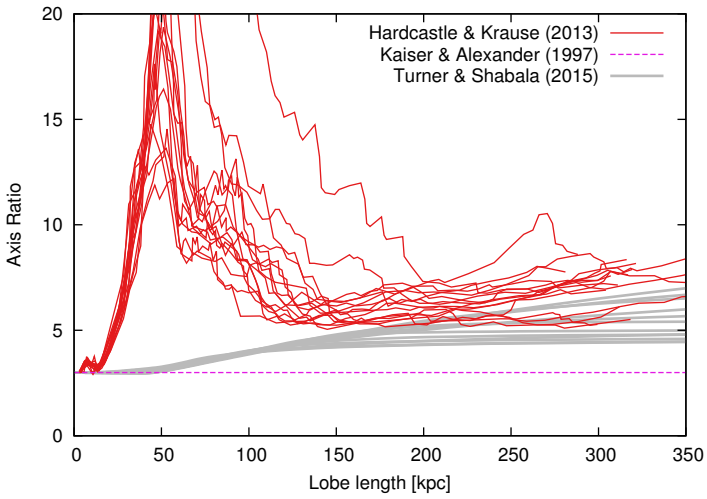

Figure 3.9: Axis ratio evolution as a function of the lobe length estimated using the dynamical model compared to that predicted by the hydrodynamical simulations of Hardcastle & Krause (2013). All lines are the same as in Figure 3.8. The large spike in axis ratios predicted by Hardcastle & Krause (2013) at small sizes is due to the jet punching through the host environment before the lobe has been inflated.

this sample are well studied objects with high dynamical range (flux peak / sensitivity), ensuring the measured axis ratio is not a function of the survey sensitivity limit (see Chapter 4). The lobe axis ratio is expected to increase in part because the expansion along the longer jet axis works against a lower density environment further from the nucleus. In weaker sources the lobe expansion normal to the jet will slow greatly upon entering the subsonic expansion phase, whilst the supersonic part of the lobe expanding along the jet axis is unaffected (e.g. Alexander 2002; Gaibler et al. 2009). The axis ratio of such 'transonic' sources can increase rapidly even without the inclusion of additional processes such as Rayleigh-Taylor mixing or Kelvin-Helmholtz instabilities (c.f. Gaibler et al. 2009, Figure 16).

The axis ratio evolution as a function of the lobe length predicted by my dynamical model is compared to that estimated by the hydrodynamical simulations of Hardcastle & Krause (2013) in Figure 3.9. The initial axis ratios of my dynamical model and that of Kaiser & Alexander (1997) are set to $A = 3$ corresponding to the 15° jet opening angle selected by Hardcastle & Krause (2013). Their simulated axis ratios spike at approximately 50 kpc as the jet reaches its maximal length before lobe formation commences, fattening the radio source and decreasing the axis ratio. The lobes form later due to the backflow of plasma from the jet terminal hotspot, reducing the axis ratio back to values similar to those predicted by my dynamical model for larger

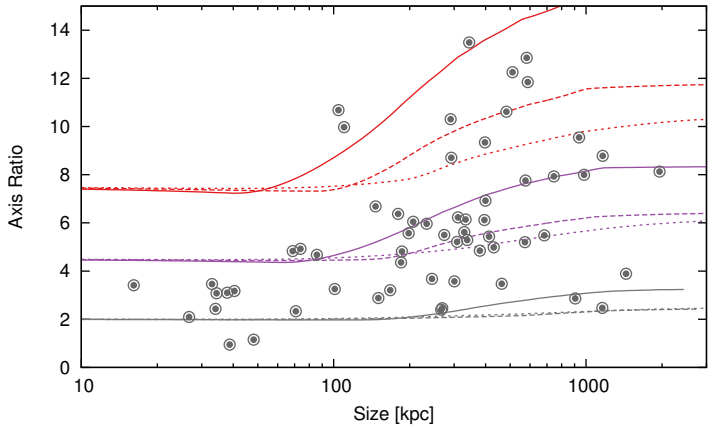

Figure 3.10: The axis ratio evolution predicted by the lobed FR-I/II dynamical model as a function of source size for a range of jet powers and opening angles (i.e. initial axis ratios). The modelled evolution for the mean initial axis ratio of the 3C sub-sample (purple) and the $\pm 1\sigma$ values (grey and red) is plotted assuming typical modelled jet powers. For each initial axis ratio, I plot the axis ratio evolution for the mean host galaxy stellar mass (dashed line), the mean lowered 1σ (solid line) and raised 1σ (dotted line). Superimposed on this plot are the observed present-time axis ratios of the sources in my sample. Clearly, using the typical jet powers and environments, the large spread in observed axis ratios can be simulated with a narrow initial range.

source sizes. My dynamical model and the hydrodynamical simulations thus are in reasonable agreement for larger sources (lobe length >150 kpc) and are consistent with an axis ratio that increases with age. By contrast, the Kaiser & Alexander (1997) analytical model assumes a constant axis ratio throughout the radio source expansion, in disagreement with the axis ratio evolution in the other models.

I further compare the axis ratio evolution predicted using the lobed FR-I/II dynamical model to that of observed 3C radio sources in Figure 3.10. I simulate this evolution for three host halo environments and initial axis ratios, corresponding to the median and 1σ uncertainties of the 3C radio source sub-sample. The initial axis ratios are estimated to have a median and 1σ uncertainty of $A = 4.7^{+2.9}_{-2.4}$. The jet power has a similar but weaker effect on the axis ratio evolution to that of the environment and is omitted from the plot for simplicity. Superimposed on the plot are the observed present-time axis ratios of these sources taken from Mullin et al. (2008). The lobed FR-I/II dynamical model reproduces the rapid increase in axis ratio observed for sources larger than 100 kpc. However, the Mullin et al. (2008) observations in isolation cannot distinguish between the possibilities of the hypothesised axis ratio

evolution throughout the source lifetime, or some selection effect whereby high initial axis ratio sources tend to be visible at larger sizes (e.g. because they have higher surface brightness).

3.4.2 Calibration of boot-strapped luminosity model

The jet power estimates derived in Chapter 2 and similar work (e.g. Shabala et al. 2008) have been made incognisant of the scaling factors in the synchrotron emission model. However, the physics of these objects is not fully understood leading to large uncertainties in the kinetic power-to-luminosity conversion factor. Willott et al. (1999) described these uncertainties using a single factor f such that $L \propto f^{-3/2} Q^{7/6}$, which is observationally constrained to lie between ~ 1 and 20. There are three main causes of uncertainty in the calculation of the radio luminosity: (1) knowledge of the deviation of the magnetic field strength from equipartition, (2) the energies of the injected synchrotron electrons, and (3) the particle composition of the lobe plasma. The uncertainty in the lobe filling factor considered by Willott et al. (1999) is directly modelled through the Rayleigh-Taylor mixing of the lobed FR-I/II dynamical model[4]. The equipartition factor and lobe composition will be constrained in this section by dynamical model fits to 3C radio sources, whilst constraints on the low-energy cut-off to the electron population will be guided by observations. In this manner, my synchrotron luminosity model can be used to infer the intrinsic properties of AGNs using the luminosity as a constraint.

Minimum electron Lorentz factor

The modelled radio source luminosity is moderately sensitive to the low-energy cut-off of the acceleration-time synchrotron electron population. This parameter primarily affects the normalisation of the simulated radio luminosity which I calibrate using observations. It additionally introduces a dependence on the injection spectral index, $\alpha_{\rm inj} = (s-1)/2$. Specifically, the minimum Lorentz factor of this electron energy distribution is related to the luminosity as $L_{\rm rad} \propto {\gamma_{\rm min}}^{s-2}$ (Equation 8 of Kaiser et al. 1997). The minimum Lorentz factor in the hotspot has been estimated by other authors for selected radio sources including: Cygnus A (McKean et al. 2016), PKS 1421-490 (Godfrey et al. 2009), 3C123, 3C196 and 3C295 (Hardcastle 2001). These hotspot Lorentz factor estimates are mostly in the order of a few hundred although these estimates

[4]The powerful FR-IIs in the 3C sample are found to have filling factors close to unity; i.e. the transonic expansion of their lobes make them largely impervious to Rayleigh-Taylor mixing.

are quite uncertain due to the confounding effects of free-free and synchrotron self-absorption. The Lorentz factor of the electron population in the lobe is expected to be approximately an order of magnitude lower due to the adiabatic expansion of the plasma. The lossy luminosity model described in Chapter 4, based on the work of Kaiser et al. (1997), simulates the adiabatic expansion of the packets of synchrotron electrons from the higher pressure hotspot to the lobe at the time of emission. The minimum Lorentz factor of the electron energy distribution at the hotspot reduces accordingly as the electrons propagate throughout the lobe; the Lorentz factor in the lobe does not need to be explicitly measured. Hydrodynamical simulations of the pressure and magnetic field distributions throughout the radio source will further improve results. Following Godfrey et al. (2009), I assume a typical hotspot minimum Lorentz factor of $\gamma_{\rm min} = 500$ for the sources in my sample. Systematic errors in AGN intrinsic parameter estimates are derived for realistic Lorentz factors in the range $\gamma_{\rm min} = 100$-1000, yielding a 0.19 dex uncertainty in jet power estimates, 0.06 dex in source ages, and 0.01 dex in equipartition factors. This observationally informed choice should ensure a realistic luminosity dependence on the injection index, whilst the normalisation remains to be fully calibrated.

Lobe magnetic field strength

The scaling and shape of the radio spectrum depend on the magnetic field strength; the fraction of energy stored in the magnetic field must therefore be quantified in order to constrain the AGN kinematics. This energy fraction is considered here as the deviation of the field strength B from the equipartition value $B_{\rm eq}$, in which equal energy is assumed to be in both the field and the synchrotron-emitting electrons. This equipartition factor is related to the ratio of energy density in the magnetic field to that in the synchrotron-emitting particles, q, through $B/B_{\rm eq} = q^{2/(s+5)}$ (e.g. Croston et al. 2005). Below, I use the radio lobe dynamics alone to show that the 3C radio sources cannot be in equipartition, then use further observations to precisely constrain the magnetic field strength.

A Bayesian fitting algorithm (see Section 3.5.1) is used to determine the most likely dynamical and spectral age for 37 3C radio sources based on their observed size and spectral break frequency. The ages are fitted assuming a range of magnetic field strengths (or equivalently equipartition factors $B/B_{\rm eq}$) and halo environments taken from the semi-analytic SAGE model for their observed stellar mass. For each equipartition factor I determine the difference between the best fit spectral and dynamical age for each source, with the median and 1σ of the distribution shown in Figure 3.11.

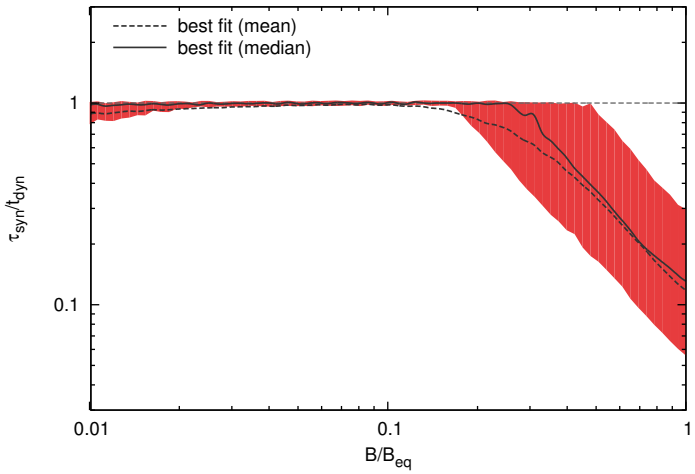

Figure 3.11: Ratio of fitted synchrotron and dynamical ages as a function of the deviation from the equipartition magnetic field strength. The black line plots the mean ratio for a reduced sample of 37 3C sources with sufficient data. The median ratio is plotted in red with the 1σ uncertainties shown by the shading. Radio lobes close to equipartition have unrealistically young spectral age estimates which can not be reproduced by my dynamical model for these sources.

The dynamical and spectral ages are inconsistent for all of these sources if the lobes are assumed to be in equipartition. By contrast, the two age estimates agree if the 3C sample has a median equipartition factor of $B/B_{\rm eq} \lesssim 0.3$, corresponding to an energy density ratio of $q \lesssim 0.01$. These upper bounds are derived entirely using the radio source dynamics and fits to the spectral curvature, and thus are not affected by any uncertainties associated with the power-to-luminosity conversion factor.

The spectral age is inversely related to the lobe magnetic field strength and thus higher field strengths lead to younger ages. Then the jet power must be higher for the source to expand to the observed size in this shorter time, $Q \propto B^{4.5}$. However, the lobe field strength increases with increasing jet power as $B \propto Q^{(2-\beta)/2(5-\beta)}$, further reducing the spectral age. For example, an order of magnitude perturbation to the field strength converges to a 45 order of magnitude increase in jet power in a flat environment or a seven order of magnitude increase for a more typical $\beta = 1.5$ environment. The observed size and break frequency can thus not be reconciled for any physical dynamical age–jet power combination if unrealistically high field strengths close to the equipartition value are assumed.

The distribution of equipartition factors for these 37 3C sources can be quantified

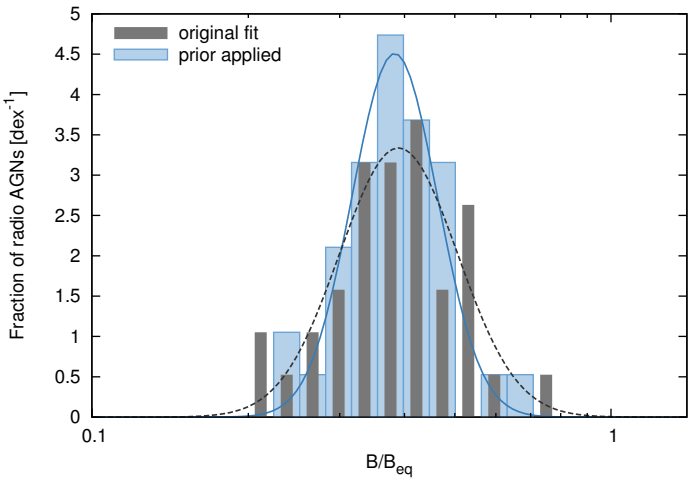

Figure 3.12: Fitted distribution for the equipartition factor using the FULL FIT algorithm (see Section 3.5), both with (blue) and without (grey) the use of the prior probability distributions. The solid and dashed lines are Gaussian fits to these probability distributions respectively.

using the calibrated monochromatic luminosity as an additional constraint. The resulting distribution shown in Figure 3.12 is approximately normal having a median of $B/B_{\rm eq} = 0.38$, 1σ point uncertainty of 0.17 dex, and standard error of 0.10 dex (including systematic uncertainties from the environment and electron population). The lobe magnetic field strengths of the sources in the reduced 3C sample are thus lower than the equipartition value by a factor of three (significant at the 5σ level). The stability of the parameter fitting algorithm is tested by using the original distribution as a prior probability distribution instead of a flat prior. This choice of prior does not affect these conclusions, as shown in Figure 3.12.

These equipartition factors are consistent with the observations of other authors. Croston et al. (2005) and Ineson et al. (2017) found the energy density in powerful FR-IIs peaks at $B/B_{\rm eq} \sim 0.5$ (corrected to observed spectral index $s = 2\alpha_{\rm inj} + 1$) and 0.4 respectively based on X-ray inverse-Compton emission from the synchrotron emitting electron population. The dynamical model based equipartition factors are also in good agreement with the 3C observations of Ineson et al. (2017) on a source-by-source basis. These measurements are all consistent to within the 2σ uncertainties, as shown in Figure 3.13. Note that the Ineson et al. (2017) equipartition factors are calculated assuming an injection index of $s = 2.4$, in contrast to the $s = 2.05$-2.6 range fitted to the 3C spectra; I have therefore adjusted their measurements for this variation in injection index. Hardcastle & Krause (2014) similarly find that radio synchrotron and inverse

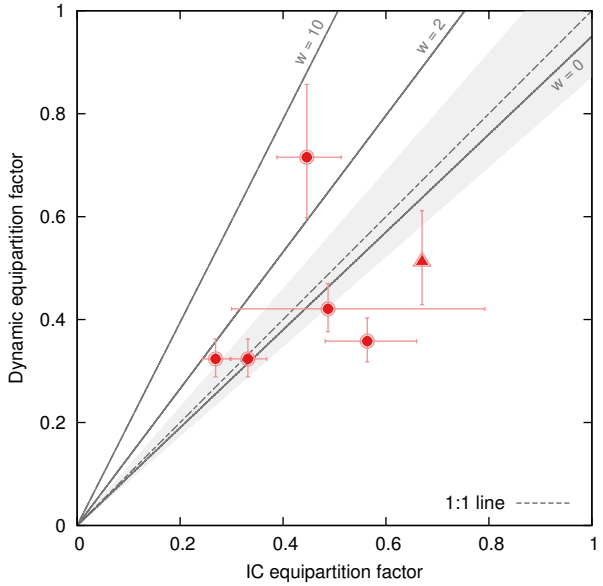

Figure 3.13: Estimated equipartition factor $B/B_{\rm eq}$ for 3C219N, 3C219S, 3C244.1, 3C330, 3C427.1 and Pictor A as a function of the X-ray inverse-Compton (IC) measurements of Hardcastle et al. (2016, triangle) and Ineson et al. (2017, circles). The six unique measurements of the field strength for the 3C sources are plotted assuming $w = 0$ with 1σ errorbars included for each data point except Pictor A (triangle at top). The best linear fits to this and equivalent distributions assuming alternative proton-to-lepton energy density ratios (of $w = 2$ and 10) are shown as solid lines, with the 1σ standard errors in the fits shaded and centred on the one-to-one line.

Compton emission properties derived from substantially sub-equipartition magneto-hydrodynamic (MHD) simulations are broadly in good agreement with observations. The general consensus is thus of FR-II lobes with field strengths approximately a factor two to three less than the equipartition value, or equivalently magnetic field energy densities approximately a factor of 40 less than that in the electrons.

The similarity between my dynamical model equipartition factor estimates and those of Ineson et al. (2017) is encouraging, however all but a single source (3C427.1) have dynamical equipartition factors fitted in the narrow range $0.32 < B/B_{\rm eq} < 0.42$. The veracity of my fitting algorithm is further tested against observations of Pictor A, which has a measured equipartition factor of $\sim$0.7 (Hardcastle et al. 2016). The spectrum of Pictor A is fitted using the continuous injection model (see Section 3.1) based on data taken from Kuehr et al. (1981), whilst other properties are taken from Hardcastle et al. (2016). The equipartition factor thus derived for Pictor A is $B/B_{\rm eq} =$

0.51 ± 0.07. The distribution of equipartition factors estimated for the 3C sources is therefore not an artefact of the fitting algorithm; this method appears capable of accurately determining the magnetic field strength in close-to-equipartition sources.

Radio lobe plasma composition

The particle composition of the lobes of radio AGN is arguably most directly probed through X-ray observations of the inverse-Compton emission; although incapable of directly detecting any non-radiating particles, observations of close-to-equipartition lobes are used to suggest at most a small fraction of the energy density is present in relativistic protons or a thermal plasma (e.g. Hardcastle et al. 2002; Croston et al. 2004, 2005; Ineson et al. 2017). In this technique the X-ray emission upscattered from the synchrotron-emitting electrons is compared to that expected if their energy densities are in equipartition with the magnetic field. This direct measurement of the equipartition factor is therefore unaffected by the inclusion of non-radiating particles into the lobe plasma. By contrast, the dynamical model measurements are dependent upon the lobe plasma composition; the equipartition factors derived using my model for 3C219, 3C244.1, 3C330, 3C427.1 and Pictor A are thus recalculated for a range of proton-to-lepton (or non-radiating to radiating particle) energy density ratios, as shown by the fitted lines in Figure 3.13. The inclusion of non-radiating particles does permit the possibility of radio lobes in equipartition, although the energy density in thermal particles is required to be up to 35 times that of the leptons. By contrast, proton-to-lepton energy density ratios between $w = 0$ and 2 are consistent with the equipartition factors measured by Hardcastle et al. (2016) and Ineson et al. (2017) to within the 2σ uncertainties.

The energy density in relativistic protons or a thermal plasma is tested further by comparing the jet powers estimated for the 3C sub-sample (see Section 3.5, and Tables A2.1 and A2.2) to independent measurements. Ineson et al. (2017) use their inverse-Compton modelling to derive jet power estimates from their measurements of the lobe internal pressure and its expansion speed (which provides an age estimate). The correlation between these jet power measurements and the dynamical model based estimates is shown in Figure 3.14. However, this strong relationship results primarily from the redshift dependent nature of the survey detection limits. Examining only radio sources from a small redshift range may therefore yield largely scatter (Figure 3.14), as shown conclusively by Godfrey & Shabala (2016) for a range of jet power measurement techniques. Regardless, the results in Figure 3.14 provide some confidence in the jet power-to-luminosity conversion factor of my model and support the

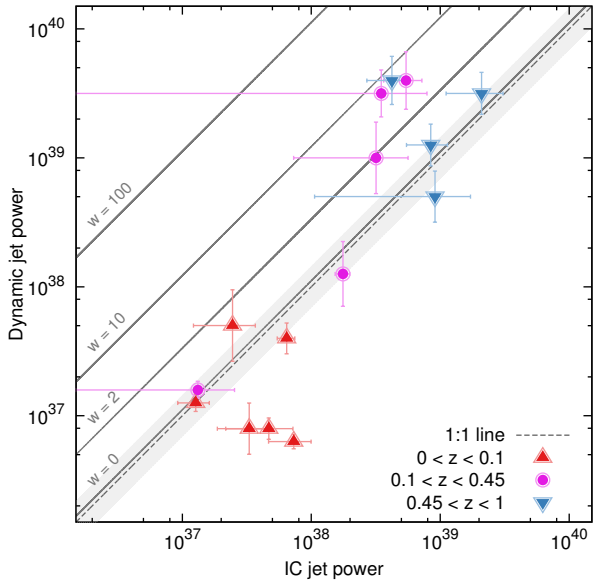

Figure 3.14: Correlation between my dynamical model based jet power estimates (either FULL FIT or SOURCE SIZE fitting algorithm, see Section 3.5) and the Ineson et al. (2017) powers calculated from X-ray inverse-Compton measurements. The apparent strength of the correlation results largely from the redshift-dependent flux-detection limits. Radio sources at $z < 0.1$ are shown in red (triangles), those at $z > 0.45$ in blue (inverted triangles), with the remainder plotted in pink (circles). The jet powers for these plotted points are calculated assuming $w = 0$. The best linear fits to this and equivalent distributions assuming alternative proton-to-lepton energy density ratios (of $w = 2$, 10 and 100) are shown as solid lines, with the 1σ standard errors in the fits shaded and centred on the one-to-one line.

previous conclusions about the composition of the lobe plasma. Radio sources with lobe plasma exclusively comprising radiating particles have jet powers consistent with the X-ray inverse-Compton measurements. By contrast, a lobe comprising an energetically dominant population of relativistic protons or thermal plasma (i.e. $w > 2$) is inconsistent with my estimates at the 2σ level.

The comparison of the dynamical model based jet power and equipartition factor estimates to independent measurements from Hardcastle et al. (2016) and Ineson et al. (2017) have yielded the same outcome: a proton-to-lepton ratio of $w < 2$ at the 2σ level. There is therefore strong evidence against an energetically dominant population of relativistic protons or thermal plasma (i.e. $w > 2$). These results are entirely consistent with a lobe excluding any significant energy in a population of

non-radiating particles, although based on these findings $w \lesssim 2$ is quite plausible. In this work, I will therefore adopt a pair-plasma with no energetically-dominant proton population (i.e. $w = 0$). The possibility of a population of non-radiating particles with up to double the energy of that in the leptons cannot be excluded, however these results are not greatly affected for $w \lesssim 2$.

3.5 Parameter estimation

The intrinsic AGN parameters, including the kinetic jet power, source age and magnetic field strength, are derived from the CI model fits to the radio spectra and other observables using a Bayesian approach. In this section, I consider various fitting algorithms utilising either all the observed parameters or only a limited set that might be expected to be available in large-scale surveys. The versatility of the AGN parameter fitting technique potentially enables intrinsic properties to be estimated for high-redshift, unresolved sources for which no size constraint can be determined.

3.5.1 Bayesian parameter estimation

The most likely jet powers Q, source ages t, and equipartition factors $B/B_{\rm eq}$ are estimated for the sub-sample of 3C radio sources using a Bayesian approach. These intrinsic parameters are constrained based on the observed luminosity, spectral break frequency and source size, and the host galaxy environment (see Section 3.3). The fitting algorithms tested here include: utilising all the observables (Full Fit); size and calibrated monochromatic luminosity (Source Size); spectral break frequency and luminosity (Spectral Break); and using only the monochromatic luminosity at 178 MHz (Luminosity Only). I simulate the radio source evolution for a range of jet powers, ages and equipartition factors assuming typical environments for each source's stellar mass and redshift. The goodness of fit of these evolutionary models for each age/jet power/equipartition factor triplet to some observable x is assessed using the chi-squared probability

$$P(x) = \exp\left(-\left[\frac{\log x_{\rm mod} - \log x_{\rm obs}}{\sigma_{\log x}}\right]^2 \Big/ 2\right), \tag{3.16}$$

where $\log x_{\rm mod} - \log x_{\rm obs}$ is the log-space difference between the observed and simulated values of parameter x. The uncertainty due to the model dominates and is taken as $\sigma_{\rm x} = 0.3$ dex, noting that values anywhere in this region yield stability in the solution

Table 3.1: Bayesian fitting algorithms used to derive the jet powers, source ages, sizes and equipartition factors for the 3C radio source sub-sample. These algorithms use the probability of the evolutionary track matching the observed size $P_{\rm D}$, spectral break frequency $P_{\nu_{\rm b}}$, and luminosity $P_{\rm L}$, in various combinations. In the final column, the number of 3C objects with the requisite data for each algorithm is shown.

Algorithm Name	$P_{\rm D}$	$P_{\nu_{\rm b}}$	$P_{\rm L}$	$n_{\rm obs}$
FULL FIT	yes	yes	yes	37
SOURCE SIZE	yes	-	yes	71
SPECTRAL BREAK	-	yes	yes	37
LUMINOSITY ONLY	-	-	yes	71

space. The parameters used for each fitting algorithm are listed in Table 3.1. The likelihood of each simulation matching the observations is calculated as the product of the probabilities for each parameter, with the age/jet power/equipartition factor triplet associated with the maximum likelihood taken as best estimates.

The radio source evolution is additionally affected by the jet opening angle which in turn affects the axis ratio of the young lobe (Komissarov & Falle 1998). I model the evolution of the sources in the 3C sub-sample for a range of initial axis ratios and estimate the most likely ratio at the time of observation based on the source age, jet power and equipartition factor estimates. The initial axis ratio yielding a present-time ratio closest to the observed value from Mullin et al. (2008) is taken as the best estimate.

3.5.2 Ill-conditioned fitting algorithms

The SOURCE SIZE, SPECTRAL BREAK and LUMINOSITY ONLY fitting algorithms are underdetermined, potentially leading to unstable solutions. However, rather than yielding no solution, these algorithms derive some parameters robustly whilst others are completely unconstrained. As I explain below, the source age and lobe pressure are degenerate variables, enabling the omission of the parallel size constraint in the SPECTRAL BREAK algorithm. The jet power and equipartition factor are also somewhat degenerate yielding reliable source age estimates using the SOURCE SIZE algorithm. The intrinsic parameters for the 37 radio sources with a complete set of observational constraints are included in Table A2.1.

Source age–lobe pressure degeneracy

The spectral break frequency constraint of Equation 3.6 relates the source age and lobe pressure as $t \propto p^{-0.75}$, where $B \gg B_{\rm ic}(z)$. This assumption is justified since all 37 3C sources fitted using the Full Fit algorithm have lobe magnetic field strengths greater than the cosmic microwave background equivalent, typically by at least a factor of a few. By contrast, the luminosity constraint depends on the age and pressure only through the $p(t)^{(s+5)/4}V(t)$ term (Equation 4.14), where in the strong-shock expansion limit $V(t) \propto t^{9/(5-\beta)}$ (Kaiser & Alexander 1997). The pressure and age are therefore related as $t \propto p^{(s+5)(\beta-5)/36}$ in this constraint. For typical values of $\beta = 1.5$ and $s = 2.5$ this relationship becomes $t \propto p^{-0.73}$, mirroring that of the spectral break frequency constraint. The source age and lobe pressure can therefore not be distinguished solely by the luminosity and break frequency constraints.

The degeneracy between the age and lobe pressure has the unexpected benefit that these parameters can effectively be treated as a single variable, reducing the number of unknown parameters in the fitting algorithm. The jet power and equipartition factor parameters can thus be determined accurately with one less observable than required in the full model. The Spectral Break fitting algorithm should therefore be capable of estimating jet powers and equipartition factors with comparable accuracy to the Full Fit model, but have no ability to constrain the source age. I return to this point in Section 3.5.3.

Jet power–equipartition factor degeneracy

The size constraint relates the source age and jet power in the strong-shock supersonic limit as $D \propto t^{3/(5-\beta)}Q^{1/(5-\beta)}$ (Equation 4 of Kaiser & Alexander 1997). The much stronger dependence on the source age parameter places a tighter constraint on this parameter in an underdetermined fitting algorithm, with good source age estimates expected for only order of magnitude accurate estimates of jet powers. Source ages estimated using the Source Size algorithm should therefore have close to comparable accuracy to the Full Fit algorithm; I discuss this further in Section 3.5.3.

By contrast, the luminosity constraint relates these parameters and the equipartition factor in the strong-shock limit as

$$L = L_0 t^{[36-(s+5)(4+\beta)]/4(5-\beta)} Q^{[12+(s+5)(2-\beta)]/4(5-\beta)} q^{(s+1)/4}. \tag{3.17}$$

where L_0 is a constant of proportionality including the loss processes and lobe plasma

composition, and again $q = (B/B_{\rm eq})^{(s+5)/2}$. For typical values of $\beta = 1.5$ and $s = 2.5$, this relationship becomes $L \propto t^{-0.38} Q^{1.13} q^{0.875}$, or for a given best-fit source age is $L \propto Q^{1.25} q^{0.875}$. The similar exponents on Q and q mean neither the jet power nor equipartition factor can be well constrained. Typical values for one of these parameters must be assumed in order to better constrain the other. In this work I assume a prior probability distribution for the equipartition factor (see Section 3.4.2 and Figure 3.12) to enable the jet power to be well constrained in the SOURCE SIZE algorithm; note that this prior is not applied in Figures 3.15, 3.16 and 3.17.

3.5.3 Stability of ill-conditioned algorithms

In this section, the stability of the underdetermined SOURCE SIZE, SPECTRAL BREAK and LUMINOSITY ONLY algorithms is directly compared to the results of the full model. Prior probability distributions are also applied during the fitting process to test if more stable results are obtained for some algorithms.

Size–luminosity fitting algorithm

The Mullin et al. (2008) 3C sample could only have spectral break frequencies confidently fitted to 52% of radio sources, after the removal of AGNs with bright cores, peculiar spectra or no observations of their spectra. Further, in weaker sources than observed here, the low signal-to-ratio noise may preclude an accurate fit of the break frequency. There may therefore be numerous instances where using the spectral break frequency in the fitting algorithm is not viable, but the source size is known. However, by excluding the break frequency the model is no longer capable of constraining all free parameters, and a typical value must be assumed for the lobe equipartition factor, e.g. $B/B_{\rm eq} = 0.38$ (Section 3.5.2). This fitting method was used in Chapter 2 and by others including Shabala et al. (2008).

The stability of the FULL FIT algorithm to the removal of the spectral break frequency parameter is examined in the top panel of Figures 3.15, 3.16 and 3.17. Without the use of a prior probability distribution for the equipartition factor the jet powers estimated using the SOURCE SIZE algorithm differ considerably from the full model ($r^2 = 0.20$). The inclusion of the equipartition factor prior (not shown in figure) enables the SOURCE SIZE fitting algorithm to explain 75% of the variation in the jet powers estimated by the full model. The source ages are only marginally better recovered than the jet powers without the use of an equipartition prior, with only 46% of the variation in the full fit explained. This is increased to 87% when the equipartition

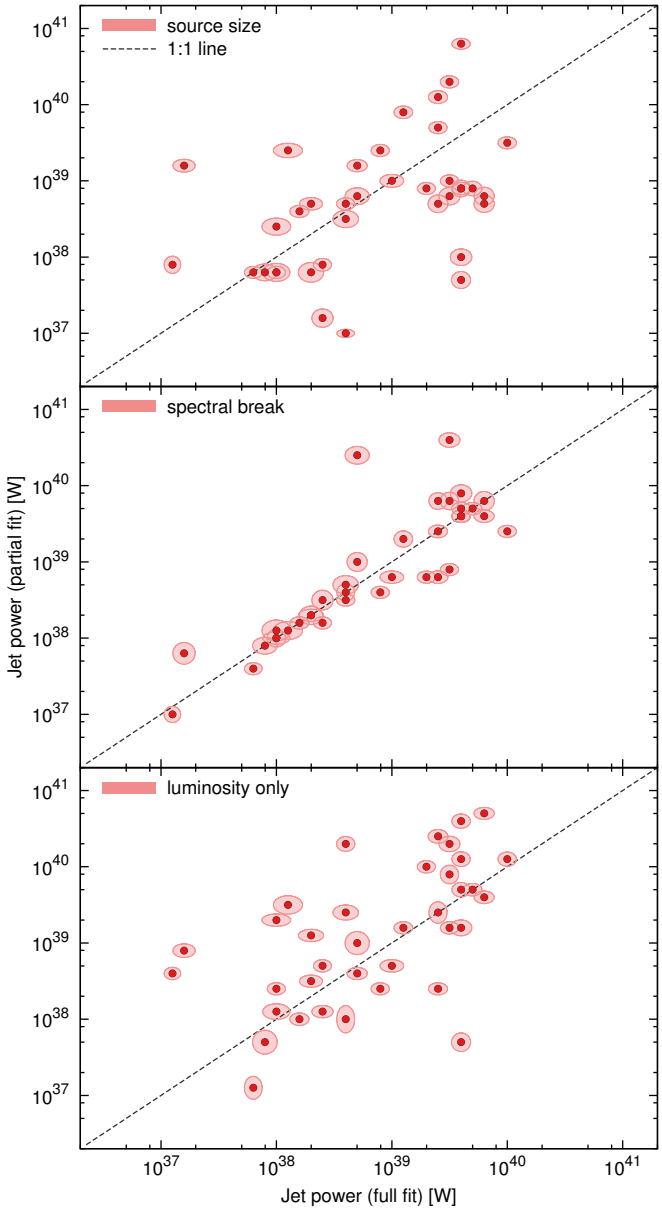

Figure 3.15: The consistency of jet power estimates is compared to the best estimates for fitting algorithms using the two observables size and luminosity (top panel), break frequency and luminosity (middle panel), and a single variable fit using only luminosity (bottom panel). The jet powers estimated using the three variable full fit are plotted on the horizontal axis with the jet powers of the simpler models on the vertical axis. The red circles and associated ellipses mark the 1σ model uncertainties for each radio source with the dashed line marking a one-to-one relationship.

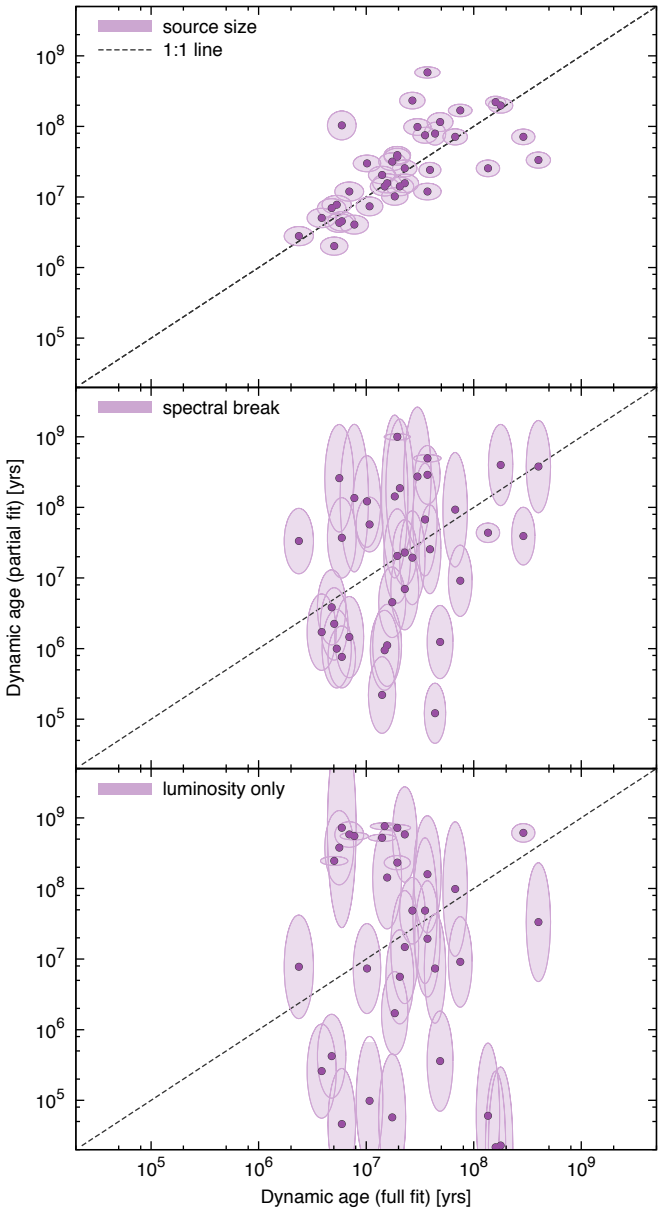

Figure 3.16: Same as Figure 3.15 but comparing the consistency of the source age estimates to the full fitting algorithm for each model simplification.

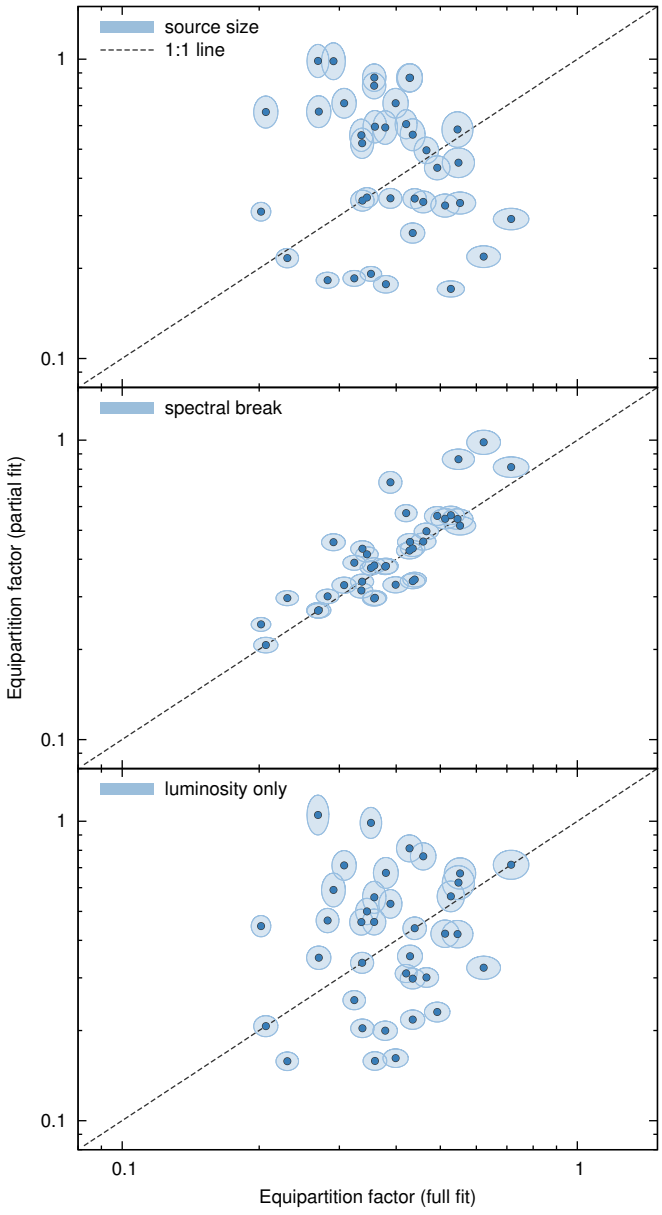

Figure 3.17: Same as Figure 3.15 but comparing the consistency of the equipartition factor estimates to the full fitting algorithm for each model simplification.

factor prior is assumed. However, the SOURCE SIZE algorithm is incapable of estimating the equipartition factor ($r^2 < 0.05$), with the use of priors simply yielding the peak value of the equipartition factor prior probability distribution. This is consistent with the analytical expectations discussed in Section 3.5.2.

The jet power and age estimates from the simpler size–luminosity method are very consistent with those of the full fitting algorithm with the use of a prior for the equipartition factor. This simplification is likely quite reasonable in any case where the break frequency cannot be measured. The jet powers of the 34 3C radio sources without break frequency measurements are therefore calculated using this method and included in Table A2.2.

Break frequency–luminosity fitting algorithm

The resolution of the radio lobes for all but the largest sources may not be possible at high-redshifts even with future all-sky surveys; for example, a 10 arcsec beam FWHM corresponds to 80 kpc limit at $z \sim 1$ for ASKAP EMU (Norris et al. 2011). The ability to understand the effect AGNs have on galaxy formation and evolution in the early universe is thus hindered severely if size is required to constrain their intrinsic properties. Developing a stable fitting algorithm excluding the source size would aid greatly further understanding AGN feedback at this epoch.

The stability of the FULL FIT algorithm to the removal of the size parameter can now be examined (centre panel of Figures 3.15, 3.16 and 3.17). The jet power estimates are quite consistent with those estimated using the full model for all but two sources (3C244.1 and 3C247), with 88% of the variation explained by the simpler model (excluding size) if these two poorly fitted sources are excluded from the statistic. The equipartition factors are similarly well reproduced by the simpler fitting algorithm ($r^2 = 69\%$). The adoption of an equipartition factor prior slightly reduces the strength of these correlations. By contrast, the SPECTRAL BREAK fitting algorithm is completely incapable of estimating the source ages ($r^2 < 0.05$) due to the degeneracy between the age and lobe pressure (see Section 3.5.2). The source age estimates are improved for most sources by assuming a prior probability distribution for the lobe pressure based on empirical relationships between observed and intrinsic parameters; e.g. lobe pressure–luminosity. However, this approach is not physically based and can worsen the estimates for some less typical sources by several orders of magnitude; such prior probability distributions are not examined in this work.

The SPECTRAL BREAK fitting algorithm is therefore capable of reliably estimating the jet powers of unresolved radio sources, although it requires size information or at

least an upper bound to determine their ages. New radio surveys may not observe at more than two frequencies (though see e.g. Bannister et al. 2016; Callingham et al. 2017), and hence it may not be possible to determine the break frequency for all radio sources. This problem should be resolved by combining observations from multiple surveys, with coverage at 1.4 GHz (e.g. ASKAP EMU) or lower frequencies (e.g. MWA GLEAM/SKA-low, LOFAR, VLSS). Break frequencies above 1.4 GHz may require follow-up observations to these surveys at higher frequencies. The AT20G survey (Murphy et al. 2010) has previously obtained simultaneous three-frequency data (at 5-20 GHz) for several thousand bright sources, almost all of which also have lower-frequency data available from NVSS/SUMSS. However, the break frequency may not be able to be observed at all for radio sources younger than approximately 1 Myr where the spectral break will be at very high frequencies (e.g. >20 GHz). Very young sources will additionally exhibit curvature at lower frequencies due to free-free and synchrotron or self-absorption.

Luminosity-only fitting algorithm

Numerous authors have attempted to predict the jet powers of radio sources based solely on their luminosities (jet power–luminosity relationship, e.g. Willott et al. 1999). However, these empirical relationships are significantly weakened when corrected for the confounding distance variable (Godfrey & Shabala 2016). The validity of such methods are further examined here by fitting the 3C sources which have a complete set of constraints using solely the monochromatic luminosity. The stability of the method is shown in the bottom panel of Figures 3.15, 3.16 and 3.17. The jet powers shown are weakly related to those estimated using the full algorithm ($r^2 = 0.34$), though with the jet powers of some sources differing by over an order of magnitude. This is because radio sources undergo significant luminosity evolution (Shabala & Godfrey 2013) whilst the environment also plays an important role (Kaiser et al. 1997; Hardcastle & Krause 2013). The adoption of an equipartition factor prior probability distribution improves the relationship ($r^2 = 0.60$), though this algorithm is still far worse at estimating jet powers than with the inclusion of a size or spectral break measurements. By contrast, both the age and size estimates show very little resemblance to those calculated using the full algorithm ($r^2 < 0.05$). These jet power–luminosity relationships are therefore acceptable only for an order-of-magnitude estimate of the jet power even if priors can be assumed, whilst using the luminosity on its own as a fit constraint for the age and size is unviable. This is not surprising given the large luminosity evolution experienced by sources over their lifetimes (see Chapter 2).

3.6 Conclusions

I have presented a new method to measure the AGN jet kinetic power, radio source age and lobe magnetic field strength based on the observed radio lobe luminosity and length, the shape of the AGN synchrotron emission spectrum, and the properties of their host halo environment. My approach differs in two important respects from previous jet power estimation methods: (1) all parameters in the synchrotron emission model are either fitted or constrained using observations; and (2) confounding variables such as the lobe length and host halo environment are considered. Specifically, the low-frequency cut-off to the synchrotron electron energy distribution is observationally constrained, whilst the filling factor (model dependent) and any departure from the equipartition magnetic field strength are fitted using a Bayesian approach. My work in Chapter 2 and that of Shabala et al. (2008) also consider this size and environment dependence, but do not constrain the uncertainties in the luminosity model or consider the full radio spectrum.

The dynamics predicted by my lobed FR-I/II evolution model is found to closely match hydrodynamical simulation results (Hardcastle 2013; Hardcastle & Krause 2014). By contrast, the existing self-similar analytic model of Kaiser & Alexander (1997) yields results which are largely inconsistent with both my model and the simulations, mainly because of the insufficient modelling of the host environments. Further, the axis ratio evolution predicted by my dynamical model for the 3C sub-sample is capable of reproducing the present-time axis ratios from a narrow range of initial axis ratios and host halo environments.

I applied the combined dynamical and synchrotron luminosity model to a sample of 71 3C Fanaroff & Riley type II radio galaxies to infer the jet powers, ages and equipartition factors based on combinations of their observed sizes, luminosities and spectral shapes (where available). The synchrotron spectrum of a subset comprising 37 of these objects was fitted using a continuous injection model, and curvature was parametrised with the break frequency parameter. I tested the sensitivity of estimated AGN physical parameters to availability of data and found:

1. The full set of observables (break frequency, lobe length and luminosity) allow accurate inference of the jet power, source age and lobe equipartition factor.
2. Excluding the break frequency (e.g. observing only a low-frequency monochromatic luminosity) allows the source age to be constrained, but not the jet power or the equipartition factor.
3. The spectral break frequency and lobe luminosity accurately infer the jet power

and lobe equipartition factor, but not the source age.

4. Luminosity alone poorly estimates the jet power, and is incapable of inferring the source age and equipartition factor.

I find that the average energy in the lobe magnetic field is approximately a factor of 40 lower than the energy in the particles, or equivalently the lobe field strength is $B/B_{\rm eq} = 0.38$ lower than the equipartition value (significant at the 5σ level). These findings are consistent with the X-ray inverse-Compton observations of Ineson et al. (2017) with higher equipartition factors of $B/B_{\rm eq} \sim 0.4$ for a similar sample of powerful FR-II radio sources. Radio lobes comprising a pair-plasma with at most a small pressure contribution from a population of relativistic protons or heated thermal plasma (i.e. a ratio of the energy density in the non-radiating particles to that in the leptons of $w = u_{\rm t}/u_{\rm e} \lesssim 2$) are found to yield results consistent with both the X-ray inverse-Compton measurements of the equipartition factor and jet powers measurements of Ineson et al. (2017).

The parameters used in the Bayesian fitting algorithm may be further varied or optimised to explore currently poorly understood objects. The development of versatile tools for estimating source ages and jet powers is especially pertinent with the large volumes of data expected from the *Square Kilometre Array* pathfinder surveys (e.g. ASKAP EMU and MeerKAT MIGHTEE; Norris et al. 2011; Jarvis 2012). In particular, I have shown that the spectral break frequency and lobe luminosity alone can estimate jet power without the size constraint, enabling both compact and high-redshift sources to be probed.

Chapter 4

Correcting for Sensitivity Biases in Future Surveys

The active galactic nuclei (AGN) lobe radio luminosities modelled in hydrodynamical simulations and most analytical models do not address the redistribution of the electron energies due to adiabatic expansion, synchrotron radiation and inverse-Compton scattering of CMB photons. In this chapter, I present a synchrotron emissivity model for resolved sources which includes the bulk flow of lobe plasma and a full treatment of the loss mechanisms spatially across the lobe. Further, this model can be applied atop general simulated radio sources with known pressure and volume expansion rates as a function of time (such as described in Chapter 2). The inclusion of these loss mechanisms enables the limitations of future radio surveys when measuring AGN energetics to be quantified. Section 4.1 describes a generalised form of the Kaiser et al. (1997) synchrotron emission model which can be applied to radio sources with arbitrary volume and pressure evolution, whilst in Section 4.2 an extension to model the three-dimensional spatial luminosity distribution is discussed. In Section 4.3, I apply this spatial luminosity model to lobed FR-II/I sources from the dynamical model developed in Chapter 2, comparing the predicted spectral age distribution to observations. Then I develop a new model for low-powered "flaring jet" FR-I sources in Section 4.4, and investigate the potential for these FR-Is to explain the spectral features and compact nature of GPS and CSS sources. Finally, the effect of observing radio sources close to the flux detection limit in future surveys is explored in Sections 4.5.

4.1 Lobe emissivity model

Here I propose a radio source luminosity model that can be applied to any dynamical model, be it analytical or numerical. This means that the radiative losses are not taken into account self-consistently in the evolution of the lobe pressure. The assumption is valid in a situation where the radiative losses do not change the lobe pressure significantly. This is always a good assumption if the lobe pressure is dominated by non-radiating particles such as protons. However, the assumption is also reasonable for purely leptonic plasmas; given electron injection indices steeper than $s = 2$, most of the energy is contributed by the low energy electrons. I confirm the validity of neglecting radiative losses a posteriori. Note that adiabatic losses are taken into account in numerical and published analytical dynamical models.

Kaiser & Alexander (1997) and Kaiser et al. (1997) developed a model describing the temporal evolution of the powerful FR-II class of radio sources, including a full treatment of the radiative loss mechanisms for the lobe integrated luminosity. However, these models make a number of simplifications to remain analytically tractable: (1) the external density profile is approximated by a single power law with a constant exponent (inconsistent with X-ray cluster observations; Vikhlinin et al. 2006), and (2) the radio lobes are assumed to expand in a self-similar manner and in the strong shock supersonic expansion limit. In this section, I rederive their luminosity model for general radio sources which are not constrained by these restrictions.

I have eliminated many significant simplifying assumptions from previous radio source models; however some assumptions must still be made to keep the model analytically tractable including: (1) a spherically symmetric ambient medium, (2) a homogeneous magnetic field (excepting any gradients across the lobe) which contributes a constant and uniform fraction of the total internal pressure, and (3) no reacceleration of the synchrotron-emitting electrons by weak shocks or turbulence. The FR-II/I lobed dynamical model described in Chapter 2 can simulate radio AGN with each lobe expanding into different environments, and moreover the mathematical framework enables different density and temperature profiles to be assumed along every radial line from the central engine. However, without a compelling reason to choose a more complicated description in this work a spherically symmetric environment is similarly adopted. By contrast, hydrodynamical simulations must be used to understand inhomogeneities in the magnetic field (but see e.g. Hardcastle 2013) and equipartition factor (i.e. the ratio of energy densities in the field and particles). The assumption of a uniform and temporally constant fraction of total energy density in the magnetic field is verified by the three-dimensional MHD simulations of Hardcastle & Krause

(2014, their Figure 2). The turbulent nature of the flow is not expected to lead to a strong amplification of the magnetic field; it will however lead to fluctuations of the magnetic field and $\beta = 8\pi p/B^2$ of a factor of a few to ten (Gaibler et al. 2009). This leads to a corresponding lack of noise in my model on all scales. I show throughout this work that despite these shortcomings the model still captures the main features of observed sources.

4.1.1 Unresolved, continuously injected electron model

The radio luminosity can be initially calculated analytically under the assumption that only the adiabatic expansion of the lobe affects the luminosity evolution of the source. The emissivity of the lobe per unit volume can be calculated as Longair (2010)

$$J(E) = \frac{\kappa(s)\sqrt{3\pi}Be^3N(E)E}{16\pi^2\epsilon_0 cm_e(s+1)}, \tag{4.1}$$

where B is the lobe magnetic field strength at the time of observation, $N(E)dE$ is the number density with energies between E and $E+dE$, c is the speed of light, e and m_e are the electron charge and mass, ϵ_0 is the vacuum permittivity, and κ is a constant dependent solely on the injection index s through

$$\kappa(s) = \frac{\Gamma(\frac{s}{4}+\frac{19}{12})\Gamma(\frac{s}{4}-\frac{1}{12})\Gamma(\frac{s}{4}+\frac{5}{12})}{\Gamma(\frac{s}{4}+\frac{7}{12})}. \tag{4.2}$$

The energy of the electrons E emitting at the rest-frame observing frequency ν is found through the relation

$$E = \gamma m_\mathrm{e}c^2 = \left(\frac{2\pi\nu m_\mathrm{e}^3c^4}{3eB}\right)^{1/2}. \tag{4.3}$$

The lobe pressure is related to the electron energy density u_e, thermal energy density in the particles u_T and the magnetic field energy density u_B as $p = (\Gamma_\mathrm{c}-1)(u_\mathrm{e}+u_\mathrm{B}+u_\mathrm{T})$. The adiabatic index of the lobe plasma, Γ_c, is generally assumed to be non-relativistic Kaiser & Alexander (e.g. 1997) though Hardcastle & Krause (2013) propose a relativistic lobe material. If it is assumed that there is no energy in thermal particles (i.e. $u_\mathrm{T} = 0$; Kaiser et al. 1997) and we introduce q as the ratio of the energy density in the magnetic field to the sum of the energies in the particles, then the electron energy density is given by

$$u_{\rm e} = \frac{p}{(\Gamma_{\rm c}-1)(q+1)}. \tag{4.4}$$

The magnetic field strength is similarly related to the pressure as $B = \sqrt{2\mu_0 u_{\rm B}}$ for vacuum permeability μ_0, and so

$$B = \left(\frac{2\mu_0 p}{\Gamma_{\rm c}-1}\frac{q}{q+1}\right)^{1/2}. \tag{4.5}$$

Electron energy distribution

The electron energy distribution at the time of injection follows a power law with exponent s and normalisation N_0, i.e. $N(E_{\rm i}, t_{\rm i})\,dE_{\rm i} = N_0 {E_{\rm i}}^{-s} dE_{\rm i}$. In the lossless case this distribution remains unchanged through to the time of observation, i.e. $N(E)\,dE = N_0 E^{-s} dE$. The normalisation constant N_0 is calculated from the electron energy density $u_{\rm e}$ and the kinetic energy of the injected electrons $E_{\rm kin}$ (i.e. excluding their rest mass) through

$$\begin{aligned} N_0 &= u_{\rm e}(t_{\rm i}) \left(\int_{E_{\rm min}}^{E_{\rm max}} E_{\rm kin}\, {E_{\rm i}}^{-s} dE_{\rm i}\right)^{-1} \\ &= \frac{u_{\rm e}(t_{\rm i})}{(m_{\rm e}c^2)^{2-s}} \left[\frac{\gamma_{\rm min}^{2-s} - \gamma_{\rm max}^{2-s}}{s-2} - \frac{\gamma_{\rm min}^{1-s} - \gamma_{\rm max}^{1-s}}{s-1}\right]^{-1} \end{aligned} \tag{4.6}$$

where $E_{\rm min}$ and $E_{\rm max}$ are the low- and high-energy cut-offs to the injection electron energy distribution, and $\gamma_{\rm min}$ and $\gamma_{\rm max}$ are the corresponding Lorentz factors. These high- and low-energy cut-offs are for the energy distribution of the electrons once they have reached the uniform pressure lobes. However, the electron energy distribution is more readily measured in the hotspots (e.g. Godfrey et al. 2009); I therefore derive a conversion between the hotspot and lobe energy distributions. The change in the internal energy of a packet of synchrotron-emitting electrons as it expands adiabatically from the hotspot pressure to the lower pressure lobes is given by Kaiser et al. (1997, Equation 12). The adiabatic expansion work done by the fluid reduces the energy in the synchrotron-emitting electrons at the expense of increasing the volume of the electron packet. Equating this change in energy with the electron energy density in my Equation 4.6 we find the low-energy cut-off of electrons in the lobe is related to the hotspot value (subscript h) as

$$\frac{E_{\rm min}}{E_{\rm min,h}} = \frac{\gamma_{\rm min}}{\gamma_{\rm min,h}} \approx \left(\frac{p_{\rm h}(t_{\rm i})}{p(t_{\rm i})}\right)^{(1-\Gamma_{\rm c})/\Gamma_{\rm c}(s-2)} \tag{4.7}$$

Kaiser (2000) proposed an empirical relationship between the hotspot and lobe pressure based on the hydrodynamical simulations of Kaiser & Alexander (1999), $p_{\rm h}(t_{\rm i})/p(t_{\rm i}) = (2.14 - 0.52\beta)(A/2)^{2.04-0.25\beta}$, where the density profile is approximated locally as $\rho \propto r^{-\beta}$. For a typical radio source with an axis ratio of $A = 4$, initial injection index $s = 2.4$ and expanding into a gas density profile $\rho \propto r^{-1.5}$, I find the low-energy cut-off to the electron energy distribution is a factor of 2.5 lower than at the hotspot assuming $\Gamma_{\rm c} = 4/3$, and a factor of 4.3 lower for $\Gamma_{\rm c} = 5/3$.

The electron energy spectrum evolves from the moment of injection through to the time of observation as the electron population loses internal energy. The rate of change of the Lorentz factor for the electron population is given by

$$\frac{d\gamma}{dt} = \frac{a_{\rm p}}{3\Gamma_{\rm c}}\frac{\gamma}{t} - \frac{4}{3}\frac{\sigma_{\rm T}}{m_{\rm e}c}\gamma^2(u_{\rm B} + u_{\rm C}). \tag{4.8}$$

where $\sigma_{\rm T}$ is the electron scattering cross-section. The first term on the right-hand side accounts for adiabatic expansion losses of a packet of electrons which expands adiabatically as $dV_{\rm packet} \propto t^{-a_{\rm p}/\Gamma_{\rm c}}$, whilst the second term combines the loss rate from both synchrotron radiation and inverse-Compton scattering of cosmic microwave background radiation.

The distribution of electron energies at time t is given by Kaiser et al. (1997) as

$$\begin{aligned} N(\gamma, t, t_{\rm i})\, d\gamma &= N_0 \frac{{\gamma_{\rm i}}^{2-s}}{\gamma^2}\left(\frac{t}{t_{\rm i}}\right)^{4a_{\rm p}/3\Gamma_{\rm c}} d\gamma \\ &= N_0 \frac{{\gamma_{\rm i}}^{2-s}}{\gamma^2}\left(\frac{p(t)}{p(t_{\rm i})}\right)^{4/3\Gamma_{\rm c}} d\gamma. \end{aligned} \tag{4.9}$$

The second equality is added in order to model emission from lobes with arbitrary expansion rates, described by evolution of pressure $p(t)$. I generalise the analysis of Kaiser et al. (1997) to treat arbitrary lobe expansion. The injection Lorentz factor $\gamma_{\rm i}$ of electrons emitting at the observing frequency $\gamma(\nu)$ is obtained by modifying their Equation 10 to yield the following recursive relation:

$$\gamma_{\rm n} = \frac{\gamma_{\rm n-1} t_{\rm n}^{a_{\rm p}(t_{\rm n-1},t_{\rm n})/3\Gamma_{\rm c}}}{t_{\rm n-1}^{a_{\rm p}(t_{\rm n-1},t_{\rm n})/3\Gamma_{\rm c}} - a_2(t_{\rm n}, t_{\rm n-1})\gamma_{\rm n-1}}, \tag{4.10}$$

where the time at the n-th time-step $t_{\rm n}$ and the corresponding Lorentz factor $\gamma_{\rm j}$ decrease from $(t_0, \gamma_0) = (t, \gamma)$ through to $(t_{\rm N}, \gamma_{\rm N}) = (t_{\rm i}, \gamma_{\rm i})$. Electrons injected into the lobes at very early times will suffer strong losses, and as a result not appear in the observable range of Lorentz factors at time t. These electrons are determined to have infinite injection Lorentz factors using Equation 4.10 and will not contribute to the emissivity of the radio lobe. Finally, the constant $a_2(t_{\rm n}, t_{\rm n-1})$ in this equation is defined in each time-step through the relation

$$a_2(t_{\rm n},t_{\rm n-1}) = \frac{4\sigma_{\rm T}}{3m_{\rm e}c} \times \left[\frac{u_{\rm B}(t_{\rm n})}{a_3} {t_{\rm n}}^{-a_{\rm p}}({t_{\rm n-1}}^{a_3} - {t_{\rm n}}^{a_3}) + \frac{u_{\rm C}}{a_4}({t_{\rm n-1}}^{a_4} - {t_{\rm n}}^{a_4})\right], \tag{4.11}$$

where $a_3 = 1 + a_{\rm p}(1 + 1/3\Gamma_{\rm c})$, $a_4 = 1 + a_{\rm p}/3\Gamma_{\rm c}$ and $a_{\rm p}$ is the exponent with which the lobe pressure changes locally, i.e. $p \propto t^{a_{\rm p}}$. Through this method I enable $a_{\rm p}$ to be parametrised as a function of time, which allows the emissivity to be modelled for generalised environments and lobe expansion.

Lobe volume evolution

In the previous section, I derived an expression for the energy spectrum of the synchrotron-emitting electrons throughout the source lifetime which contribute to the observed radio emission. The luminosity of a lobe with constant emissivity is found using $L(\nu) = 4\pi J(\nu) V$ where V is the emitting volume of the entire lobe. In general, the emissivity depends on the electron populations which are injected at different times in the radio source evolutionary history. The lobe has very different volumes at these times and thus the volume is expressed in integral form. That is,

$$V(t) = \int_0^t \frac{dV(t_{\rm i})}{dt_{\rm i}} dt_{\rm i} = \int_0^t \frac{a_{\rm v}(t_{\rm i}) V(t_{\rm i})}{t_{\rm i}} dt_{\rm i}, \tag{4.12}$$

where the volume $V(t)$ of the entire lobe expands from some volume $V(t_{\rm i})$ when a given packet of electrons is injected. The lobe volume expands over this time as $V \propto t^{a_{\rm v}}$, where $a_{\rm v}$ can be a slowly varying function of time. The luminosity of the radio AGN lobe is then found from the emissivity and volume expressions:

$$L(\nu, t) = \int_0^t \frac{4\pi J(\nu, t, t_{\rm i}) a_{\rm v}(t_{\rm i}) V(t_{\rm i})}{t_{\rm i}} dt_{\rm i}. \tag{4.13}$$

These expressions can be rewritten solely in terms of the key parameters in the model: lobe pressure p, volume V and the equipartition factor q. That is,

$$L(\nu,t) = K(s)\nu^{(1-s)/2}\frac{q^{(s+1)/4}}{(q+1)^{(s+5)/4}} \times p(t)^{(s+5)/4}V(t)\mathcal{Y}(t), \tag{4.14}$$

where the equation for the losses over the entire radio lobe at source age t is given by

$$\mathcal{Y}(t) = \int_0^t \frac{a_{\rm v}(t_{\rm i})}{t_{\rm i}}\left[\frac{p(t_{\rm i})}{p(t)}\right]^{1-4/(3\Gamma_{\rm c})}\frac{V(t_{\rm i})}{V(t)}\left[\frac{\gamma_{\rm i}}{\gamma}\right]^{2-s} dt_{\rm i}, \tag{4.15}$$

and the radio source specific constant $K(s)$ is defined through

$$K(s) = \frac{\kappa(s)}{{m_{\rm e}}^{(s+3)/2}c(s+1)}\left[\frac{e^2\mu_0}{2(\Gamma_{\rm c}-1)}\right]^{(s+5)/4} \times \left[\frac{3}{\pi}\right]^{s/2}\left[\frac{\gamma_{\rm min}^{2-s}-\gamma_{\rm max}^{2-s}}{s-2} - \frac{\gamma_{\rm min}^{1-s}-\gamma_{\rm max}^{1-s}}{s-1}\right]^{-1}. \tag{4.16}$$

In the case of impulsive electron injection at the present time, $t_{\rm i} = t$, the integral in Equation 4.15 evaluates to unity, as expected in the case of no energy losses.

4.1.2 Modelling mock radio sources

The radio lobe luminosity model derived in the previous section can be boot-strapped atop analytical or numerical lobe dynamical models for which the pressure and volume temporal evolution is known. This process is demonstrated with a simulated radio lobe from the dynamical model developed in Chapter 2. This model fits a series of broken power laws to the pressure profile, and evaluates lobe pressure, volume and axis ratio at each time-step. Here, I further fit a broken power law time series to these model outputs, namely the volume and pressure of the lobe. Simulated lobe pressures and volumes at numerous time-steps are recorded, with select values tabulated in Table 4.1. The temporal evolution of these simulation parameters is represented by the power law exponents $a_{\rm p}$ and $a_{\rm v}$, where $p \propto t^{a_{\rm p}}$ and $V \propto t^{a_{\rm v}}$. These exponents are calculated by interpolating log-linearly at each time-step, $p(t_{\rm n+1}) = p(t_{\rm n})(t_{\rm n+1}/t_{\rm n})^{a_{\rm p}(t_{\rm n})}$ and $V(t_{\rm n+1}) = V(t_{\rm n})(t_{\rm n+1}/t_{\rm n})^{a_{\rm v}(t_{\rm n})}$. Here, the time-steps run backwards in time from the source age to the time of electron injection as for the Lorentz factor recurrence

Table 4.1: Example radio lobe kinematic data simulated using the dynamical model developed in Chapter 2. This radio lobe is simulated for an AGN with a 10^{38} W jet power in a typical environment of a low-redshift host galaxy in a 10^{14} $M_{\odot}$ dark matter halo.

t (yrs)	p (Pa)	V (kpc^3)	$a_{\rm p}$	$a_{\rm v}$
6.00	-10.18	2.45		
			-1.17	2.17
6.02	-10.20	2.50		
			-1.17	2.17
6.05	-10.23	2.55		
			...	...
...	...	...		
			...	...
8.95	-14.33	9.55		
			-1.98	2.95
8.98	-14.37	9.62		
			-1.99	2.95
9.00	-14.42	9.69		

relation in Equation 4.10, i.e. $t_0 = t$ and $t_{\rm N} = t_{\rm i}$. The Lorentz factor at the time of observation and the time of electron injection can thus be calculated. The precision of the loss mechanism integral is increased by interpolating the data points from the dynamical model enabling higher cadence sampling in injection time.

4.1.3 Evolutionary tracks

Radiative loss mechanisms, including adiabatic, synchrotron and inverse-Compton, can change the jet power–luminosity relation by over an order of magnitude as a radio source ages (Kaiser et al. 1997; Blundell et al. 1999; Manolakou & Kirk 2002; Shabala & Godfrey 2013). Kaiser et al. (1997) proposed a method for simulating the losses in self-similar FR-II radio lobes expanding into environments modelled by a single power law density profile. At the other extreme, hydrodynamical simulations can only consider losses by tracing the histories of each electron in the lobe, leading to very long computation times. Here I discuss the importance of properly describing the loss processes throughout the entire radio lobe. In my prescription both the density and temperature profiles can vary with radius in an arbitrary manner, and differ for each radio lobe. This enables observed environments of a real source or any an arbitrary environments to be used as the basis for the radio source dynamics.

The differences in the evolutionary tracks modelled using either the simple Kaiser et al. (1997) environments and a more realistic environment allowed by my model are shown in Figure 4.1. The single power law assumption leads to a power law fall-off in luminosity for the lossless case and when including losses due to the adiabatic expan-

sion of the self-similar lobe. Losses due to synchrotron radiation preferentially reduce the luminosity at early times whilst losses due to the inverse-Compton scattering of cosmic microwave background radiation are only noticeable after $\sim 100\,\mathrm{Myrs}$. By contrast, fitting a declining density profile to the host sub-halo environment yields significant curvature in the lossless luminosity with values two-orders of magnitude lower in the core regions. The adiabatic losses no longer yield a constant difference in luminosity either since the dynamical model does not assume self-similar expansion.

These results show the importance of correctly modelling the host environment through use of a detailed hydrodynamical simulation or dynamical model. Further, the difference in luminosity between the lossless case and full-loss case varies by between a factor of three and ten for this mock radio source. The full modelling of both the host environment and the loss mechanisms in the calculation of the lobe luminosity is therefore vital to understanding the properties of radio AGN.

4.2 Spatially resolved lobe losses

The method described thus far for calculating the lobe luminosity implicitly assumes synchrotron emitting electrons are uniformly injected at locations throughout the entire lobe volume. An alternative interpretation is that the model assumes the radio source is unresolved and these injection locations cannot be determined. Either way, when considering the emission from a resolved source, in which all[1] electrons are accelerated at a compact hotspot in FR-IIs or flare point in FR-Is, a different approach must be taken.

4.2.1 Spatially distributed and impulsively injected electron model

The different injection locations and pressure distributions seen in type I and II radio sources lead to different evolution of their electron populations. The volume and pressure evolution used for the electron populations in lobed FR-II radio sources continues to be described by the large-scale dynamics of the lobe. This assumption is valid because the high sound speed in the lobe brings the entire lobe into approximate pressure equilibrium (corrections can be applied for the higher pressure expected at the hotspot; Kaiser & Alexander 1999). The volume initially occupied by each injection of electrons should similarly increase in proportion to volume of the entire lobe.

[1]Shocks throughout the radio lobe may re-accelerate electrons back up to higher energies, however this is assumed to have only a minor effect on the electron energy distribution. This is especially true for the subsonic flow of plasma beyond the flare point in FR-Is .

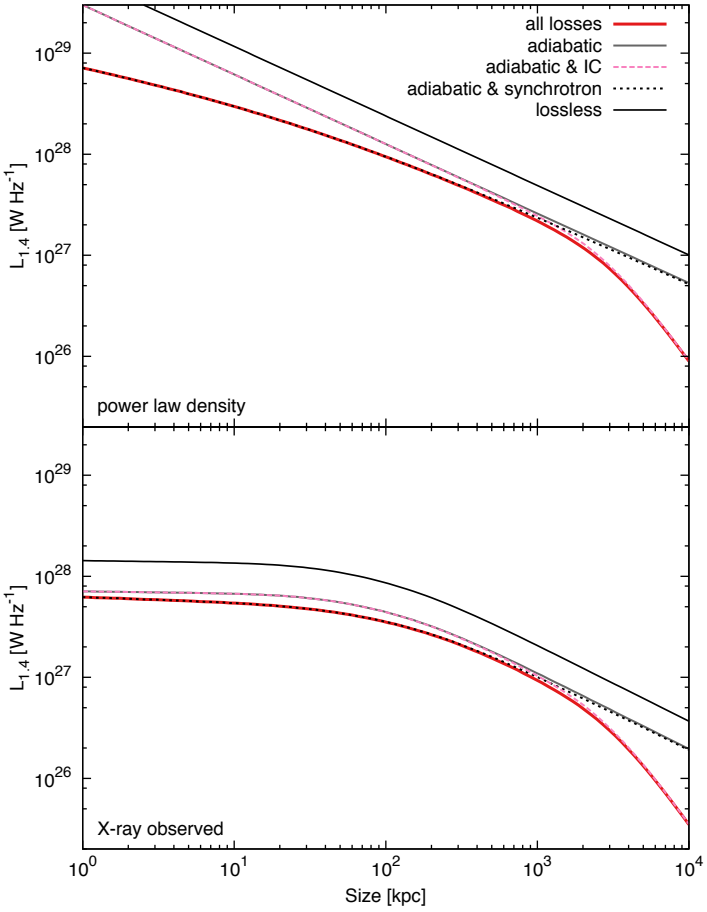

Figure 4.1: Top panel – Luminosity-size tracks for a 1.3×10^{39} W jet power radio source at $z = 0.5$, expanding into an environment with density $\rho = 7.2 \times 10^{-22}\,\mathrm{kg\,m^{-3}}$ at a radius of 2 kpc falling off with a power law profile with constant exponent $\beta = 1.9$. Five profiles are plotted, showing the luminosity for the lossless case, with only adiabatic losses, with adiabatic and inverse-Compton losses, with adiabatic and synchrotron losses, and with all loss mechanisms. Bottom panel – Same as top panel but for an environment based on X-ray cluster observations with the same sub-halo mass and virial radius as simulated for the power law density profile.

The situation is different for the smoke-like plumes of plasma seen in "flaring jet" FR-Is, which are in approximate pressure equilibrium with their surroundings and slowly coast down the declining pressure gradient beyond the flaring point. The pressure and volume occupied by an electron packet at this acceleration site remains constant throughout the source lifetime. The subsequent evolution can be characterised using an FR-I dynamical model (see Section 4.4; Luo & Sadler 2010).

In the following, I assume that the losses at a given location in the lobe result from electrons all accelerated at the same time. These synchrotron-emitting electrons traverse the distance from the site of particle acceleration to their present time location as part of the large scale motions of plasma in the lobe (e.g. backflow from the hotspot for FR-II sources, or forward flow from the flare point for twin-jet FR-I sources). The emission at individual locations in the lobe now arises solely from a single injection time. The volume occupied at the present-time by an electron packet injected between t_i and $t_\mathrm{i} + dt_\mathrm{i}$ is given by

$$dV(t, \mathbf{r}) = \int_0^t \delta(t'_\mathrm{i} - t_\mathrm{i}(\mathbf{r})) \frac{dV(t'_\mathrm{i})}{dt'_\mathrm{i}} dt'_\mathrm{i}, \tag{4.17}$$

where $\mathbf{r}$ is the radial position vector of the present-time electron emission region from the acceleration site. For lobed FR-II type radio sources the differential volume element of the plasma comprising electrons of the age at position $\mathbf{r}$ can be written more neatly as

$$dV(t, \mathbf{r}) = \frac{a_\mathrm{v}(t_\mathrm{i}(\mathbf{r}))V(t_\mathrm{i}(\mathbf{r}))}{t_\mathrm{i}(\mathbf{r})} dt_\mathrm{i}. \tag{4.18}$$

This form enables the integrated luminosity to be easily calculated using numerical integration.

By contrast, in low-powered flaring jet FR-I sources the flare point acceleration site is stationary and unchanging in pressure throughout the source lifetime (flaring jet dynamics discussed in Section 4.4). The volume of the injected electron packets at the time of acceleration is thus constant; i.e. $V(t_\mathrm{i}(\mathbf{r})) = V_\mathrm{i}$ and hence $dV_\mathrm{i}/dt_\mathrm{i} = 0$, where the volume V_i is related to the size of the flare point. The synchrotron-emitting electrons propagate outwards from the flaring point towards the maximal extent of the radio plume reaching their present-time location $\mathbf{r}$ in time $t_\mathrm{e}(\mathbf{r}) = t - t_\mathrm{i}(\mathbf{r})$. The volume integral in Equation 4.17 is therefore recast in terms of this electron travel time t_e for low-powered sources.

The luminosity of the lobe section at radial position $\mathbf{r}$ is now given by

$$dL(\nu, t, \mathbf{r}) = 4\pi J(\nu, t, t_{\rm i}(\mathbf{r}))dV(t, \mathbf{r}). \tag{4.19}$$

Then as for the unresolved radio lobe, upon substituting in the expressions for the lobe volume and emissivity we obtain

$$\begin{aligned} dL(\nu, t, \mathbf{r}) = K(s)\nu^{(1-s)/2}\frac{q^{(s+1)/4}}{(q+1)^{(s+5)/4}}dV(t, \mathbf{r}) \\ \times\, p(t, \mathbf{r})^{(s+5)/4}\left[\frac{p(t_{\rm i}(\mathbf{r}))}{p(t, \mathbf{r})}\right]^{1-4/(3\Gamma_{\rm c})}\left[\frac{\gamma_{\rm i}(\mathbf{r})}{\gamma}\right]^{2-s}, \end{aligned} \tag{4.20}$$

where in lobed FR-IIs, $p(t, \mathbf{r})$ and $p(t_{\rm i}(\mathbf{r}))$ are the modelled lobe pressure at the present-time and the time of electron injection respectively. Low-powered flaring jet radio sources, which do not have constant pressure lobes, instead take $p(t_{\rm i}(\mathbf{r}))$ as the flare point pressure and $p(t, \mathbf{r})$ as the pressure of an electron packet which has propagated for time $t_{\rm e}(\mathbf{r})$ along the plume. This equation can also be applied to the local variations in the pressure of powerful FR-IIs predicted by hydrodynamical simulations.

4.2.2 Temporal evolution of synchrotron-emitting electrons

The entire lobe radio luminosity is reduced at higher frequencies due to the power-law fall-off in the energy of the electron population, i.e. $L_\nu \propto \nu^{(1-s)/2}$ for $s \sim$ 2-3. The frequency-dependent nature of the loss mechanisms implicitly included in Equation 4.20 further reduces the intensity of emission at higher frequencies as the synchrotron-emitting electrons age. This can be demonstrated by combining Equations 4.9 and 4.10 for the number of synchrotron-emitting electrons injected at some time $t_{\rm i}$ which are emitting at frequency $\nu \propto \gamma^2$ at the time of observation t. That is,

$$N(\nu, t, t_{\rm i})\, d\nu = N_1(t^{-a_{\rm v}/3} - a_2(t, t_{\rm i})k_1\nu^{1/2})^{s-2}\, d\nu, \tag{4.21}$$

where N_1 is some arbitrary constant of proportionality and k_1 is defined such that $\gamma = k_1\nu^2$ (see Equation 4.3). The function $a_2(t, t_{\rm i})$ derived by Kaiser et al. (1997) is not a function of frequency, and increases as $t_{\rm i}/t$ gets very small. The number density of synchrotron-emitting electrons emitting at the present time at a given frequency may therefore reduce to zero for suitably small $t_{\rm i}/t$, i.e. $a_2(t, t_{\rm i}) \geqslant t^{-a_{\rm v}/3}/(k_1\nu^{1/2})$. That is, there is a cut-off injection age below which synchrotron-emitting electrons cannot

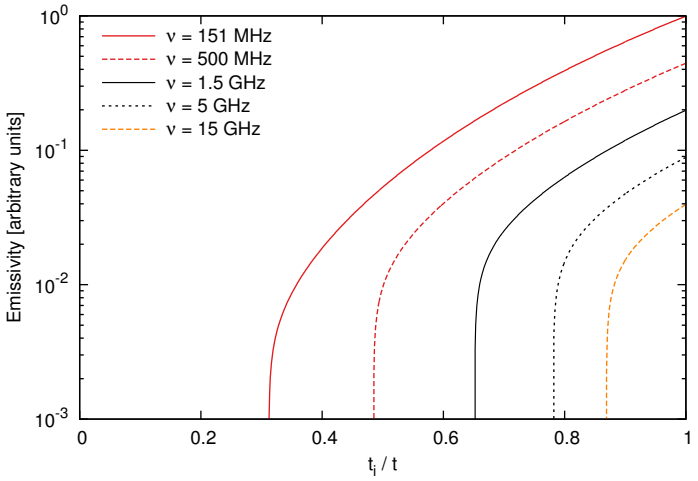

Figure 4.2: Synchrotron-emitting electrons emissivity as a function of the electron injection time (for a typical 100 Myr source at $z = 0.5$; refer to Figure 4.1) for five typical observing frequencies of 151 MHz, 500 MHz, 1.5 GHz, 5 GHz and 15 GHz. Electrons injected at younger than approximately half the source age for this example source emit no radiation at the time of observation.

emit at a given rest frequency at the present time. Moreover, this cut-off injection age is expected to be a strong increasing function of frequency, i.e. $t_{\mathrm{i\,cut}} = f(\nu^{1/2})$.

The loss function for a typical radio source is shown in Figure 4.2 for five standard observing frequencies. The spacing of the emissivity curves for each frequency at the present time $t_{\mathrm{i}}/t = 1$ is set by $S \propto \nu^{(1-s)/2}$. The loss mechanisms preferentially reduce the emissivity for the oldest synchrotron-emitting electrons at higher frequencies first; the cut-off injection age is greater for the higher frequencies as discussed above. The losses due to the inverse-Compton upscattering of CMB photons are a strong function of both the age of synchrotron-emitting electrons and the source redshift. The cut-off injection ages shown in Figure 4.2 are therefore likely to vary greatly for different sources; I investigate this effect in later sections. At high frequencies, the observed size of the emitting region may appear much smaller than the physical size, due to low number densities (and hence surface brightness) of old, high-energy electrons at large distances from the site of particle acceleration. The spatial distribution of the injected synchrotron-emitting electrons must therefore be considered to understand the emission from resolved radio sources.

4.2.3 Spatial distribution of electron ages

The synchrotron age distribution throughout radio AGN lobes is likely a complicated function of position, however spectral ageing does identify a general linear increase in age away from the hotspots of FR-II class sources (e.g. Jamrozy et al. 2008; Harwood et al. 2013). This increase in synchrotron age arises due to a backflow of plasma carrying freshly injected electrons away from the hotspot towards the AGN core in FR-IIs. In unconfined FR-Is, a similar role is played by forward flow from outflowing jets. These observations, although informative, can only estimate the average electron age in a three-dimensional slice along the line-of-sight. Hydrodynamical simulations or some other physically based argument are required to properly characterise the spatial distribution of synchrotron-emitting electrons. In this work, I assume the synchrotron age increases with radial distance from the injection site at some speed $b(\mathbf{r}) + db(\mathbf{r})$, guided by hydrodynamical simulations for FR-IIs and analytic theory for FR-Is. Typical values for this flow rate estimated using spectral ageing lie somewhere in the range $b = 0.01\text{-}0.1\,\mathrm{pc/yr}$ (Jamrozy et al. 2008).

4.3 Powerful radio galaxies

The spatial distribution of energy losses in the synchrotron-emitting electron population is typically not considered in analytical models (e.g. Kaiser et al. 1997) and hydrodynamic simulations (e.g. Hardcastle & Krause 2013, 2014; but see e.g. Jones et al. 1999). This, in turn, leads to oversimplified predictions for the spatial distribution of radio continuum emissivity. The framework derived in Section 4.2 is employed in this section using the output from the lobed FR-I/II dynamical model developed in Chapter 2 for sources with initially collimated jets. The spatial distribution of the synchrotron-emitting electrons in FR-II type sources after they are injected into the lobe near the jet terminal shock depends entirely on the fluid motions in the lobe plasma. The emission from freshly injected electrons is much greater than that from the older population leading to a different normalisation and spectra of radio continuum emissivity in different parts of the lobes. The hydrodynamics of typical radio lobes is simulated in this section in order to quantify the spatial distribution of synchrotron-emitting electrons ages.

Table 4.2: Hydrodynamical simulations run in this work using the PLUTO code. The reliability of the results from the main simulation Base are tested for changes to the Mach number (column 2), jet-environment density ratio (column 3), the profile assumed for the host gas density (column 5), and the resolution (column 6). The ages to which the radio lobe is simulated are also included (column 4).

Simulation	$\mathcal{M}$	A_ρ	Age (sim. unit)	Profile	Resolution (cells, $r_{\rm cyl} \times z$)
Base	100	0.01	8, 9, 10	flat	750×1800
Jet Power	50	0.01	8, 9, 10	flat	750×1800
Axis Ratio	100	0.001	8, 9, 10	flat	750×1800
Density	100	0.01	10	$\rho = 1/r$	750×1800
Resolution	100	0.01	10	flat	1500×3600

4.3.1 Hydrodynamical simulations

The hydrodynamical simulations in this work use the freely available PLUTO[2] code, version 4.2, described by Mignone et al. (2007). The radio lobes are modelled in two-dimensional cylindrical coordinates to ensure an ample number of cells along the length of the jet, and in particular at dynamically complex regions such as the working surface. Modelling of the lobe using cylindrical coordinates in the PLUTO code ensures the correct three-dimensional spatial dependency of physical parameters as the fluid from the jet terminal shock disperses along the lobe. Krause & Camenzind (2001) find a resolution of greater than approximately 50 pixels across the jet width yields internal energies, axial momentum, mass and average bow shock velocities within 5% of the convergent true value. This study was performed in two-dimensions with the PLUTO code. The simulations in this work will therefore use either a low-resolution grid of 750×1800 with 60 pixels across the jet for the sensitivity analyses, or a high-resolution map with 1500×3600 and 120 pixels across the jet for the final analysis. The jets of powerful FR-II radio sources are assumed to quickly collimate; a constant width jet is therefore injected into the simulation grid to reduce computation time.

4.3.2 Tracing the rate of backflow

The spatial distribution of synchrotron-emitting electrons throughout the radio lobe is simulated by injecting tracer fields into the jet (and thus lobe) at regular intervals and tracking their motion. The location of these tracer fields within the lobe at any given radio source age is used to calculate the contribution to the emission in any region from the various age electrons. Tracer fields are injected every 0.2 simulation units up to the source age of $t = 10$ simulation units. The use of the hydrodynamical simulations is maximised by examining the distribution of the tracer field at source ages of $t = 8$, 9 and 10 simulation units. Hydrodynamical simulations are run for three high-powered radio sources using the low-resolution grid, with the key parameters varied between runs. The external Mach number of the jet (jet velocity / ambient sound speed) $\mathcal{M}$, which is directly related to the jet power, is simulated for a base case of $\mathcal{M} = 100$ and varied to a lower $\mathcal{M} = 50$. The ratio of the density in the jet and ambient medium, related to the lobe axis ratio, is simulated for $A_\rho = 0.01$ and 0.001, as listed in Table 4.2. The single high-resolution grid is used to confirm the stability of these results. Note that the non-dimensionalised parameters in these simulations can be scaled (one-to-many) into equivalent physical properties following the method of Krause et al. (2012). A further simulation was run with a non-constant slope density profile to confirm the backflow of plasma within the high sound speed radio lobe is unaffected by environment as theoretically expected.

The backflow of lobe plasma simulated using PLUTO for the BASE case is plotted in Figure 4.3. The fluid injected at the jet terminal hotspot initially flows smoothly back towards the core, but the flow becomes more turbulent after travelling back less than half of the lobe length. The tracers become somewhat dispersed thereafter, though their progression along the length of the lobe is still apparent. The average location of the tracer field is plotted in the top half of the figure. This shows an initially rapid progression towards the core before the tracer accumulates at approximately one-fifth the lobe length (from the core). The tracer of course spreads out well beyond this mean position; the distribution of the tracer to the 2σ noise level is therefore taken when modelling the spatial distribution of the synchrotron-emitting electrons.

The injection age for the synchrotron-emitting electrons is taken as the time they begin to spread radially, which I have confirmed visually coincides with passing through the terminal shock of the jet. The spread of synchrotron-emitting electrons of each injection age is calculated along a radial axis extending outwards from the hotspot injection site, i.e. we are only concerned with travel time from the hotspot. The

[2] `http://plutocode.ph.unito.it/`

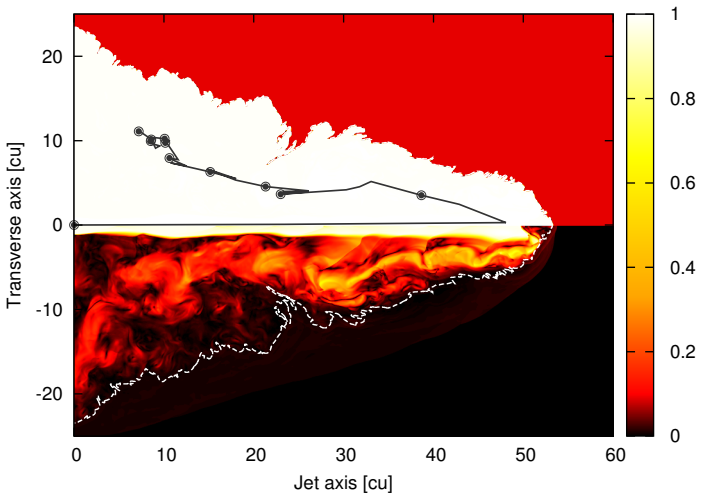

Figure 4.3: Hydrodynamical simulation (Base run) of backflow of packets of synchrotron emitting electrons from the hotspot injection site towards the core. The bottom half of the plot shows the magnitude of the velocity of the lobe plasma as it travels both along the jet with velocity scaled to unity, then back towards the core once injected into the lobe. The white dashed line marks the contact discontinuity between the lobe plasma and the shocked ISM. The solid black line in the top half of the plot shows the average location of the tracer fields injected at the current source age (point at start of jet) through to the packet injected at the instantiation of the source. The points are spaced along the average backflow path every one-tenth of the source age of $t = 10$ simulation units.

spatial distribution of the various age electrons along the axis is plotted in Figure 4.4 for each of the three low-resolution simulations at $t = 8$, 9 and 10 simulation units. The radial axis is scaled to the total lobe length (i.e. the length of the lobe is one in simulation units) and the age of the electrons is scaled to the source age (i.e. freshly injected electrons have zero age, the oldest electrons have age unity). The fits to the mean location of the tracer are consistent for each simulation (solid red points) suggesting these results are scalable to any high-powered FR-II radio source. Similarly the plotted 1σ spread in the tracer is comparable for each simulation. Importantly, this figure shows that the bulk of freshly injected electrons emit close to the hotspot, and thus much of the lobe may not be visible in sources where the loss mechanisms prevail.

The average location of the electron packets as a function of synchrotron age is determined from these simulations by fitting a fourth order polynomial to the data. The spread is similarly characterised by fitting a fourth order polynomial to the distribution of the standard deviations. These two fits are:

$$\tilde{\mathbf{r}}(\tau) = 3.5\tau - 6.6\tau^2 + 6.4\tau^3 - 2.4\tau^4 \quad (4.22a)$$

$$d\tilde{\mathbf{r}}(\tau) = 0.1 + 1.6\tau - 4.2\tau^2 + 4.3\tau^3 - 1.6\tau^4, \quad (4.22b)$$

where the non-dimensionalised synchrotron age and radial vector are $\tau = 1 - t_\mathrm{i}/t$ and $\tilde{\mathbf{r}}$ respectively. For a typical source age of 10 Myrs and distance from the hotspot injection site of 10 kpc this yields a backflow velocity of approximately 0.02c (c.f. Alexander & Leahy 1987) until the electrons begin to accumulate near the core. This relation is applied in the spatially resolved loss model of Section 4.2 to more realistically estimate the multi-frequency emissivity of spatially resolved radio sources.

4.3.3 Three-dimensional emissivity distribution

The prescription for calculating the three-dimensional emissivity distribution of arbitrarily shaped radio lobes was detailed in Section 4.2. The shape of the lobe occupied by synchrotron emitting plasma is modelled using the outputs of my dynamical model developed in Chapter 2. In this work, this model is only used to represent powerful FR-II sources whose jets extend to a terminal hotspot at the end of the radio lobe[3].

[3]This model can produce radio sources with jets that are disrupted before reaching the end of the lobe, however I do not explore the effect of these different electron injection locations at this time.

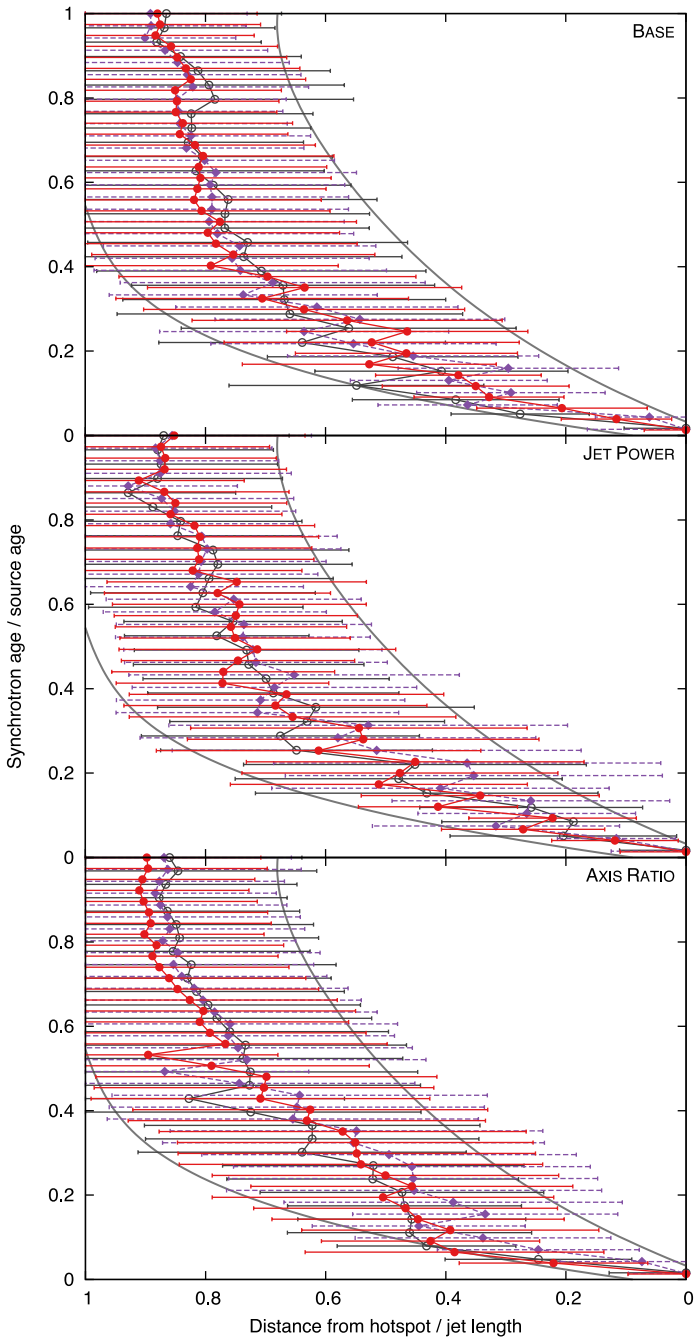

Figure 4.4: Age of synchrotron-emitting electrons as a function of distance from the hotspot injection site for the three low-resolution simulations (as indicated in panels). The points show the mean position of the tracer field for a packet of injected electrons at times $t = 8$ in grey (open circles), $t = 9$ in purple (triangles), and $t = 10$ simulation units in red (filled circles). The error bars show the 1σ spread in the tracer field along the radial vector $\mathbf{r}$. Polynomial fits to the 1σ spread in the tracer field are plotted with solid grey lines, showing that the bulk of freshly injected electrons emit close to the hotspot.

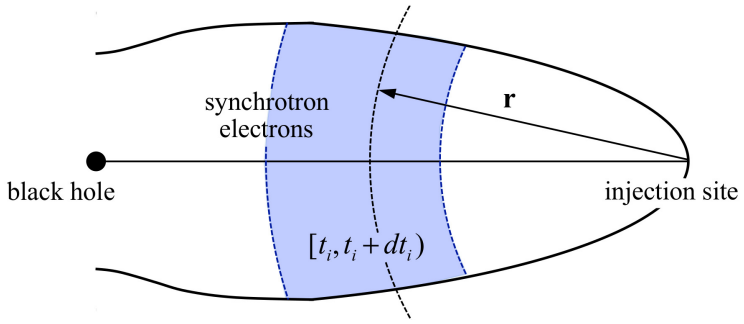

Figure 4.5: Schematic of method used to apply spatial loss model to the output of the FR-I/II dynamical model. At the time-step of interest the spatial distribution of the synchrotron-emitting electrons is calculated, e.g. the blue shading shows the spread of electrons injected at times $[t_\mathrm{i}, t_\mathrm{i} + dt_\mathrm{i})$. The spread of these electrons and their emissivity are both calculated in terms of the radial position vector $\mathbf{r}$.

The origin of the radial vector $\mathbf{r}$ is therefore positioned along the jet axis at the maximal extent of each lobe in my simulated radio sources, as shown in Figure 4.5. The spatial loss model requires knowledge of only the evolutionary history of the spatial pressure distribution and the volume of the lobe as a whole. The pressure of high-powered FR-IIs is approximately constant across the lobe at any given time due to the high internal sound speed, and an average lobe value can thus be assumed. The final location of the synchrotron-emitting electrons is therefore unimportant to the calculation of the emissivity from a given age electron packet, only the effect they have on the emissivity distribution of the resolved lobe. The contribution to the total lobe emissivity from synchrotron-emitting electrons in each injection age range $[t_\mathrm{i}, t_\mathrm{i} + dt_\mathrm{i})$ can therefore be calculated using Equations 4.18 and 4.20, based on the lobe pressure and volume taken from my dynamical model.

The location of a given age packet of electrons within an FR-II radio source is determined from: (1) their location within the non-dimensionalised lobe modelled using hydrodynamical simulations, and (2) scaled to the physical size and age of the radio lobe using my dynamical model. The radio source emissivity is visualised by constructing a three-dimensional grid of pixels. Any pixels determined to lie outside the lobe defined at any given time-step by my dynamical model are flagged and excluded from the emissivity calculation. The synchrotron-emitting electrons of each age are distributed through the lobe grid following a Gaussian profile described by the mean radius and standard deviation fitted by Equation 4.22. This Gaussian distribution is truncated at the 2σ level. The synchrotron emissivity arising from a given pixel is then calculated by summing the contribution from every age electron packet allocated

to that cell.

The analytic resolved emissivity model derived here can be boot-strapped atop the output of detailed hydrodynamical simulations of the radio lobe. These models typically use a lossless model for the synchrotron luminosity radiating from each volume element in their simulation space. The pressure in each element may differ greatly under this full numerical treatment unlike that in my analytical model (Chapter 2) which assumes constant lobe pressure. Applying the spatially resolved loss model (Section 4.2) to such simulations therefore combines the most realistic type of luminosity model with the most detailed, albeit very computationally intensive, dynamical models. This application of the luminosity model is not pursued in this paper.

4.3.4 Two-dimensional emissivity

The observed surface brightness distribution from real sources is the integral of the luminosity from all volume elements along a given line-of-sight. The two-dimensional brightness distribution is calculated by simply summing the contribution from every cell along the depth of the source, assuming the low density lobe plasma is optically thin (Peterson 1997). In this work, for simplicity I assume that the radio lobes are viewed perpendicular to the axis of the jets. The surface brightness distribution can easily be determined for other viewing angles by rotating the line-of-sight through the three-dimensional grid, however the Doppler boosted jet emission will begin to dominate as the jet axis approaches the line-of-sight.

The emissivity distribution modelled for a typical FR-II is shown in Figure 4.6 at three standard observing frequencies. The integrated lobe radio luminosity is lower at higher frequencies due to the power law fall-off in the number counts of high-energy electrons. The frequency dependent nature of the loss mechanisms also reduces the timescales over which electrons emit detectable radiation at a given frequency. The size of the emitting region of the radio lobe therefore decreases with increased observing frequency, in addition to the overall reduction in lobe luminosity. Moreover, for an ellipsoidal radio lobe as assumed in Chapter 2, the observed axis ratio will appear to be greater at higher frequencies due to the lack of emission at the wider, older parts of the lobe near the nucleus.

The maximal extent of injected electrons producing any synchrotron emission at the time of observation is investigated in Figure 4.7. The 2σ spread in the radial location of the synchrotron emitting electrons is used to determine the maximum distance from the hotspot injection site that any emission is physically present. In reality such

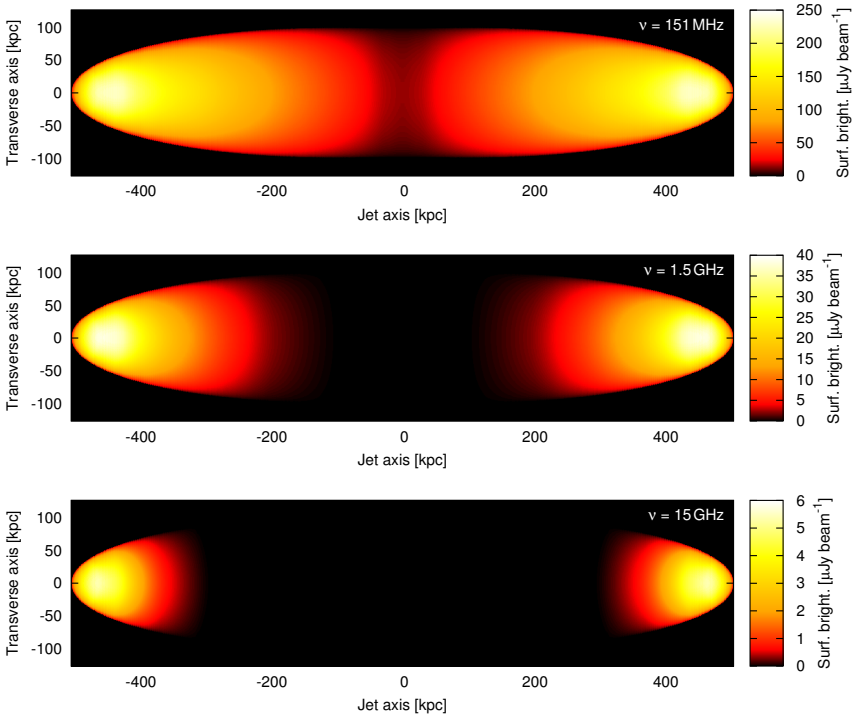

Figure 4.6: Radio source emissivity as a function of lobe position including all loss mechanisms for three typical observing frequencies. The surface brightness is calculated assuming a $1\,\mathrm{arcsec}^2(\lambda/\lambda_{1.5\,\mathrm{GHz}})^2$ beam. The top plot shows 151 MHz radio emission, the middle plot is for 1.5 GHz, and the bottom plot shows 15 GHz emission. The modelled source has a jet power of $Q = 10^{40}\,\mathrm{W}$, age of $t = 100\,\mathrm{Myrs}$, inhabits a $10^{14}\,\mathrm{M}_\odot$ halo mass environment at $z = 1$, expands with an initial axis ratio of $A = 4$ and has an electron energy injection index of $s = 2.4$.

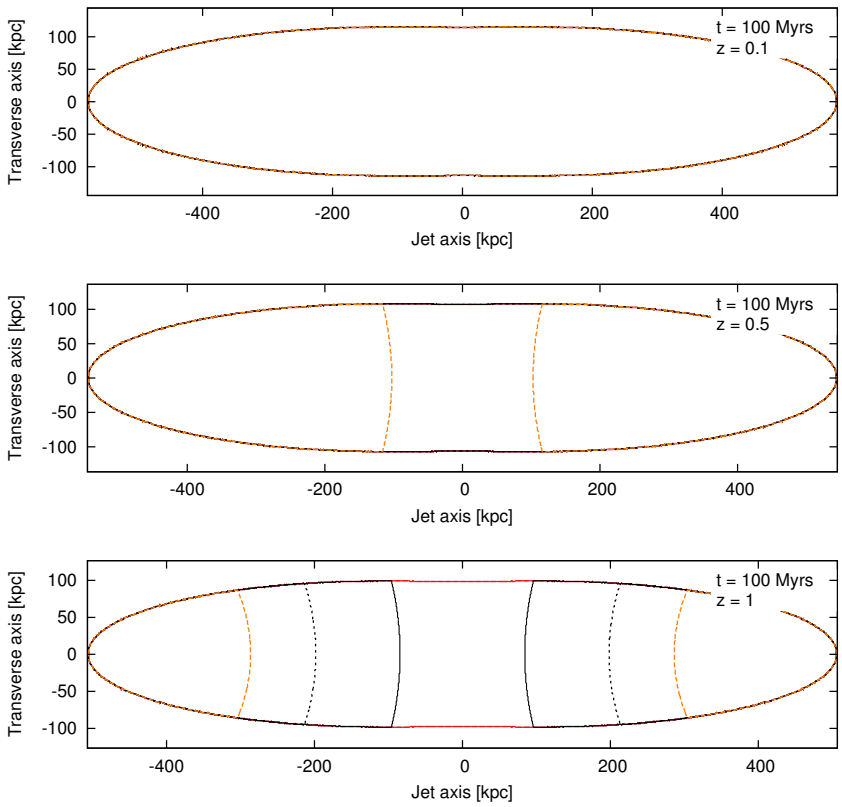

Figure 4.7: Emitting region (i.e. theoretical limit of non-zero emission at observing frequency) of radio source lobes as a function of observing frequency; the lobes are shown expanding such that the jet axis is normal to the line-of-sight. The emitting regions are shown at 151 MHz (solid red), 500 MHz (dashed red), 1.5 GHz (solid grey), 5 GHz (dashed grey) and 15 GHz (dashed orange) in each plot. The modelled source has a jet power of $Q = 10^{40}$ W, age 100 Myrs, inhabits a 10^{14} $M_{\odot}$ halo mass environment, expands with an initial axis ratio of $A = 4$ and has an electron energy injection index of $s = 2.4$. This radio source is viewed at three redshifts: $z = 0.1$ (top), $z = 0.5$ (middle) and $z = 1$ (bottom).

emission will be so weak that the detected radio emissivity will be confined much closer to the hotspot. This analysis places an upper limit on the size of the observable lobe emission region. The plots in Figure 4.7 show this upper limit for the lobe emission at five observing frequencies, for the high-powered source shown in Figure 4.6 viewed at redshifts $z = 0.1$, 0.5 and 1. The size of the emission region reduces with both increasing redshift and source age (not shown in figure) due primarily to the inverse-Compton loss mechanism.

4.3.5 Spatial radio SED analysis

The resolved emissivity model (Section 4.2) can be used to calculate the emissivity in the lobe as a function of frequency and position; the spectral energy distribution (SED) can thus be derived at any location in the lobe. The two-dimensional distribution of spectral ages observed in resolved radio sources can be simulated by fitting an appropriate spectral model to the radio SED in small cells across the mock radio lobe. Spectral age measurements (e.g. Jamrozy et al. 2008; Harwood et al. 2013) are typically made using an impulsive injection model. The electrons in each cell (or slice) of the lobe are assumed to be injected at approximately the same time, though in reality likely cover a range in electron ages (see Figure 4.4). Regardless, in this analysis an impulsive injection model will be used to enable direct comparison with existing observations. The radio SED must therefore be fitted using either the Jaffe-Perola (JP; Jaffe & Perola 1973) or Kardashev-Pacholczyk (KP; Kardashev 1962) models. These models both assume that the entire electron population is accelerated at time $t = 0$ then undergoes radiative losses thereafter. The validity of using these impulsive injection models on the well-mixed lobes of FR-IIs can be tested by comparing their spectral age estimates to the source dynamical age.

The lobed FR-II/I dynamical model and the new resolved emissivity model are tested using the spectral ages measured for real sources. In particular, I reproduce the spectral age distribution of 3C436 observed by Harwood et al. (2013). The intrinsic properties of 3C436 are fitted using the Bayesian algorithm described in Chapter 3 based upon multi-frequency luminosity observations (Laing & Peacock 1980) with the lobe size and axis ratio taken from the 8.4 GHz FITS file (Hardcastle et al. 1997). The host environment of 3C436 is modelled here using semi-analytic galaxy evolution (SAGE Croton et al. 2006) models informed by the host stellar mass ($M_\star = 10^{11.8}\,\mathrm{M}_\odot$). I obtain a jet power of $10^{39}\,\mathrm{W}$, source age of 37 Myrs and an equipartition factor of $B/B_{\mathrm{eq}} = 0.28$. The observed spectral ages are recalculated assuming the dynamical model magnetic field strength to enable a more direct comparison between the

electron flow predicted by my model and that of real sources. The spectral age is directly proportional to the magnetic field strength and break frequency; differences between the spectral age distributions must therefore be due to: (1) inhomogeneities in the magnetic field, (2) the reacceleration of synchrotron-emitting electrons, or (3) discrepancies in the electron flow model.

The multi-frequency surface brightness of 3C436 is calculated using the resolved emissivity model for the best fit jet power, source age and magnetic field strength. The radio SED arising from the synchrotron-emitting electrons at a given distance from the hotspot is fitted using the JP model. The spectral curvature of the emission arising from different aged regions of the lobes can therefore be quantified using the break frequency. The spectral age of the electrons at a given location is then calculated based on the field strength of the lobe using Equation 3.6 in Chapter 3. The spectral age distribution derived for 3C436 using the spatial emissivity model is shown in the centre panel of Figure 4.8. The measured ages (Harwood et al. 2013) are shown in the top panel and are corrected for the equipartition factor fitted using the Bayesian algorithm; the original ages of Harwood et al. (2013) were calculated assuming an equipartition magnetic field. Finally, the bottom panel of Figure 4.8 plots the absolute difference between the measured and modelled ages, showing there is at most a 2 Myr difference across the radio lobe, except for some few more isolated regions along the source edge which are likely not as well-mixed as predicted by my analytic model. This discrepancy may in part be due to edge effects in combining the observed maps at different spatial resolutions.

The modelled and observed spectral age distributions are further compared in Figure 4.9. The spectral age is measured along the jet axis to enable a more direct comparison; the jet axis is defined as the space curve which passes through the central engine and elsewhere is centred on the circular cross-section. The modelled spectral age along the centre of the lobes shows an approximately linear increase in age away from the hotspot consistent with the observations of Harwood et al. (2013). The modelled spectral ages agree with observations along the entire length of the jet. Both the observed and modelled spectral ages are only a small fraction of the source dynamical age close to the hotspots, but increase up to approximately one-third the fitted dynamical age near the core. The general agreement between the two spectral age distributions suggests that our electron flow model is a reasonable approximation to the physical situation, and that neither inhomogeneities in the magnetic field nor the reacceleration of electrons are particularly important. Further investigation of these processes is deferred to future work.

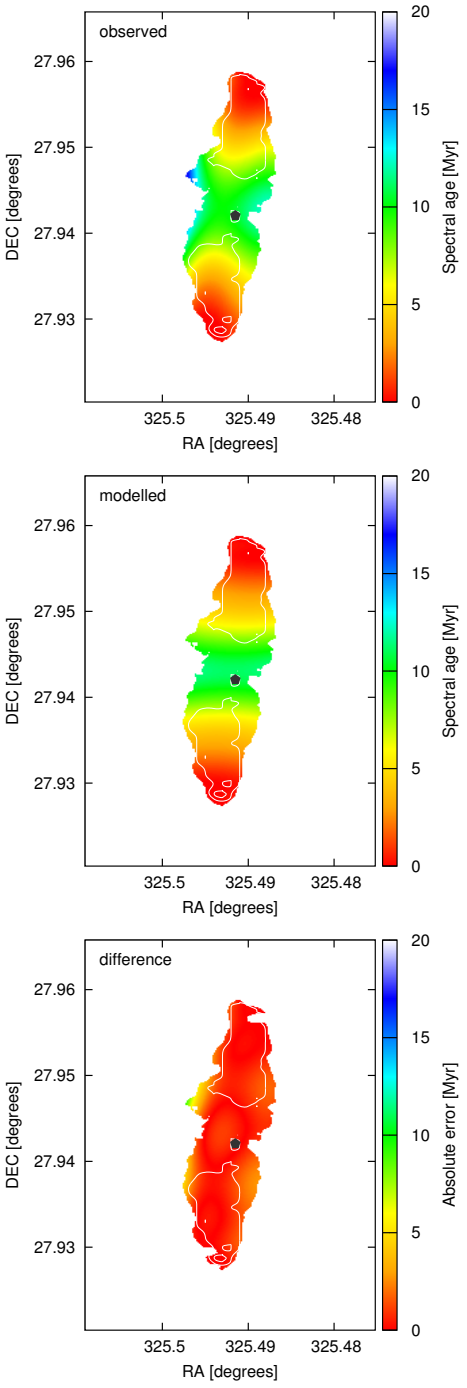

Figure 4.8: Modelled spectral age distribution (middle) for the lobes of 3C436 calculated using the lobed FR-II/I dynamical model and resolved emissivity model; the size, axis ratio and total luminosity is constrained by observations (top). The absolute error between the modelled and measured spectral age distribution is shown in the bottom plot using the same colour scheme. Overlaid on each plot are 8.4 GHz radio contours showing that the older regions are also the faintest.

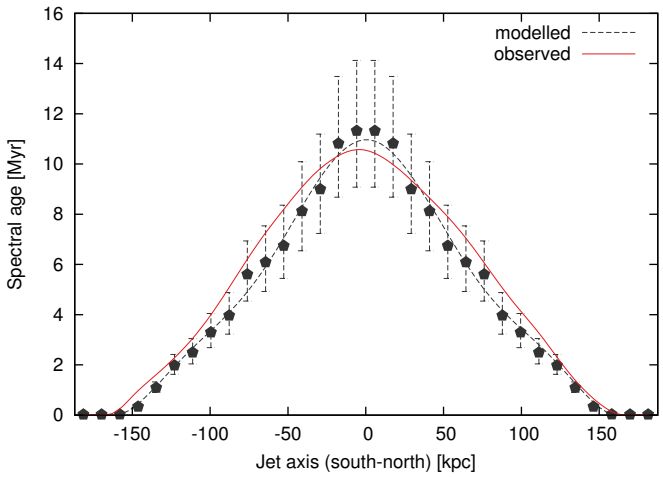

Figure 4.9: Modelled (dashed black) and measured (solid red) spectral age along the jet axis of 3C436; i.e. the space curve passing through the central engine and otherwise centred on the circular lobe cross-section. The black pentagons show the modelled spectral age with 1σ uncertainties in the fitting of the radio SED, including those from the Bayesian fit. The measured spectral ages have comparable uncertainties in their fits. The modelled spectral age along the centre of the lobes well matches the near-linear rise in age away from the hotspot observed by Harwood et al. (2013).

The discrepancy between the spectral and dynamical ages here is likely due to the invalidity of the assumptions used by the impulsive injection models, i.e. not all electrons in each slice have the same age. In particular, the hydrodynamical simulations shown in Figure 4.4 predict electrons injected as recently as $t_{\rm i} = 0.6t$ to be present in regions of the lobe closest to the core at the 1σ level. These younger electrons will extend the break in the radio SED out to higher frequencies; the JP and KP models largely fit the frequency above which no emission occurs yielding a peak age estimate of around $(1 - 0.6)t = 0.4t$. That is, these impulsive injection models tend to fit the spectral age of the youngest electrons that are contributing significantly to the emissivity of the radio SED.

By contrast, applying the continuous injection model to the radio SED for the entire lobe reproduces the source dynamical age within uncertainties; this is expected since the CI model actually describes the situation, i.e. a region of homogeneous magnetic field strength with a continuous supply of freshly injected elections. Caution should be taken when measuring the spectral age of resolved radio sources; the measured age does not relate to the maximum or even average age of the electrons contributing to the SED.

4.4 Low-power radio AGN

The radio AGN counts at $z < 1$ are dominated by faint low-powered FR-I class objects (Willman et al. 2008), which will only become more prevalent in future surveys as sensitivity continues to increase. It is therefore vital to not only understand the powerful FR-II objects comprising much of the existing surveys, but also develop techniques to model the ubiquitous FR-Is. The definition of an FR-I radio source is not physically based, and simply specifies that the location of the surface brightness within the lobes is concentrated towards the core, i.e. brightest region less than one-half the lobe length from the core (Fanaroff & Riley 1974). Some FR-Is are observed to behave like FR-IIs without hotspots (the fat doubles), while others are twin jets which never inflate a lobe but instead expand out until they are disrupted by interaction with the intra-cluster medium. The dynamics of lobed FR-Is is similar to the FR-IIs, with the exception of the sites of electron acceleration. In this work, we will examine the flaring jet FR-Is, the archetypal example being 3C31 (e.g. 3C31 Leahy et al. 2013). The synchrotron-emitting electrons in these sources are assumed to undergo a single instance of acceleration at the jet flare point. The dynamics of the flaring jet FR-I radio plume as a whole are modelled using the subsonic expansion limit of the dynamical model developed in Chapter 2, however the dynamics of the lobe plasma remain to

be described. The bulk flow of particles and the pressure gradient within the lobe must be considered to derive the radio SED and estimate the maximum extent of the observable lobe (i.e. surface brightness above detection limit).

4.4.1 FR-I formation and evolution

Both the formation of the jet flaring point and the internal lobe plasma dynamics need to be characterised for FR-Is so that their spatial emissivity distribution can be determined. In this section, the dynamics of the lobe evolution and the bulk flow of lobe plasma is investigated using hydrodynamical simulations; this work is used to verify the results of my FR-I flaring jet dynamical model.

Synchrotron-emitting electrons and lobe dynamics

The large-scale radio source morphology depends crucially upon whether the jet maintains forward thrust during its interaction with the host environment. If the jet does run out of thrust a flare point will form, resulting in the formation a type-I radio source. This can happen through one of two mechanisms: (1) the jet has a large opening angle causing it to run out of thrust before a recollimation shock forms (see discussion in Krause et al. 2012), or (2) the jet expands into an environment with a rising temperature profile (e.g. observations in Vikhlinin et al. 2006) leading to a flare point even after the jet has collimated (see simulations of Massaglia et al. 2016).

In the first case, the ram pressure of the jet plasma reduces as it widens ($p_{\rm j} \propto 1/r^2$ for a conical jet) until it equals that of the ambient medium $p_{\rm x}$. The jet material will generate a recollimation shock upstream of this point when the sidewards ram pressure $\rho_{\rm j} v_{\rm j}^2 \sin^2\theta$ and the external medium equilibrate. This recollimation shock stabilises the jet if it reaches the jet axis before the progress of the jet stalls. In flat environments, analytical models (Alexander 2006) and numerical simulations (Krause et al. 2012) show that the recollimation shock in jets with half-opening angles $\theta > 25^\circ$ occurs so far downstream that the terminal shock is unable to reach it and an FR-I flaring region forms (Krause et al. 2012). The plasma downstream of the flare point streams transonically towards the maximum extent of the lobe. The lobes produced in this manner are very turbulent and have significantly elevated gas density and pressure at their ends. The simulated flare points well match those of typical astrophysical FR-Is (e.g. 3C31; Leahy et al. 2013), however this approach is less capable of modelling their radio plumes.

Massaglia et al. (2016) investigated the formation of FR-I radio sources through the

disruption of a collimated jet by a rising temperature profile. Their hydrodynamical simulations assume a standard falling density profile and prescribe the corresponding temperature profile which yields a constant pressure environment. The jet is disrupted in this case when a small pressure enhancement forms downstream (i.e. $p_{\rm j} \lesssim p_{\rm x}$). The plasma streams outwards with an approximately laminar flow from the flare point, leading to much less turbulence in the lobe than in the simulations of Krause et al. (2012). Both the simulated flare points and the radio lobes are consistent with observed radio sources. The initially conical jets of these sources may not be collimated on the small distance scales involved in these objects, especially for larger opening angles. The flare points in astrophysical FR-Is are likely formed through a combination of the techniques explored by Krause et al. (2012) and Massaglia et al. (2016).

The bulk flow of plasma simulated in the low-power radio sources of Massaglia et al. (2016, e.g. reference simulation in their Figure 4) is directed outwards from the core throughout almost the entirety of the radio plume. Entrainment between the plume and the ambient medium leads to a small region with a receding velocity; this region contains few synchrotron-emitting electrons and in any case has a near-zero negative velocity. In this scenario, the packets of synchrotron-emitting electrons accelerated at the flare point are expected to flow outwards indefinitely. Further, the injected electrons are expected to be approximately layered in the plume, with the newly accelerated particles closest to the core and the oldest electrons furthest from the central nucleus. The hydrodynamical simulations show that even the fastest electrons travelling along the jet axis take at least one-quarter of the source age to reach the end of the plume. However, the vast majority of electron population is in slower moving plasma away from the axis taking close to the source age to traverse this distance. The plasma towards the end of the plume will therefore be strongly skewed towards the oldest electrons in the population. The flow rate of the oldest synchrotron-emitting electrons is therefore simply the instantaneous expansion rate of the radio source. The pressure profile within the plume of a flaring jet FR-I should stabilise to the downstream external profile encountered by these initial synchrotron-emitting electrons; the internal sound speed must be low noting that the material in the plume originates approximately evenly from both the jet and the dense ambient medium (comparison between FR-Is and -IIs provided in Massaglia et al. 2016). I therefore assume all subsequent electrons flow forwards at the same rate as a function of distance from the core.

Flaring jet dynamical model

The dynamical model for twin-jet FR-I sources is constructed using the framework of the analytical model of developed in Chapter 2. In that chapter the evolutionary history of initially supersonic lobed radio sources was modelled with an ellipsoidal geometry; now I treat the jets/plumes as spherical cones (i.e. a spherical sector). The jets initially expand supersonically, but upon forming a lobe quickly transition to subsonic pressure-limited expansion (e.g. Luo & Sadler 2010). The radio lobe of my dynamical model is an ensemble of small angular volume elements in pressure equilibrium. Each element of fixed angular width is assumed to receive an unchanging fraction of the jet power as the lobe expands to ensure the lobe maintains its initial shape. The lobe in the flaring jet model is a spherical sector and it is therefore expected that each element will expand identically. The angular volume elements are instead used to define which angles comprise the lobe and those which lie beyond the jet half-opening angle. The conical shape of the flaring jet lobe is therefore modelled by setting the lobe length $R(\theta) = 0$ for $\theta > \chi$, where χ is the half-opening angle of the lobe beyond the flaring point.

The luminosity of low-powered radio sources resembling a flaring jet is spatially much more complicated than that of the high-powered radio sources so far examined. Most notably, the magnetic field cannot be assumed to be homogeneous (on large scales) throughout the radio source due to the steeply falling pressure profile. Further, Croston & Hardcastle (2014) found that twin-jet FR-Is are more entrained further along the jets. Here I assume that the synchrotron plasma downstream of the flare point is well mixed with entrained ambient gas, so that the emitting electrons are effectively distributed across the prescribed cone cross section. This situation is is expected to be approached for the large-scale radio plumes modelled in this work.

4.4.2 Luminosity from synchrotron-emitting electrons

The synchrotron emissivity in flaring jet radio plumes is calculated in the same manner for both resolved and unresolved sources; the synchrotron-emitting electrons are accelerated at the flare point and flow outwards at the rate described by the dynamical model to their present-time location with ambient pressure.

FR-I surface brightness distribution

The two-dimensional brightness distributions for flaring jet radio sources are calculated following the method described in Section 4.3. The surface brightness distribution modelled for a typical flaring jet type FR-I is shown in Figure 4.10 for frequencies of 151 MHz, 1.5 GHz and 15 GHz. As in the case of FR-IIs (Section 4.3.4), the frequency dependent nature of the loss mechanisms reduces the duration over which the electron population emits synchrotron radiation at higher frequencies. However, unlike the powerful FR-II sources the acceleration site is close to the core with the electrons propagating outwards. The linear size out to which synchrotron emitting electrons reach may therefore be different at each frequency, with larger observable emitting regions expected at low frequencies where the losses are less severe. The size is thus poorly defined for FR-Is, and will depend on both observing frequency and sensitivity; unlike the FR-IIs, where the measured length is unaffected as long as hotspots are visible.

The spatial extent reached by synchrotron emitting electrons at the time of observation is investigated in Figure 4.11. The plots in the figure show an upper limit to the spatial extent of the detectable emission region at five frequencies, for the flaring jet source shown in Figure 4.10 viewed at redshifts $z = 0.1$, 0.5 and 1. The linear size of the flaring jet sources reduces both with increasing redshift and source age (not shown in figure), in a similar manner to the high-power FR-IIs. As with FR-IIs, the greater losses at higher redshifts are again primarily due to the inverse-Compton loss mechanism reducing the energy of the electron distribution. The older flaring jet radio source population is identical to their younger counterparts close to the core, but has older electrons with the highest loss rates placed at larger radii. These plots further emphasise the difficulty faced in measuring the physical source linear size in the weak FR-I class, especially at higher redshifts or in the older population. The correct measurement of the source size is vital to correctly estimate the source age, and thus total energy output of the AGN into its surroundings, using dynamical models. Further, the corresponding lobe volume must be correctly calculated to properly understand the suppression of cooling resulting from pushing gas to greater cluster-centric radii with longer cooling times (e.g. Cavagnolo et al. 2010; Raouf et al. 2017).

FR-I unresolved luminosity model

The luminosity calculation for unresolved flaring jet FR-I radio sources is much more involved than their high-powered FR-II counterparts. In particular, the pressure gra-

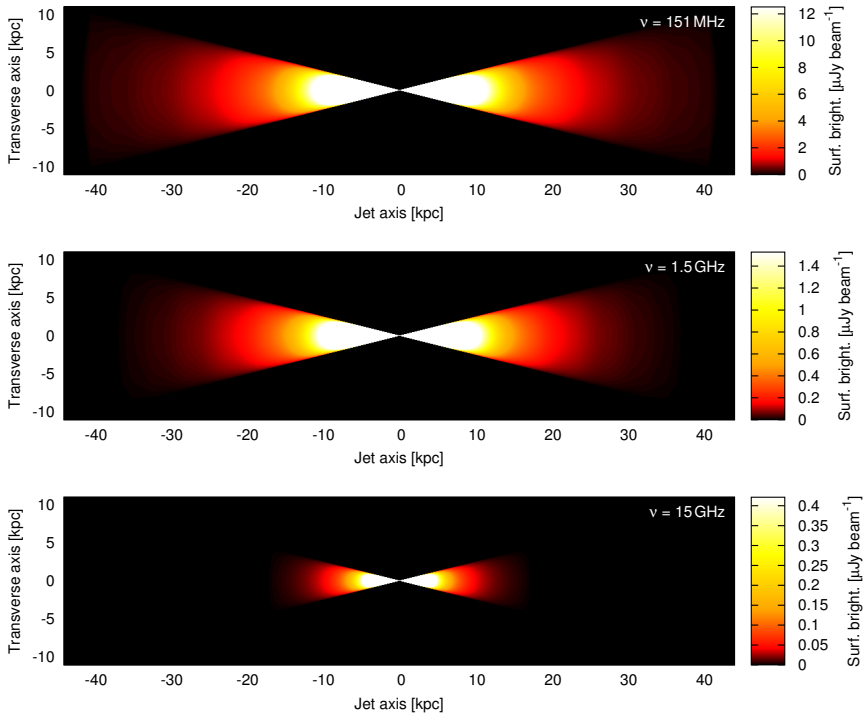

Figure 4.10: Radio source emissivity as a function of lobe position including all loss mechanisms for three typical observing frequencies. The top plot shows 151 MHz radio emission, the middle plot is for 1.5 GHz, and the bottom plot shows 15 GHz emission. The modelled source has a jet power of $Q = 10^{36}$ W, age of $t = 100$ Myrs, inhabits a 10^{14} $M_{\odot}$ halo mass environment at $z = 0.03$, expands with an plume half-opening angle of $\chi = 15^{\circ}$ and has an electron energy injection index of $s = 2.4$. The axes are scaled to the dimensions of the physical source size, i.e. the entire lobe does not emit radiation at any of these frequencies. The colour-bar scale is cropped to provide more contrast in the lobe at the expense of excluding the brightest emission near the core.

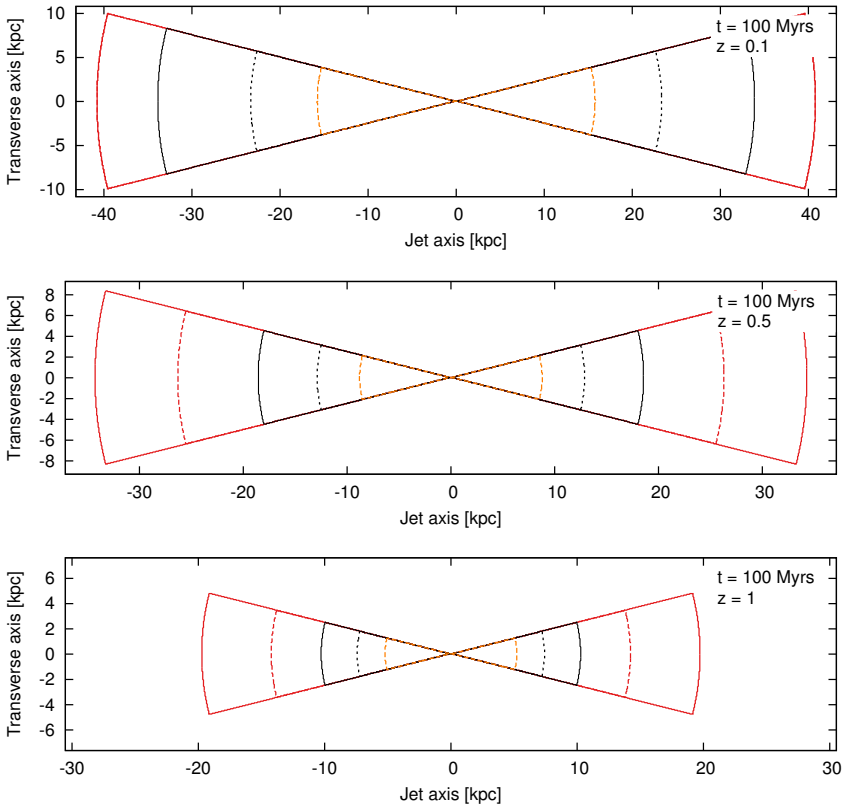

Figure 4.11: Emitting region (i.e. theoretical limit of non-zero emission at observing frequency) of flaring jet radio source lobes as a function of observing frequency. Same as Figure 4.7 except the modelled flaring jet source has a jet power of $Q = 10^{36}$ W. The jet axis is scaled so that the physical radio source extends to the plot border, e.g. in the bottom plot the physical radio source is 60 kpc in size but is emitting synchrotron radiation over less than a third of this length.

dient down the flaring jet necessitates the use of the full resolved emissivity model, with the total luminosity derived by integrating the emissivity across all volume elements. The algorithm can be improved for the unresolved case though since the location of the electron packets is unimportant; each electron age is directly mapped to a present-time magnetic field strength (i.e. electrons of different ages coast down the pressure gradient independently), resulting in a model as computationally efficient as for unresolved FR-IIs. The size-luminosity track for a typical FR-I with jet power $Q = 1.3 \times 10^{35}\,\mathrm{W}$ is shown in Figure 4.12. In the absence of radiative losses, the luminosity rises throughout the source lifetime until instabilities between the lobe and external medium (included in the Chapter 2 dynamical model) lead to the infilling of the lobe. The size-luminosity track is largely unaffected by the inclusion of loss mechanisms; these only reduce the emission of the electrons found furthest from the core where the contribution to the total luminosity was already small due to the lower pressures. This monotonic increase occurs because freshly injected plasma continually replaces the older material near the bright constant pressure core; the displaced plasma expands the plume and increases the overall luminosity. By contrast, the pressure of the lobe and hotspot in FR-IIs reduce as they expand somewhat negating the increase in luminosity due to the addition of synchrotron-emitting electrons.

4.4.3 Modelling spatial emissivity of real sources

In this section, the analytical spatial emissivity model is tested by attempting to reproduce the surface brightness distribution of the typical FR-I source 3C31 (Leahy et al. 2013). The intrinsic properties of 3C31 are fitted using the Bayesian framework described in Chapter 3 (though assuming the flaring jet dynamical model), based upon the observed source size, luminosity and break frequency arising from the oldest electrons, in addition to properties of the host environment. Heesen et al. (2014) combined high-resolution observations of 3C31 from the *Low Frequency Array* (LOFAR), the *Very Large Array* (VLA) and *Giant Metrewave Radio Telescope* (GMRT) to produce radio SEDs as a function of position within the radio lobe. I fit the JP model to their observed spectra for the furthest regions of the lobe to obtain estimates for the spectral break frequency. The properties of NGC383, the galaxy group hosting 3C31, are taken from Komossa & Böhringer (1999). The shape of the pressure profile, gas mass and virial temperature for NGC383 are used here. I use the Bayesian approach from Chapter 3 to derive a jet power of both jets of $10^{37.2}\,\mathrm{W}$, source age of 200 Myrs and an equipartition factor of 0.31, consistent with the range found for this object by considering pressure balance at various points along the lobe surface (Croston et al. 2008a).

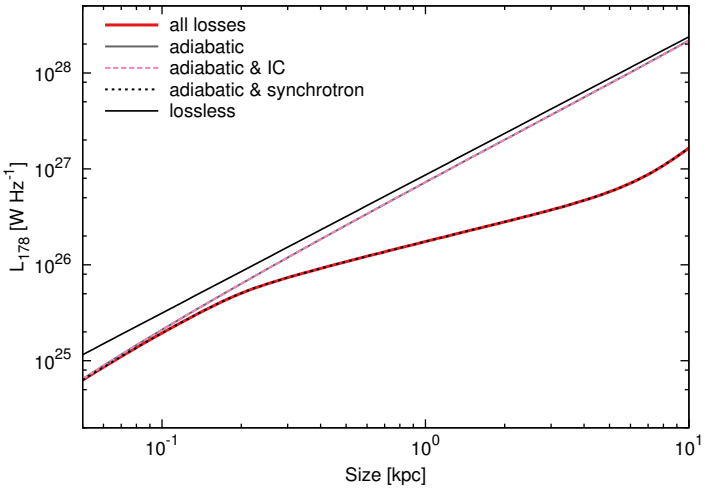

Figure 4.12: Luminosity-size tracks for a flaring jet radio source at $z = 0.5$ with jet power of 1.3×10^{35} W, expanding into an X-ray observed environment (Vikhlinin et al. 2006) scaled to a density of $\rho = 7.2 \times 10^{-22}\,\mathrm{kg\,m^{-3}}$ at radius 2 kpc. Five profiles are plotted, showing the luminosity in the lossless case (solid black), with only adiabatic losses (solid grey), with adiabatic and synchrotron losses (dashed black), with adiabatic and inverse-Compton losses (dashed pink), and with all loss mechanisms (solid red).

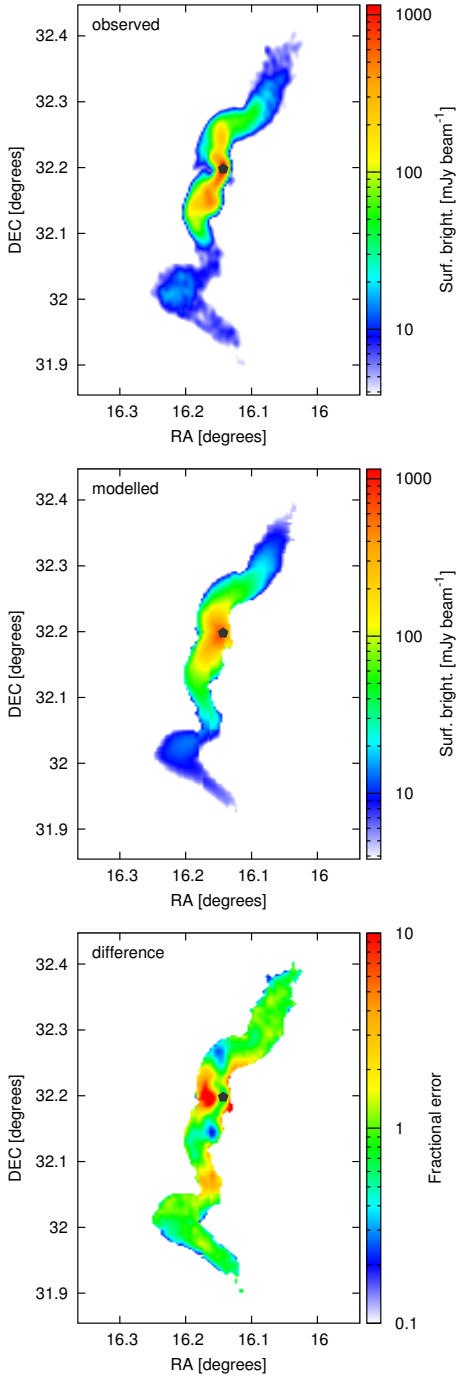

Figure 4.13: Modelled 608 MHz radio emission (middle) from the lobes of 3C31 calculated using the flaring jet dynamical model and resolved emissivity model; the shape of the lobes and total luminosity are constrained by observations (top). The fractional error between the modelled and observed luminosity distribution is shown in the bottom plot. The modelled results agree everywhere except around the core; the modelling does not consider the early jet before the flaring point leading to underestimated emission along parts of the jet and overestimated emission off axis.

The resolved emissivity model (Section 4.2) is used to predict the emissivity from the electrons of various ages in 3C31 for the best fit jet power, source age and magnetic field strength. These electrons are distributed within the observed volume occupied by 3C31 (i.e. an approximately helical shape; Leahy et al. 2013); the pressure-limited expansion model I assume from the growth of flaring jet radio sources dictates the radial location of the electrons of different ages. The modelled radio source emissivity for 3C31 calculated at 608 MHz is plotted in Figure 4.13. The pressure-gradient, loss processes and $1/r^2$ expansion lead to a rapid decrease in surface brightness away from the central engine, i.e. $S \propto r^{-\beta-\xi-1}$ where β and ξ are the exponents of the density and temperature profile, and one dimension of the $1/r^2$ volume expansion is assumed to lie along the line-of-sight. Further, the three-dimensional nature of the radio source leads to decreased emission from line-of-sights passing through the edge of the source (i.e. less plasma here than towards the centre), as seen in observations of 3C31. This effect also results in the region of enhanced brightness in the westwards kink in the tail of 3C31. The observed emissivity of 3C31 is well characterised by the combined FR-I dynamical and luminosity model, as shown in the bottom panel of Figure 4.13 which plots the fractional error between the modelled and observed emissivity distributions. However, the spatial emissivity model does not accurately reproduce every detail of 3C31. In particular, the region around the central engine is unrealistically modelled assuming isotropic jets. As a result, my model greatly overestimates the emission off the jet axis and slightly underestimates the brightness along the jet. This can largely be corrected by assuming that constant opening angle jets feed into the lobes of 3C31, though I do not pursue this further since we aim solely to validate the analytic model at this time.

The similarity of the modelled and observed surface brightness distribution is further examined in Figure 4.14. The surface brightness is measured along the jet axis to enable a more direct comparison; the jet axis is defined as the space curve following the path of the jets where visible near the core or the centre of the circular lobe cross-section at larger radii. The overall shape of the modelled surface brightness along this jet axis is very close to that of the observed profile. The peak near the central engine and the spikes in emissivity due to the bends in the lobe at around 300 and 450 kpc south of the core are also reproduced by my modelling. The higher than modelled surface brightnesses approximately 100 kpc from the core result from the jets, whilst the lower than expected surface brightness approximately 200 kpc south of the nucleus is likely due to either an unmodelled feature in the environment or any cork-screwing of the jet being poorly captured by the model. This comparison is also made with a simpler model assuming a conical cross-section (see Figure 4.14). This model

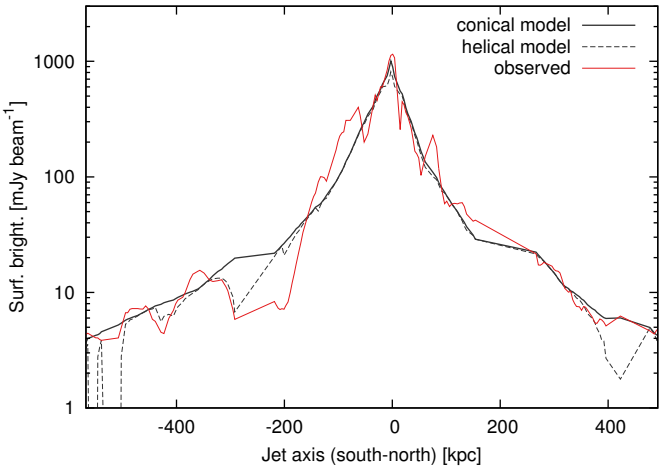

Figure 4.14: Modelled and observed (solid red) 608 MHz radio emission along the jet axis of 3C31; i.e. the space curve passing through the central engine and otherwise centred on the circular lobe cross-section. The modelled surface brightness is shown assuming either a simple conical cross-section (solid black) or a more complicated helical structure (dashed black) based on the observed width of the plume. The modelled emissivity along the centre of the plumes matches the overall shape of the observed profile well. Further, the helical model reproduces some of the finer details such as the peak near the central engine, and the spikes in luminosity due to the bends in the lobe at around 300 and 450 kpc south of the core.

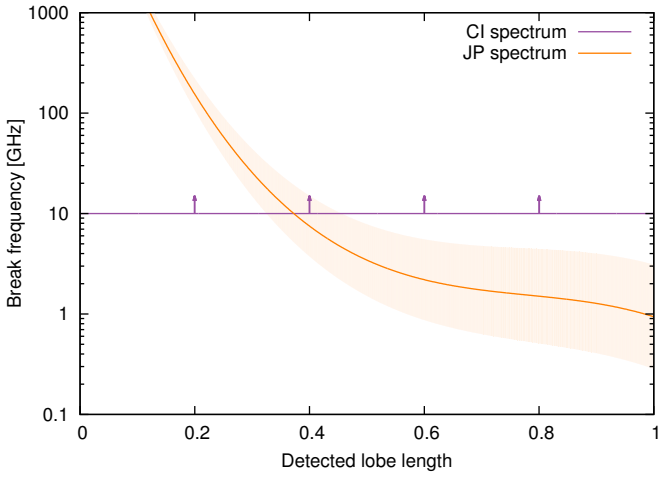

Figure 4.15: Break frequency fitted to the radio SED from strips $[r - dr, r + dr)$ along a typical flaring jet radio source (parameters as in Figure 4.10, though same result at any low-redshift $z \ll 1$). The shading plots the 1σ uncertainties in the JP model fits of the spectral break. The lower limit for the continuous injection model fit to the spectrum is also included; the break frequency cannot be fitted to the unresolved spectrum since the inhomogeneous magnetic field violates a model assumption.

successfully matches the general shape of the observed emissivity profile but cannot reproduce the finer details. The surface brightness in the plumes of low-powered radio sources can therefore be well described by considering only the reduced electron density and magnetic field strength along the length of the source. In particular, this agreement is possible despite my model ignoring entrainment, turbulent electron reacceleration, and any small-scale structure in the magnetic field.

4.4.4 Flaring jet FR-I spectral classification

The radio SED measured for radio sources depends crucially on the sky area over which the flux density is integrated to generate the spectrum. The difficulty in measuring the linear size of flaring jet FR-I radio sources may lead to significant emission from the radio lobes being excluded if it lies below the noise floor of the survey. The weak synchrotron emission from the large volume surrounding the detected regions of the lobe should be spatially coherent and may be recoverable; this of course assumes such consideration is taken during observations.

The radio SED arising from an unresolved flaring jet FR-I source is not well modelled by either the standard impulsive (e.g. JP and KP) or continuous injection models.

In particular, these sources violate the assumption of a homogeneous magnetic field leading to a flatter SED[4] beyond the break frequency than expected. Any spectral break observed in the SED therefore can not be related to the age of the source. Moreover, the location of the break is largely determined by the bright, freshly injected electrons near the core. The lower bound of the spectral break (fitted using only the start of the turnover) is determined to be greater than 10-100 GHz for typical FR-Is at low-redshift ($z \ll 1$) with jet powers of $\sim 10^{36}\,\mathrm{W\,Hz^{-1}}$, sources ages less than a few hundred Myrs, and environments with halo mass 10^{12}-$10^{15}\,\mathrm{M_\odot}$. Spectral turnovers much above the highest observing frequency are unlikely to be detected and the radio source SED will therefore be assumed to have no curvature implying a very young source. Further, the host galaxy may significantly impact the low frequency emission ($< 1\,\mathrm{GHz}$) near the core due to synchrotron self-absorption or free-free absorption. The spectrum arising from the bright inner regions of flaring jet radio sources may thus resemble that of Gigahertz-Peaked Spectrum (GPS) or Compact Steep Spectrum (CSS) radio sources.

The emission arising from narrow radial strips of the radio lobe can instead be examined, to avoid the radio SED being dominated by the young electrons near the acceleration site, and to satisfy the assumption of a homogeneous magnetic field. The spectral break frequency fitted to the similar age electrons (i.e. impulsive injection model) in strips at different radii from the central engine is shown in Figure 4.15. The break frequency measured at the electron acceleration site is consistent with that fitted for the unresolved radio source, however the spectral break falls off rapidly with radius to approximately 1 GHz at about half the source size. The break frequency remains approximately constant at 1 GHz (for this typical FR-I) for the strips at larger radii. This is theoretically expected since the age of the electron packets increases with radius as $\tau \propto r^{3-\beta}$ and the magnetic field as $B \propto r^{-\beta/2}$ (from subsonic limit of dynamical model in Chapter 2), hence the break frequency $\nu_\mathrm{b} = \tau^{-2}B^{-3}$ becomes independent of radius in steep environments with $\beta \sim 1.7$ (i.e. those far from the core). This result enables the spectral age of resolved flaring jet sources to be easily calculated. Following the method of described in Chapter 3 the spectral age can be used to constrain the intrinsic source age in the dynamical models.

The full extent of flaring jet radio sources may not be detected in objects viewed at close to the surface brightness detection limit. The possibility of extended emission

[4]The radiative losses from the oldest synchrotron-emitting electrons lead to the steepening of the radio SED at high-frequencies. However, in flaring jet FR-Is these electrons are located furthest from the core where the magnetic field strength is weakest, and thus contribute less to the total luminosity than expected under the assumption of a homogeneous magnetic field.

surrounding the cores of these sources must be considered to properly understand the AGN population and their energetics. Integrating the surface brightness to well beyond the observed source size (and perhaps in new surveys also providing better uv coverage) may be required to include the contribution from all synchrotron emitting electrons originating from the radio AGN. Any high-frequency curvature observed in an SED measured over such an extended region would suggest the source is not compact, but rather has faint, extended emission. The large FR0 population comprising GPS and CSS radio sources could at least partly be explained be explained by low jet power flaring jet FR-I type sources. The emission in such sources would be dominated by the young and bright electrons in the high emissivity core, whilst older electrons at larger distances would be too faint to be detected.

4.5 Understanding AGN feedback and energetics

The energy imparted on the AGN host galaxy and its larger-scale environment is largely driven by two mechanisms: (1) the energy input into the host environment directly from the jets (i.e. $E = Qt$), and (2) the suppression of cooling by pushing gas out to large galactocentric radii with longer cooling times. The calculation of the source active lifetime, and thus energy, using dynamical models requires accurate source size estimates. The linear size of an FR-II radio source can be easily measured in any resolved source since the brightest regions are located at the extremities of the lobes. By contrast, the full extent of FR-Is with core-dominated emission may not be observed. Estimating the volume of gas cleared by the expanding radio lobes may be miscalculated in both morphological classes; FR-IIs may have their width underestimated whilst the length of FR-Is is likely to be miscalculated.

4.5.1 Measuring lobe sizes and axis ratios

Survey sensitivity may greatly affect the measurement of radio AGN energetics through the underestimation of either their width or length. In this section, a well-studied sample of 3C sources is used to quantify the degree to which the width and length are underestimated. The surface brightness of 3C sources is typically several orders of magnitude greater than the surface brightness limit of the observations; this ensures the full extent of the AGN is visible. The change in length, width and axis ratio of these sources can then be determined as a function of sensitivity to understand observations in future surveys.

Radio source FITS images for 3C sources with $z < 1$ are taken from the online database

of Laing et al. (1983)[5]. The lengths, widths and axis ratios of the radio source lobes are recalculated with various survey surface brightness sensitivity limits, in addition to a physical measurement based on the actual signal-to-noise of the image. The 3CRR survey selected bright and then unresolved objects with 178 MHz flux densities > 10.9 Jy (Laing et al. 1983), these have since been observed at higher resolutions and with several orders of magnitude greater sensitivity. The FITS images are available from observations at different frequencies for many of the 3C sources, typically 1.4, 4.9 or 8.5 GHz. The brightnesses in each of these maps are arbitrarily scaled to a 1.5 GHz observing frequency with a 1 arcsec^2 beam to enable a cross-frequency comparison.

The processing of the FITS images to measure the shape of the radio lobes proceeds as follows. Material potentially belonging to the lobes is firstly identified by flagging out all emission below the 5σ noise level of the image. Connected regions of emission are identified; proceeding outwards from the optical host galaxy, these clumps of emissions are flagged as lobes until at least 90% of the image flux density has been included in lobes. The lobe selections made using this technique are confirmed with a visual inspection. The most distant two points (from each other) in the flagged region are identified as belonging to different lobes. The lobe length is measured as the distance from the core to the most distant pixel in each lobe, and the width taken as the greatest width across the lobe normal to this axis. The axis ratio is calculated as the ratio of the lobe length to its cross-sectional radius, the radius of the third of the lobe closest to the hotspot is not included. This decision is made to allow a fair comparison with my model which does not consider the enhanced emission near the overpressured hotspot. The morphology of the lobe is additionally characterised by taking the emissivity weighted mean length. That is,

$$FR = \frac{2\sum s_{\rm i} x_{\rm i}}{\max\{x\}\sum s_{\rm i}} + 0.5 \tag{4.23}$$

where $s_{\rm i}$ is the flux density from a cell distance $x_{\rm i}$ along the jet axis. Here an *FR* number of 0.5 corresponds to a source with all emission at the core and a number of 2.5 to all emission at the hotspot. By definition, Fanaroff & Riley type I sources have an *FR* number less than 1.5 whilst FR-IIs comprise the reminder of the population (c.f. Krause et al. 2012). The observing frequency may affect the morphological classification determined for a particular source, however the effect of changing the surface brightness sensitivity limit on these classifications should be frequency independent.

[5] `http://3crr.extragalactic.info`

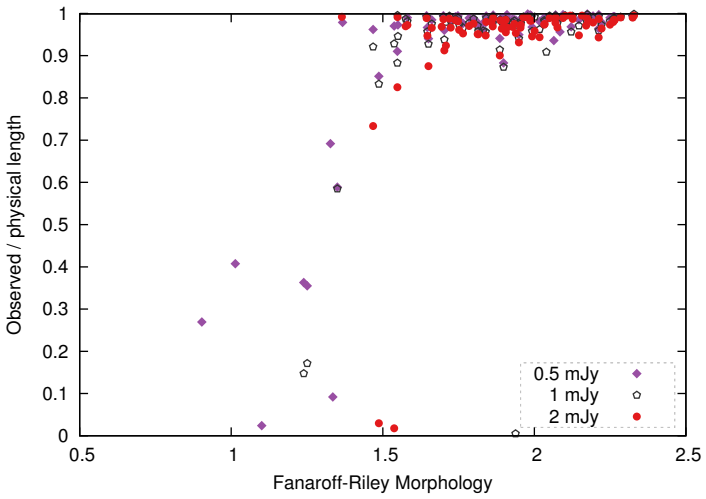

Figure 4.16: Lengths of 3C radio sources detected for three survey sensitivities (per beam) as a function of the morphological classification. Radio lobes with an FR-II morphology (i.e. number greater than 1.5) have their lengths measured correctly irrespective of the survey sensitivity, whilst the length of lobes with emission concentrated towards the core is a strong function of sensitivity.

4.5.2 Sensitivity and Fanaroff-Riley morphology

Biases in the measurement of radio source properties due to observing with insufficient sensitivity are expected to depend on the Fanaroff & Riley morphology. The fractional difference in the detected and physical length and axis ratio of the lobes of the 3C sources is investigated for different survey sensitivities in Figures 4.16 and 4.17. Radio lobes with an FR-II morphology have their lengths measured correctly irrespective of the survey sensitivity, whilst the length of lobes with emission concentrated towards the core is a strong function of sensitivity. This makes qualitative sense as the bright hotspots of FR-IIs should remain visible after any other region in the lobe, whereas in FR-Is the regions furthest from the core tend to be the faintest. Meanwhile, the lobes of FR-I sources tend to have their axis ratios correctly measured irrespective of sensitivity, however the measured axis ratios of type 2 objects can vary significantly with sensitivity. The axis ratios of type 1 objects are likely measured correctly despite their incorrect lengths because of their approximately conical shape. The axis ratios of FR-IIs will be incorrectly measured if emission from the lobe falls below the detection limit whilst that close to the hotspots remains detected.

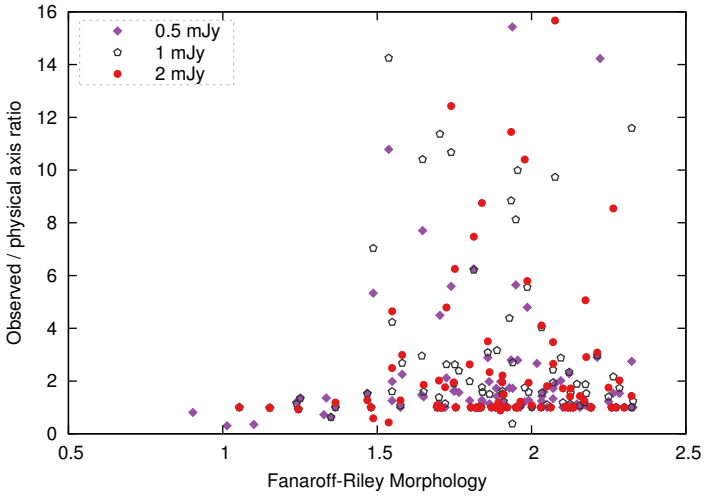

Figure 4.17: Axis ratios of 3C radio sources detected for three survey sensitivities (per beam) as a function of the morphological classification. The radio lobes of FR-I sources tend to have their axis ratios correctly measured irrespective of the survey sensitivity, however the measured axis ratios of FR-II objects can vary drastically with sensitivity.

4.5.3 Observed axis ratio of powerful FR-II sources

The axis ratio of lobed FR-IIs is expected to vary with sensitivity for one of three reasons: (1) only the hotspots may be detected leading to a very high axis ratio, (2) synchrotron loss mechanisms may reduce emission away from the hotspot so that the luminosity from the widest region near the core is greatly reduced, or (3) in weaker sources the circular cross-section of the lobe may cause the emissivity to reduce as $\sqrt{1-y^2}$, where y is the fractional distance from the jet axis to the edge of the lobe. I attempt to exclude the first of these reasons from our analysis by measuring the source width across only the two-thirds of the source closest to the core; if zero width is measured then it can be assumed that only the hotspots are visible. Moreover, the size of the hotspot as a function of sensitivity has no bearing on the physical width of the lobe. By contrast, the other two mechanisms are included in my model enabling observations of radio sources taken near the detection limit to potentially have their axis ratio corrected.

The observed axial ratios for FR-II radio sources in the 3C survey is investigated in Figure 4.18. The Fanaroff & Riley classification in Equation 4.23 is used to robustly classify type 2 sources, with $FR < 1.75$ excluded due to their more core dominant nature and $FR > 2.25$ excluded due to the lack of lobe emission. The axis ratio of these

sources is measured at various survey sensitivities and compared to the best estimate measure using the FITS image. The detected axis ratio of each source falls off steeply as the sensitivity decreases. Note that this slope depends on the inverse-Compton losses, and so I thus decide to group the 3C sources into three redshift bins. The sensitivity scale for each of the 3C sources is shifted such that unity corresponds to the point when a given lobe first becomes detectable. The shapes of the 3C source profiles are compared with each other and to the model prediction for a radio source typical of the 3C population in the redshift bin, as shown in Figure 4.18. The theoretical model prediction for the measured axis ratio and lobe volume as a function of survey sensitivity is again found to be consistent with that of the observed 3C sources in each of the three redshift bins.

The rate at which the detected lobe width reduces as observations become less sensitive is expected to be a function of the strength of the inverse-Compton loss mechanism. The oldest synchrotron-emitting electrons are most subject to inverse-Compton losses; these electrons are found furthest from the hotspot in the widest regions of the lobe closer to the core. The inverse-Compton loss mechanism is most prevalent at higher redshifts where the CMB radiation is stronger, and in older sources where it has longer to act on the electrons. Both the observed 3C sources and my model show that the axis ratio will be measured incorrectly for a greater range of sensitivities in higher redshift sources than at lower redshifts (see Figure 4.18). Equivalently, it can be said that the surface brightness distribution of low-redshift FR-II radio lobes is more homogeneous than in their high-redshift counterparts.

I find that the detected lobe width will be accurately measured except when the brightest emission from the source is within a factor of a few of the survey detection limit. However, in a volume-limited survey radio sources are preferentially seen near the detection limit since lower luminosity objects are more ubiquitous. The detected lobe width and volume may therefore not reflect that of the physical radio source in much of the observed population.

4.5.4 Visible linear size of flaring jet FR-Is

The surface brightness of flaring jet FR-I radio sources falls off rapidly away from the acceleration site near the AGN core, both due to the falling pressure profile and the radiative loss mechanisms. The sensitivity of the survey observing these sources may therefore lead to very different measurements of the source linear size. Further, the loss mechanisms reduce the energy of the electron distribution sufficiently that at some frequencies sections of the lobe cannot be observed irrespective of the sensitivity.

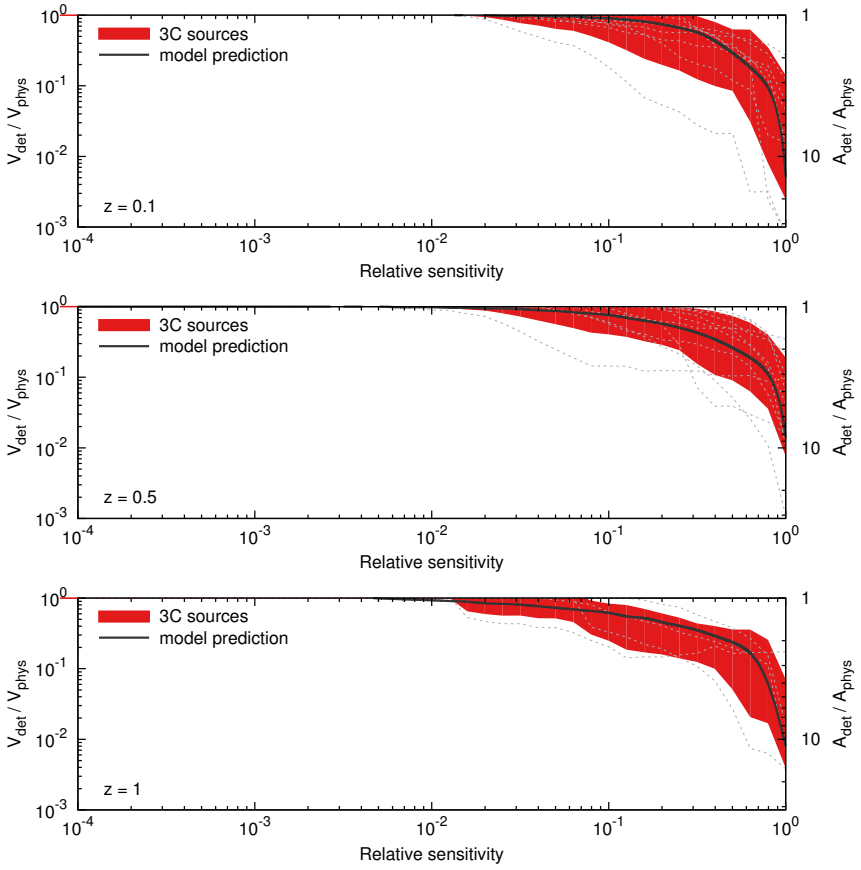

Figure 4.18: Volume of lobed FR-II sources in the 3C survey detected as a function of the survey sensitivity binned by the host galaxy redshift. The left-hand vertical axis shows the fraction of the "total" lobe volume detectable by an arbitrary sized beam for various survey sensitivities; the sensitivity is scaled so that unity corresponds to the point when a given lobe first becomes detectable. The right-hand vertical axis similarly shows the fraction of the lobe width detectable, i.e. the detected axis ratio divided by the physical axis ratio. The grey dashed lines show the tracks of each 3C radio lobe in this phase-space, with the red shading indicating the 1σ spread in the distribution. The solid black line plots the theoretical expectation from my model, using the average redshift and age of the sources in the plot. This is again scaled so that a sensitivity of unity corresponds to the point at which the source first becomes detectable, and is additionally scaled so that with the entire volume is detected with infinite sensitivity. The 3C radio sources are grouped into three redshifts: $z \leqslant 0.3$ (top), $0.3 < z \leqslant 0.7$ (middle) and $z > 0.7$ (bottom).

In Section 4.4.3, I found that the surface brightness in flaring jet FR-Is is theoretically expected to fall off with radius from the core as $S \propto r^{-\beta-\xi-1}$. The detected length of these sources is therefore expected to increase with improving survey sensitivity as $D \propto S^{-1/(\beta+\xi+1)}$, though this simplistic formalism ignores the frequency-dependent loss processes. For typical FR-I environments ($\beta \sim 1$ and $\xi \sim 0$) this relation simplifies to $D \propto S^{-0.5}$.

The volume and length detected for flaring jet and core dominated FR-I radio sources in the 3C survey is investigated in Figure 4.19. The Fanaroff & Riley classification in Equation 4.23 is used to initially identify type 1 radio source lobes before being visually classified. The length of these sources is measured at various survey sensitivities and compared to the best estimate measured using the FITS image. The detected length of each of these FR-Is falls off approximately log-linearly as the sensitivity limit is raised and with similar slope, though there are sharp jumps in the detected length due to the presence of knots in the flow. The rate at which the detected lobe length reduces with sensitivity is expected to be approximately the same for all sources expanding into environments falling-off with similar power-laws; inverse-Compton losses also affect the maximum distance out to which emission occurs and slightly steepens the luminosity profile. The sensitivity scale for each of the 3C sources is therefore shifted such that the profile for each source is stacked on top each other. This enables a direct comparison of their shapes with each other and to the model prediction, as shown in Figure 4.19. My model is run for a radio source typical for the 3C population inhabiting a host halo environment of mass $10^{14}\,\mathrm{M}_{\odot}$ at redshift $z = 0.5$. This theoretical prediction for the measured length as a function of survey sensitivity is found to be consistent with that of observed 3C sources.

Radio sources in deeper large-scale surveys such as the *NRAO VLA Sky Survey* (NVSS; Condon et al. 1998) and *Faint Images of the Radio Sky at Twenty-Centimeters* (FIRST; Becker et al. 1995), in addition to the upcoming ASKAP *Evolutionary Map of the Universe* survey (EMU; Norris et al. 2011), will predominately lie close to the detection limit. The weaker sources populating these surveys are expected to be predominately FR-Is (Willman et al. 2008), or perhaps FR0s (Baldi et al. 2016) if these are completely separate populations. The measured length of most radio sources detected in these surveys is thus likely to be a lower limit on the true source size. Extended sources comprising multiple beams may still be detectable even if the flux density in each beam is below the survey detection limits, i.e. several beams with flux densities below the minimum sensitivity will have correlated "noise" and may yield a statistically significant detection (better uv coverage will more directly improve this situation). In general, simulating these flaring jet radio sources using my dynamical

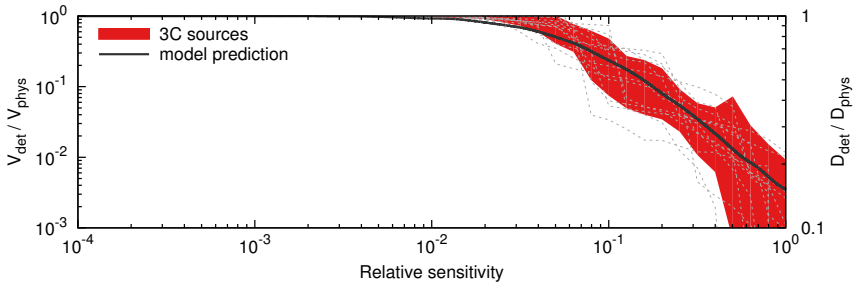

Figure 4.19: Volume of flaring jet and core dominated radio sources in the 3C survey detected as a function of the survey sensitivity. The left-hand vertical axis shows the fraction of the "total" lobe volume detectable by a beam of arbitrary size for various survey sensitivities; the sensitivity scale for every source is shifted so that all the profiles lie on top of each other. The right-hand vertical axis similarly shows the fraction of the lobe length detectable. The grey dashed lines show the tracks of a each 3C radio lobe in this phase-space, with the red shading indicating the 1σ spread in the distribution. The solid black line plots the theoretical expectation from my model, using the average redshift and age of the sources in the plot.

and resolved emissivity models should provide a means to constrain their energetics by fitting their observed surface brightness profile.

4.5.5 Sensitivity limited feedback energetics

The kinetic-mode of feedback is the main mechanism though which AGN impart energy into their host environments since $z = 1$; specifically the clearing out the hot gas at cluster centres through radio bubbles, or directly through shock heating in FR-IIs and the viscous dissipation of sound waves in FR-Is (Bower et al. 2006; Croton et al. 2006, 2016; Shabala & Alexander 2009a; Fanidakis et al. 2011; Fabian 2012; Dubois et al. 2013; Vogelsberger et al. 2014; Schaye et al. 2015). The radio-only observations of the lobe volume are susceptible to surface brightness sensitivity limits, but in practice X-rays are generally used to directly measure the gas displaced from the cluster centre (e.g. Boehringer et al. 1993; Fabian et al. 2000, 2003; Fabian 2012). However, the energy input directly through the FR-I/II jets is determined based upon the properties of the radio source, including its length and width; these are dependent on the sensitivity limit, potentially leading to a similar dependency for the energy.

The uncertainty in measuring the energy input by powerful FR-IIs directly into their environments through shock heating is quantified by fitting the jet powers, ages and

magnetic field strengths of the 3C sources (see Chapter 3). These parameters describing the AGN energetics are fitted for a range of axis ratios (A = 2, 4, 6 and 8) to enable their variation with the measured lobe width to be characterised. The jet power is found to scale with the axis ratio as $Q \propto A^{1.08\pm0.09}$ whilst the source age is inversely related as $t \propto A^{-1.07\pm0.02}$. As a result, the energy input directly by the jet into the host environment is independent of the axis ratio measurement within 1σ uncertainties. By contrast, the magnetic field strength is somewhat dependent on the axis ratio, with the equipartition factor increasing as $B/B_{\rm eq} \propto A^{0.21\pm0.02}$. However, the axis ratio should be correct to within a factor of a few leading to only a modest error in the magnetic field strength. The feedback energetics measured for shock heating in FR-IIs (using dynamical models) is therefore quite robust to the surface brightness sensitivity limit. Note however that the efficiency with which jet energy can couple to the gas will depend on the details of the energy injection (Omma et al. 2004; Mukherjee et al. 2016).

The dependences of the jet power and source age on the measured source size are difficult to disentangle for FR-Is. Instead, the total energy must be directly related to the source size as $E \propto D^{3-\beta-\xi}$ as derived from the subsonic limit of the FR-II/I lobed dynamical model. The energy input by the jet therefore depends on the measured source size as $E \propto D^2$ for typical FR-I environments with $\beta + \xi \sim 1$. The measured feedback energy is thus related to the surface brightness sensitivity limit (see Section 4.5.4) as $E \propto S^{(\beta+\xi-3)/(\beta+\xi+1)}$, or $E \propto S^{-1}$ for typical environments. The size of 3C sources can plausibly be underestimated by at least factor of ten (see Figure 4.19), corresponding to a factor of 100 underestimate in the feedback energy input directly from the source. Hence, it is possible that FR-Is impart feedback on significantly larger scales than inferred from their small observable sizes (see also Shabala et al. 2017).

4.6 Conclusions

I have presented a new synchrotron emissivity model that can be applied to mock radio lobes from existing hydrodynamical simulations and analytical models. The resolved emissivity model considers: (1) radiative loss processes as a function of position, (2) lobe dynamics in an arbitrary atmosphere, and (3) an analytical framework for dynamics and synchrotron emission. The large-scale dynamics of the radio lobe is modelled in this work following the method described in Chapter 2. Meanwhile, the bulk flow and dispersion of the synchrotron-emitting electrons is tracked through the lobes using two-dimensional hydrodynamical simulations with a large number of

tracer fields, with simulation results incorporated in the analytical model.

JP ageing model inappropriate for resolved FR-IIs— The resolved emissivity model was applied to the lobed (FR-II) and flaring jet (FR-I) dynamical models to reproduce observations of 3C436 and 3C31 respectively, to demonstrate the validity of these models. Specifically the model can reproduce: (1) the 608 MHz surface brightness map of 3C31, and (2) the spatial distribution of spectral ages in 3C436 inferred from X-ray observations. I find that the oldest electron ages measured by fitting the JP model to the spectra across the 3C436 radio lobes are a factor of a few younger than its dynamical age. This discrepancy seen in lobed FR-IIs is due to a violation of the JP model assumption that all electrons contributing to the SED are of similar age; their well-mixed lobes ensure electrons at least as young as half the source age are present at every point in the lobe.

FR-I size and FR-II width vary with sensitivity (and frequency)— Limitations in measuring AGN energetics with future radio surveys were quantified using the resolved emissivity model and my dynamical models. In particular, the observed size and imparted feedback energy from FR-Is sources is dependent on the survey surface brightness detection limit, S, reducing as $D \propto S^{-0.5}$ and $E \propto S^{-1}$ respectively for typical environments, though the frequency-dependent loss mechanisms also are important. Meanwhile, the observed lobe widths of FR-IIs are up to ten times narrower than the physical width when viewed close to the survey detection limit. The axis ratio of these objects is also a strong function of the observing frequency.

GPS and CSS sources are cores of FR-Is?— The emerging FR0 class of radio sources (Ghisellini 2011), comprising gigahertz peaked and compact steep spectrum sources (GPS and CSS), may be explained by a population of low powered FR-Is. My modelling predicts that, for uncollimated jets close to the detection limit, the surface brightness of the radio emission decreases rapidly with distance. Moreover, the radio SED is dominated by the luminosity from the younger electrons near the core acceleration site; a high-frequency turnover will not be detected in the spectra of FR-Is, with the host environment instead affecting the lower frequencies through free-free and synchrotron self-absorption.

Low powered FR-I and FR0 type objects are expected to comprise the vast majority of radio sources identified in next-generation surveys such as ASKAP EMU and MeerKAT MIGHTEE. Developing a greater understanding of the observational limitations encountered when measuring the properties of these objects in particular is therefore crucial. The analytical model presented in this work is intended as a step in this direction; I have shown it can accurately determine the energetics of large

numbers of radio AGN using an (mostly) analytical model.

Chapter 5

Radio AGN as Standard Candles

Immensely bright quasars and radio-loud active galactic nuclei (AGNs) provide an enticing opportunity to construct standard candles detectable up to the very early universe. In this chapter, I present a new technique for creating standardisable candles from radio observations of the very large synchrotron emission lobes inflated by the most powerful AGNs; specifically this method uses radio flux density, lobe angular size, and the radio SED spectral index and break frequency. The theory behind this method is described in Section 5.1 using a simplified analytic form of the radio source dynamical model developed in Chapter 2. The radio source environments assumed for the dynamical model are discussed in Section 5.2 and the other parameters in the Bayesian fitting algorithm for the observer-to-source distance are detailed in Section 5.3. In Section 5.4, radio photometric redshifts are derived for radio sources taken from a survey covering redshift $0 < z < 2$, and then in Section 5.5, the ability of these distance measures to constrain cosmological parameters is tested. Finally, in Section 5.6, standard candles are constructed from the objects in the high-redshift HeRGE survey, enabling tight constraints to be placed on the energy and matter content of the universe. I conclude by comparing results from this method with other astrophysical techniques.

5.1 Constructing radio AGN standardisable candles

The giant radio lobes emanating from the nuclei of active galaxies are well modelled, both analytically (e.g. Chapter 2; Kaiser & Alexander 1997; Blundell et al. 1999; Luo & Sadler 2010) and numerically (e.g. Krause et al. 2012; Hardcastle & Krause 2013, 2014), enabling intrinsic parameters such the source age and power to be estimated from observables. In this section, I develop a technique for measuring the distance to

these powerful FR-II radio sources based on observables including their flux density, angular size and spectral energy distribution.

5.1.1 Distances in the ΛCDM cosmology

The standard concordance model of Big Bang cosmology is the ΛCDM (Lambda cold dark matter) model, in which the universe contains dark energy and matter at densities Ω_Λ and Ω_m respectively. Distance measures depend crucially on the values of the cosmological parameters; the Hubble constant H_0 describes the expansion rate of the universe whilst the energy and matter densities parametrise its shape.

The Hubble distance is defined in terms of the Hubble constant H_0 and speed of light c through the relation

$$d_\mathrm{H} = \frac{c}{H_0}. \tag{5.1}$$

The comoving distance, the distance between two objects as measured at the present cosmological time, is related to the Hubble distance d_H through

$$d_\mathrm{C}(z) = d_\mathrm{H} \int_0^z \frac{dz'}{\sqrt{\Omega_\mathrm{m}(1+z')^3 + \Omega_\mathrm{k}(1+z')^2 + \Omega_\Lambda}}, \tag{5.2}$$

where the denominator is the cosmic evolution of the Hubble constant (i.e. $E(z) = H(z)/H_0$), $\Omega_\mathrm{k} = 1 - \Omega_\mathrm{m} - \Omega_\Lambda$ describes the curvature of the universe, and z is the redshift. In a flat universe $\Omega_\mathrm{k} = 0$, for an open (hyperbolic) universe $\Omega_\mathrm{k} > 0$ and for a closed (spherical) universe $\Omega_\mathrm{k} < 0$. This curvature of the universe is considered in the modified form of the comoving distance, the transverse comoving distance:

$$d_\mathrm{M}(z) = \begin{cases} \frac{d_\mathrm{H}}{\sqrt{\Omega_\mathrm{k}}} \sinh(\sqrt{\Omega_\mathrm{k}} d_\mathrm{C}(z)/d_\mathrm{H}) & \text{if } \Omega_\mathrm{k} > 0 \\ d_\mathrm{C}(z) & \text{if } \Omega_\mathrm{k} = 0 \\ \frac{d_\mathrm{H}}{\sqrt{\Omega_\mathrm{k}}} \sin(\sqrt{-\Omega_\mathrm{k}} d_\mathrm{C}(z)/d_\mathrm{H}) & \text{if } \Omega_\mathrm{k} < 0. \end{cases} \tag{5.3}$$

The angular diameter and luminosity distances are directly related to this distance and the redshift as

$$\begin{aligned} d_\mathrm{A}(z) &= \frac{d_\mathrm{M}(z)}{1+z} \\ d_\mathrm{L}(z) &= (1+z) d_\mathrm{M}(z). \end{aligned} \tag{5.4}$$

These two distances may be constrained for an observed radio source based on its physical size D and luminosity L_ν, where ν is the observing frequency. The measured angular size θ and flux density S_ν are related to their intrinsic counterparts as

$$\begin{aligned} D &= d_{\rm A}(z)\theta = \frac{d_{\rm M}(z)\theta}{1+z} \\ L_\nu &= 4\pi {d_{\rm L}}^2(z) S_\nu = 4\pi (1+z)^2 {d_{\rm M}}^2(z) S_\nu. \end{aligned} \tag{5.5}$$

The physical source size and luminosity map to the redshift and transverse comoving distance with different functional dependencies; hence we can use their combination to constrain either redshift or the cosmology. The complication is that the relationship between size and luminosity depends both on properties of the radio galaxy (e.g. jet kinetic power and environment) and the temporal evolution of the lobes.

5.1.2 Standard candles from analytic AGN models

The injection of particles into the radio lobe produces an initial power law distribution of electron energies $N(E) = N_0 E^{-s}$, where N_0 is a constant and $s = 2\alpha_{\rm inj} + 1$ for injection-time spectral index $\alpha_{\rm inj} > 0$. The population of synchrotron-emitting electrons has a minimum and maximum particle energy, $\gamma_{\rm min}$ and $\gamma_{\rm max}$ respectively; the low-energy cut-off is observationally constrained to lie between approximately 100 and 1000 (Godfrey et al. 2009). The luminosity arising from the synchrotron-emitting electrons in the lobes of powerful radio sources is a function of the observing frequency ν, energetics of the electron population, and the shape and pressure of the lobe. Alexander (2000) derived the luminosity for self-similar FR-II radio sources expanding into a power law environment (i.e. $\rho \propto r^{-\beta}$) assuming no radiative loss processes:

$$L_\nu = \frac{f_1(\gamma_{\rm min}, s)\, \nu^{-(s-1)/2}}{A^2 \chi^{(s+5)/4}} \left(\frac{q\rho}{q+1}\right)^{(s+5)/4} t^{-(s+5)/2} D^{(22+2s-s\beta-5\beta)/4}, \tag{5.6}$$

where D is the physical source size, t is the source dynamical age, ρ is the density of the host galaxy environment, and q is the ratio of energy in the magnetic field to that in the particles. Here, A is the axis ratio of the lobe (i.e. length divided by radius) and χ is the ratio of the hotspot-to-lobe pressures, which is a complicated function of the axis ratio (e.g. Kaiser & Alexander 1999). Finally, the function $f_1(\gamma_{\rm min}, s)$, and later f_2 and f_3, describe the properties of the synchrotron-emitting electron energy distribution.

The lobe pressure of the FR-II is similarly derived in terms of the source age, size and host environment as (c.f. dynamical model in Chapter 2)

$$p = \kappa_1 \rho t^{3(\beta-2)/(5-\beta)} D^{2-\beta}, \tag{5.7}$$

where κ_1, and later κ_2 and κ_3, are constants of proportionality. The lobe magnetic field strength $B = \sqrt{2\mu_0 u_\mathrm{B}}$ follows directly from this equation and the relationship between the pressure and energy density of the magnetic field u_B (Equation 15 of Kaiser et al. 1997). That is,

$$B = \kappa_2 \left(\frac{q\rho}{q+1}\right)^{1/2} t^{3(\beta-2)/2(5-\beta)} D^{(2-\beta)/2}. \tag{5.8}$$

The relationship between the physical size and luminosity as it stands is a function of variables which can largely be constrained observationally, or statistically using a prior probability distribution. The exception to this is the source dynamical age, which cannot be directly measured and can vary by several orders of magnitude in observed sources. The spectral, and thus dynamical age ($t = \tau$, see Chapter 3), of the radio source is related to the break frequency in the observer frame ν_b through

$$\tau = \frac{\upsilon B^{1/2}}{B^2 + {B_\mathrm{ic}}^2} \left[\nu_\mathrm{b}(1+z)\right]^{-1/2}, \tag{5.9}$$

where B is the average lobe magnetic field strength, $B_\mathrm{ic} = 0.318(1+z)^2\,\mathrm{nT}$ is the magnitude of the magnetic field equivalent to the microwave background, and the constant υ is defined in Equation 3.7 of Chapter 3. For powerful FR-II radio sources the lobe magnetic field strength is much greater than the field equivalent to the cosmic microwave background (i.e. $B \gg B_\mathrm{ic}$). This is true even at high redshifts where the microwave background radiation is much stronger because still greater lobe field strengths are required for the source to have detectable luminosity. Substituting the lobe field strength of Equation 5.8 into Equation 5.9 gives an expression for the source dynamical age as a function of size and known parameters:

$$t = \kappa_3 \left[\left(\frac{q\rho}{q+1}\right)^3 \left[\nu_\mathrm{b}(1+z)\right]^2 D^{3(2-\beta)} \right]^{(\beta-5)/(5\beta+2)}. \tag{5.10}$$

The radio source luminosity and physical size can thus be related to each other and the spectral break frequency observable by substituting this Equation 5.10 into Equation 5.6. That is,

$$L_\nu = \frac{f_2(\gamma_{\rm min}, s)\,\nu^{-(s-1)/2}}{A^2\chi^{(s+5)/4}} \left(\frac{q\rho}{q+1}\right)^w [\nu_{\rm b}(1+z)]^x D^y, \tag{5.11}$$

where the exponents w, x and y are constant functions of s and β defined as

$$\begin{aligned} w &= \frac{(s+5)(32-\beta)}{4(5\beta+2)} \\ x &= \frac{(s+5)(5-\beta)}{(5\beta+2)} \\ y &= \frac{344+64s-110\beta-34s\beta+5\beta^2+s\beta^2}{4(5\beta+2)}. \end{aligned} \tag{5.12}$$

Here, the exponent of the electron energy distribution takes values between $s = 2$ and 3, whilst the slope of the host gas density profile steepens from $\beta \gtrsim 0$ near the core to $\beta = 2$ at higher radii.

The expressions in Equation 5.5 for the radio source luminosity and physical size can now be coupled using Equation 5.11. We thus arrive at a relation for the transverse comoving distance in terms of the source flux density, angular size, spectral break frequency and redshift observables. That is,

$$\begin{aligned} d_{\rm M}(z) =& \left[A^2\chi^{(s+5)/4} f_3(\gamma_{\rm min}, s)\,\nu^{(s-1)/2} S_\nu\right]^{-1/(2-y)} \\ &\times\ \theta^{y/(2-y)} {\nu_{\rm b}}^{x/(2-y)} \left(\frac{q\rho}{q+1}\right)^{w/(2-y)} (1+z)^{(x-y-2)/(2-y)}. \end{aligned} \tag{5.13}$$

The exponents of the flux density, angular size, break frequency, gas density and equipartition factor, and redshift terms are computed in Table 5.1 for typical values of s and β. The transverse comoving distance is strongly related to the angular size, gas density and equipartition factor, and moderately dependent on both the break frequency and redshift. By contrast, it has a very weak dependence on the flux density, shape of the lobe, and properties of the electron distribution (e.g. $\gamma_{\rm min}$). The dynamical model developed in Chapter 2, although more sophisticated in its treatment of the host environment and lobe dynamics, is expected to have at least somewhat similar dependences to the simpler analytical model used here in this theoretical study.

Table 5.1: Density and equipartition factor, spectral break frequency, and source size exponents, x, y and z respectively, for typical values of s and β.

		S_ν, A	θ	ν_b	q, ρ	$1+z$
β	s	$\frac{-1}{2-y}$	$\frac{y}{2-y}$	$\frac{x}{2-y}$	$\frac{w}{2-y}$	$\frac{x-y-2}{2-y}$
0.5	2	0.05	-1.10	-0.36	-0.63	0.85
0.5	3	0.05	-1.09	-0.36	-0.64	0.82
1	2	0.11	-1.23	-0.46	-0.89	1.00
1	3	0.10	-1.20	-0.46	-0.90	0.94
1.5	2	0.26	-1.53	-0.68	-1.47	1.37
1.5	3	0.24	-1.48	-0.70	-1.53	1.25

5.2 Redshift and Hubble dependence of host environments

The dependence of the radio source host environment on cosmology and redshift must be quantified if either of these parameters is to be constrained observationally. In this section, I use the Bolshoi dark matter simulation (Klypin et al. 2011) and semi-analytic galaxy evolution models (SAGE; Croton et al. 2016) to simulate realistic galaxy populations. Relationships between the observables used to characterise the environment and the shape of the density and temperature profiles are explored.

5.2.1 Host environment properties

The expansion of radio sources is greatly impacted by the host environment into which they expand. The properties of this ambient medium are typically summarised in dynamical models by a spherically symmetric density (Kaiser & Alexander 1997; Hardcastle & Krause 2013) and temperature profile (Chapter 2). In this thesis, density profiles are generated for observed sources based on their stellar mass, which is typically measured by optical or near-infrared photometry. Semi-analytic galaxy evolution models provide a conversion to the mass and radius of the dark matter halo, as described in Section 5.2.2. The gas mass is then derived using a further relation between the gas fraction and the halo mass.

Bolshoi dark matter simulation

The semi-analytic galaxy evolution (SAGE; Croton et al. 2016) model (update of original model; Croton et al. 2006) traces the evolutionary history of baryonic matter on top of existing large scale simulations of the dark matter, e.g. the Millennium or Bolshoi simulations. In this work I use the Bolshoi model (Klypin et al. 2011) to construct the dark matter framework for SAGE. This simulation traces the galaxies in a box of side length $250\,\mathrm{Mpc}/h$ through cosmic time with outputs at regular intervals in redshift. The Bolshoi dark matter simulation assumes a WMAP5 cosmology with $\Omega_\mathrm{m} = 0.27$, $\Omega_\Lambda = 0.73$, $\Omega_\mathrm{b} = 0.0469$, $\sigma_8 = 0.82$, $h = 0.70$ and $n = 0.95$.

Host environment relations

Relationships between the stellar mass observable and the relevant halo mass and gas fraction must be derived in order to construct host galaxy environments for observed radio sources. Bolshoi simulation outputs at 15 redshifts up to $z = 5$ are run through SAGE to obtain mock galaxy populations across cosmic time. The relationship between the stellar mass and halo mass is investigated by binning galaxies every 0.1 dex in mass and calculating the median and percentiles of the distribution. In Figure 5.1 an example of the stellar-halo mass phase space and these statistics is shown for the redshift $z = 1$ snapshot. The relationship between the two masses can be fitted based on the medians in the mass bins, and the redshift dependence included by fitting data across the 15 redshift snapshots (see Section 5.2.2). The gas fraction relationship is similarly derived by binning the halo masses and calculating the median and percentiles of the distribution.

Gas density profile

The gas density and temperature profiles are calculated using the Vikhlinin et al. (2006) cluster observations following the method described in Chapter 2. They found the same shape profile could fit clusters with very different masses by scaling the core density or temperature to the virial radius of the halo. The mass and virial radius of dark matter haloes simulated using semi-analytic galaxy evolution models varies greatly with cosmology. The effect different cosmologies have on the density profile therefore needs to be considered if these environments are to be used to construct standardisable candles.

The properties of the host environment are characterised observationally using the

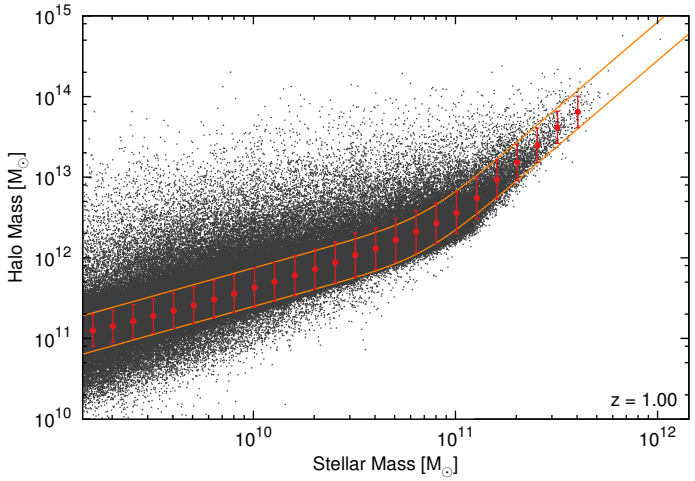

Figure 5.1: Mock brightest cluster galaxies at redshift $z = 1$ taken from the semi-analytic galaxy evolution (SAGE) model in halo mass–stellar mass space (fine grey points). The red circles plot the median halo mass in each 0.1 dex wide stellar mass bin, with the errorbars showing the 1σ uncertainty in the distribution. The orange lines are fits to the medians plus or minus fits to the uncertainties as a function of stellar mass and redshift.

stellar mass which is converted into a halo mass using semi-analytic models. The virial radius of the halo is then calculated from its mass and the cosmic evolution of the Hubble constant $H(z)$ through

$$r_{\rm halo} = \left(\frac{G M_{\rm halo}}{100 H^2(z)} \right)^{1/3}, \tag{5.14}$$

where G is Newton's gravitation constant, and $M_{\rm halo}$ is the simulated dark matter halo mass taken from the SAGE model. This halo mass is inversely proportional to the Hubble constant (i.e. $H(z) = H_0 E(z)$ Croton et al. 2016), and so it follows from the above equation that the virial radius also has the same dependence. The total matter density at an arbitrary radius a of a halo modelled by a simple power law density profile (i.e. $\rho \propto r^{-\alpha}$) is thus dependent on the cosmology as

$$\begin{aligned} \rho(a) =& \frac{M_{\rm halo}}{4\pi\delta(z)} \Big/ \int_0^{r_{\rm halo}/\delta(z)} \frac{\rho(r) r^2 dr}{\rho(a)} \\ =& \frac{(3-\alpha)\delta^{2-\alpha}(z)}{4\pi a^\alpha} \frac{M_{\rm halo}}{{r_{\rm halo}}^{3-\alpha}}, \end{aligned} \tag{5.15}$$

where $\delta(z)$ is the fractional difference between the Hubble constant for a trial cosmology and that used in the SAGE model (e.g. due to different h, $\Omega_{\rm m}$ or Ω_Λ).

The density profile of dark matter haloes is known to steepen from $\alpha = 1$ at the core to $\alpha = 3$ at high radii (Navarro et al. 1997, NFW) with an average slope of $\alpha \sim 2$. The dark matter density and thus total matter density in haloes is therefore largely unaffected by moderate changes to the Hubble constant, dark energy density and matter density. The conversion from total matter density to baryonic gas density does not affect this result; the simulated gas fraction is constant irrespective of cosmology and observed clusters have comparable gas density profiles to the NFW dark matter profile. The sensitivity of my results to any such relations is fully tested on simulated data in Section 5.5 before analysing real sources.

5.2.2 Functional form of redshift dependence

The numerical form of the stellar-halo mass relationship and the gas fraction needs to be represented by an analytic expression, both to enable faster computation times and allow interpolation between redshift and stellar mass bins. These relationships and their uncertainty functions are fitted using multivariate regressions of an appropriate functional form.

Stellar–halo mass relationship

The mass of the dark matter halo as a function of galaxy stellar mass is found using the SAGE mock galaxies to be well fitted by a broken power law of the form:

$$M_{\rm halo} = \frac{10^{12.78-8.88a_0(z)} {M_\star}^{a_0(z)}}{\left(1 + [M_\star/M_{\rm crit}(z)]^4\right)^{a_0(z)/4-a_1(z)/4}}, \tag{5.16}$$

where $M_{\rm halo}$ and the stellar mass $M_\star$ are in solar masses, and $a_0(z)$, $a_1(z)$ and $M_{\rm crit}(z)$ are functions of redshift. The redshift dependence of these coefficients is simply fitted with polynomials enabling the simulated evolution in the relationship to be precisely matched whilst also permitting interpolation (shown in Table 5.2). This relationship is derived for a Hubble constant of $H_0 = 70\,{\rm km\,s^{-1}\,Mpc^{-1}}$, it can be easily modified to different cosmologies by multiplying both masses by $0.70/h$. The Bolshoi model output cannot be as easily corrected for different energy and matter densities; the sensitivity of my analysis to the cosmology assumed for the environment is tested for simulated radio sources.

Table 5.2: Functional form of the coefficients in the stellar-halo mass relationship of Equation 5.16. The first column lists the redshift dependent coefficient, columns three through six the constants of the polynomial fits, and the second column lists any transformations applied to these functions. The second cubic for the critical mass is not well constrained at higher redshifts since the turnover is pushed outside the range of simulated masses; this is of no consequence when simulating host environments within this mass range.

Function	Prefix	z^0	z^1	z^2	z^3
$a_0(z)$	...	0.62	0.08	...	...
$a_1(z)$	max{	3.02	-0.87	...	...
		1.13	...	...	...
$M_{\rm crit}(z)$	$10^{\rm max\{}$	10.92	-0.04	0.03	-0.05
		5.95	3.49	-1.05	0.12

The spread in the halo masses around the fit line is calculated by fitting the 1σ uncertainty in these estimates as a function of redshift. The spread is approximately constant in log-space for all stellar mass bins across cosmic time. The redshift dependence of the uncertainty in halo masses around the fit line of Equation 5.16 is thus fitted with the quadratic $\delta M_{\rm halo} = 0.30 - 0.07z + 0.01z^2$ dex.

The functional form of the stellar–halo mass relationship described in Equation 5.16 is plotted as a function of redshift in Figure 5.2. The halo mass at a given stellar mass increases with redshift for stellar masses below the break. By contrast, above the break the halo mass decreases with redshift.

Although the stellar mass is the observable and thus logically the independent variable, the halo mass is perhaps a more suitable choice when considering the physics of galaxy evolution. Below the break in the function, the stellar mass for a given halo mass increases with decreasing redshift. That is, galaxies in the present universe have more stars than those at higher redshifts. By contrast, in more massive haloes the stellar mass decreases with decreasing redshift. This is due to the inclusion of AGN feedback in SAGE. The stellar–halo mass relationship considered here may depend on the feedback implementation in SAGE, however as discussed in the following section the gas density scaling derived from this relation is purely cosmetic. The shape of the pressure profile encountered by an expanding radio lobe is however expected to vary somewhat over the 10^{12} to $10^{15}\,{\rm M}_\odot$ range of plausible halo masses, though not appreciably for some small error in the stellar–halo mass relationship.

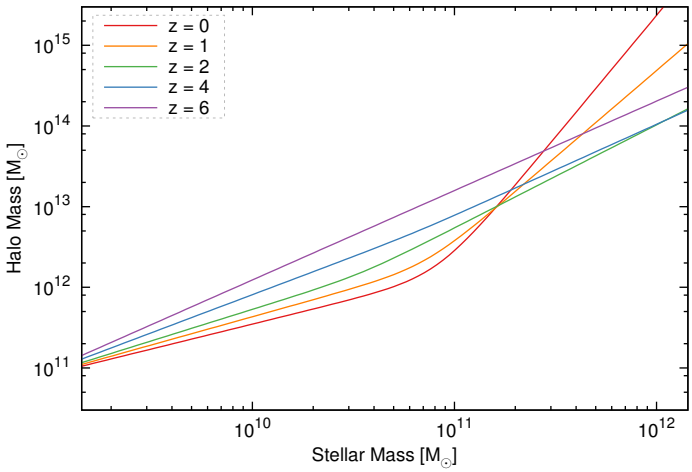

Figure 5.2: Simulated relationship between galaxy stellar mass and the mass of the dark matter halo for brightest cluster galaxies (BCGs). These functions are fits to the median halo mass of the mock galaxies at each stellar mass taken from the semi-analytic galaxy evolution model (SAGE). The line colours show this relationship at five redshifts $z = 0$, 1, 2, 4 and 6. The stellar and halo masses in this plot assume a Hubble constant of $70\,\mathrm{km\,s^{-1}\,Mpc^{-1}}$ and both scale as h^{-1}.

Gas fraction

The gas fraction within the virial radius of the dark matter halo is derived as a function of redshift and halo mass using the mock galaxies obtained from SAGE. These gas fractions are considerably higher than the cosmic baryon fraction (Komatsu et al. 2011); it is therefore not sensible to use them in their raw form. By contrast observations of the gas fraction in massive haloes (e.g. McGaugh et al. 2010; Gonzalez et al. 2013) are limited to low-redshift objects. Taking gas fractions directly from SAGE also has the significant advantage that the same overdensity is used when defining the virial radius for all quantities. The raw gas fractions taken from SAGE are therefore scaled based on low-redshift observations (Gonzalez et al. 2013). The gas fraction is correspondingly scaled by the same factor. These modified SAGE gas fractions are comparable to the low-redshift observations in massive haloes ($M_{\mathrm{halo}} > 10^{13}\,\mathrm{M_\odot}$) but overestimate the matter content in less massive spirals.

The scaling of the gas density in this work is purely cosmetic since the density and equipartition factor appear together in the distance measure equation; an incorrect gas density ρ will be entirely corrected for by the equipartition factor q (see Equation 5.13). In principle, the two could be separated either by taking X-ray inverse-Compton

Table 5.3: Functional form of coefficients in the gas fraction relationship. The column descriptions are the same as for Table 5.2.

Function	Prefix	z^0	z^1
$b_0(z)$	max{	-0.88	-0.03
		-0.92	0.001
$b_1(z)$	...	0.05	...

measurements to constrain the lobe magnetic field strength or by measuring the density profile of the cluster directly. The host environment is still very important since the rate at which the density falls-off with galactocentric radius has a profound effect on the radio source evolution. In other words, it is the shape of the profile that matters, not the gas density (at least within a factor of a few).

The relation between the gas fraction, halo mass and redshift is fitted using a multivariate regression of the form:

$$f_{\rm gas} = 10^{b_0(z)-14b_1(z)} {M_{\rm halo}}^{b_1(z)}, \tag{5.17}$$

where $M_{\rm halo}$ is in solar masses, and $b_0(z)$ and $b_1(z)$ are functions of redshift. The redshift dependences of these coefficients are fitted with polynomials, as shown in Table 5.3. The uncertainty in the distribution of gas fractions is approximately constant in log-space across all halo mass bins for each redshift. The spread of gas fractions around the fit of Equation 5.17 is thus found to depend on redshift as $\delta f_{\rm gas} = 0.05 - 0.002z$ dex.

The best fit relationship describing the gas fraction (Equation 5.17) is plotted as a function of redshift in Figure 5.3. The dependence of the gas fraction on the halo mass is very consistent across cosmic time (see Table 5.3). The gas fraction content is however a weak function of redshift; low-redshift haloes have marginally more associated gas than their high-redshift counterparts. The rise in the gas fraction occurs mostly between redshifts $z = 1$ and 0, likely a result AGN feedback suppressing the formation of stars from the interstellar gas.

5.2.3 Stellar mass observations

The properties of the radio source environment are constrained using relationships in terms of the stellar mass of the associated host galaxy. The stellar mass of this galaxy may be measured using optical or near-infrared photometry, if available (see

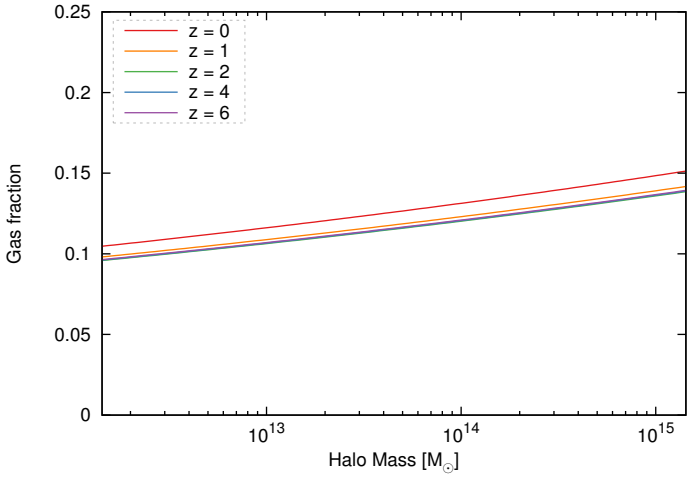

Figure 5.3: Simulated relationship between average gas fraction within the virial radius of the dark matter halo as a function of the halo mass. The halo mass assumes a Hubble constant of $70\,\mathrm{km\,s^{-1}\,Mpc^{-1}}$ and scales as h^{-1}. Same as Figure 5.2.

Section 5.3). The magnitudes at a single band (e.g. K band) may be converted to mass using a stellar population model (e.g. Bruzual & Charlot 2003), though several bands are often used to distinguish the spectral energy distributions of different age populations. The stellar mass calculated from these magnitudes will vary if either the redshift or cosmology is unknown due to: (1) the luminosity distance, and potentially (2) k-corrections to the observing filter frequency. The host galaxy stellar mass can be related to the redshift dependent k-correction $kcor_\lambda$ and the luminosity distance d_{pc} (in parsecs) through (Longhetti & Saracco 2009)

$$\log(M_\star) = \log(M/\mathcal{L}_\lambda) + 2\log(d_{\mathrm{pc}}) - 2.0 + 0.4kcor_\lambda + 0.4\mathcal{M}_\lambda^{\mathrm{sun}} - 0.4m_{\lambda'}, \qquad (5.18)$$

where $M/\mathcal{L}_\lambda$ is the mass-to-light ratio, $\mathcal{M}_\lambda^{\mathrm{sun}}$ is the absolute magnitude of the sun, and $m_{\lambda'}$ is the apparent magnitude of the source at the redshifted frequency. These other observables should be constant irrespective of the redshift or distance to the galaxy. The k-corrections should not be affected by the cosmology since they only relate to the redshifting of light. The stellar masses of real or simulated radio source host galaxies therefore need to be modified for both the luminosity distance and k-corrections of any trial redshift. The stellar masses similarly need to be corrected for the luminosity distance between cosmologies.

5.3 Bayesian fitting algorithms

The evolution of powerful radio sources is simulated for a grid of jet powers Q, source ages t, equipartition factors q, and either the redshift z or transverse comoving distance $d_{\rm M}$. Each of these parameters is simulated uniformly in log-space at a resolution finer than 0.1 dex; specifically $\triangle Q = 0.1\,\mathrm{dex}$, $\triangle t = 0.05\,\mathrm{dex}$, $\triangle q = 0.1\,\mathrm{dex}$, and $\triangle z = 0.01\,\mathrm{dex}$ (or $\triangle d_{\rm M}$). The external pressure profile for radio sources with these intrinsic parameters is simulated with 5128 variations following a random normal distribution (see Section 5.2). The goodness of the fit of the simulated radio source for each such environment to the observed source angular size θ, flux density S_ν and observer-frame spectral break frequency $\nu_{\rm b}$ is assessed using the χ^2 statistic,

$$\chi^2 = \sum_{x=\theta,S_\nu,\nu_{\rm b}} \left(\frac{x_{\rm pred} - x_{\rm obs}}{\sigma_{\rm x}} \right)^2, \tag{5.19}$$

where $x_{\rm obs}$ and $x_{\rm pred}$ are the observed and simulated values of each of the three observables, and $\sigma_{\rm x}$ is the model uncertainty. The likelihood of each simulation matching the observations is $\mathcal{P} = e^{-\chi^2/2}$, with the total probability for each set of intrinsic parameters found by summing the probabilities over the 5128 environments. This yields a joint probability distribution $\mathcal{P}(Q,t,q,z)$ or $\mathcal{P}(Q,t,q,d_{\rm M})$. Some of the variables in the dynamical model remain unconstrained, in particular the properties of the electron energy distribution. The range of values assumed for these parameters is based on measurements of real radio sources, as discussed in Section 5.3.3.

In Chapter 2, I proceeded to fit the intrinsic parameters by marginalising over this probability distribution. Unfortunately, when using observer-frame quantities (e.g. flux density rather than luminosity), many of the intrinsic parameters are expected to be at least somewhat degenerate (see Section 5.3.1). This leads to a ridge of moderate probability across the distribution rather than a tight Gaussian peak. The true peak will still be associated with a strong local maximum along this ridge, but the absolute maximum of the distribution may lie elsewhere if the degenerate nature of the parameters preferences extreme values. It is therefore necessary to correct for the bias introduced by the degeneracy between parameters before the true peak of the probability distribution can be found.

5.3.1 Parallel constraint vectors

The Bayesian fitting algorithm may not always be capable of correctly determining the distance to the radio source if varying the intrinsic source properties affects the

observables the same as a change in distance. In particular, increasing the source age is theoretically expected to result in a larger source size, lower luminosity due to the loss processes, and a lower spectral break frequency. These correspond to larger observed angular size, lower flux density, and lower observer-frame spectral break. However, increasing the distance to a high-redshift ($z \gg 1.7$) radio source yields the same observations. By contrast, the angular size of a low-redshift radio source decreases as the source is moved to a greater distance. It is necessary therefore to assess at which redshifts (or distances) the fitting algorithm is stable; i.e. at which redshifts the vector of observables move in the same direction for either a small change in distance or an intrinsic parameter. This is quantified by calculating the derivative of this constraint vector with respect to the distance measure and the intrinsic parameters.

The log-space derivatives of the observables are calculated for a small change in the redshift of the radio source (or the transverse comoving distance to within a constant) using the analytic form of the transverse comoving distance of Equation 5.13. These derivatives estimate the measured uncertainty required to yield a given error in the estimated redshift of the source. That is,

$$\frac{\delta \log \mathbf{v}}{\delta \log z} = \begin{bmatrix} -2z\ln(10)\left(\frac{1}{1+z} + \frac{1}{d_{\mathrm{M}}(z)}\frac{d[d_{\mathrm{M}}(z)]}{dz}\right) \\ z\ln(10)\left(\frac{1}{1+z} - \frac{1}{d_{\mathrm{M}}(z)}\frac{d[d_{\mathrm{M}}(z)]}{dz}\right) \\ -\ln(10)\frac{z}{1+z} \end{bmatrix}, \tag{5.20}$$

where $\mathbf{v} = \begin{bmatrix} S_\nu & \theta & \nu_{\mathrm{b}} \end{bmatrix}^T$ is the column vector of observables. Here, log is the base-ten logarithm, ln is the natural logarithm, and the units of the log-space derivatives are dex^{-1}. The stability of the Bayesian fitting algorithm is compromised if this three-dimensional vector can be easily replicated by any variation of the intrinsic source parameters, i.e. source age, jet power, density and equipartition factor. In particular, the derivatives of the observables with respect to the source age are given by

$$\frac{\delta \log \mathbf{v}}{\delta \log t} = \begin{bmatrix} \frac{-(s+5)}{2} \\ \frac{6(s+5)}{66+6s-3s\beta-15\beta} \\ \frac{5\beta+2}{2(\beta-5)} \end{bmatrix}, \tag{5.21}$$

where here I have shown the derivative of the analytically tractable expressions derived in Section 5.1, rather than those for the full dynamical model (Chapter 2) for simplicity. Similar expressions exist for the other source intrinsic parameters, though these have the opposite sign in at least one of the observables when compared to the redshift derivatives at all distances. These variables may interact with the source

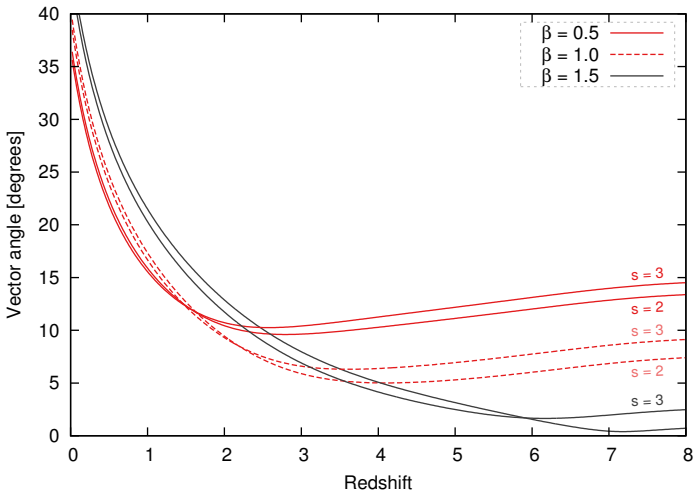

Figure 5.4: Angle between constraint vector derivatives with respect to the redshift and age of the radio source. Lines are plotted for three gas density profiles with exponents $\beta = 0.5$, 1 and 1.5, and two electron energy distributions, $s = 2$ and 3.

age constraint to more closely match the redshift vector, however an event involving several variables will have much lower probability of occurring and can largely be ignored.

The angle between the derivative vectors as a function of redshift is determined using vector calculus, whilst also varying the values of the radio source model parameters s and β. That is,

$$\phi = \arccos\left(\frac{\frac{\delta \log \mathbf{v}}{\delta \log t} \cdot \frac{\delta \log \mathbf{v}}{\delta \log z}}{\left\|\frac{\delta \log \mathbf{v}}{\delta \log t}\right\| \left\|\frac{\delta \log \mathbf{v}}{\delta \log z}\right\|}\right), \tag{5.22}$$

where the vectors are parallel for an angle of $\phi = 0$, perpendicular for $\phi = \pi/2$, and anti-parallel when $\phi = \pi$. The angle between the constraint vector derivatives with respect to the redshift and age of the radio source are shown in Figure 5.4 as a function of redshift. The constraint vector derivatives point in different directions at low-redshifts ($z \ll 1.7$), but become close to parallel at higher redshifts for certain host environments. Radio sources in flat environments ($\beta \ll 1$) maintain vector derivatives separated by at least $\phi = 10$ degrees for all redshifts. Radio sources in the most massive galaxies are likely to spend most of their evolutionary history expanding in the flatter core regions of the gas density profile.

The constraint vector derivatives are therefore not parallel for low-redshift radio

sources and the most massive objects (i.e. flatter profiles expected at a given radius) located at higher redshifts. Reliable distance and redshift estimates for these objects should be retrievable from the joint probability distribution upon correcting for any biases in the distribution.

5.3.2 Degeneracy de-biasing

The intrinsic radio source parameters (in particular the source age) and the distance measure (transverse comoving distance or redshift) are degenerate parameters for radio sources expanding in all but the flattest host environments, or those at very low-redshift. If the constraint vector derivatives for the two parameters are orthogonal, a single sharp peak in the joint probability distribution is expected corresponding to the best fit set of intrinsic parameters. By contrast, if the constraint vector derivatives are parallel the values of the intrinsic parameters will not be recoverable. For the most part, this degeneracy will lead to a ridge of moderate probability emanating from a shallow peak at the true value of the parameters. This degenerate ridge will have a slope along its length if the probability distribution has a bias towards the extremes of any of the intrinsic parameters. The slope along the ridge, if steep enough, may cause the true peak to be overwhelmed by higher probabilities towards one of the extremes. The true peak can be identified by eye in most cases despite this slope (e.g. Figure 5.5), however I seek to correct for the bias so the peak can be more robustly identified.

The fitting algorithm is expected to have a strong bias towards younger radio sources located closer to the observer. This occurs because the spectral break frequency does not provide a direct constraint on the source age; rather it constrains the age in combination with the magnetic field strength taken from the radio source model. The simulated radio sources have a preference for high magnetic field strengths since the host environment gas density profile gets progressively steeper with galactocentric radius rather than following a power law. Radio sources therefore spend less time within a log-space range of gas density (and thus field strength) at radii further from the core where the lobe field strength is lower. The preference to fit stronger magnetic fields leads to younger source ages for a given spectral break frequency observation (see Equation 5.9), and in turn lower transverse comoving distances (Equations 5.10 and 5.13).

This bias in the joint probability distribution is modelled by populating the sample space with a uniform grid of mock radio sources. The joint probability distribution is calculated for each of these mock radio sources in the same manner as for the observed radio source. The sum of the probability distributions from every mock source is

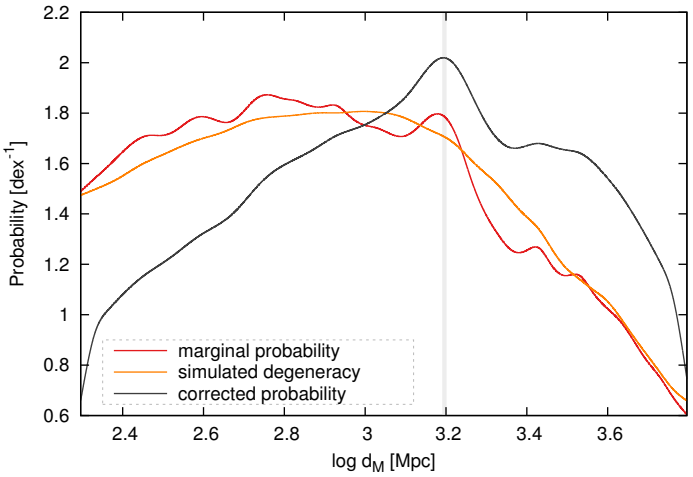

Figure 5.5: Marginal probability distribution for the moderate redshift ($z = 0.43$) radio source 3C244.1. The raw joint probability distribution for 3C244.1 is marginalised along the distance measure axis, and plotted in red. This distribution is corrected based on a joint probability distribution arising from a grid of mock radio sources uniformly covering the sample space. The preference for radio sources to be fitted with certain characteristics due to the degenerate nature of the solution space is shown by the marginal distribution in orange. The joint probability distribution for 3C244.1 is corrected using these simulations (grey line).

expected to produce a symmetric distribution with a peak at the centre of the sample space if there is no bias; every mock source should yield a Gaussian, and the sources are uniformly distributed through the sample space. Any asymmetry in this simulated distribution therefore is the result of a preference in the fitting algorithm towards an extreme in at least one of the intrinsic parameters. This bias in the four-dimensional sample space is modelled by fitting a hyperplane (in log-space); the fractional increase in probability found towards the extremes in this simulated distributed can be removed from the probability distributions of the observed radio sources.

The corrected joint probability distribution for a typical radio source in the sample is shown in Figure 5.5, with the probabilities marginalised along the distance measure axis. The unmodified probability distribution for this source and the distribution for the grid of uniformly spaced mock radio sources is also shown. These both yield high probabilities for sources close to the observer, with the true peak at $d_{\rm M} \sim 10^{3.2}\,{\rm Mpc}$ obscured by the height of the degenerate ridge. By contrast, upon correcting for the biases, the true peak becomes dominant and noise from smaller local maximum near the extremes is greatly reduced. The best estimate for the distance measure, and the source age, jet power and equipartition factor parameters, is thus taken as the peak of the corrected marginal probability distribution. The stability of this method is tested for sample spaces which are not centred on the expected values for the intrinsic parameters, and for tighter and weaker bounds on the space.

5.3.3 Prior probability distributions

The parameters associated with the electron energy distribution, lobe shape and magnetic field strength, and the host environment in Equation 5.13 may be constrained statistically rather than through observations.

Axis ratios and electron energy distribution

The transverse comoving distance is only weakly dependent on both the axis ratio of the lobe and the electron energy distribution. Measurements of the axis ratios of individual sources are therefore not required; fortuitous since the faint emission along the sides of the lobe is undetectable (see Chapter 4) even in the very powerful 3C sample beyond $z \sim 1$. Mullin et al. (2008) measured the axis ratios of 98 powerful 3C radio sources at these lower redshifts finding a median value of $A = 4.4$ and log-space 1σ uncertainty of 0.2 dex. Mock radio sources are randomly simulated with axis ratios from this distribution.

The low-energy cut-off of the electron energy distribution is measured through the observed low-frequency flattening of the hotspot radio spectrum. The minimum Lorentz factor has been estimated in this manner by other authors for selected radio sources including: PKS 1421-490 (Godfrey et al. 2009), Cygnus A, 3C123, 3C196 and 3C295 (Hardcastle 2001). These hotspot Lorentz factor estimates lie between approximately 100 and 1000; the value will be lower for the electron population in the lobe due to the adiabatic expansion of the plasma, though this is considered in the synchrotron emissivity model (see Chapters 3 and 4). The value chosen for this parameter is not critical since it appears as ${\gamma_{\rm min}}^{s-2}$ in the $h(\gamma_{\rm min}, s)$ term of Equation 5.13, nevertheless I sample values from the observed range.

Stellar mass of host galaxy

The radio source environment is simulated based on the stellar mass of the host galaxy (see Section 5.2.2). If optical or infra-red observations are available the prior probability distribution is a very narrow Gaussian centred at the measured value. However, radio photometric redshifts will be much more valuable if they can work for surveys without any cross-matched optical observations; there is presently no mechanism available to measure the redshift in such surveys.

The range of plausible stellar masses is restricted by calculating the number density of AGN host galaxies as a function of mass (i.e. massive galaxies are more likely to host AGN but there are fewer of them). This is achieved by convolving the low-redshift radio-loud fraction of Best et al. (2007) with the stellar mass function (i.e. number density of galaxies with a given stellar mass). This combined probability distribution peaks at a stellar mass of approximately $10^{11}\,{\rm M}_{\odot}$, with the probability falling to less than one-hundredth of that at the peak outside the range $10^{10} < M_{\star}/{\rm M}_{\odot} < 10^{12.5}$. This result holds at higher redshifts if the AGN radio-loud fraction is assumed to maintain a somewhat similar mass dependence (though see e.g. Williams & Röttgering 2015). I therefore assume the host stellar mass may lie anywhere in this range (with log-linear weighting) when analysing radio sources with no host galaxy optical or infra-red observations. In this work, I apply this flat prior instead of using the observed masses for all analyses aimed at deriving the photometric redshift to ensure my conclusions are valid for surveys lacking these measurements.

Magnetic field equipartition factor

The magnetic field strength in the radio lobes is a function of their pressure and the equipartition factor q. The gas density of the host environment and this equipartition factor appear together in the analytic expression for the transverse comoving distance (Equation 5.13). The large random variation in the scaling of the density profile, and the potential for systematic errors in this scaling from SAGE, necessitate a rather loose constraint on the possible value of the equipartition factor. I therefore assume a log-linear prior probability distribution with the factors covering four orders of magnitude.

5.4 Radio photometric redshifts

Radio source redshifts are typically measured based on the optical spectroscopy or photometry of the host galaxy. Future radio surveys using next-generation telescopes such as the *Square Kilometre Array* pathfinders (e.g. ASKAP, MWA and MeerKAT) will probe large swathes of sky with limited optical and infra-red observations. Developing an exclusively radio-frequency based technique for measuring the redshift of galaxies is therefore crucial to properly interpret these observations. Moreover, the population of infrared-faint radio sources (IFRS) are bright, high-redshift ($z > 1.7$) radio AGN with faint or absent near-infrared emission (Herzog et al. 2016). The selection of radio sources which are suitable candidates for the reshift estimation technique described in Sections 5.1 through 5.3 is considered; I then calculate radio photometric redshifts for the candidate objects in a well-studied radio source sample. The redshift of the radio source, and thus its host galaxy, may then be used in combination with projected galaxy clustering to estimate the redshifts of some other nearby galaxies. Note that in some cases the 21cm HI radio-frequency absorption line can be used to measure redshifts, e.g. Allison et al. (2015) found a redshift of $z = 0.44$ for a galaxy with no previous optical measurement.

5.4.1 Radio source sample and selection

Testing of the radio photometric redshift measurement technique must take place using radio sources with observations of both the spectral energy distribution and source size. The spectroscopic redshift of the associated host galaxy must also be measured so that the veracity of my estimates can be assessed. The source size is difficult to measure accurately at high-redshifts ($z \gg 1$) in all but the most powerful radio sources; I therefore choose to analyse sources in the *Third Cambridge Catalogue of*

Radio Sources (3CRR)[1]. Each object includes the measured 178 MHz radio lobe luminosity and largest angular size, with sources found at redshifts between $z = 0.05$ and 2. The radio SEDs are constructed using literature observations from the numerous authors as listed in the *NASA/IPAC Extragalactic Database* (NED); total flux density measurements are preferentially used here whilst core and peak flux densities are excluded.

Radio source dynamics

The dynamics of the radio lobe has the greatest effect on the photometric redshift or transverse comoving distance measures (see Equation 5.13). Ensuring the observed radio source behaves in the manner predicted by the dynamical and synchrotron emissivity models is therefore of great importance if reliable estimates are to be obtained. The radio lobes simulated using these models are approximately ellipsoidal in shape and expand anti-parallel to each other with no bending or twisting. Radio sources in the 3C sample which do not exhibit such behaviour in their FITS images are excluded here from further analysis. The robustness of the distance measure fitting technique to the assumptions of the dynamical model is not tested in this work (e.g. can anything be fitted approximately), however it is assumed that it will be possible to obtain good estimates for only some run-of-the-mill sources. These can be used to provide redshift measurements for nearby galaxies through projected clustering, and importantly the largest clusters containing multiple AGN will have some redundancy to the exclusion of some radio sources. Further, these robust radio AGN can be used as standardisable candles to measure cosmological parameters (see Section 5.5).

Spectral energy distribution

The spectral energy distribution of powerful radio AGNs is characterised by an initial power law decrease in flux density as a function of increasing frequency (i.e. $S \propto \nu^{-\alpha_{\rm inj}}$, where $\alpha_{\rm inj}$ is the injection index) followed by a steepening of the spectrum at high-energies due to the synchrotron loss mechanism. The location of this steepening is defined as the spectral break frequency $\nu_{\rm b}$, beyond which the flux density falls-off with power law $\alpha_{\rm inj} + 0.5$. The sharp low-frequency ($\lesssim 100$ MHz) turnover seen in some sources is instead a result of either synchrotron self-absorption (Kellermann 1966) or free-free absorption (Bicknell et al. 1997).

The injection index and break frequency parameters are fitted to the spectra arising

[1] http://zl1.extragalactic.info/

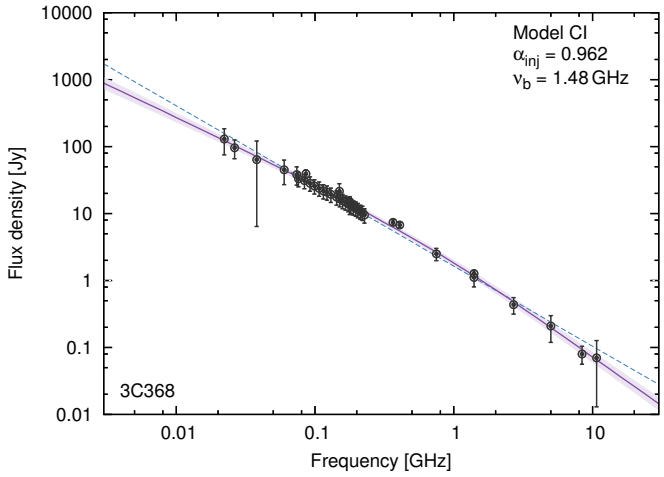

Figure 5.6: Spectral fit to the lobe synchrotron emission of the typical radio source 3C368. The observed flux densities taken from literature observations are plotted with grey circles and 2σ errorbars. These multi-frequency observations are fitted using the continuous injection model (see Chapter 3), with the fitted injection spectral index $\alpha_{\rm inj}$ and break frequency $\nu_{\rm b}$ parameters stated on the plot. The purple shading about the plotted fit line shows the 2σ uncertainties in the continuous injection (CI) model fit. The blue dashed line is the best fit linear relationship for comparison with the CI model fit.

from the total emission (i.e. integrated over the whole source) of each source using the continuous injection model described in Chapter 3. The radio SEDs of all sources in the 3C sample with sufficient frequency coverage and consistent flux density measurements taken from the literature are fitted using the continuous injection model. Radio sources showing the sharp low-frequency turnover, inconsistent measurements, very noisy spectra, or no curvature are flagged and not included in further analysis. Further those sources whose fitted break frequency lie beyond the observed frequency range are excluded. The spectrum of 3C217, a typical radio source included in the sample, is shown in Figure 5.6.

The removal of radio sources either with a morphology inconsistent with the physics assumed in the dynamical model or a radio SED unable to reliably fit a break frequency results in a sample of 47 3C radio sources.

5.4.2 Photometric redshifts of 3C radio sources

Radio photometric redshifts are measured for the sample of powerful 3C radio sources discussed in the previous section. The degenerate nature of the distance measure and radio source intrinsic parameters at high-redshifts, especially in steep environments, precludes photometric redshifts being derived for every source. Clear peaks are seen in the probability distributions of approximately 85% of radio sources at (spectroscopic) redshifts $z < 0.82$. By contrast, between 35 and 40% of objects above this redshift have non-degenerate solutions (range due to inclusion/exclusion of source at $z = 0.82$). This finding may provide a crude photometric redshift for radio sources with degenerate solutions; i.e. it is much more likely an object with no clear peak in the probability distribution lies at high-redshift ($z > 0.82$).

The accuracy of the radio photometric redshift measurements for objects with non-degenerate solutions is assessed by comparing the results to the spectroscopic redshifts of the host galaxies. These initial photometric redshift estimates differ from the spectroscopic redshifts by a mean of 17% (mean absolute error). This variation is largely a result of having applied no constraint on the properties of the host environment; the host stellar mass is permitted to take any value between 10^{10} and $10^{12.5}\,\mathrm{M}_{\odot}$ (Section 5.3.3). However, in addition to this dependence on the host environment, these photometric redshift estimates depend crucially upon the assumed cosmology and weakly on dynamical model parameters. It may therefore be beneficial to calibrate the fitting algorithm using a subset of radio sources with measured spectroscopic redshifts. I choose to use one-third of the 3C radio sources as a calibration sample. This is a realistic technique to improve the precision of the redshift fitting algorithm in future surveys, which will have at least some objects with spectroscopic redshifts. The calibration sample is used to determine any systematic errors in this method due to the assumed cosmology or host environment. These corrections (i.e. the best-fit polynomial relationship between the spectroscopic and photometric redshifts) are then be applied to the remaining radio sources. The calibration subset is chosen by selecting every third source when sorted by redshift to ensure both samples maintain a comparable redshift distribution.

The radio photometric redshift estimates I obtain for the 3C sources are plotted in Figure 5.7 as a function of the independent spectroscopic redshift. These photometric redshift estimates now differ from the measured spectroscopic redshifts by a mean of 6%. I find that 95% of estimates are accurate to within 15% and 88% of sources to within 10%. This redshift measurement technique therefore provides both a reliable and precise method, for the first time, based exclusively on radio frequency observa-

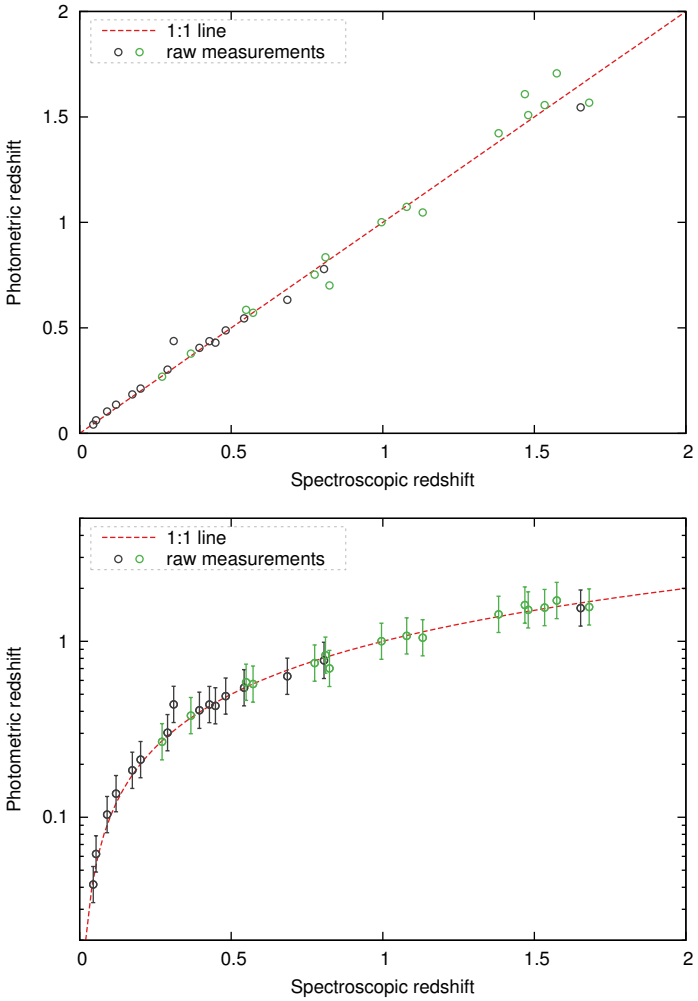

Figure 5.7: Best fit radio photometric redshifts for 3C radio sources as a function of their measured spectroscopic redshifts. The colour coding of these circles is a qualitative assessment of the level of degeneracy; less (grey) to more (green) degenerate. The top panel shows this relation in real space; the bottom panel plots the same data with the photometric redshift axis in log-space (as used in the fitting algorithm) with 2σ errorbars. The redshift dependence of the flux density, angular size and radio source environment is calculated for $70\,\mathrm{km\,s^{-1}\,Mpc^{-1}}$, $\Omega_\mathrm{m} = 0.27$ and $\Omega_\lambda = 0.73$.

tions. This technique will be further tested by applying it to a more typical radio source survey to ensure that these strong results for the 3C sub-sample are generally applicable. These radio photometric redshifts provide a direct measurement of the observer-to-source distance, which in conjunction with a spectroscopic redshift measurement can be used to investigate the motion of the radio source along the line-of-sight within their host galaxy clusters. In particular, the recession velocity at $z = 0.01$ is comparable to typical galaxy cluster velocity dispersions of between 500 and 1000 $\mathrm{km\,s^{-1}}$ (Owers et al. 2017). Differences between the spectroscopic and standardisable candle distance measurements should thus be well above the noise level for $z < 0.1$.

5.5 Radio AGN standardisable candles

Radio AGNs in well-studied fields, such as those in the 3C and 7C surveys, the *Herschel Radio Galaxy Evolution Project* (HeRGE; Seymour et al. 2007; De Breuck et al. 2010) and *GAMA Legacy ATCA Southern Survey* (GLASS; Huynh et al. 2016), have sufficient observational constraints to derive not only properties of the radio source, but also the cosmology of the universe they inhabit. In this section, I apply the technique developed in Sections 5.1 through 5.3 to a sample of 3C radio sources (described in Section 5.4.1) in order to constrain several cosmological constants, including the dark energy and matter densities.

5.5.1 Radio AGN cosmological distance measures

The sample of 47 powerful 3C radio sources discussed in Section 5.4.1 is now used to construct standardisable candles to measure the cosmology. The degeneracy seen in the probability distributions of some sources prevents the entire sample from being studied; however, this is of little concern since non-degenerate solutions remain from low- to high-redshifts. The transverse comoving distances I fit for these non-degenerate sources are plotted in Figure 5.8 as a function of the spectroscopic redshift. The distances to these 32 non-degenerate radio AGNs are for the most part consistent with the other objects at the same redshift; i.e. this technique can successfully estimate the same distance for radio sources with different intrinsic properties located at the same redshift.

The robustness of fitting the distance to radio AGNs using the more degenerate probability distributions at higher redshifts can be greatly enhanced by stacking the distributions from several sources at the same spectroscopic redshift. Combining multiple

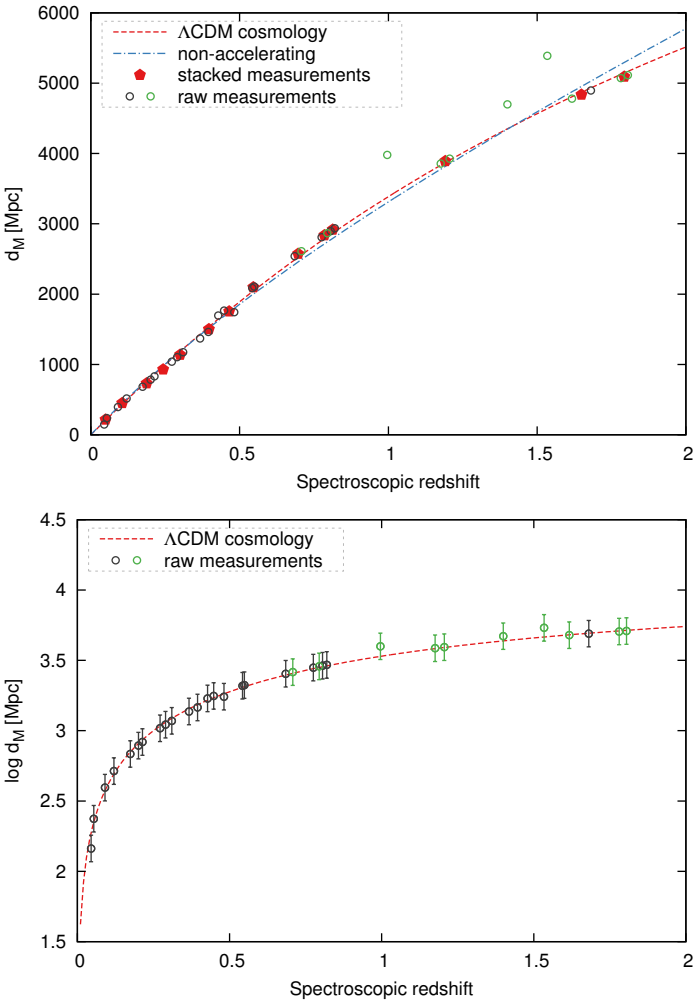

Figure 5.8: Best fit transverse comoving distances for 3C radio sources as a function of their measured spectroscopic redshifts. The best estimates are shown by the open circles, with the 1σ uncertainties shown by the errorbars in the bottom panel. The colour coding of these circles is a qualitative assessment of the level of degeneracy, as for Figure 5.7. The red pentagons are the best estimates obtained from stacking the probability distributions of sources at the same redshift. The red dashed line plots the best fit ΛCDM cosmology for this population and the blue dashed line the best fit cosmology assuming no acceleration.

probability distributions strengthens the peak at the true value of the distance measure and cancels noise. However, some radio sources which have a weak, or poorly-defined peak may yield a completely degenerate solution when stacked if their distance is inconsistent with the other radio sources (e.g. the three green circles above the fit line in Figure 5.8). The stacked probability distributions will therefore indicate which sources are so inconsistent with the other measurements that they make the solution degenerate.

The standard ΛCDM cosmological model is fitted to the distances obtained from the stacked probability distributions, as shown in Figure 5.8. I derive a best estimate Hubble constant of $H_0 = 71\,\mathrm{km\,s^{-1}\,Mpc^{-1}}$, matter density of $\Omega_\mathrm{m} = 0.2$, and a dark energy density of $\Omega_\Lambda = 0.71$. The sensitivity of these cosmological parameters to systematic uncertainties in the construction of radio AGN standardisable candles is discussed in the following section. For comparison, I also fit a simpler cosmological model assuming no acceleration to the distance measurements (also shown in Figure 5.8). The best fit to the 3C standardisable candles assuming no dark energy is an empty universe with $H_0 = 67\,\mathrm{km\,s^{-1}\,Mpc^{-1}}$. However, this cosmology diverges from the distance measurements at the highest redshifts; the inclusion of radio AGNs from high-redshift surveys such as HeRGE (discussed in Section 5.6.1) enable us to provide a very tight constraint on the matter and energy content of the universe.

5.5.2 Stability of cosmological parameters

The stability of radio AGN standardisable candles to the assumed Bayesian prior on the host environment is tested in this section. I further show that the distance measure is not biassed towards the concordance cosmology due to the use of dark matter simulations in the modelling of the host environment.

Stability to uncertainty in environment

The properties of the radio source environment are by far the largest contribution to uncertainty in the distance to the AGN standardisable candles. The transverse comoving distance in Equation 5.13 depends most strongly on the angular size and density terms, the equipartition factor intrinsic parameter is largely used to compensate for uncertainty in the gas density (and entirely so in this limiting form). However, the strength with which the distance measure depends on the observables is a function of the rate at which the gas density profile falls-off with galactocentric radius (i.e. β). The shape of the gas density profile is modelled based on X-ray observations of

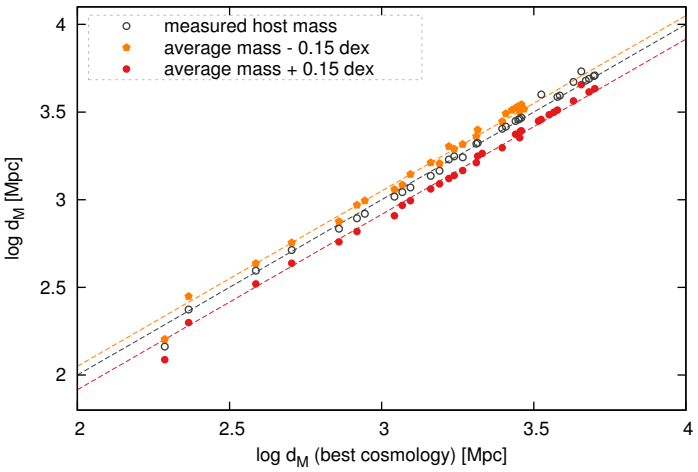

Figure 5.9: Best fit transverse comoving distances for 3C radio sources as a function of the expected value for their measured spectroscopic redshifts, calculated assuming: (1) the best estimate host environment based on near-infrared observations (grey open circles), (2) host galaxy stellar mass systematically lower by 0.15 dex (orange filled pentagons), and (3) stellar mass systematically higher by 0.15 dex (red filled circles). Systematic shifts in the properties of the host environment lead to a constant shift in the distance measure, i.e. the energy and matter content are not affected.

clusters taken from Vikhlinin et al. (2006) and scaled to the virial radius of the dark matter halo, as measured from near-infrared photometry of the host galaxy. Both the cluster observations and the conversion from galaxy near-infrared flux density to virial radius are subject to the introduction of systematic uncertainties into the steepness of the gas density profile; i.e. the density profile may be systematically flatter or steeper, leading to derived radio sources distances shifted further from or closer to the observer respectively.

The effect of systematically varying the shape of the gas density is explored by raising or lowering the near-infrared magnitudes by $\sim$0.4 mag. This variation is modelled as a 0.15 dex shift in the stellar mass of the host galaxy, which flows through to the virial radius following the method in Section 5.2. These systematic variations to the near-infrared magnitudes therefore lead to a stretching of the gas density profile along the radial axis. The best estimate distances for the 3C radio sources assuming these modified environments is plotted in Figure 5.9. The systematically flatter or steeper gas density profiles lead to a constant shift in the distance to the source, irrespective of redshift. The Hubble constant ($H_0 \propto 1/d_{\rm M}$) is therefore dependent on the shape of the density profile and the conversion from near-infrared magnitude to the scaling virial

radius. Crucially, the dark energy and matter densities are unaffected by a constant and redshift-independent shift in the distance measure. Low-redshift AGNs with X-ray observations of their host gas density profile may be able to provide a tight enough constraint to fit for Hubble's constant; but for now I will focus my efforts on the dark energy and matter densities.

Finally, examining the probability distributions it is evident that more of the lower host mass radio sources (especially at high-redshift) have degenerate distance measures than their higher mass counterparts; this trend can be seen in Figure 5.9 where only the non-degenerate solutions are plotted. This result is expected since the lower stellar mass hosts are associated with more compact dark matter haloes; the density profile in these haloes is therefore steeper (higher β) at any radius encountered by the source throughout its expansion. I previously found that radio sources with steep environments and high-redshift give very degenerate solutions (Section 5.3.1), consistent with these results. It may be possible to model radio sources with systematically flatter environments to reduce the level of degeneracy without affecting the fitted cosmology, though I do not pursue this in this work.

Independence of model cosmology

I proceed to show that cosmological parameters fitted using the radio AGN technique are independent of the inbuilt cosmology of the dark matter simulations used to model the host environments, or any other potential biases. The properties of the radio source host environment were characterised in Section 5.2 based on the Bolshoi dark matter simulation and the SAGE prescription for baryonic matter. However, the Bolshoi model is run for a fixed cosmology with $h = 0.70$, $\Omega_{\rm m} = 0.27$, and $\Omega_\Lambda = 0.73$, I also argued that the gas density profile is quite insensitive to the chosen cosmology of the SAGE and Bolshoi models (Section 5.2.1).

The independence of the fitting algorithm to an unintended inbuilt cosmology is tested by applying my method to simulated sources inhabiting universes with a variety of different cosmologies. These are modifications to the concordance cosmology, including: (1) no dark energy, (2) an empty universe, and (3) increased Hubble constant. The 3C sources used in the previous sections are relocated to different distances from the observer according to the new cosmology. The intrinsic properties and spectroscopic redshift of these objects remain unchanged, and thus only their radio frequency (and near-infrared, measuring the environment) flux density and angular size are modified in this transformation.

The best estimate transverse comoving distances for the real and transformed vari-

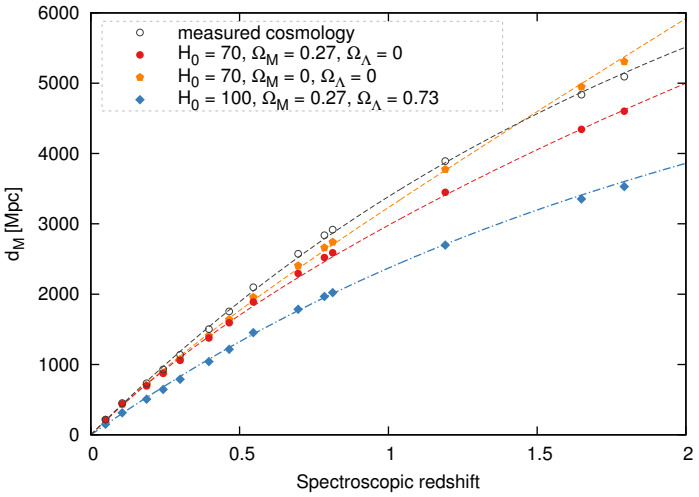

Figure 5.10: Best fit transverse comoving distances as a function of their measured spectroscopic redshifts for mock variants of the 3C radio sources inhabiting a range of cosmologies. The best estimate distances obtained from stacking the probability distributions of several sources at the same redshift are shown for the observed 3C sources in grey (open circles), and for three alternate cosmologies (red, orange and blue). The dashed lines show the expected relations for the three simulated cosmologies, and a best fit for the observed sources.

ants of the 3C radio sources are shown in Figure 5.10 (only distances from stacked probability distributions shown). The mock variants of the 3C sources have very different distances at all redshifts compared to each other and the sources in the real cosmology. Moreover, the distances fitted for these mock 3C sources are consistent with the cosmology used to transform their flux densities and angular sizes (i.e. the dashed lines in Figure 5.10). The radio AGN standardisable candles are therefore independent of the inbuilt cosmology of the Bolshoi model, and any cosmology fitted using this technique is not unintentionally biassed towards concordance values.

5.6 Measuring the cosmology using AGN

High-powered radio AGNs have been shown to be excellent standardisable candles, producing consistent distance measurements for sources located at the same redshift but with different intrinsic properties. The cosmology of our universe can be constrained by applying the methods presented in this chapter to radio sources covering a broad range of redshifts. The limited redshift coverage of the 3C sample (i.e. only a few usable sources above $z = 1$) poses a serious concern; although cosmological measurements from type 1a supernovae also only extend to $z \sim 1$, their uncertainties are a factor of a few smaller on a source-by-source basis. The redshift coverage must be greatly extended to better capture the curvature in the redshift–distance relationship if we seek to provide a tighter constraint on the cosmology. The high-redshift *Herschel Radio Galaxy Evolution Project* (HeRGE; Seymour et al. 2007; De Breuck et al. 2010) sample is thus used to extend coverage beyond $z > 4$. Radio AGN based measurements of the cosmological parameters from this sample can be combined with those from cosmic microwave background (CMB), baryon acoustic oscillations (BAO) and type 1a supernovae to tighten current values, or at least verify them using this unrelated technique.

5.6.1 HeRGE sample and candles

The HeRGE project sample combines literature and *Australia Telescope Compact Array* (ATCA) observations of the integrated lobe luminosity at frequencies between 10 MHz to above 10 GHz in the observer-frame. Further, each object includes a spectroscopic redshift and lobe angular size measurement, in addition to an estimate of the stellar mass from visible to infrared SEDs (Seymour et al. 2007; De Breuck et al. 2010). In this section, the radio spectral energy distributions of these objects are fitted with a continuous injection model to obtain the spectral break frequency (Fig-

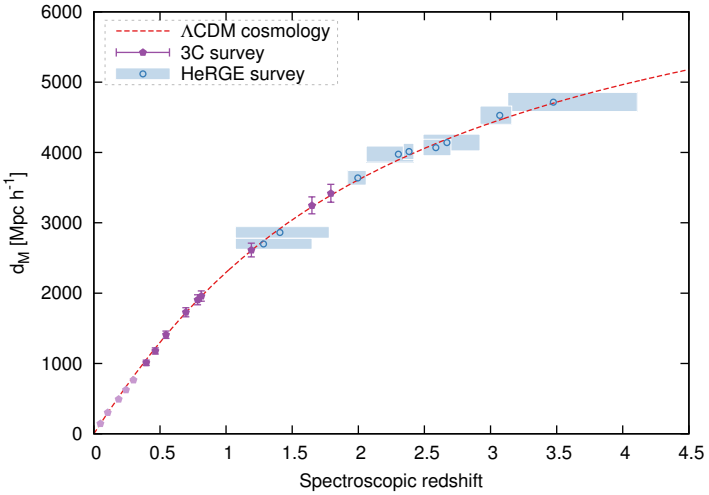

Figure 5.11: Best fit transverse comoving distances for the stacked groupings of HeRGE radio sources as a function of the stack average spectroscopic redshifts (unfilled blue circles). The distance is expressed in terms of the dimensionless Hubble parameter since the absolute scaling is sensitive to the gas density. The blue shading shows the uncertainties in the measurements as follows: the horizontal width of the shaded region shows the redshift range of the objects included in each stack, and the vertical height plots the 2σ uncertainties from both the measurement and intrinsic scatter. The best estimates obtained from the stacked 3C radio source probability distributions are also shown on this plot (c.f. Figure 5.8). The red dashed line plots the best fit ΛCDM cosmology to both these populations, though sources at low-redshift (faded) are excluded since cluster velocity dispersion leads to noticeable variance in their spectroscopic redshifts.

ure 5.6); sources whose fit is consistent with a straight line or shows a low-frequency turnover (i.e. due to free-free or synchrotron self-absorption) are excluded. This leaves 35 high-redshift HeRGE radio sources. However, 14 of these objects are omitted as they do not have robust stellar mass measurements. The probability distributions of these excluded objects have peaks in the plausible range (i.e. not noise) shifted slightly closer to the observer than comparable sources at the same redshift if these upper limits are assumed, consistent with our findings in Figure 5.9.

The probability distributions obtained for the HeRGE sample objects have a peak close to the observer-to-source distance expected for the current best estimate cosmology, but also show "noise" peaks due to the degeneracy between the distance measure and the intrinsic parameters. Probability distributions from several radio sources at comparable redshift are therefore stacked to enhance the real peak and suppress any false,

noise peaks. The probability distributions are shifted along the distance axis based on the relative redshifts of the sources (using $\triangle d_{\rm M}/\triangle z$ for some plausible cosmology, and where $\triangle z$ is small) so that the distance of the stacked distribution coincides with the average redshift of the stack. The objects in the HeRGE sample are grouped in two different manners to ensure a single errant distribution does not exclude the contribution from neighbouring redshift sources. The 21 HeRGE objects are stacked into 12 different grouping containing between three and five sources; nine of these stacked probability distributions exhibit a single peak (e.g. Figure 5.5) whilst the other three either have an broad, flat peak or a secondary noise peak. The redshift range of these groupings and the peak distance obtained from their stacked probability distributions are plotted in Figure 5.11, alongside our previous measurements for the 3C standardisable candles. The uncertainty in each stacked measurement of the distance measure is taken as the quadrature sum of the error in fitting the peak and the intrinsic scatter in the measurements.

5.6.2 Radio AGN cosmology

The radio AGN standardisable candles constructed from the 3C and HeRGE samples are used to constrain the energy and matter content of the universe, and determine Hubble's constant in conjunction with CMB power spectra measurements. Low-redshift radio sources (i.e. $z < 0.3$) are excluded from the cosmology sample since motion within their host galaxy clusters leads to noticeable variation in their spectroscopic redshift compared to that expected for their distance. Typical galaxy cluster velocity dispersions of between 500 and 1000 $\mathrm{km\,s^{-1}}$ (Owers et al. 2017) result in up to a 12% error in spectroscopic redshift at $z = 0.1$ though this reduces to less than 5% for $z > 0.3$.

The best estimates and uncertainties in the cosmological constants are derived by fitting Monte Carlo realisations of the standard ΛCDM cosmology to the radio AGN standardisable candles. These cosmological model fits to my distance measurements yield dark energy and matter densities of $\Omega_{\rm m} = 0.28 \pm 0.02$ and $\Omega_{\Lambda} = 0.76 \pm 0.07$ respectively. The confidence ellipse for these two parameters is tilted and highly eccentric (top panel of Figure 5.12); i.e. radio galaxies yield an inverse relationship between the energy and matter content in the universe. The cosmology fitted to the radio AGN standardisable candles is inconsistent with a non-accelerating universe at greater than the 6σ level. By contrast, the distance measurements are consistent with a flat universe to within the 1σ uncertainties ($\Omega_{\rm k} = -0.04 \pm 0.07$). The best fit parameters are therefore recalculated under the assumption of a flat universe by

removing all previous fits with $\Omega_\mathrm{m} + \Omega_\Lambda \neq 1$. The cosmological parameters tighten to $\Omega_\mathrm{m} = 0.289 \pm 0.012$ and $\Omega_\Lambda = 0.711 \pm 0.012$ under this assumption.

The Hubble constant varies considerably along the length of the dark energy–matter density confidence ellipse (colouring in Figure 5.12); however, the absolute scaling of our distances is somewhat uncertain preventing the Hubble constant from being constrained without independent cosmological probes. The Hubble constant found from CMB temperature and polarisation spectra (i.e. TT, TE and EE, also plotted in Figure 5.12; Planck Collaboration 2016) in the small region of overlap with the radio AGN confidence interval is used to calibrate the absolute distance to the AGN standardisable candles (bottom panel of Figure 5.12). The Hubble constant in this region of overlap is $H_0 = 67.88 \pm 0.58$. This measurement is consistent with those obtained from baryon acoustic oscillations or JLA type 1a supernovae in this region of dark energy–matter density space. The Hubble constant measurement for this dark energy–matter density pair is used to calibrate the absolute distance to the AGN standardisable candles (i.e. correct for the systematic uncertainty due to the environment). This calibration enables the Hubble constant to be correctly determined for all the dark energy–matter density pairs in the original confidence ellipses for the AGN standardisable candles (best estimate in Table 5.4).

5.6.3 Independent cosmological measurements

The cosmology derived using radio AGN standardisable candles is combined with measurements from other astrophysical datasets: the JLA sample of type 1a supernovae (SNe1a; Nielsen et al. 2016), BOSS BAO measurements from galaxy clustering and the Lyman-α forest (Aubourg et al. 2015), *Planck* CMB lensing reconstruction, and temperature and polarisation spectra (i.e. TT, TE and EE; Planck Collaboration 2016), and a *Hubble Space Telescope* (HST) Cepheid and supernovae based estimate of the Hubble constant (used as a prior for CMB measurements). The region of dark energy–matter density space occupied by the confidence ellipses of the CMB power spectra with and without the inclusion of lensing reconstruction is shown in Figure 5.12. Both radio AGN standardisable candles and the CMB power spectra yield only a narrow line of possible parameter sets in Hubble constant, dark energy and matter density space. By contrast, the power of the other techniques is much weaker effectively producing a plane of possible parameters sets in the three-space (e.g. linear relation between Ω_m and Ω_Λ for constant h in SNe1a; Nielsen et al. 2016). These other cosmological measurement techniques are therefore only considered here in conjunction with both the CMB power spectra and the radio AGN standardisable candles

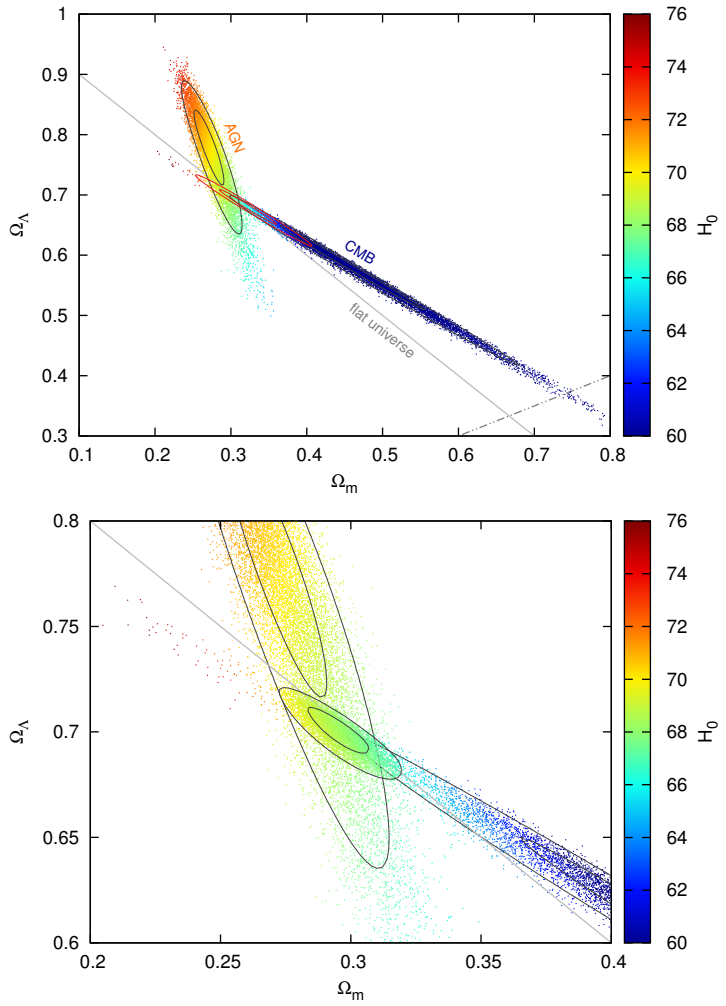

Figure 5.12: Constraints in the dark energy–matter density plane from radio AGN standardisable candles and cosmic microwave background temperature and polarisation spectra (i.e. TT, TE and EE). The top panel shows the 1 and 2σ confidence intervals for these two techniques using grey ellipses, with pixels approximately plotting the probability density function. The colour scheme shows the mean Hubble constant fitted for each location in dark energy–matter density space. The red confidence ellipses show the 1 and 2σ interval for the CMB power spectra including lensing reconstruction. Lines corresponding to non-accelerating expansion (dot-dot-dashed) and a flat universe (solid grey–labelled) are overplotted. The bottom panel provides a zoom-in of the intersection of the two confidence ellipses. The combined probability distribution is also overplotted with a further set of confidence ellipses.

Table 5.4: Parameter 1σ confidence intervals for the standard ΛCDM model, assuming either a flat or general universe, from radio AGN standardisable candles, in combination with JLA type 1a supernovae, BOSS BAO measurements, *Planck* CMB observations, and a complementary HST H_0 estimate.

Parameter	AGN		AGN+Planck		AGN+Planck+ BAO+JLA+H_0	
Ω_k	-0.039 ± 0.069		0.004 ± 0.015		0.0008 ± 0.0040	
	flat	general	flat	general	flat	general
H_0	68.84 ± 0.67	69.97 ± 1.53	67.88 ± 0.58	68.35 ± 0.79	68.02 ± 0.43	68.25 ± 0.50
Ω_m	0.289 ± 0.012	0.276 ± 0.021	0.299 ± 0.010	0.294 ± 0.011	0.3032 ± 0.0064	0.3019 ± 0.0067
Ω_Λ	0.711 ± 0.012	0.763 ± 0.066	0.701 ± 0.010	0.702 ± 0.010	0.6968 ± 0.0064	0.6972 ± 0.0064

to yield a joint constraint.

The intersection of the highly eccentric confidence ellipses in dark energy–matter density space from both radio AGN standardisable candles and the CMB power spectra including lensing yields curvature of $\Omega_k = 0.004 \pm 0.015$. This tightens further to $\Omega_k = 0.0008 \pm 0.0040$ with the inclusion of the other cosmological measurement techniques as priors. The matter and dark energy densities comprising this flat cosmology are $\Omega_m = 0.303 \pm 0.006$ and $\Omega_\Lambda = 0.697 \pm 0.006$. The full list of cosmological parameters obtained upon combining AGN measurements with the independent cosmological measurements is included in Table 5.4. These cosmological parameter estimates are consistent with those obtained without radio galaxies (c.f. Planck Collaboration 2016). Radio AGN standardisable candles therefore provide a viable means to constrain cosmological parameters, both on their own and in conjunction with other techniques.

Further, radio AGN standardisable candles have smaller confidence intervals than SNe1a measurements when determining the energy and matter content of the universe (c.f. Figure 2 of Nielsen et al. 2016). The inclusion of standard candles out to $z = 4$ for the radio AGN measurements compared to $z \sim 1$ for the SNe1a observations rotates and tightens the confidence ellipse, despite measurement uncertainties a factor of a few worse on a source-by-source basis. By contrast, the precision of radio galaxy and BAO measurements are comparable (c.f. Figure 3 of Aubourg et al. 2015) due to their similar redshift coverage. Radio AGN standardisable candles should therefore provide a valuable addition to the cosmology measuring tool-set, complementing CMB power spectra and lensing. The inclusion of more radio sources across a broad redshift range (e.g. $0.3 < z < 7$) will enable this technique to provide an even tighter constraint on the matter and energy content of the universe.

5.7 Conclusions

I have presented a new approach to measure the redshift of the most distant objects in our universe, based exclusively on radio frequency observations. Very bright and large radio-loud active galactic nuclei (AGNs) are readily observable out to the early universe at $z > 7$, providing an exclusively radio frequency tool with which to probe distance across cosmic time. Moreover, the physics of the very large synchrotron emission lobes inflated by the most powerful AGNs are well modelled (Falle 1991; Kaiser & Alexander 1997; Kaiser et al. 1997; Krause et al. 2012; Hardcastle & Krause 2013). In this chapter, I built on this theoretical foundation to develop a technique for constructing standardisable candles based exclusively on radio frequency observations of

AGNs. Specifically this method uses radio flux density, lobe angular size, and the radio SED spectral index and break frequency. These radio AGN standardisable candles can be used for three purposes: (1) to obtain radio photometric redshifts assuming a standard cosmology, (2) measure cluster velocity dispersion at low-redshifts, and (3) constrain our cosmology by combining these distance measurements with spectroscopic redshifts. I applied this technique to radio sources in the 3C survey, providing redshift coverage from $z = 0.05$ up to 2, and the HeRGE sample to extend coverage to $z > 4$.

The redshifts of radio AGNs are typically measured based on the optical spectroscopy or photometry of the host galaxy. However, future surveys using precursors to the *Square Kilometre Array* (SKA), such as ASKAP EMU (Norris et al. 2011) and MeerKAT MIGHTEE (Jarvis 2012), will probe large portions of sky with limited observations outside radio frequencies. In this chapter, I showed that the radio AGN distance measure provides reliable photometric redshifts based exclusively upon multi-frequency radio observations. These radio photometric redshift measurements differ from the host galaxy spectroscopic redshifts by less than 15% for 95% of sources, and less than 10% for 88% of radio AGNs. This technique can be applied to any prototypical FR-II radio source (e.g. straight jets and with minimal host galaxy emission); non-degenerate solutions are obtained for >85% of objects at redshifts $z < 0.82$, and approximately half at higher redshifts.

These cosmological model fits to the radio AGN standardisable candles yield dark energy and matter densities of $\Omega_{\rm m} = 0.28 \pm 0.02$ and $\Omega_\Lambda = 0.76 \pm 0.07$ respectively. These measurements are inconsistent with a non-accelerating universe at greater than the 6σ level, but consistent with a flat universe ($\Omega_{\rm k} = -0.04 \pm 0.07$). The cosmological parameters tighten to $\Omega_{\rm m} = 0.289 \pm 0.012$ and $\Omega_\Lambda = 0.711 \pm 0.012$ under the assumption of a flat universe. Combining my results with cosmic microwave background power spectra (Planck Collaboration 2016) to calibrate the absolute distance to the AGN standardisable candles yields a Hubble constant of $H_0 = 67.88 \pm 0.58$. These measurements are consistent with those obtained from baryon acoustic oscillations and JLA type 1a supernovae. The inclusion of further radio AGNs from high-redshift surveys will enable my technique to provide an even tighter constraint on the matter and energy content of the universe. However, high-redshift radio sources are especially susceptible to inverse-Compton losses from the upscattering of CMB photons; only the youngest radio sources will have appreciable radio emission (Blundell & Rawlings 1999). These young radio sources must also expand well beyond their host galaxy to avoid free-free and synchrotron self-absorption severely curtailing their low-frequency radio emission. These two effects limit the detectable high-redshift population to

young radio sources with very-high jet powers, capable of rapidly inflating large lobes. Future improvements to this distance measuring technique would logically model the photons scattered up to X-ray energies to provide a means of detecting a potential population of old high-redshift radio sources.

Chapter 6

Conclusions

The key outcomes of this thesis include: (1) a new theoretical model describing the dynamics and synchrotron luminosity evolution of radio active galactic nuclei (AGN), (2) a new resolved emissivity model enabling selection biases in future surveys to be understood and corrected, (3) a new technique to measure redshifts of AGN based exclusively on radio-frequency observations, and (4) a new high-redshift standardisable candle capable of constraining the cosmological parameters.

In this thesis, I have described a new dynamical model for the jet-driven evolution of radio AGN lobes from the strong shock supersonic phase through to late-time subsonic expansion. The model differs from previous analytic radio source models (e.g. Falle 1991; Kaiser et al. 1997; Luo & Sadler 2010) in three main respects: it (1) simulates expansion beyond the strong-shock and subsonic limits, (2) uses external pressure profiles based on semi-analytic galaxy evolution models and X-ray observations, and (3) includes the Rayleigh-Taylor mixing of the cocoon with the surrounding material. The lobe size and volume evolution predicted by the dynamical model is shown to closely match that of hydrodynamical simulations (Hardcastle 2013; Hardcastle & Krause 2014). However, some weaker sources never form lobes, instead flaring close to the core as their jets get disrupted by the dense external medium. The dynamics of these "flaring jet" radio sources are incorporated in the dynamical model by considering a plume rising outward under pressure-limited expansion.

The radio emission arising from the mock radio sources in this thesis is described using a new luminosity model which considers: (1) radiative loss mechanisms as a function of position, (2) arbitrary environment or lobe expansion, and (3) an analytical framework which allows observations of large numbers of radio AGN to be interpreted. This resolved emissivity model can be readily applied atop both existing hydrodynamical

simulations and analytic models. This synchrotron emissivity model in conjunction with the FR-II dynamical model can reproduce the spatial distribution of spectral ages measured in 3C436 using X-ray inverse-Compton upscattered CMB radiation. Further, when applied atop the flaring jet dynamical model it can reproduce key features of the observed surface brightness distribution in the archetypal twin-jet FR-I 3C31.

Kinetic jet power estimates based exclusively on observed monochromatic radio luminosities are highly uncertain due to confounding variables and a lack of knowledge about some aspects of the physics of AGNs. In this thesis, I proposed a new methodology to calculate the jet powers of the largest, most powerful radio sources based on combinations of their size, lobe luminosity and shape of their radio spectrum. The jet powers and lobe magnetic field strengths of 3C radio sources are shown to be reliably estimated using solely the lobe luminosity and spectral curvature, enabling the intrinsic properties of unresolved high-redshift sources to be inferred. By contrast, the radio source ages cannot be estimated without knowledge of the lobe volumes, whilst the monochromatic lobe luminosity alone is incapable of accurately estimating the jet power or source age without knowledge of the lobe magnetic field strength and size respectively. This analysis can be applied to future survey design to ensure the maximum scientific benefit can be derived from any allocated time; specifically the minimal set of observables required to measure key AGN physical parameters.

The improved characterisation of the interaction between AGN and their host galaxies resulting from my work will provide invaluable input into galaxy formation and evolution models. For example, applying my AGN dynamical model to a volume-limited sample shows that radio sources in massive galaxies remain active for longer, spend less time in the quiescent phase, and inject more energy into their hosts than their less massive counterparts. I also found that the environments of these AGN are in or close to long-term heating-cooling balance. This model will be a useful tool in the interpretation of high-redshift survey data, especially with the plethora of data expected from *Square Kilometre Array* (SKA) pathfinder surveys. At lower redshifts, future sensitive X-ray surveys of the gas density and temperature profiles of the AGN environments (e.g. ATHENA) will be complementary to my work. This will enable asymmetries in the environments of hybrid objects (i.e. FR-I one side, FR-II the other) to be accurately modelled to test whether environment is the cause of lobe morphology.

The limitations of future radio surveys when measuring AGN energetics have been quantified using my radio source model. In particular, the observed size of FR-I sources is found to reduce as $D \propto S^{-0.5}$ and the energy input into their host through AGN feedback as $E \propto S^{-1}$, where S is the survey flux detection limit. The emerging

FR0 class of radio sources, comprising Gigahertz Peaked and Compact Steep Spectrum sources (GPS and CSS), can potentially be explained by a population of these low-powered FR-Is. Low powered FR-I and FR0 (many may be FR-Is) type objects are expected to comprise the vast majority of radio sources identified in next-generation surveys such as ASKAP EMU and MeerKAT MIGHTEE. It is therefore crucial to develop a greater understanding of the observational limitations encountered when measuring the properties of these objects. Bayesian fitting algorithms for the radio source energetics may need to consider the array sensitivity and configuration to accurately match observations to modelled sources, in particular, due to difficulty in creating a robust metric for the lobe size. Further, the magnetic field strength may be constrained using as few as two observing frequencies with the spatial distribution of the spectral index providing the additional model constraint. These future model enhancements would enable the energetics of resolved low powered FR-I to be readily calculated.

Very bright and large radio-loud AGNs are readily observable to very high ($z > 7$) redshifts, providing an opportunity to probe distance scales across cosmic time. I have presented a new technique for creating standardisable candles, based exclusively on radio-frequency observations of the most powerful AGNs; specifically their radio flux, lobe angular size, and radio spectrum. I have constructed radio AGN standardisable candles from objects in the 3C and HeRGE surveys, and have shown these to be inconsistent with a non-accelerating universe at greater than the 6σ level, but are consistent with a flat universe. These cosmological model fits to my radio AGN standardisable candles yield dark energy and matter densities of $\Omega_{\rm m} = 0.289 \pm 0.012$ and $\Omega_{\Lambda} = 0.711 \pm 0.012$ under the assumption of a flat universe. Combining my results with cosmic microwave background power spectra (Planck Collaboration 2016) to calibrate the absolute distance to my AGN standard candles yields a Hubble constant of $H_0 = 67.88 \pm 0.58$. These measurements are consistent with those obtained from baryon acoustic oscillations and JLA type 1a supernovae. The inclusion of further radio AGNs from high-redshift surveys will enable my technique to provide an even tighter constraint on the matter and energy content of the Universe.

At present, the redshifts of radio AGNs are measured using the optical spectroscopy or photometry of the associated host galaxy. This could prove problematic for future surveys using precursors to the *Square Kilometre Array* (SKA), such as ASKAP EMU (Norris et al. 2011) and MeerKAT MIGHTEE (Jarvis 2012), which will probe large portions of sky with limited observations outside radio frequencies. In this thesis, I have shown that my radio AGN distance measure provides accurate photometric redshifts based exclusively upon multi-frequency radio observations. These radio pho-

tometric redshift measurements for a sample of objects from the 3C survey differ from the host galaxy spectroscopic redshifts by less than 15% for 95% of sources, and less than 10% for 88% of radio AGNs. Construction of a high-speed and automated process to estimate the redshift of the millions of AGNs in these surveys will be essential to fully capitalise on the scientific potential of these observations, and the telescopes themselves. This method could be combined with a galaxy clustering algorithm so that redshift estimates can be obtained for the vast majority of galaxies in these surveys.

The new, comprehensive AGN evolution model presented in this thesis combines several established branches of radio source physics to yield high-quality estimates for the energetics of radio AGN. The results of this model are in good agreement with those of hydrodynamical simulations, yet it is much less computationally intensive making it suitable for the analysis of the millions of sources in future large-sky surveys. Further, the radio source model predictions match direct observations of the spectral age and spatial luminosity distributions, successfully reproduce the spectroscopic redshifts of distant sources and fit a cosmology for our Universe consistent with independent measurements.

Bibliography

Abramowicz, M. A., Czerny, B., Lasota, J. P., & Szuszkiewicz, E. 1988, ApJ, 332, 646

Alexander, P. 2000, MNRAS, 319, 8

Alexander, P. 2002, MNRAS, 335, 610

Alexander, P. 2006, MNRAS, 368, 1404

Alexander, P., & Leahy, J. P. 1987, MNRAS, 225, 1

Allen, S. W., Rapetti, D. A., Schmidt, R. W., et al. 2008, MNRAS, 383, 879

Allen, S. W., Taylor, G. B., Nulsen, P. E. J., et al. 2001, MNRAS, 324, 824

Allison, J. R., Sadler, E. M., Moss, V. A., et al. 2015, MNRAS, 453, 1249

Arévalo, P., Churazov, E., Zhuravleva, I., Forman, W. R., & Jones, C. 2016, ApJ, 818, 14

Arnaud, M., & Evrard, A. E. 1999, MNRAS, 305, 631

Asada, K., & Nakamura, M. 2012, ApJ, 745, 28

Aubourg, E., et al. 2015, Phys.Rev., D92, 123516

Bahcall, J. N., Kirhakos, S., Saxe, D. H., & Schneider, D. P. 1997, ApJ 479, 642

Baldi, R. D., Capetti, A., & Giovannini, G. 2016, AN, 337, 114

Bannister, K. W., Stevens, J., Tuntsov, A. V., et al. 2016, Science, 351, 354

Barthel, P. D., & Arnaud, K. A. 1996, MNRAS, 283, 45

Baugh, C. M. 2006, A&G, 47b, 10

Becker, R. H., White, R. L., & Helfand, D. J. 1995, ApJ, 450, 559

Bell, E. F., McIntosh, D. H., Katz, N., & Weinberg, M. D. 2003, ApJS, 149, 289

Bender, R., & Saglia, R. P. 1999, in *Galaxy Dynamics*, eds. D. Merritt, J. A. Sellwood, & M. Valluri, ASP Conf. Series, 182, 113

Best, P. N. 2000, MNRAS, 317, 720

Best, P. N. 2009, AN, 330, 184

Best, P. N., & Heckman, T. M. 2012, MNRAS, 421, 1569

Best, P. N., Kauffmann, G., Heckman, T. M., et al. 2005, MNRAS, 362, 25

Best, P. N., Longair, M. S., & Röttgering, H. J. A. 1998, MNRAS, 295, 549

Best, P. N., von der Linden, A., Kauffmann, G., Heckman, T. M., & Kaiser, C. R. 2007, MNRAS, 421, 1569

Bicknell, G. V. 1995, ApJ Supp., 101, 29

Bicknell, G., Dopita, M. A., & O'Dea, C. P. 1997, ApJ, 485, 112

Binney, J., Alouani Bibi, F., & Omma, H. 2007, MNRAS, 377, 142

Bîrzan, L., McNamara, B. R., Nulsen, P. E. J., Carilli, C. L., & Wise, M. W. 2008, ApJ, 686, 859

Blandford, R. D., & Payne, D. G. 1982, MNRAS 199, 883

Blandford, R. D., & Znajek, R. L. 1977, MNRAS 179, 433

Blundell, K. M., Fabian, A. C., Crawford, C. S., Erlund, M. C., & Celotti, A. 2006, ApJ, 644, L13

Blundell, K. M., & Rawlings, S. 1999, Nature, 399, 330

Blundell, K. M., & Rawlings, S. 2000, ApJ, 119, 1111

Blundell, K. M., Rawlings, S., & Willott, C. J. 1999, AJ, 117, 677

Boehringer, H., Voges, W., Fabian, A. C., Edge, A. C., & Neumann, D. M. 1993, MNRAS, 264, 25

Bower, R. G., Benson, A. J., Malbon, R., et al. 2006, MNRAS, 370, 645

Boyle, B. J., & Terlevich, R. J. 1998, MNRAS, 293, 49

Brighenti, F., & Mathews, W. G. 2003, ApJ, 587, 580

Bruzual, G., & Charlot, S. 2003, MNRAS, 344, 1000

Burbidge, G. R., 1956, ApJ, 124, 416

Callingham, J. R., Ekers, R. D., Gaensler, B. M., et al. 2017, ApJ, 836, 174

Carilli, C. L., Perley, R. A., Dreher, J. W., & Leahy, J. P. 1991, ApJ, 383, 554

Carroll, S. M. 2001, LLR, 4, 1

Cattaneo, A., & Best, P. N. 2009, MNRAS, 395, 518

Cavagnolo, K. W., McNamara, B. R., Nulsen, P. E. J., et al. 2010, ApJ, 720, 1066

Celotti, A., & Fabian, A. C. 1993, MNRAS, 264, 228

Churazov, E., Bruggen, M., Kaiser, C. R., Böhringer, H., & Forman, W. 2001, ApJ, 554, 261

Churazov, E., Sunyaev, R., Forman, W., & Böhringer, H. 2002, MNRAS, 332, 729

Condon, J. J., Cotton, W. D., Greisen, E. W., et al. 1998, AJ, 115, 1693

Cook, A. W., Cabot, W., & Miller, P. L. 2004, J. Fluid Mech., 511 333

Cowie, L. L., Songaila, A., Hu, E. M., & Cohen, J. G. 1996, AJ, 112, 839

Croston, J. H., Birkinshaw, M., Hardcastle, M. J., & Worrall, D. M. 2004, MNRAS, 353, 879

Croston, J. H., & Hardcastle, M. J. 2014, MNRAS, 438, 3310

Croston, J. H., Hardcastle, M. J., Birkinshaw, M., Worrall, D. M., & Laing, R. A. 2008a, MNRAS, 386, 1709

Croston, J. H., Pratt, G. W., Böhringer, H., et al. 2008b, A&A, 487, 431

Croston, J. H., Hardcastle, M. J., Harris, D. E., et al. 2005, ApJ, 626, 733

Croston, J. H., Kraft, R. P., Hardcastle, M. J., et al. 2009, MNRAS, 395, 1999

Croton, D. J., Springel, V., White, S. D. M., et al. 2006, MNRAS, 365, 11

Croton, D. J., Stevens, A. R. H., Tonini, C., et al. 2016, ApJS, 222, 22

Czerny, B., Hryniewicz, K., Maity, I., et al. 2013, A&A, 556, 97

Daly, R. A. 2009, ApJ, 691, L72

Daly, R. A., Sprinkle, T. B., O'Dea, C. P., Kharb, P., & Baum, S. A. 2012, MNRAS, 423, 2498

De Breuck, C., Seymour, N., Stern, D., et al. 2010, ApJ, 725, 36

Dimonte, G., Youngs, D. L., Dimits, A., et al. 2004, Phys. Fluids, 16, 1668

Drell, P. S., Loredo, T. J., & Wasserman, I. 2000, ApJ, 530, 593

Dubois, Y., Gavazzi, R., Peirani, S., & Silk, J. 2013, MNRAS, 433, 3297

Dubois, Y., Pichon, C., Welker, C., et al. 2014, MNRAS, 444, 1453

Einstein, A. 1917, Sitzungsber. K. Akad., 6, 142

Eisenstein, D.J., et al. 2005, ApJ, 633, 560

English, W., Hardcastle, M. J., & Krause, M. 2016, MNRAS, 461, 2025

Erlund, M. C., Fabian, A. C., & Blundell, K. M. 2008, MNRAS, 386, 1774

Fabian, A. C. 1994, ARA&A, 32, 277

Fabian, A. C. 2012, ARA&A, 50, 455

Fabian, A. C., Sanders, J. S., Allen, S. W., et al. 2003, MNRAS, 344, L43

Fabian, A. C., Sanders, J. S., Ettori, S., et al. 2000, MNRAS, 318, L68

Falle, S. A. E. G. 1991, MNRAS, 250, 581

Fanaroff, B. L., & Riley, J. M. 1974, MNRAS 167, 31

Fanidakis, N., Baugh, C. M., Benson, A. J., et al. 1974, MNRAS 410, 53

Fermi, E., & von Neumann, J. 1953, Taylor instability of incompressible liquids, Technical Report no. AECU-2979, Los Alamos Scientific Laboratory

Forman, W., Jones, C., Churazov, E., et al. 2007, ApJ, 665, 1057

Gaibler, V., Krause, M., & Camenzind, M. 2009, MNRAS, 400, 1785

Garofalo, D., Evans, D. A., & Sambruna, R. M. 2010, MNRAS, 406, 975

Gendre, M. A., Best, P. N., & Wall, J. V. 2010, MNRAS, 404, 1719

Ghisellini, G. 2011, American Institute of Physics Conference Series, 1381, 180

Ghisellini, G., Tavecchio, F., Maraschi, L., Celotti, A., & Sbarrato, T. 2014, Nature, 515, 376

Giavalisco, M., Dickinson, M., Ferguson, H. C., et al. 2004, ApJ, 600, 103

Giovannini, G., Cotton, W. D., Feretti, L., Lara, L., & Venturi, T. 1998, ApJ, 493, 632

Godfrey, L. E. H., et al. 2009, ApJ, 695, 707

Godfrey, L. E. H., & Shabala, S. S. 2013, ApJ, 767, 12

Godfrey, L. E. H., & Shabala, S. S. 2016, MNRAS, 456, 1172

Gonzalez, A. H., Sivanandam, S., Zabludoff, A. I., & Zaritsky, D. 2013, ApJ, 778, 14

Graham, J., Fabian, A. C., & Sanders, J. S. 2008, MNRAS, 386, 278

Guidetti, D., Laing, R. A., Croston, J. H., Bridle, A. H., & Parma, P. 2008, MNRAS, 386, 278

Gültekin, K., Richstone, D. O., Gebhardt, K., et al. 2009, ApJ, 698, 198

Haas, M., Chini, R., Ramolla, M., et al. 2011, A&A, 535, 73

Hamuy, M., Phillips, M. M., Suntzeff, N. B., et al. 1996, ApJ, 112, 2408

Hardcastle, M. J. 2001, A&A, 373, 881

Hardcastle, M. J. 2013, MNRAS, 433, 3364

Hardcastle, M. J., Alexander, P., Pooley, G. G., & Riley, J. M. 1997, MNRAS, 288, 859

Hardcastle, M. J., Alexander, P., Pooley, G. G., & Riley, J. M. 1998, MNRAS, 296, 445

Hardcastle, M. J., Birkinshaw, M., Cameron, R. A., et al. 2002, ApJ, 581, 948

Hardcastle, M. J., Evans, D. A., & Croston, J. H. 2006, MNRAS, 370, 1893

Hardcastle, M. J., Evans, D. A., & Croston, J. H. 2007, MNRAS, 376, 1849

Hardcastle, M. J., Evans, D. A., & Croston, J. H. 2009, MNRAS, 396, 1929

Hardcastle, M. J., & Krause, M. G. H. 2013, MNRAS, 430, 174

Hardcastle, M. J., & Krause, M. G. H. 2014, MNRAS, 443, 1482

Hardcastle, M. J., Lenc, E., Birkinshaw, M., et al. 2016, MNRAS, 455, 3526

Häring, N., & Rix, H-W. 2004, ApJ, 604, L89

Harwood, J. J. 2017, MNRAS, 466, 2888

Harwood, J. J., Hardcastle, M. J., & Croston, J. H. 2015, MNRAS, 454, 3403

Harwood, J. J., Hardcastle, M. J., Croston, J. H. & Goodger, J. L. 2013, MNRAS, 435, 3353

Heckman, T. M., & Best, P. N. 2014, ARA&A, 52, 589

Heckman, T. M., Kauffmann, G., Brinchmann, J., et al. 2004, ApJ, 613, 109

Heesen, V., Croston, J. H., Harwood, J. J., Hardcastle, M. J., & Hota, A. 2014, MNRAS, 439, 1364

Herzog, A., Norris, R. P., Middelberg, E., et al. 2016, A&A, 593, 130

Hönig, S. F., Watson, D., Kishimoto, M., et al. 2017, MNRAS, 464, 1693

Hönig, S. F., Watson, D., Kishimoto, M., & Hjorth, J. 2014, Nature, 515, 528

Hooda, J. S., & Wiita, P. J. 1996, ApJ, 470, 211

Hu, W., Dodelson, S. 2002, ARAA, 40, 171

Huarte-Espinosa, M., Krause, M., & Alexander, P. 2011, MNRAS, 417, 382

Hubble, E. 1929, Proceedings of the National Academy of Science, 15, 168

Huynh, M., et al. 2016, GAMA Legacy ATCA Southern Survey (GLASS): A Legacy 4cm Survey of the GAMA G23 Field, www.atnf.csiro.au/observers/apply/gama_4cm_legacy_EOI.pdf

Illustris Collaboration 2017, Illustris Simulation, `http://www.illustris-project.org/`

Ineson, J., Croston, J. H., Hardcastle, M. J., et al. 2015, MNRAS, 453, 2682

Ineson, J., Croston, J. H., Hardcastle, M. J., & Mingo, B. 2017, MNRAS, 467, 1586

Jaffe, A. H., Ade, P. A., Balbi, A., et al. 2001, PRL, 86, 3475

Jaffe, W. J., & Perola, G. C. 1973, A&A, 26, 423

Jamrozy, M., Konar, C., Machalski, J., & Saikia, D. J. 2008, MNRAS, 385, 1286

Jarvis, M. J. 2012, AfrSk, 16, 44

Jester, S. 2005, ApJ, 625, 667

Jones, T. W., Ryu, D., & Engel, A. 1999, ApJ, 512, 105

Kaiser, C. R. 2000, A&A, 362, 447

Kaiser, C. R., & Alexander, P. 1997, MNRAS, 286, 215

Kaiser, C. R., & Alexander, P. 1999, MNRAS, 305, 707

Kaiser, C. R., & Best, P. N. 2007, MNRAS, 381, 1548

Kaiser, C. R., & Cotter, G. 2002, MNRAS, 336, 649

Kaiser, C. R., Dennett-Thorpe, J., & Alexander, P. 1997, MNRAS, 292, 723

Kardashev, N. S. 1962, SvA, 6, 317

Kauffmann, G., Colberg, J. M., Diaferio, A., & White, S. D. M. 1999, MNRAS, 303, 188

Kauffmann, G., Heckman, T. M., & Best, P. N. 2008, MNRAS, 384, 953

Kellermann, K. I. 1966, Australian Journal of Physics, 19, 195

Kim, A. 2004, LBNL Report, LBNL-56164

King, A. L., Davis, T. M., Denney, K. D., Vestergaard, M., & Watson, D. 2014, MNRAS, 441, 3454

King, A. L., Martini, P., Davis, T. M., et al. 2015, MNRAS, 453, 1701

Klypin, A., Trujillo-Gomez, S., & Primack, J. 2011, ApJ, 740, 102

Komatsu, E., et.al. 2011, ApJS, 192, 18

Komissarov, S. S., & Falle, S. A. E. G. 1998, MNRAS, 297, 2087

Komossa, S., & Böhringer, H. 1999, A&A, 344, 755

Kraft, R. P., Nulsen, P. E. J., Birkinshaw, M., et al. 2007, ApJ, 665, 1129

Krause, M. 2005, A&A, 431, 45

Krause, M., Alexander, P., Riley, J., & Hopton, D. 2012, MNRAS, 427, 3196

Krause, M., & Camenzind, M. 2001, A&A, 380, 789

Krishna, G-., & Wiita, P. J. 1988, Nature, 333, 49

Krishna, G-., & Wiita, P. J. 2000, A&A, 363, 507

Krolik, J. H. 1994, Active Galactic Nuclei, Princeton Univ. Press, New Jersey

Kuehr, H., Witzel, A., Pauliny-Toth, I. I. K., & Nauber, U. 1981, A&AS, 45, 367

Kwan, J., et al. 2017, MNRAS, 464, 4045

Lacey, C., & Cole, S. 1993, MNRAS, 262, 627

Laing, R. A., & Bridle, A. H. 2014, MNRAS, 437, 3405

Laing, R. A., Jenkins, C. R., Wall, J. V., & Unger, S. W. 1994, in *The Physics of Active Galaxies*, eds. G. V. Bicknell, M. A. Dopita, & P. J. Quinn, ASP Conf. Series, 54, 201

Laing, R. A., & Peacock, J. A. 1980, MNRAS, 190, 903

Laing, R. A., Riley, J. M., & Longair, M. S. 1983, MNRAS, 204, 151

Laor, A. 2001, ApJ, 553, 677

Leahy, J. P., Bridle, A. H., & Storm, R. G. revised 2013, An Atlas of DRAGNs, Jodrell Bank Centre for Astrophysics, `http://www.jb.man.ac.uk/atlas/`

Leahy, J. P., Muxlow, T. W. B., & Stephens, P. W. 1989, MNRAS, 239, 401

Leahy, J. P., & Williams, A. G. 1984, MNRAS, 210, 929

Ledlow, M. J., & Owen, F. N. 1996, AJ, 112, 9

Lilly, S. J., & Longair, M. S. 1984, MNRAS, 211, 833

Lin, Y. -T., Shen, Y., Strauss, M. A., Richards, G. T., & Lunnan, R. 2010, ApJ, 723, 1119

Livio, M., Ogilvie, G. I., & Pringle, J. E. 1999, ApJ, 512, 100

Longair, M. S. 2010, High Energy Astrophysics, Cambridge University Press

Longhetti, M., & Saracco, P. 2009, MNRAS, 394, 774L

Luo, Q., & Sadler, E. M. 2010, ApJ, 713, 398

Machalski, J., Chyży, K. T., & Jamrozy, M. 2004, PASA, 54, 249

Magorrian, J., Tremaine, S., Richstone, D., et al. 1998, AJ, 115, 2285

Manolakou, K., & Kirk, J. G. 2002, A&A, 391, 127

Marconi, A., & Hunt, L. K. 2003, ApJ, 589, L21

Marecki, A., Spencer, R. E., & Kunert, M. 2003, ACTA Astron., 20, 46

Martínez-Sansigre, A., & Rawlings, S. 2011, MNRAS, 414, 1937

Massaglia, S., Bodo, G., Rossi, P., Capetti, S., & Mignone, A. 2016, A&A, 596, 12

Massaro, F., Tremblay, G. R., Harris, D. E., et al. 2012, ApJS, 203, 31

Mauch, T., & Sadler, E. M. 2007, MNRAS, 375, 931

McConnell, N. J., & Ma, C. 2013, ApJ, 764, 184

McGaugh, S. S., Schombert, J. M., de Blok, W. J. G., & Zagursky, M. J. 2010, ApJ, 708, L14

McKean, J. P., Godfrey, L. E. H., Vegetti, S., et al. 2016, MNRAS, 463, 3143

McLure, R. J., Jarvis, M. J., Targett, T. A., Dunlop, J. S., & Best, P. N. 2006, MNRAS, 369, 1395M

McNamara, B. R., & Nulsen, P. E. J. 2007, ARA&A, 45, 117

Meier, D. L. 2001, ApJ, 548, L9

Meier, D. L. 2002, NewAR, 46, 247

Mignone, A., Bodo, G., Massaglia, S., et al. 2007, ApJS, 170, 228

Miley, G. 1980, ARA&A, 18, 165

Milne, P. A., Foley, R. J., Brown, P. J., & Narayan, G. 2015, ApJ, 803, 1

Mittal, R., Hudson, D. S., Reiprich, T. H., & Clarke, T. 2009, A&A, 501, 835

Mukherjee, D., Bicknell, G. V., Sutherland, R., & Wagner, A. 2016, MNRAS, 461, 967

Mullin, L. M., Riley, J. M., & Hardcastle, J. M. 2008, MNRAS, 390, 595

Munari, E., Biviano, A., Borgani, S., Murante, G., & Fabjan, D. 2013, MNRAS, 430, 2638

Murgia, M., Fanti, C., Fanti, R., et al. 1999, A&A, 345, 769

Murphy, T., Sadler, E. M., Ekers, R. D., et al. 2010, MNRAS, 402, 2403

Myers, S. T., & Spangler, S. R. 1985, ApJ, 291, 52

Nagai, H., Inoue, M., Asada, K., Kameno, S., & Doi, A. 2006, ApJ, 648, 148

Narayan, R., Mahadevan, R., & Quataert, E. 1998, *Theory of Black Hole Accretion Disks*, eds. M. A. Abramowicz, G. Bjornsson, & J. E. Pringle, Cambridge Univ. Press, Cambridge

Narayan, R., McClintock, J. E., & Yi, I. 1996, ApJ, 457, 821

Narayan, R., & Medvedev, M. V. 2001, ApJ, 562, L129

Narayan, R., & Quataert, E. 2005, Sci, 307, 77

Narayan, R., & Yi, I. 1995, ApJ, 444, 231

Navarro, J. F., Frenk, C. S., & White, S. D. 1997, ApJ, 490, 493

Neumann, D. M., & Arnaud, M. 1999, A&A, 348, 711

Nielsen, J. T., Guffanti, A., & Sarkar, S. 2016, NatSR, 635596

Norris, R. P., et al. 2011, PASA, 28, 215

Oknyanskij, V. L., & Horne, K. 2001, ASPC, 224, 149

Oknyanskij, V. L., Lyuty, V. M., Taranova, O. G., & Shenavrin, V. I. 1999, AstL, 25, 483

Omma, H., Binney, J., Bryan, G., & Slyz, A. 2004, MNRAS, 348, 1105

Orr, M. J. L., & Browne, I. W. A. 1982, MNRAS, 200, 1067

Ortiz-Gil, A., Guzzo, L., Schuecker, P., Böhringer, H., & Collins, C. A. 2004, MNRAS, 348, 325

O'Sullivan, E., Forbes, D. A., & Ponman, T. J. 2001, MNRAS, 328, 461

Owen, F. N., & Ledlow, M. J. 1994, ASPC, 54, 319

Owers, M. S., et al. 2017, MNRAS, 468, 1824

Pacholczyk, A. G. 1970, Radio Astrophysics, Freeman & Co., San Francisco

Padilla, N., & Strauss, M. 2008, MNRAS, 388, 1321

Park, M. G., & Ostriker, J. P. 2001, ApJ, 549, 100

Penrose, R., & Floyd, R. M. 1971, NPhS, 229, 177

Peres, C. B., Fabian, A. C., Edge, A. C., et al. 1998, MNRAS, 298, 416

Perlmutter, S., et al. 1999, ApJ, 517, 565

Peterson, B. M. 1997, An Introduction to Active Galactic Nuclei, Cambridge University Press

Peterson, J. R., Paerels, F. B. S., Kaastra, J. S., et al. 2001, A&A, 365, L104

Phillips, M. M. 1993, ApJ, 413, L105

Pimbblet, K. A., Shabala, S. S., Haines, C. P., Fraser-McKelvie, A., & Floyd, D. J. E. 2012, MNRAS, 429, 1827

Planck Collaboration 2014, A&A, 571, A16

Planck Collaboration 2016, A&A, 594, A13

Ponman, T. J., Sanderson, A. J. R., & Finoguenov, A. 2003, MNRAS, 343, 331

Pope, E. C. D., Mendel, J. T., & Shabala, S. S. 2012, MNRAS, 419, 50

Pratt, G. W., & Arnaud, M. 2002, A&A, 394, 375

Pratt, G. W., Arnaud, M., & Pointecouteau, E. 2006, A&A, 446, 429

Pryke, C., Halverson, N. W., Leitch, E. M., et al. 2002, ApJ, 568, 46

Pu, H.-Y., Hirotani, K., & Chang, H.-K. 2012, ApJ, 758, 113

Punsly, B. 2011, MNRAS, 418, 2736

Rafferty, D. A., McNamara, B. R., Nulsen, P. E. J., & Wise, M. W. 2006, ApJ, 652, 216

Raouf, M., Shabala, S. S., Croton, D. J., Khosroshahi, H. G., & Bernyk, M. 2017, MNRAS, in press

Rawlings, S., & Jarvis, M. J. 2004, MNRAS, 355, 9

Rayleigh, Lord 1883, Proc. London Math. Soc., 14, 170

Riess, A. G., et al. 1998, AJ, 116, 1009

Riess, A. G., Strolger, L. G., Casertano, S., et al. 2007, ApJ. 659, 98

Ristorcelli, J. R., & Clark, T. T. 2004, J. Fluid Mech., 507, 213

Rudnick, L., Katz-Stone, D. M., & Anderson, M. C. 1994, ApJS, 90, 955

Rybicki, G. B., & Lightman, A. P. 1979, Radiative processes in astrophysics. Wiley, New York

Sadler, E. M., Jackson, C. A., Cannon, R. D., et al. 2002, MNRAS, 329, 227

Schaye, J., Crain, R. A., & Bower, R. G. 2015, MNRAS, 446, 521

Seymour, N., Stern, D., De Breuck, C., et al. 2007, ApJS, 171, 353

Shabala, S. S., & Alexander, P. 2009a, MNRAS, 392, 1413

Shabala, S. S., & Alexander, P. 2009b, ApJ, 699, 525

Shabala, S. S., Ash, S., Alexander, P., & Riley, J. M. 2008, MNRAS, 388, 625

Shabala, S. S., Deller, A., Kaviraj, S., et al. 2017, MNRAS, 464, 4706

Shabala, S. S., & Godfrey, L. E. H. 2013, ApJ, 769, 129

Shabala, S. S., Kaviraj, S., & Silk, J. 2011, MNRAS, 413, 2815

Shabala, S. S., Yuan-Sen, T., Sugata, K., et al. 2012, MNRAS, 423, 59S

Shakura, N. I., & Sunyaev, R. A. 1973, A&A, 24, 337

Shelton, D. L., Hardcastle, M. J., & Croston, J. H. 2011, MNRAS, 418, 811

Silk, J., & Rees, M. J. 1998, A&A, 331, L1

Simpson, C., Rawlings, S., & Lacy, M. 1999, MNRAS, 306, 828

Somerville, R. S., & Davé, R. 2015, ARA&A, 53, 51

Spergel, D. N., Bean, R., Doré, O., et al. 2007, ApJ Supp., 170, 377

Spitzer, L. 1962, *Physics of Fully Ionized Gases*, Wiley, New York

Springel, V., et al. 2005, Nature, 435, 629

Sutherland, R. S., & Dopita, M. A. 1993, ApJS, 88, 253

Szuszkiewicz, E., Malkan, M. A., & Abramowicz, M. A. 1996, ApJ, 458, 474

Tamura, T., Kaastra, J. S., Peterson, J. R., et al. 2001, A&A, 365, L87

Taylor, G. I. 1950, Proc. London Math. Soc., A201, 192

Thoul, A. A., & Weinberg, D. H. 1995, ApJ, 442, 480

Tremaine, S., Gebhardt, K., Bender, R., et al. 2002, ApJ, 574, 740

Tremonti, C. A., Heckman, T. M., Kauffmann, G., et al. 2004, ApJ, 613, 898

Tribble, P. C. 1991, MNRAS, 253, 147

Venturi, T., Dallacasa, D., & Stefanachi, F. 2004, A&A 422, 515

Vikhlinin, A., Forman, W., & Jones, C. 1999, ApJ, 525, 47

Vikhlinin, A., Kravtsov, A., Forman, W., et al. 2006, ApJ, 640, 691

Vogelsberger, M., Genel, S., Springel, V., et al. 2014, Nature, 509, 177

Voit, G. M. 2005, RevMP, 77, 207

Wardle, J. F. C., Homan, D. C., Ojha, R., & Roberts, D. H. 1998, Nature, 395, 457

Watson, D., Denney, K. D., Vestergaard, M., & Davis, T. M. 2011, ApJ, 740, L49

Weinberg, S. 1989, Rev. Mod. Phys., 61, 1

White, S. D. M., & Frenk, C. S. 1991, ApJ, 379, 52

White, S. D. M., & Rees, M. J. 1978, MNRAS, 183, 341

Williams, W. L., & Röttgering, H. J. A. 2015, MNRAS, 450, 1538

Willman, R. J., Miller, L., Jarvis, M. J., et al. 2008, MNRAS, 388, 1335

Willott, C. J., Rawlings, S., Blundell, K. M., & Lacy, K. 1999, MNRAS, 309, 1017

Willott, C. J., Rawlings, S., Jarvis, M. J., & Blundell, K. M. 2003, MNRAS, 339, 173

Wold, M., Lacy, M., & Armus, L. 2007, A&A, 470, 531

Worrall, D. M., & Birkinshaw, M. 2014, ApJ, 784, 36

Wright, E. L. 2006, PASP, 118, 1711

Yang, X., Mo, H. J., & van den Bosch, F. C. 2007, ApJ, 671, 153

Yoshii, Y., Kobayashi, Y., Minezaki, T., Koshida, S., & Peterson, B. A. 2014, ApJ, 784, L11

Zel'dovich, Y. B. 1968, Sov. Phys. Usp., 11, 381

Zhuravleva, I., Churazov, E., Arévalo, P., et al. 2015, MNRAS, 450, 4184

Appendicies

A1 Ellipsoidal trigonometry

The working surface pressure at each angle θ differs from that along the jet axis due to the non-spherical nature of the lobe. There are two relevant pressures here: the external pressure due to the ambient medium, and ram pressure due to the lobe expansion. The latter requires a conversion from the radial expansion rate of each lobe element to the velocity normal to its surface. Sections of the lobe expanding supersonically will maintain self-similar growth (approximately self-similar when outside strong-shock limit) and can thus be modelled by an ellipsoid with a constant axis ratio A. The component of the velocity normal to the surface at angle θ is related to the expansion rate along the jet axis $v_\perp(\theta = 0)$ through

$$\zeta(\theta) = \frac{v_\perp(\theta)}{v_\perp(\theta = 0)} = \left[\frac{A^2 \sin^2\theta + \cos^2\theta}{A^4 \sin^2\theta + \cos^2\theta}\right]^{1/2}, \tag{1}$$

where we have defined a dimensionless velocity ζ. This coefficient can be calculated with a typical value of the lobe axis ratio for powerful FR-II sources. This normal velocity along the jet axis, $v_\perp(\theta = 0)$, is now related to the rate of lobe expansion in the θ direction for the assumed ellipsoidal lobe. The radial distance to the working surface at angle θ from the central black hole is related to the radius along the jet axis $R(\theta = 0)$ by

$$\eta(\theta) = \frac{R(\theta)}{R(\theta = 0)} = \frac{\dot{R}(\theta)}{v_\perp(\theta = 0)} = \frac{1}{\sqrt{A^2 \sin^2\theta + \cos^2\theta}}, \tag{2}$$

where I have defined a dimensionless radius η. The velocity normal to the surface at each angle θ is therefore related to the radial expansion rate of the relevant lobe volume element through $v_\perp = \zeta\dot{R}/\eta$.

These definitions for the dimensionless radius and velocity are also useful in describing

the initial self-similar growth phase of the entire lobe. Here, these equations allow for analytically tractable solutions for the expansion of each volume element and thus the fraction of the jet power required by each element to maintain self-similarity. In the strong-shock supersonic limit, the jet power is proportional to the angular location of the volume element as

$$\frac{8\pi k \sin\theta d\theta}{3(\Gamma_{\rm x}+1)}\left[(3\Gamma_{\rm c}-\beta)R^{2-\beta}\dot{R}^3+2R^{3-\beta}\dot{R}\ddot{R}\right]_{\theta=0}\eta^{3-\beta}(\theta)\zeta^2(\theta)=(\Gamma_{\rm c}-1)Q\,d\lambda(\theta), \quad (3)$$

using Equations 2.3, 2.5 and 2.6.

A2 3C radio source parameters

The key observed and derived parameters of the 3C radio sources are summarised in Tables A2.1 and A2.2 on the following pages.

Table A2.1: Radio source jet powers, ages and equipartition factors estimated for the sample of 37 3C radio AGN with the requisite data to be fitted using the FULL FIT algorithm. The redshift, size and luminosity observables are extracted from Mullin et al. (2008), the stellar masses are calculated using flux densities taken from Willott et al. (2003) and Mullin et al. (2008), and the spectral break frequencies are derived from fits to the multi-frequency luminosity observations of Laing & Peacock (1980). The goodness of fit of the CI model to their spectra across the entire 0.01-10 GHz frequency range is included in the final column (i.e. probability that the CI model fits the data); spectra which are well fitted with the removal of a single outlying low-frequency point are marked with a dagger and those with multiple inconsistent points with stars. The break frequencies of these noisy spectra are well fitted by supplementing the Laing & Peacock (1980) observations with additional literature data. Pictor A is calculated using observations by Kuehr et al. (1981) and Hardcastle et al. (2016); some caution should be exercised when comparing these results due to the use of different datasets.

Source	z	$M_\star$	D	L_{178}	ν_b	Q	t_age	B/B_eq	CI Fit
		[log $\mathrm{M}_\odot$]	[kpc]	[log W/Hz]	[log Hz]	[log W]	[log yrs]		[p-value]
3C6.1	0.8404	-	207±8	28.62	9.5±0.6	39.6±0.2	7.3±0.2	0.34±0.04	0.93
3C19	0.482	11.89	40±1	28.00	9.8±0.6	38.6±0.2	6.8±0.3	0.36±0.04	0.88
3C20	0.174	11.52	151±2	27.57	9.7±1.2	38.4±0.2	7.5±0.3	0.43±0.06	0.91
3C41	0.795	11.62	185±7	28.41	9.9±0.5	39.7±0.2	7.2±0.3	0.27±0.03	0.59
3C42	0.395	11.73	150±1	27.82	9.7±0.7	38.3±0.2	7.7±0.2	0.34±0.04	0.76
3C55	0.735	11.75	510±7	28.77	8.1±1.3	39.0±0.2	8.2±0.2	0.55±0.09	0.19
3C67	0.3102	-	15±2	27.48	9.8±1.0	38.0±0.2	6.4±0.3	0.43±0.05	0.10
3C79	0.2559	11.66	366±23	27.82	9.0±1.0	38.0±0.2	8.3±0.2	0.43±0.05	0.17
3C123	0.2177	11.73	110±7	28.43	10.0±0.4	38.9±0.2	7.4±0.3	0.28±0.03	<0.05†
3C132	0.214	11.66	77±1	27.27	10.0±0.6	38.3±0.2	7.0±0.2	0.44±0.05	<0.05**
3C153	0.2769	11.80	34±3	27.57	9.3±1.0	38.2±0.2	6.8±0.3	0.51±0.07	<0.05†
3C171	0.2384	11.49	38±0	27.55	10.0±0.6	37.8±0.2	7.2±0.3	0.35±0.04	0.69
3C175.1	0.92	11.58	61±3	28.70	9.4±0.7	39.5±0.2	6.7±0.3	0.34±0.04	0.58
3C184	0.994	-	38±5	28.83	9.0±0.5	39.3±0.2	6.6±0.3	0.38±0.05	0.68
3C196	0.871	-	48±4	29.38	9.0±1.2	39.6±0.2	6.8±0.3	0.31±0.04	0.64
3C217	0.8975	11.48	104±24	28.63	9.0±0.8	39.6±0.2	6.7±0.3	0.53±0.07	<0.05**
3C219	0.1744	11.77	566±8	27.57	9.6±1.2	38.1±0.3	8.5±0.2	0.32±0.04	0.99
3C220.3	0.685	-	70±5	28.49	8.8±0.4	38.6±0.2	7.2±0.3	0.49±0.06	<0.05†
3C226	0.82	11.34	301±16	28.69	9.5±0.8	39.4±0.2	7.6±0.2	0.35±0.04	0.76
3C244.1	0.428	-	289±7	28.14	9.9±0.5	39.5±0.2	7.3±0.2	0.42±0.05	0.97
3C247	0.7489	11.99	104±9	28.38	9.4±1.1	38.7±0.2	7.6±0.3	0.29±0.04	0.27
3C263.1	0.824	11.82	67±13	28.77	8.9±1.0	39.4±0.2	6.8±0.3	0.46±0.06	0.99
3C268.1	0.9731	-	339±19	28.93	9.8±0.6	39.8±0.2	7.9±0.2	0.21±0.03	0.72
3C280	0.996	11.90	135±8	29.07	10.2±0.4	40.0±0.2	7.1±0.3	0.20±0.02	0.97
3C289	0.9674	11.91	84±1	28.74	9.1±0.9	39.5±0.2	6.9±0.3	0.38±0.05	0.93
3C300	0.272	11.43	402±84	27.63	9.7±0.6	38.6±0.2	7.8±0.2	0.47±0.06	0.99
3C319	0.192	11.25	340±14	27.24	8.2±1.5	37.2±0.2	8.6±0.2	0.62±0.11	0.98
3C325	0.86	12.18	140±11	28.71	9.1±0.6	39.8±0.2	7.0±0.3	0.40±0.05	0.07
3C330	0.549	11.86	399±3	28.51	9.7±0.5	39.6±0.2	7.6±0.2	0.36±0.04	0.23
3C340	0.7754	11.64	327±10	28.42	9.6±0.8	39.4±0.2	7.5±0.2	0.36±0.04	0.76
3C352	0.806	11.75	101±3	28.55	8.4±0.3	38.7±0.2	7.3±0.3	0.55±0.09	<0.05**
3C388	0.0908	11.85	85±5	26.73	9.7±1.0	37.1±0.1	8.1±0.2	0.23±0.03	0.87
3C401	0.201	-	80±3	27.40	9.0±0.5	37.9±0.2	7.4±0.2	0.55±0.09	0.77
3C427.1	0.572	11.47	178±7	28.58	8.3±1.3	39.1±0.2	7.3±0.2	0.72±0.13	0.99
3C438	0.29	11.96	96±3	28.10	9.0±0.3	38.0±0.2	7.6±0.2	0.39±0.05	<0.05†
3C441	0.708	11.85	261±52	28.45	10.1±0.6	39.6±0.2	7.4±0.2	0.27±0.03	0.55
3C455	0.5427	-	27±4	28.16	9.2±0.7	38.4±0.2	6.7±0.3	0.43±0.05	0.75
PictorA	0.03506	-	56±2	27.04	8.8±1.1	37.0±0.2	7.6±0.2	0.51±0.07	-

Table A2.2: Radio source jet powers and ages estimated for the sample of 34 3C radio AGN with only sufficient data to be fitted using the SOURCE SIZE algorithm. These results are calculated assuming a prior probability distribution for the equipartition factor. The redshift, size and luminosity observables are extracted from Mullin et al. (2008), and the stellar masses are calculated using flux densities taken from Willott et al. (2003) and Mullin et al. (2008). The goodness of fit of the CI model across the 0.01-10 GHz frequency range is included in the final column (see Table A2.1).

Source	z	$M_\star$	D	L_{178}	Q	$t_{\rm age}$	CI Fit
		[log $M_\odot$]	[kpc]	[log W/Hz]	[log W]	[log yrs]	[p-value]
3C16	0.405	11.45	413±78	27.84	39.6±0.2	7.6±0.2	0.29
3C22	0.938	11.73	206±7	28.71	40.1±0.2	7.1±0.2	0.86
3C33	0.0595	11.59	292±13	26.70	38.7±0.2	7.6±0.2	0.24
3C33.1	0.181	-	707±99	27.09	38.4±0.3	8.4±0.2	0.94
3C34	0.689	11.83	327±2	28.45	39.9±0.2	7.4±0.2	0.84
3C35	0.0677	11.68	905±5	26.10	37.9±0.3	9.0±0.1	0.14
3C46	0.4373	11.95	978±99	27.91	39.9±0.2	7.9±0.2	0.93
3C47	0.425	-	424±17	28.27	39.6±0.2	7.8±0.2	0.40
3C61.1	0.186	11.54	563±46	27.50	39.4±0.2	7.7±0.2	$<0.05^\dagger$
3C98	0.0306	11.40	169±1	26.04	36.9±0.1	8.8±0.4	<0.05**
3C172	0.5191	11.78	584±7	28.21	39.9±0.2	7.7±0.2	0.58
3C173.1	0.292	11.88	261±11	27.64	38.9±0.2	7.7±0.2	0.40
3C175	0.768	-	392±36	28.71	40.2±0.2	7.4±0.2	0.86
3C184.1	0.1187	11.37	395±29	26.70	38.9±0.2	7.6±0.2	0.12
3C192	0.0598	11.43	234±10	26.29	38.4±0.2	7.5±0.2	0.28
3C200	0.458	11.69	147±9	27.95	39.2±0.2	7.3±0.3	0.99
3C223	0.1368	11.45	738±5	26.89	39.0±0.2	8.0±0.2	0.95
3C225B	0.58	11.62	33±3	28.49	39.5±0.2	6.3±0.3	0.97
3C228	0.5524	11.60	307±10	28.46	40.0±0.2	7.3±0.2	0.18
3C234	0.1848	11.83	295±52	27.51	38.2±0.3	8.3±0.2	1.00
3C249.1	0.311	-	222±25	27.54	38.8±0.2	7.7±0.2	0.67
3C265	0.8108	12.06	585±58	28.81	39.6±0.2	8.3±0.1	0.99
3C274.1	0.422	11.71	921±31	28.04	40.1±0.2	7.7±0.2	0.95
3C277.2	0.766	11.61	439±96	28.55	40.4±0.2	7.3±0.2	0.83
3C284	0.2394	11.79	701±65	27.32	38.9±0.3	8.2±0.2	0.74
3C285	0.0794	11.55	265±13	26.28	37.2±0.1	8.9±0.3	0.65
3C303	0.141	11.70	121±9	26.80	37.3±0.2	8.4±0.3	<0.05**
3C336	0.927	-	201±19	28.66	39.9±0.2	7.2±0.2	0.76
3C341	0.448	11.77	449±34	27.88	39.9±0.2	7.4±0.2	0.99
3C337	0.635	11.62	307±44	28.26	39.7±0.2	7.5±0.2	0.10
3C349	0.205	11.48	287±7	27.23	39.0±0.2	7.6±0.2	0.27
3C381	0.1605	11.63	202±8	27.09	38.6±0.2	7.6±0.3	0.30
3C436	0.2145	11.76	375±14	27.40	38.8±0.2	7.9±0.2	0.95
3C452	0.0811	11.73	428±5	26.98	37.7±0.3	8.5±0.2	0.72